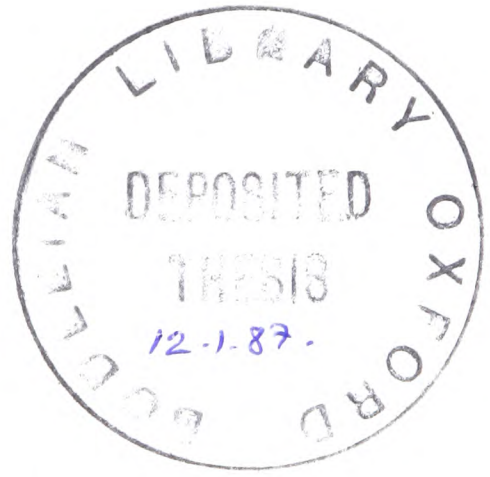
SPECTROSCOPIC STUDY OF ^{80}Sr

Raoul Francis Davie
Lincoln College



A thesis submitted in partial fulfillment of the requirements
for the degree of Doctor of Philosophy
in the University of Oxford
September 1986

to my wife

Gay

ABSTRACT

SPECTROSCOPIC STUDY OF ^{80}Sr

Raoul Francis Davie, Lincoln College, Oxford

Submitted for the degree of Doctor of Philosophy

Trinity Term 1986

High spin states in ^{80}Sr have been studied using the techniques of in-beam γ-ray spectroscopy. The reaction used was ^{54}Fe(^{29}Si, $2pn$)^{80}Sr at beam energies between 85 and 110 MeV. γ-γ coincidence measurements were performed with a thin target to investigate the level structure. Both neutron gated and singles angular distribution measurements were carried out to aid in the assignment of level spins. The directional correlation ratios extracted from the γ-γ coincidence data provided a consistency check for the spin assignments. Level lifetimes were measured by the Doppler shift attenuation method in a thick target γ-γ coincidence measurement. The ground state band has been identified up to (26^+) and three previously unobserved sidebands have been discovered.

The deduced level scheme is compared with cranking model calculations; the predicted transformation to mostly non-collective excitations of an oblate shape is not observed experimentally. The behaviour of the $J^{(1)}$ and $J^{(2)}$ moments of inertia is discussed and presented as evidence for either static or dynamic γ-deformation in the light Sr isotopes. In addition, the level structure is compared with IBM-2 calculations. These calculations indicate the importance of proton excitations across the Z=40 subshell gap, into the $g_{9/2}$ orbital, and suggest that the lowest lying ^{80}Sr sideband can be identified with the collective IBM-2 quasi-γ band.

NUCLEAR REACTIONS ^{54}Fe(^{29}Si, $2pn$), $E = 85 - 110$ MeV; measured E_γ, $I_\gamma(\theta)$, γ-γ, n-γ coincidences, DCO ratios, Doppler shifted γ-ray lineshapes. ^{80}Sr deduced levels, J, π, τ. Enriched target, Ge(Li), Ge, NE213 detectors.

ACKNOWLEDGEMENTS

I would like to thank Professor D.H. Perkins and his predecessor Professor K.W. Allen for allowing me to use the excellent facilities of the Nuclear Physics Laboratory over the last three years. I would also like to thank Dr. P.J. Twin for the use of the N.S.F. Tandem and the TESSA detector array at the S.E.R.C. Daresbury Laboratory. In addition, my supervisor Dr. D. Sinclair deserves special thanks for his help, guidance and encouragement. I am also grateful Dr. M.A. Grace for supervising me while Dr. Sinclair was on sabbatical.

Throughout the course of my studies many people have given me assistance and helped to make my stay in Oxford a pleasant one. Although it is not possible to mention everyone individually, I would like to make a few special acknowledgements. Firstly, I am extremely grateful to my fellow student Stanley Ooi for his endless help and support, particularly with anything and everything to do with computers and experimental apparatus. In addition, I would like to thank Stanley and Susan Allcock for being such pleasant company throughout my stay in room 613; and also my fellow students Alicia Kucharska, Gaynor Field, Andy Street and Shane Kościelniak for their friendship. Elspeth Garman also deserves a special mention for her constructive criticism during the final stages of the preparation of my thesis. Furthermore, I would like to thank: Kim Lister, Arthur Smith, Nina Poffé, Hewyl Price, Ian Wright and Brian Varley, in addition to David Sinclair and Stanley Ooi, for their help in collecting data and their interest in the results; Neil Rowley, for trying to explain the cranking model to me over morning tea; Sven Åberg, for bringing the γ degree of freedom to my attention; Jirina Rikovska, for her help with the IBM calculations; and Peter Twin and Paul Nolan *et al.* for all the work that they have put into TESSA. Thanks are also due to Ian McArthur for maintaining the computer facilities, and to the accelerator operators and technical staff at both the Nuclear Physics Laboratory and the Daresbury

Laboratory.

My path towards learning did not start in Oxford, but in New Zealand. For setting me in the right direction, I would like to thank: my Parents, for encouraging me to question the world around me; my old school teachers Mr. Brown and Mr. Smith for fostering my interest in mathematics and physics; and Professor A.R. Poletti, without whose help, encouragement, and confidence in me I would not have come to Oxford.

My stay in Oxford would not have been the same without Lincoln College or the many friends whom I have met there. Therefore, I would like to thank the Rector, The Revd Dr. V.H.H. Green for the privilege of being a member of that institution. The many hours spent with Nancy, Nick, Andrew, Liz, Dan, Joan, Véronique, Frances, Debbie, Dave, Phillipe.... will always be remembered alongside visions of Oxford's spires and gardens.

Most of all, I would like to thank my Family, and in particular my wife, Gay, for their love, support, patience, and understanding throughout my studies.

Finally, I am very grateful for financial support received from a Sims Empire Scholarship, which made my studies in Oxford possible, and also for an Overseas Research Student Award.

Raoul Davie

Lincoln College, Oxford

September 1986

CONTENTS

Abstract

Acknowledgements

Contents

Tables

Figures

Chapter 1. Introduction 1

Chapter 2. Theoretical Background 9

2.1 Introduction 9

2.2 The Shell Correction Method of Predicting Nuclear Shapes 10

2.2.1 The Strutinsky Shell Correction Method 10

2.2.2 Parameterization of the Nuclear Shape 11

2.2.2.1 The Lund convention 13

2.2.3 Total Potential Energy Surfaces and the Nuclear Shape 15

2.3 The Cranking Model 16

2.3.1 Routhians 16

2.3.2 The Signature Quantum Number 18

2.3.3 Quasiparticles and Pairing 19

2.3.4 Extraction of ω, I_x, $J^{(1)}$ and $J^{(2)}$ from the Experimental Data 21

2.4 Recent Developments in the Treatment of the γ Degree of Freedom 22

2.5 The Interacting Boson Model 24

2.5.1 Introduction 24

2.5.2 The IBM-2 Hamiltonian and Microscopic Interpretation 26

2.5.3 Dynamical Symmetries 29

Chapter 3. Experimental Study of ^{80}Sr 32

3.1 Introduction 32

3.2 Choice of Reaction 36

3.2.1 Introduction to Heavy-Ion Reactions 36

3.2.2 The ^{54}Fe(^{29}Si, $2pn$)^{80}Sr Reaction 38

3.3 The γ-γ Coincidence Measurement 41

3.3.1 Introduction 41

3.3.2 The TESSA II Detector Array 43

3.3.2.1 The germanium detectors 43

3.3.2.2 The Compton-suppression shields 45

3.3.2.3 The BGO ball 46

3.3.2.4 Writing events onto tape 47

3.3.3 Analysis of the γ-γ Coincidence Data 48

3.3.3.1 Efficiency calibration 51

3.3.3.2 Energy calibration 51

3.3.3.3 Lineshape calibration 51

3.3.3.4 Determination of γ-ray energies and intensities 55

3.3.3.5 γ-ray directional correlations 55

3.4 γ-Ray Angular Distribution Measurements 59

3.4.1 Introduction 59

3.4.2 Singles Angular Distribution 62

3.4.3 Neutron Detection 66

3.4.4 Neutron Gated Angular Distribution 67

3.5 The DSAM Lifetime Measurement 72

3.5.1 Introduction 72

3.5.2 Analysis of the DSAM Lifetime Data 73

3.5.2.1 Energy calibration of the γ-ray detectors 74

3.5.3 Calibration of the Attenuation Coefficient F 77

3.5.4 Side Feeding Times and Corrections For Feeding 79

Chapter 4. Experimental Results 85

4.1 Introduction 85

4.2 The Ground State Band 99

4.3 The Slow Feeding Times Identified by Belmont Moreno 106

4.4 Sideband 1 109

4.4.1 Introduction 109

4.4.2 The 777, 798, 1817 and 1838 keV Transitions 115

4.4.3 The 1678 keV Transition 121

4.5 Sideband 2 121

4.5.1 Introduction 121

4.5.2 The 724 keV Transition 126

4.5.3 The 1185 and 1316 keV Interband Transitions 127

4.6 Sideband 3 132

4.7 Unplaced Transitions 134

Chapter 5. Discussion 135

5.1 Introduction 135

5.2 The 3601 and 3580 keV 7^+ States 138

5.3 Comparison with Cranked Shell Model Calculations 139

5.4 The $J^{(1)}$ and $J^{(2)}$ Moments of Inertia in ^{80}Sr and the Light Sr Isotopes 144

5.4.1 Introduction 144

5.4.2 ^{80}Sr 145

5.4.3 The Light Sr Isotopes 149

5.5 Comparison with IBM-2 Calculations 153

5.5.1 Introduction 153

5.5.2 The Model 156

5.5.3 Results and Discussion of the IBM-2 Calculations 157

5.5.3.1 Introduction 157

5.5.3.2 IBM-2 results for the light Sr isotopes 158

5.5.3.3 IBM-2 ($N_\pi = 3$) results for ^{80}Sr sideband 1 and sideband 2 165

5.5.3.3.1 Sideband 2 165

5.5.3.3.2 Sideband 1 167

Chapter 6. Summary and Conclusions 171

Appendix A. Units **173**

Appendix B. Nuclear γ-ray Transitions **174**

B.1 Introduction 174

B.2 Conservation of Energy, Angular Momentum and Parity 174

B.3 γ-rays of Mixed Multipolarity 175

B.4 Angular Distribution of γ-rays 176

B.4.1 Angular Distribution of γ-rays Emitted From Aligned States 178

B.5 γ-ray Transition Probabilities 180

B.5.1 Total Transition Probabilities and Reduced Transition Probabilities 182

B.6 The Electric Quadrupole Moment 185

Appendix C. Energy Loss of Moving Ions in Matter **187**

Appendix D. Side Feeding Times in Heavy-Ion Fusion-Evaporation Reactions **191**

References **193**

TABLES

Chapter 2. Theoretical Background

Table 2.1 Dynamical Symmetries in IBM-2 30

Chapter 3. Experimental Study of ^{80}Sr

Table 3.1 Summary of Experimental Measurements 35

Table 3.2 Yrast Side Feeding Times and Cascade Feeding Times in ^{80}Sr 81

Chapter 4. Experimental Results

Table 4.1 Energies, Intensities, Placement, Angular Distributions, DCO Ratios and Mixing Ratios of γ-Ray Transitions in ^{80}Sr 88

Table 4.2 Mean Lifetimes and Rates of γ-Ray Transitions in ^{80}Sr 92

Table 4.3 γ-γ Coincidences for the Ground State Band 95

Table 4.4 γ-γ Coincidences for Sideband 1 96

Table 4.5 γ-γ Coincidences for Sideband 2 97

Table 4.6 γ-γ Coincidences for Sideband 3 98

Chapter 5. Discussion

Table 5.1 Parameters of the IBM-2 Hamiltonian 159

Table 5.2 Comparison Between IBM-2 Calculations and Experiment for SB2 166

Table 5.3 Comparison Between IBM-2 Calculations and Experiment for SB1 168

Appendix B. Nuclear γ-ray Transitions

Table B.1 Weisskopf Estimates of Single Particle Transition Rates 184

FIGURES

Chapter 1. Introduction

Fig. 1.1 Neutron single particle levels in ^{80}Sr 3

Chapter 2. Theoretical Background

Fig. 2.1 Lund convention for the nuclear shape parameters 14

Fig. 2.2 Energy spectrum of the triaxial rotor 23

Chapter 3. Experimental Study of ^{80}Sr

Fig. 3.1 The level scheme of ^{80}Sr as proposed by Higo *et al.* 33

Fig. 3.2 Schematic diagram of the ^{54}Fe(^{29}Si, $2pn$)^{80}Sr reaction 40

Fig. 3.3 Summed γ-γ spectrum for the reaction of 110 MeV ^{29}Si on ^{54}Fe 42

Fig. 3.4 Schematic diagram of TESSA II 44

Fig. 3.5 γ-ray sum energy and multiplicity spectra 50

Fig. 3.6 Efficiency calibration for the γ-γ coincidence data 52

Fig. 3.7 Energy calibration for the γ-γ coincidence data 53

Fig. 3.8 FWHM calibration for the γ-γ coincidence data 54

Fig. 3.9 Theoretical and experimental DCO ratios 58

Fig. 3.10 Excitation functions for γ-rays produced in the reaction of ^{29}Si on ^{54}Fe ... 61

Fig. 3.11 Electronics for singles angular distribution measurement 64

Fig. 3.12 End view of the neutron detector 69

Fig. 3.13 Electronics neutron-gated angular distribution measurement 70

Fig. 3.14 DSAM γ-γ spectrum gated by the 386 keV transition 75

Fig. 3.15 DSAM lineshapes of the 1065 keV γ-ray 76

Fig. 3.16 Extraction of τ_f from γ-γ coincidence data 80

Chapter 4. Experimental Results

Fig. 4.1 Proposed energy level scheme of ^{80}Sr 86

Fig. 4.2 The level scheme of ^{80}Sr as proposed by Higo *et al.* 87

Fig. 4.3 γ-γ spectrum gated by the 386 keV transition 100

Fig. 4.4 Summed γ-γ spectrum for the 386, 595, 783 and 937 keV transitions 101

Fig. 4.5 γ-γ spectra for the 937 and 2021 keV transitions 103

Fig. 4.6 DSAM γ-ray centroid energies for the GSB 104

Fig. 4.7 γ-ray angular distribution data for the GSB 105

Fig. 4.8 Summed DSAM γ-γ spectra for both the 386 and 595 keV transitions and the 783, 937 and 1065 keV transitions 107

Fig. 4.9 γ-γ spectra for the 798 and 1817 keV γ-rays 110

Fig. 4.10 γ-γ spectra for the 970 and 777 keV γ-rays 111

Fig. 4.11 Summed γ-γ spectra for the 777, 798, 970 and 1817 keV γ-rays 112

Fig. 4.12 DSAM γ-ray centroid energies for SB1 113

Fig. 4.13 γ-ray angular distribution data for SB1 114

Fig. 4.14 Experimental widths of spin substate distributions 117

Fig. 4.15 χ^2 analyses of the angular distribution of the 1817 keV γ-ray 118

Fig. 4.16 χ^2 analyses of the angular distribution of the 1838 keV γ-ray 119

Fig. 4.17 γ-γ spectra for the 1105 and 877 keV γ-rays 122

Fig. 4.18 DSAM γ-ray centroid energies for SB2 and SB3 124

Fig. 4.19 γ-ray angular distribution data for transitions in SB2 and SB3 125

Fig. 4.20 χ^2 analyses of the angular distribution of the 1185 keV γ-ray 129

Fig. 4.21 χ^2 analyses of the angular distribution of the 1316 keV γ-ray 131

Fig. 4.22 γ-γ spectra for the 1035 and 1343 keV γ-rays 133

Chapter 5. Discussion

Fig. 5.1 Plot of I_x, $J^{(1)}$ and $J^{(2)}$ for the bands in ^{80}Sr 136

Fig. 5.2 Transition quadrupole moments for the ^{80}Sr GSB 137

Fig. 5.3 Quasiparticle routhians in ^{80}Sr 141

Fig. 5.4 TPE surface calculations for the N$\sim$Z$\sim$40 nuclei 146

Fig. 5.5 TPE surface calculations for ^{80}Sr as a function of spin 147

Fig. 5.6 Energies and decay strengths of the 2_1^+ levels in ^{78,80,82,84,86,88}Sr 150

Fig. 5.7 I_x for the ground state bands and $2_2^+/4_1^+$ ratios in ^{78,80,82,84}Sr 151

Fig. 5.8 Experimental systematics of positive parity levels in ^{78,80,82,84,86}Sr 152

Fig. 5.9 IBM-2 energy levels with $N_\pi = 1$ for ^{78,80,82,84}Sr 160

Fig. 5.10 IBM-2 energy levels with $N_\pi = 3$ for ^{78,80,82,84,86}Sr 161

Fig. 5.11 IBM-2 energy levels with $N_\pi = 5$ for ^{78,80,82,84,86}Sr 162

Fig. 5.12 IBM-2 B($E2$) values for ^{78,80,82,84,86}Sr 163

CHAPTER 1

INTRODUCTION

There is currently considerable theoretical interest in the shapes of deformed nuclei, their rotational spectra and the changes that occur in these deformed nuclei at high angular momentum [Voi 83]. Nuclei with both N and Z close to the "magic" numbers (2, 8, 20, 28, 50, 82, 126; corresponding to the spherical closed shells) have nearly spherical shapes. However, the equilibrium shapes of nuclei away from the closed shells can be considerably deformed [Rai 50]. Recent experiments have shown that the mid-shell region with N$\sim$Z$\sim$40 contains some of the most deformed nuclei in the periodic table [Lis 82, Pie 81]. The study of nuclei with neutron and proton numbers close to 40 is of particular interest because of the wide variety of nuclear phenomena that occur in this region. For example, although it is common for the low lying excited states of a nucleus to have the same intrinsic shape, shape coexistence (similar to that of the light Hg isotopes) has been observed in the light Ge, Se and Kr isotopes [Pie 81, Hami 85] where strongly deformed states have been observed at similar energies to states with near spherical shapes. There is also some evidence [Alf 79, Buc 83, Aha 85a] for shape coexistence in the light Sr isotopes. Furthermore, although the experimental data on deformed nuclei are typically consistent with axially symmetric nuclear shapes, there is some experimental evidence for non-axially symmetric (triaxial) nuclear shapes in the light Kr isotopes [Fun 83, Kem 83].

The deformation properties of the nuclei in the N$\sim$Z$\sim$40 region vary rapidly with nucleon number, making this a particularly challenging region in which to test nuclear

models. In determining the nuclear deformation, the presence of shell gaps in deformed nuclei are particularly important [Str 67, Str 68, Bra 72], just as the spherical shell gaps play a crucial role in nuclei with N and Z near the magic numbers. It is generally considered that the region of deformation around N$\simeq$Z$\simeq$40 is a result of shell gaps that occur, for both oblate and prolate deformations, at nucleon numbers between 36 and 42 (see, for example, [Ben 84a, Hey 84, Naz 85] and fig. 1.1). The presence of these deformed shell gaps, as well as the spherical subshell closure at nucleon number 40, contributes to the rapid variation of nuclear properties which occurs in this region. Furthermore, the large influence of these shell gaps suggests that major changes in the deformation properties may occur at high spins, because of the rearrangements of the single particle energy levels due to the Coriolis force. Therefore, there is considerable interest in the behaviour of these nuclei at high spin. The well defined shell gap at nucleon number 38 with large prolate deformation ($\beta_2 \simeq 0.4$) is thought to play a dominant role in stabilizing the large prolate deformation found in this region [Naz 85, Ben 84a]. Hence, the $_{38}$Sr isotopes are of special interest.

The experimental investigation of nuclei far from stability enables nuclear models to be tested on nuclei very different from those for which they were developed. Such comparisons between theoretical predictions and experimental data often help to illuminate problems associated with certain theoretical treatments, allowing better, more general, models to be developed. In particular, the calculation of nuclear shapes is complex and presents a considerable challenge to theoreticians. Recent theoretical calculations by Ragnarsson and Sheline [Rag 84] and Möller, Nix and Bengtsson [Möl 81, Ben 84a], which seek to predict the deformations of nuclei throughout the periodic table within a unified framework, have

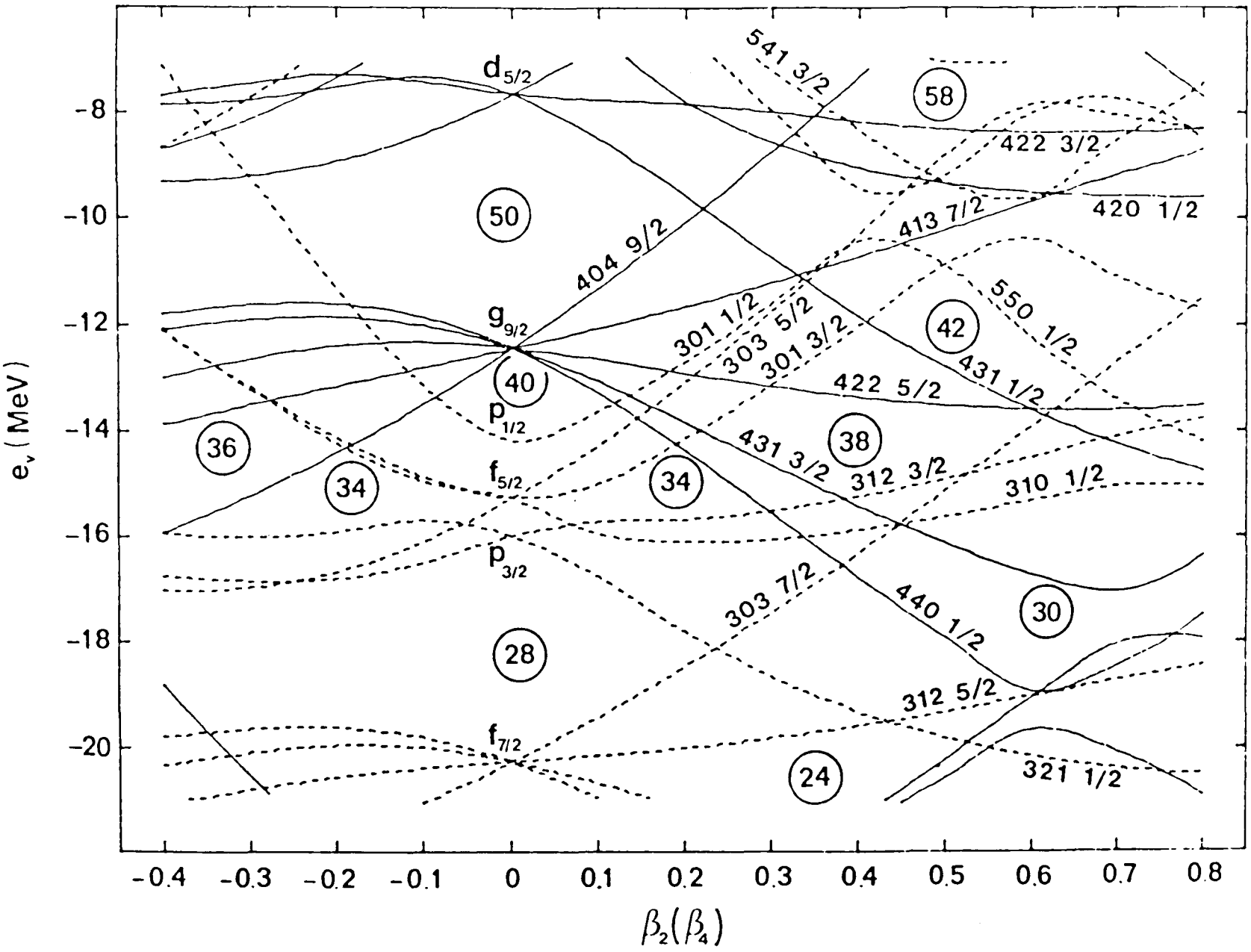


Figure 1.1 Neutron single particle levels in ^{80}Sr as functions of the quadrupole deformation β_2, calculated using a Woods-Saxon potential. The single particle levels for protons are similar. This figure is reproduced from the paper of Nazarewicz *et al.* [Naz 85].

had some success in predicting the deformed region around N∼Z∼40. These calculations obtain the nuclear total potential energy (TPE) surface (as a function of deformation) as the sum of a macroscopic liquid drop term and a microscopic term representing shell and pairing energy corrections. However, similar calculations by Åberg [Åbe 82] and Bucurescu *et al.* [Buc 79] predict ground states with nearly spherical shapes, contrary to experimental data. It has been suggested [Lis 82] that the discrepancies between these latter calculations and the experimental data may be due to incomplete treatment of possible hexadecapole deformation. In addition, Heyde *et al.* [Hey 84] have carried out detailed TPE surface calculations for the Zr isotopes over a wide range of neutron numbers. Their results, which show a strong dependence of the TPE surface on the chosen Nilsson model parameters, highlight the difficulties in making unique predictions of deformations in this mass region and the need for extensive experimental investigations of these nuclei.

There have been several theoretical attempts to describe the properties of nuclei in this region in more detail. Various forms of the interacting boson approximation (IBA) have been fairly successful in reproducing even parity yrast and low lying yrare levels in the even-even nuclei, and also transition rates and odd parity states in some cases [Buc 83, Hey 84, Kau 79, Hel 79]. In contrast with the interacting boson model descriptions, recent papers by Ahalpara *et al.* [Aha 85a, 85b] have had some success in describing the complex band structure of ^{81}Sr and ^{75,76,77}Kr in deformed Hartree-Fock shell model calculations. Furthermore, the "cranking" model was used in a recent paper by Nazarewicz *et al.* [Naz 85] to describe in detail the properties of the N∼Z∼40 nuclei as a function of both nucleon number and spin, with particular reference to the light strontium isotopes. Moreover,

Nazarewicz *et al.* make detailed predictions of the structure of ^{80}Sr as a function of spin, which can be tested by experiment.

A feature of the TPE surfaces produced in detailed calculations in this mass region [Buc 83, Naz 85, Bon 85] is varying degrees of instability towards deformation in the γ degree of freedom, with extreme instability predicted [Bon 85] for the N=42 isotones. (The γ parameter determines whether the nuclear shape is axially symmetric. Therefore, these calculations suggest that shapes which are not axially symmetric (ie. triaxial shapes) may be important for nuclei in this mass region.) Furthermore, cranking model calculations of ^{80}Sr [Naz 85] predict that some softness† to γ-deformations should persist to high spins ($I \simeq 30\hbar$). Therefore, ^{80}Sr is an ideal nucleus in which to look for evidence of γ-softness and triaxiality; particularly in the light of recent theoretical investigations of these phenomena [Hama 84, Hama 85, Oni 86].

Studies of high spin states in neutron deficient heavy nuclei (A$\sim$200) have been traditionally undertaken using (heavy-ion, xn) fusion-evaporation reactions, with beam energies several MeV above the Coulomb barrier. In these reactions, charged particle emission from the compound nucleus is inhibited by the Coulomb barrier and, therefore, the nucleus "cools" by emitting several neutrons, before decaying to its ground state by γ-ray emission. These reactions are particularly well suited to the study of neutron deficient nuclei for two major reasons. Firstly, the compound nucleus, which is already neutron deficient, emits several neutrons, thus, becoming even more neutron deficient. Secondly, since the number of emitted neutrons is a function of the excitation energy of the compound nucleus, it is

† The term "γ-soft" is used here to indicate that the TPE surface minimum is shallow in the γ degree of freedom, so that small energy perturbations will alter γ. This is not to be confused with the extreme situation where the TPE surface is independent of γ.

possible to populate a single dominant reaction channel. Unfortunately, the Coulomb barrier is considerably lower in light (A$\sim$80) nuclei. Thus, experiments to probe these nuclei at high spin are more difficult, since evaporation of protons and α-particles competes strongly with neutron evaporation from the already neutron deficient compound nucleus formed in a heavy-ion reaction. This reduces the cross-sections for the formation of very neutron deficient products and complicates the γ-ray spectra with lines from the many competing channels. Despite these difficulties, the desire to test nuclear models over as wide a range of nuclei as possible has lead to the expenditure of a large amount of experimental effort in studying neutron deficient nuclei in the lighter mass region ($70 \leq A \leq 150$). As a result, a wealth of experimental data on nuclei in this region has become available over the last 5 years, with a corresponding increase in theoretical interest. Experimental studies of these nuclei have been made possible largely as a result of the recent development of both sophisticated particle-γ coincidence techniques and large arrays of Compton-suppressed γ-ray detectors.

The experimental investigation of ^{80}Sr presented in this thesis had two major aims. The first was to investigate the possibility of a long lived isomer high up in the ground state band of ^{80}Sr, which was suggested by the earlier work of Belmont Moreno [Bel 83]. The presence of such a long lived state would signal a major change in the structure of the ground state band, so investigation of such a possibility is particularly important. Indeed, such a change in the nuclear structure is predicted by the cranking model calculations of Nazarewicz *et al.* [Naz 85] which show a transition from collective motion to mostly non-collective motion occuring at spin $\sim 20\hbar$. The second aim was to investigate the

structure of ^{80}Sr in as much detail as possible, because of the importance of the deformed shell gap at nucleon number 38 for both protons and neutrons in this mass region. In this respect, $^{80}_{38}Sr_{42}$ was seen as a compromise between studying an isotope as close as possible to $^{76}_{38}Sr_{38}$ (which has not yet been observed, but which should show effects due to the deformed prolate shell gap at nucleon number 38 for both protons and neutrons) and the restrictions put on the feasibility of such a detailed study by the decreasing cross-sections for producing the Sr isotopes with increasing neutron deficiency. In addition, the detailed cranking model predictions of the structure of ^{80}Sr by Nazarewicz *et al.* [Naz 85] were published during the course of this study, allowing the predictive power of this model to be tested experimentally. Also, the recent theoretical investigations of the behaviour of γ-soft and triaxial nuclei [Oni 86] allow the TPE surface calculations, which predict that ^{80}Sr should show some instability towards γ-deformation, to be tested.

The results of the present study considerably extend our knowledge of the ^{80}Sr ground state band, excited states being observed to an excitation energy of 17 MeV and a tentative spin assignment of 26^+. Lifetime measurements, and the level energy systematics, suggest that the ground state band remains collective to the highest observed spins. In addition, three hitherto unknown sidebands have been observed up to excitation energies ranging from 8 to 15 MeV. The slow feeding, which was formerly associated with nuclear structure changes high in the ground state band [Bel 83], was found instead to be due to previously unidentified interband transitions, which have similar transition energies to some ground state band transitions. The experimental results are compared with the predictions of microscopic calculations [Naz 85]. The deformation and general collective nature of the

ground state band predicted for low spins in these microscopic calculations is found to be in good agreement with the the experimental data. However, the transformation predicted at about spin 20 to mostly non-collective excitations of an oblate shape has not been observed, although this spin is at the limit of that which could be observed experimentally and the level assignments above this spin are tentative. The systematics of both the $J^{(1)}$ and $J^{(2)}$ moments of inertia and the energies of the 2_2^+ states are discussed and presented as evidence for softness towards γ-deformation in the light strontium isotopes. In addition, new interacting boson model (IBM-2) calculations have been performed for the neutron deficient Sr isotopes to investigate both the shell structure in these nuclei and the possibility of pure collective excitations in ^{80}Sr.

CHAPTER 2

THEORETICAL BACKGROUND

2.1 Introduction

Over the past decade there have been great advances in the understanding of both nuclear deformation and the properties of deformed nuclei on a microscopic level. In particular, the shell-correction approach to predicting nuclear shapes, first proposed by Strutinsky [Str 67, Str 68, Bra 72], is now a well established method. This method has been used with considerable success to predict the ground state deformation of nuclei throughout the periodic table [Möl 81, Ben 84a] and is used in microscopic calculations, in conjunction with the cranking model, to predict the nuclear shape and properties as a function of rotational frequency (see, for example, the microscopic calculations of Nazarewicz *et al.* [Naz 85]).

Over the same period of time, the interacting boson model (IBM), originally proposed by Arima and Iachello [Ari 75, Ari 81], has been developed as a simple algebraic model of collective phenomena. The attractions of this model are threefold. Firstly, the excited states, and the matrix elements between them, can be calculated relatively easily using the methods of group theory. Secondly, whereas in geometric descriptions of collective motion [Boh 52, Boh 53, Boh 75] rotations and vibrations are described separately, the IBM is able to accommodate both rotational and vibrational excitations, as well as intermediate situations, within a single framework. As a consequence, the IBM is very useful for describing the properties of a range of neighbouring nuclei exhibiting several types of collective

phenomena. Finally, the IBM lends itself to both a microscopic (see, for example, [Ari 77, Ots 78a, Ots 78b, Wil 82]) and a geometric interpretation [Die 83] and can thus be seen as a bridge between the microscopic and geometric models, while remaining distinct from both of these models.

In Chapter 5, predictions based on both the microscopic cranking model and the algebraic IBM are compared with the experimental data obtained in the present study. Therefore, as some of the details of these models may not be familiar to the reader, brief discussions of them are given below; for fuller details, the reader is referred to the many articles cited in this Chapter. The well known geometric model of collective motion [Boh 52, Boh 53, Boh 75] will not be discussed, although recent work on the importance of the γ degree of freedom in deformed nuclei [Hama 84, Hama 85, Oni 86], which is directly relevant to the discussion in Chapter 5, is briefly covered.

2.2 The Shell Correction Method of Predicting Nuclear Shapes

2.2.1 THE STRUTINSKY SHELL CORRECTION METHOD

As shell model approaches are unable to predict the total nuclear energies, phenomenological approaches have been devised to tackle this problem. In particular, the shell correction method of predicting nuclear shapes [Bra 72], first proposed by Strutinsky [Str 67, Str 68], has been very successful and is now widely used. This method is based on the idea that calculations of nuclear level structure are good close to the Fermi surface; thus, the total nuclear energy E is expressed as the sum of a liquid drop term E_{ld} (representing the bulk properties of the nuclear matter) and correction terms corresponding to shell

energy δU and pairing effects δP which are sensitive to the shell structure about the Fermi surface. That is

$$E = E_{ld} + \delta E_{shell} \tag{2.1}$$

with

$$\delta E_{shell} = \delta U + \delta P \tag{2.2}$$

The shell energy correction term δU is calculated as the difference between the sum of the single particle energies e_i and an energy calculated by smoothing out the discrete spectrum of single particle levels. Thus,

$$\delta U = \sum_{\pi,\nu} e_i + \int_{-\infty}^{\lambda'_\pi} \sum_{\pi} S(e_i - e)de + \int_{-\infty}^{\lambda'_\nu} \sum_{\nu} S(e_i - e)de \tag{2.3}$$

where: $S(e_i - e)$ represents, for example, a Gaussian function centred about e_i [Str 67]; and $\lambda'_{\pi(\nu)}$ are modified Fermi surfaces such that the total number of protons (neutrons) are conserved. The first summation in eq. 2.3 is over the levels occupied in the shell model calculation (the extent of the other summations in eq. 2.3 are determined by $\lambda'_{\pi(\nu)}$). Similarly, δP is the difference between the pairing energy for the calculated spectrum of single particle levels and that calculated for a uniform distribution of single particle states [Str 67, Str 68].

2.2.2 PARAMETERIZATION OF THE NUCLEAR SHAPE

If we consider the nucleus to have a well defined surface (for example, one can picture the nucleus as a "liquid drop" in much of the following discussion) then the nuclear surface can be represented by a series expansion of spherical harmonics

$$R(\theta,\phi) = R_\alpha[1 + \sum_{\lambda=0}^{\infty} \sum_{\mu=-\lambda}^{\lambda} \alpha_{\lambda\mu} Y_{\lambda\mu}(\theta,\phi)] \tag{2.4}$$

where: $\alpha_{\lambda\mu}$ are parameters which define the nuclear shape; and R_α is chosen so that the nuclear volume is conserved.

Variations in the parameter α_{00} affect only the nuclear volume, which is assumed to be constant for the low-lying excited states. In addition, changes in the parameters $\alpha_{1\mu}$ correspond to movement of the centre of mass and can therefore be ignored. Finally, although higher order multipoles are important in some nuclei, the quadrupole deformation plays the dominant role in most nuclei. Therefore, it is sufficient to consider nuclear shapes of the form

$$R(\theta,\phi) = R_0[1 + \sum_{\mu=-2}^{2} \alpha_{2\mu} Y_{2\mu}(\theta,\phi)] \tag{2.5}$$

where R_α has been replaced by the constant R_0, neglecting volume corrections higher than second order in $\alpha_{2\mu}$.

It is of interest in the present work to describe a nucleus which has a quadrupole intrinsic shape. If this deformed shape is rotating with respect to the laboratory reference frame then the $\alpha_{2\mu}$ will change with time, although the nuclear shape itself is constant. Therefore, it is convenient to describe the nuclear shape with respect to a set of axes fixed relative to the nucleus and, in addition, describe the orientation of the nucleus in space by a set of three Euler angles $(\theta_1, \theta_2, \theta_3)$. If we choose the body-fixed reference frame so that it coincides with the principal axes of the nucleus, then

$$\alpha_{21} = \alpha_{2-1} = 0 \qquad\qquad \alpha_{22} = \alpha_{2-2} \tag{2.6}$$

Therefore, only α_{22} and α_{20} are required to specify the shape. (Three of the five original $\alpha_{2\mu}$ have been replaced by the Euler angles.) It is conventional to use the variables

β and γ instead of α_{20} and α_{22}, where

$$\alpha_{20} = \beta\cos\gamma \tag{2.7}$$

$$\alpha_{22} = \frac{1}{\sqrt{2}}\beta\sin\gamma$$

The quantity β is a measure of the total deformation of the nucleus, since

$$\beta = \sum_{\mu} |\alpha_{2\mu}|^2 \tag{2.8}$$

while γ describes the type of deformation (prolate, oblate or triaxial).

2.2.2.1 The Lund convention

In the Lund convention (see, for example, [Voi 83] and fig. 2.1) $\gamma = 0$, $2\pi/3$ and $4\pi/3$ correspond to prolate nuclei with the 3-, 2- and 1-axis as the axis of symmetry, respectively, while $\gamma = \pi/3$, π and $5\pi/3$ correspond to oblate nuclei with the 1-, 3- and 2-axis as the axis of symmetry, respectively. Nuclei with values of γ between these integer multiples of $\pi/3$ have triaxial shapes. To specify the nuclear shape a range of only $\pi/3$ in the $\beta - \gamma$ plane is necessary, while to specify the axis of symmetry the full 2π is required. In the Lund convention, half of the $\beta - \gamma$ plane only is used ($-2\pi/3 \leq \gamma \leq \pi/3$). This is because the nucleus is rotated about the 1-axis in this convention and therefore it is necessary to describe both the nuclear shape and the orientation of the nucleus with respect to this axis.

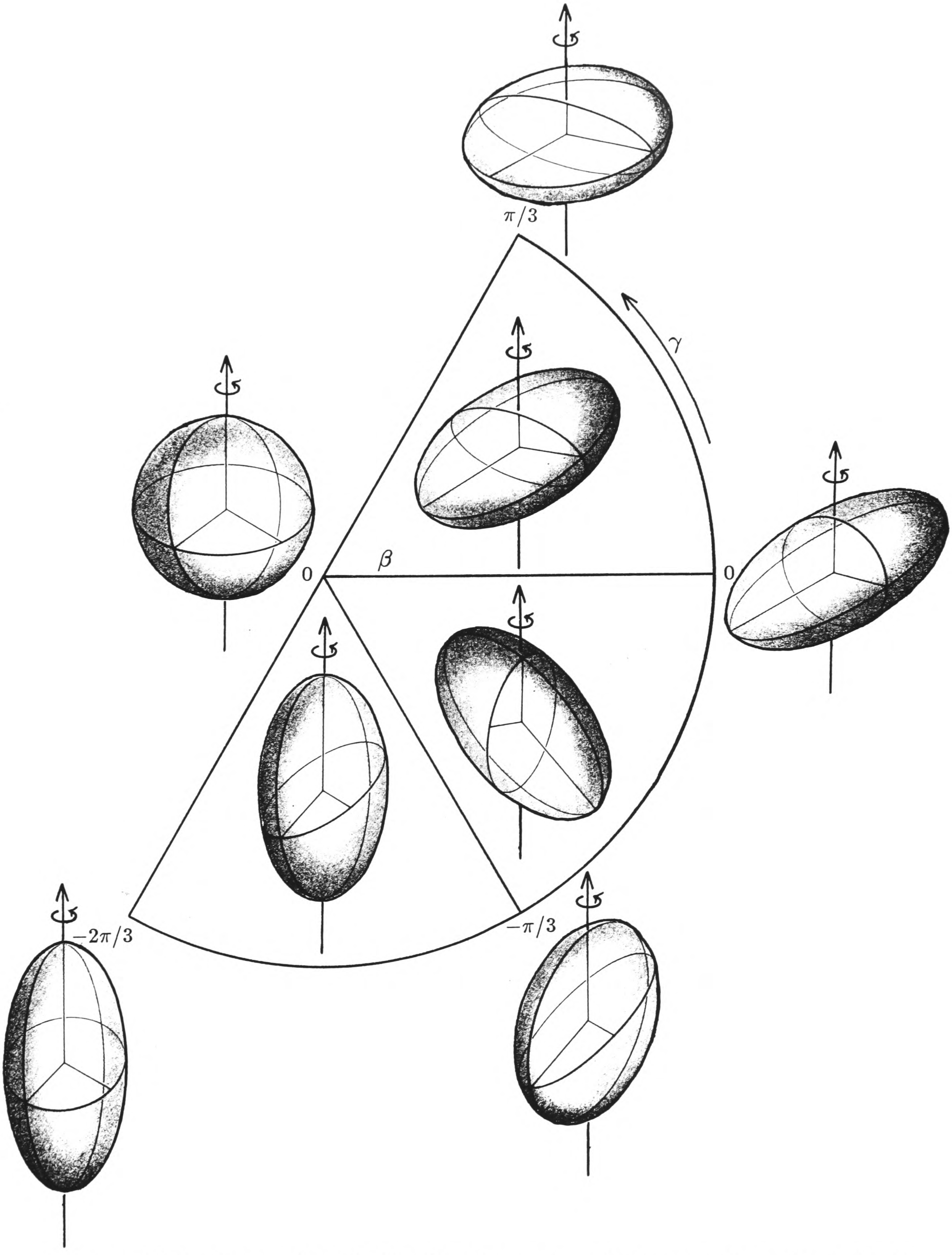


Figure 2.1 Lund convention for the β and γ nuclear shape parameters. The axis of rotation (the 1-axis) is indicated for each shape. See sect. 2.2.2.1 for details.

2.2.3 TOTAL POTENTIAL ENERGY SURFACES AND THE NUCLEAR SHAPE

The nuclear shape can be predicted by making use of the Strutinsky shell correction method outlined above, provided the single particle energy levels can be calculated as a function of deformation (as is done, for example, in the Nilsson model [Nil 55]). In order to predict the nuclear shape the nuclear total potential energy (TPE) is calculated as a function of the deformation parameters (β, γ). The resulting TPE surface is usually plotted as a contour map in the (β, γ) plane (see, for example, the calculations of Nazarewicz *et al.* [Naz 85] shown in figs 5.4 and 5.5). The absolute minimum in the TPE surface is the predicted equilibrium shape of the nucleus. Sometimes additional shape degrees of freedom, representing small higher order corrections to the nuclear shape, are included in the calculations; in which case it is usual to plot the TPE minimized with respect to these additional degrees of freedom on the (β, γ) plane.

The Strutinsky shell correction method can be generalized to rotating nuclei (see for example [Naz 85, Voi 83]). This is done by replacing the single particle energies in eq. 2.3 with those in the rotating intrinsic frame (see sect. 2.3) and by adding an additional term E_{rot}, corresponding to the bulk rotational energy of the nuclear matter, to the liquid drop energy in eq. 2.1

$$E_{rot} = \frac{\hbar^2}{2J} I^2 \tag{2.9}$$

where: J is the moment of inertia; and I is the nuclear spin.

Alternative methods of predicting the nuclear shape do exist; for example, methods based on the self-consistent Hartree-Fock approach (see, for example, the calculations of Bonche *et al.* [Bon 85]) or on the interacting boson model [Die 83, Buc 83]. However,

the shell correction approach is widely used in microscopic calculations, since it is much easier to handle than the self-consistent Hartree-Fock procedure. The shell correction approach has been shown to be closely related to the Hartree-Fock method [Bra 72] and can, therefore, be seen as a close approximation to the self-consistent procedure.

2.3 The Cranking Model

2.3.1 ROUTHIANS

In order to carry out microscopic calculations of the single particle levels in a nucleus rotating about an axis perpendicular to its symmetry axis, the procedure known as the cranking approximation is frequently employed. This procedure was first introduced by Inglis [Ing 54, Ing 55] and is covered briefly in the review article by Voigt *et al.* [Voi 83] and in depth by Bengtsson and Garrett [Ben 84b] (the present treatment follows closely sections in both of these review works). In the cranking model the deformed nuclear shape is rotated at a constant angular frequency ω about a fixed axis and the explicit time dependence of the Schrödinger equation, due to the rotational motion, is removed by transforming to a frame of reference fixed in the rotational body, as detailed below.

The time dependent Schrödinger equation is

$$i\hbar\frac{\partial}{\partial t}\psi = H\psi \tag{2.10}$$

If the nucleus is being rotated about the 1-axis at a frequency ω, then we can transform the wave function ψ and the Hamiltonian H to the body-fixed co-ordinates by using the rotational operator

$$R(\omega,t) = e^{-i\omega t I_{1'}/\hbar} \tag{2.11}$$

so that

$$\psi = R(\omega, t)\psi' \tag{2.12}$$

$$H = R(\omega, t)H'R(\omega, t)^{-1} \tag{2.13}$$

where ψ' and H' are in the body-fixed reference frame. The Schrödinger equation (eq. 2.10) can then be rewritten as

$$i\hbar\frac{\partial}{\partial t}(R(\omega, t)\psi') = R(\omega, t)H'\psi' \tag{2.14}$$

Then, by substituting eq. 2.11 into eq. 2.14, we obtain

$$i\hbar\frac{\partial}{\partial t}\psi' = (H' - \omega I_{1'})\psi'. \tag{2.15}$$

Eq. 2.15 may be rewritten as

$$i\hbar\frac{\partial}{\partial t}\psi' = H^{\omega}\psi' \tag{2.16}$$

where

$$H^{\omega} = (H' - \omega I_{1'}) \tag{2.17}$$

H^{ω} is called the cranking Hamiltonian or Routhian. Since H^{ω} does not depend on time, the solution of eq. 2.16 can be reduced to the eigenvalue problem of H^{ω}. It is assumed that the nucleon-nucleon interactions are not affected by the rotations. Thus, the operation $R(\omega, t)^{-1}HR(\omega, t)$ is equivalent to merely transforming the co-ordinates from the laboratory to the body-fixed reference frame. The term $-\omega I_{1'}$ can be shown to be analogous to the centrifugal and Coriolis terms in classical mechanics [Voi 83].

2.3.2 THE SIGNATURE QUANTUM NUMBER

In geometric models of collective excitations of axially symmetric nuclei and in models of deformed nuclear shape the nuclear states can be characterized by the K quantum number defined by

$$K = |\langle I_{3'} \rangle| \tag{2.18}$$

where the $3'$-axis is the axis of symmetry. However, in the cranking model, states of different K are mixed by the Coriolis term $-\omega I_{1'}$. Thus, K is no longer a good quantum number for $\omega \neq 0$. However, both the parity operator and the cranking Hamiltonian (eq. 2.17) do commute with $R_{1'}$, defined as

$$R_{1'} = e^{-i\pi I_{1'}/\hbar}, \tag{2.19}$$

corresponding to a 180° rotation about the $1'$-axis. Denoting the eigenvalues of $R_{1'}$ by r, one finds [Boh 75] that for a state of spin I

$$r = (-i)^I \tag{2.20}$$

Thus, for systems with an even number of nucleons, we have

$$r = +1, I = 0, 2, 4, ... \tag{2.21}$$

$$r = -1, I = 1, 3, 5, ... \tag{2.22}$$

while for systems with odd numbers of nucleons

$$r = -i, I = 1/2, 5/2, 9/2, ... \tag{2.23}$$

$$r = +i, I = 3/2, 7/2, 11/2, ... \tag{2.24}$$

The eigenvalues r of the operator $R_{1'}$ are called the signature quantum number. Both individual states and collective bands of states predicted by the cranking model can be labelled by their parity π and signature r. (Signature is a multiplicative quantum number.)

2.3.3 QUASIPARTICLES AND PAIRING

In any microscopic description of nuclei the concept of pairing (the coupling of nucleons into spin 0 pairs) is fundamental. In order to include pairing in the Routhian equations (eq. 2.17), it is usual to rewrite the Routhian in terms of single particle creation and annihilation operators. (See the review article by Bengtsson and Garrett [Ben 84b] for details.) The Routhian then has the form

$$H = \sum_{i,j}[\langle i|H|j\rangle a_i^\dagger a_j - \omega\langle i|I_{1'}|j\rangle a_i^\dagger a_j] - \sum_{i,j} G a_i^\dagger a_{\bar{i}}^\dagger a_{\bar{j}} a_j \qquad (2.25)$$

In the first term H is the single particle Hamiltonian, which is usually chosen as a deformed Nilsson or Woods-Saxon Hamiltonian. (In this approximation, except for the pairing interaction, those contributions to the Hamiltonian which are not included in the single particle Hamiltonian are ignored.) The last term, which represents the pairing interaction, transforms pairs of particles from one set of time reversed orbits $(j, \bar{j})$ to another $(i, \bar{i})$. The summation runs over all the considered basis states, which can be chosen, for example, as eigenstates of H.

The two body pairing operator makes eq. 2.25 difficult to solve. However, by making suitable approximations to the pairing interaction and then by performing a transformation from the $a_i, a_i^\dagger$ operators to a different set, which are linear combinations of a_i and $a_i^\dagger$, it is possible to solve the cranking Routhian including pairing. The resulting eigenstates,

called quasiparticles, are linear combinations of particles and holes and the corresponding energy levels are called quasiparticle Routhians.

The interpretation of the quasiparticle Routhians is well documented (see, for example, the excellent review article by Bengtsson and Garrett [Ben 84b]). Therefore, this complex subject will not be detailed here, except for four basic points. Firstly, the transition to an excited intrinsic state in a rotating deformed nucleus corresponds to the creation of quasiparticles. (In a nucleus with an even number of protons (neutrons) the total number of proton (neutron) quasiparticles is always even. Similarly, for a nucleus with an odd number of protons (neutrons) the total number of proton (neutron) quasiparticles is always odd.) In this way, excited intrinsic states are described in the quasiparticle formalism. Secondly, excited quasiparticle states and their associated rotational bands are characterized by parity and signature quantum numbers. The signature quantum number of a quasiparticle configuration determines the sequences of spins in the rotational band (see eqs. 2.21, 2.22, 2.23, 2.24). Thirdly, as can be seen from eq. 2.17, the angular momentum in the body-fixed frame $i_{1'}$ aligned with the axis of rotation is given by

$$i_{1'} = -\frac{\mathrm{d}}{\mathrm{d}\omega}\langle H^{\omega}\rangle \tag{2.26}$$

Thus, the aligned angular momentum $i_{1'}$ is -1 times the slope of the quasiparticle Routhians plotted as a function of rotational frequency ω. Finally, the Coriolis term in the cranking Hamiltonian tends to break the $I = 0$ pairs favoured by the pairing interaction and align their angular momenta with the $1'$-axis. This is the microscopic origin of backbending and is reflected in a change of the slopes of the quasiparticle Routhians.

2.3.4 EXTRACTION OF ω, I_x, $J^{(1)}$ AND $J^{(2)}$ FROM THE EXPERIMENTAL DATA

It is useful to define various macroscopic quantities, such as angular frequency ω and moment of inertia J, which can be extracted from the experimental data. The angular momentum aligned along the rotational axis is defined by

$$I_x = \sqrt{I(I+1) - K^2} \tag{2.27}$$

where K is the projection of the total angular momentum on the symmetry axis (as defined by eq. 2.18) and is an approximately good quantum number at low angular frequencies. The angular frequency ω is defined by

$$\omega = \mathrm{d}E/\mathrm{d}I_x \tag{2.28}$$

which for a quadrupole transition ($\Delta I_x \sim 2\hbar$) is equal to

$$\hbar\omega = E_\gamma/2 \tag{2.29}$$

where E_γ is the γ-ray transition energy. The $J^{(1)}$ and $J^{(2)}$ moments of inertia are defined as

$$J^{(1)} = \frac{I_x}{\omega} \tag{2.30}$$

and

$$J^{(2)} = \frac{\mathrm{d}I_x}{\mathrm{d}\omega} \tag{2.31}$$

2.4 Recent Developments in the Treatment of the γ Degree of Freedom

The extension of the geometric model to nuclei without axial symmetry was first qualitatively investigated by Davydov and Filippov [Dav 58]. They showed that the violation of axial symmetry only slightly affects the ground state rotational band obtained for an axially symmetric nucleus. However, some new rotational states with total angular momenta 2, 3, 4... do appear and the energies of these levels decrease to a minimum as γ approaches $-30°$ (see fig. 2.2).

More recently, the properties of nuclei which exhibit either static γ-deformation or dynamic γ-deformation (resulting from quantum fluctuations in the γ degree of freedom) have been investigated by Hamamoto *et al.* [Hama 84, Hama 85] and Onishi *et al.* [Oni 86]. These authors discuss the importance of rotations about all three principal axes and note that the nucleus exhibits a wobbling motion. This adds an additional term to the rotational energy which, in the limit of high angular momentum, takes on the simple form

$$E = A_1 I(I+1) + \frac{1}{2}\hbar\omega_w \tag{2.32}$$

where the wobbling frequency ω_w is

$$\hbar\omega_w = 2I[(A_2 - A_1)(A_3 - A_1)]^{1/2} \tag{2.33}$$

and

$$A_i = \frac{\hbar^2}{2J_i} \tag{2.34}$$

where A_1 is the smallest of the three A_i values (corresponding to rotation about the axis with the greatest moment of inertia J_1). As a consequence, the $J^{(1)}$ moment of inertia is systematically smaller than $J^{(2)}$, which tends to J_1 at high spin. As with the axially

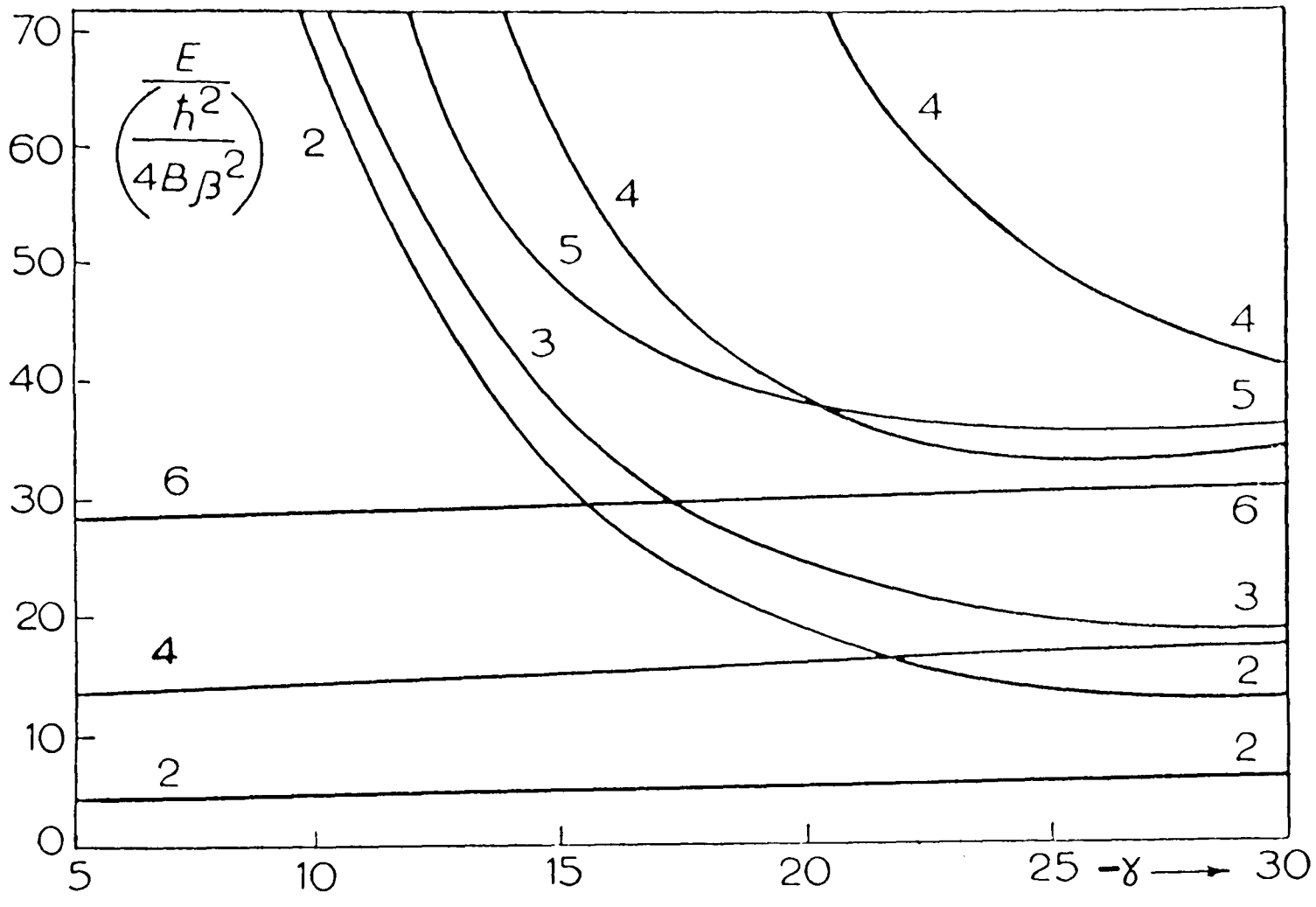


Figure 2.2 Energy spectrum of a triaxial rotor as a function of the deformation parameter γ, taken from the work of Davydov and Filippov [Dav 58].

symmetric model, the in-band transitions are strong with the reduced transition strengths (see Appendix B) for the $\Delta I = 2$ $E2$ transitions being given by

$$\mathrm{B}(E2, I \rightarrow I-2) = \frac{5}{16\pi}\langle Q_2 \rangle (IK20|I-2K)^2 \tag{2.35}$$

where the γ dependence of the quadrupole matrix element in the limit of high spins is such that

$$\langle I-2 \| Q_2 \| I \rangle \quad \alpha \quad \cos(30^\circ + \gamma) \tag{2.36}$$

where γ is defined as in the Lund convention (see sect. 2.2.2.1). It should be noted that the cranking model as discussed in sect. 2.3 cannot fully describe nuclei with either static or dynamic γ-deformation, since in the cranking approximation the nucleus is rotated about one axis only.

2.5 The Interacting Boson Model

2.5.1 INTRODUCTION

The Interacting Boson Model [Ari 75, Ari 81, Sch 80, Ell 85, Iac 83, Iac 79, Woo 83, Wil 82] (IBM) describes collective states in nuclei in terms of a small ensemble of bosons which interact both with each other and with a mean field. The bosons are interpreted as collective pairs of nucleons coupled to angular momentum states with spins of either 0 (s-boson) or 2 (d-boson) and even parity. This suggests a microscopic foundation for describing collective phenomena. In addition, the IBM has a geometric interpretation [Die 83]. Thus, it offers a bridge between the shell model [Sha 63] in which nuclei are described in terms of the states of individual nucleons, and the rotational and vibrational models of

collective motion [Boh 52, Boh 53, Boh 75] which largely ignore the motion of individual nucleons.

The IBM can be seen as a truncation of the shell model space, allowing calculation of collective states which would otherwise (in a full shell model calculation) require unreasonably large computer calculations, because of the enormous number of basis states involved. (The number of basis states in the IBM [Sch 80] is typically of the order of 10^3, smaller by a factor of about 10^{10} than the number of shell model basis states for typical mid-shell nuclei.) In four limiting cases, which are termed dynamical symmetries (see 2.5.3), the IBM Hamiltonian can be solved exactly by using group theory. Intermediate cases can be solved numerically by diagonalising a relatively small Hamiltonian matrix (typically [Sch 80] 50×50). In the geometric descriptions of collective motion [Boh 75] rotations and vibrations are described separately, however in the IBM these limiting cases, as well as intermediate situations, are described within a single framework. For example, in the rotational model of an axially symmetric nucleus, β and γ vibrations of the deformed shape had to be postulated in order to describe bands of states built on excited 0^+ and 2^+ states; in the IBM these bands arise naturally in the rotational [SU(3)] limit.

In the original IBM formulation (IBM-1) no differentiation was made between neutron and proton bosons. However, the microscopic interpretation of bosons as collective pairs of like nucleons suggests that proton and neutron bosons should be treated separately, therefore, the model has been generalized [Ari 81, Sch 80, Iac 79, Ari 77, Ots 78a, Ots 78b] to include this additional degree of freedom (IBM-2). Often the term Interacting Boson Approximation (IBA) is used instead of IBM (particularly when neutron and proton bosons

are treated separately, because of this model's closer relationship with microscopic theory); these terms are now used interchangeably in the literature. The following discussion of the IBM-2 model owes much to the very clear account of this model given by Olaf Scholten [Sch 80] in his Ph.D. thesis, which provides a full and very readable introduction to models of this type.

2.5.2 THE IBM-2 HAMILTONIAN AND MICROSCOPIC INTERPRETATION

The principal assumption of the IBM is that low-lying collective states in an even-even nucleus can be described in terms of a collection of s- and d-bosons. Shell model calculations of the interaction between pairs of identical nucleons in the same shell model orbit [Sch 76] show that the interaction is most attractive when the pair is coupled to spin 0. This is the well known pairing interaction which, for example, is responsible for the 0^+ ground states observed in even-even nuclei and which limits the number of valence nucleons active in low lying states. The next lowest pair state has spin 2, while the states with spin $I \geq 4$ are typically repulsive (i.e. they have positive interaction energies). For a given shell there are several orbits and hence several possible 0^+ or 2^+ pairs. The s- and d-bosons are identified with the lowest lying pairs with spins 0 and 2, respectively, which are in some sense collective states. Thus, the bosons are interpreted as collective pairs of protons (π) or neutrons (ν) coupled to angular momentum 0 (s-boson) or 2 (d-boson), and the full shell model space has been reduced to a much smaller model space, which should be capable of describing the low lying collective states of the nucleus. (The details of the transformation of both states and matrix elements from the shell model subspace of the lowest lying 0^+ and 2^+ states to the boson model space are technically complex. This is

discussed by Otsuka, Arima, Iachello and Talmi [Ari 77, Ots 78a, Ots 78b], and a short account is given in [Sch 80], while fuller accounts are given in [Wil 82].)

The boson Hamiltonian, therefore, reflects the interactions between the valence protons and neutrons. The Hamiltonian is written in terms of boson creation and annihilation operators and has the form

$$H = \epsilon_\nu \mathrm{n}_{d_\nu} + \epsilon_\pi \mathrm{n}_{d_\pi} + \kappa \mathrm{Q}_\nu^{(2)}.\mathrm{Q}_\pi^{(2)} + V_{\pi\pi} + V_{\nu\nu} + M_{\nu\pi} \tag{2.37}$$

where:

* $\epsilon_{\nu(\pi)}$ is the energy required to create a neutron (proton) d-boson from a neutron (proton) s-boson and $n_d = d^\dagger \tilde{d}$ counts the number of d-bosons, where $\tilde{d} = (-1)^\mu d_{-\mu}$ creates a boson hole with angular momentum $(L, M) = (2, \mu)$

* $\mathrm{Q}_{\nu(\pi)}^{(2)}$ is the neutron (proton) quadrupole operator and has the form

$$\mathrm{Q}_\nu^{(2)} = (s_\nu^\dagger \tilde{d}_\nu + d_\nu^\dagger s_\nu)^{(2)} + \chi_\nu (d_\nu^\dagger \tilde{d}_\nu)^{(2)} \tag{2.38}$$

where χ is the ratio of the d-boson conserving component to the d-boson non-conserving component, and the superscript (2) denotes that the boson operators are coupled to angular momentum $L = 2$

* κ is the strength of the quadrupole interaction between protons and neutrons

* $V_{\nu\nu(\pi\pi)}$, which has parameters c_0, c_2 and c_4, is the residual interaction between like bosons and takes the form

$$V_{\nu\nu} = \sum_{L=0,2,4} c_L \frac{\sqrt{2L+1}}{2} [(d_\nu^\dagger d_\nu^\dagger)^{(L)} (\tilde{d}_\nu \tilde{d}_\nu)^{(L)}]^{(0)} \tag{2.39}$$

* and $M_{\nu\pi}$, which has parameters ξ_1, ξ_2 and ξ_3, acts between neutron and proton bosons and has the form

$$M_{\nu\pi} = \xi_2(s_\nu^\dagger d_\pi^\dagger - d_\nu^\dagger s_\pi^\dagger)^{(2)}.(s_\nu \tilde{d}_\pi - \tilde{d}_\nu s_\pi)^{(2)} + \sum_{k=1,3} \xi_k (d_\nu^\dagger d_\pi^\dagger)^{(k)}.(\tilde{d}_\nu \tilde{d}_\pi)^{(k)} \quad (2.40)$$

The main part of the interaction between like bosons is incorporated into the boson energies $\epsilon_{\nu(\pi)}$. Furthermore, multipole expansions of the neutron-proton interaction, as determined [Moi 69] for example from the level structure of ^{208}Bi, show that the strongest multipole in the interaction is the quadrupole term (apart from the monopole interaction, which contributes to the binding energies but has little affect on the spectrum of excited states). Therefore, the quadrupole interaction between the neutron and proton bosons, $\kappa Q_\nu^{(2)}.Q_\pi^{(2)}$, is included in the Hamiltonian. Thus, the d-boson energies and the neutron-proton quadrupole interaction are the principal terms in the Hamiltonian.

Although the major part of the interaction between like nucleons is included in the d-boson energies, additional terms are taken into account by $V_{\nu\nu}$ and $V_{\pi\pi}$. These interactions are expected to be important only when either the neutrons or protons are near a closed shell, so that the neutron-proton quadrupole interaction is suppressed by the lack of valence neutrons or protons, otherwise the neutron-proton interaction is expected to dominate.

Finally, the Majorana term, $M_{\nu\pi}$, is added to the Hamiltonian. This term only affects the position of those states which are fully symmetric with respect to exchange of the proton and neutron degrees of freedom, relative to those which are not fully symmetric, and is used to adjust the relative positions of the two sets of states. It is usually found that the low lying states are fully symmetric, so $M_{\nu\pi}$ is used to push the mixed symmetry states up in energy. Until recently there has been no experimental information about

mixed symmetry states [Die 83]. However, there is now evidence in some nuclei for low lying collective states with $I^\pi = 1^+$ which have mixed symmetry [Boh 84, Van 84]. The fully symmetric states are those found in IBM-1, while the mixed symmetry states are unique to IBM-2. Thus, the states produced in an IBM-1 are a subset of those in IBM-2.

2.5.3 DYNAMICAL SYMMETRIES

For certain values of the parameters in the Hamiltonian the IBM-2 can be solved exactly by using the methods of group theory [Ari 81, Sch 80, Ari 76, Ari 78, Ari 79, Die 82, Die 83]. Furthermore, the excited spectra and transition probabilities in these limiting cases closely resemble those of the collective model [Boh 52, Boh 53, Boh 75] for the spherical vibrator, the axially symmetric rotor, the γ-unstable rotor [Wil 56], and the triaxial rotor [Dav 58]. These are termed dynamical symmetries and the associated groups are U(5), SU(3) and O(6) and SU*(3). (The SU*(3) dynamical symmetry is only apparent when an additional quadrupole interaction between like nucleons is added to the boson Hamiltonian [Die 82, Die 83].) A.E.L. Dieperink [Die 83] has reviewed analyses which associate the IBM dynamical symmetries with geometric interpretations via the boson Hamiltonian. (In addition, Casten and Feng [Cas 84] have written an interesting article on symmetries in the IBM, aimed at the non-specialist.)

The dynamical symmetries are discussed below in terms of the IBM-2 Hamiltonian (eq. 2.37) which is reproduced here, for convenience, in slightly modified form

$$H = \epsilon(\mathrm{n}_{d_\nu} + \mathrm{n}_{d_\pi}) + \kappa \mathrm{Q}_\nu^{(2)} . \mathrm{Q}_\pi^{(2)} \tag{2.41}$$

where: for simplicity, $\epsilon_\nu = \epsilon_\pi = \epsilon$; the residual interactions ($V_{\pi\pi}$ and $V_{\nu\nu}$) have been

neglected, since they are thought to be relatively unimportant; and the Majorana term ($M_{\nu\pi}$), which only breaks the SU*(3) symmetry, has also been neglected.

TABLE 2.1: Dynamical Symmetries in IBM-2

Symmetry	Parameters	Geometric Interpretation
U(5)	$\epsilon \neq 0,\ \kappa = 0$	spherical vibrator
SU(3)	$\epsilon = 0,\ \kappa \neq 0,\ \chi_\nu = \chi_\pi = \pm\frac{\sqrt{7}}{2}$	axially symmetric rotor
O(6)	$\epsilon = 0,\ \kappa \neq 0,\ \chi_\nu = \chi_\pi = 0$	γ-unstable rotor
SU*(3)	$\epsilon = 0,\ \kappa \neq 0,\ \chi_\nu = -\chi_\pi = \pm\frac{\sqrt{7}}{2}$	$\gamma = 30°$ triaxial rotor

The Hamiltonian parameters for the dynamical symmetries in IBM-2 are given in table 2.1. For the U(5) limit the energies of the $L = 2$ d-bosons dominate the Hamiltonian, yielding a vibration-like spectrum. In this case the d-bosons can be associated with the phonons of the vibrational model. In contrast, the quadrupole interaction dominates in the O(6), SU(3) and SU*(3) limits. For the SU(3) symmetry, analysis [Die 83] of the classical limit of the IBM-2 Hamiltonian for a large number of bosons yields an axially symmetric prolate (or oblate) shape ($\beta = \frac{2}{\sqrt{3}}$ and $\gamma = 0°$ ($\gamma = 60°$)) and the spectrum of excited states is similar to that obtained in the collective model for a deformed prolate (or oblate) rotor. In addition to the ground state rotational band, bands built on excited states arise naturally in this limit. Some of these bandheads can be associated with β and γ vibrations of the deformed shape, as postulated in the collective model. However additional modes of excitation, corresponding to vibrations of neutrons against protons are also predicted. (The excitation energies of these modes, which are of mixed symmetry, are primarily determined by $M_{\nu\pi}$.) In particular, it predicts small amplitude oscillations,

about the equilibrium shape, of the angle between the proton and neutron symmetry axes. Recently [Boh 84, Van 84], low lying collective states with $I^\pi = 1^+$, which decay to the ground state via strong $M1$ transitions, have been observed in some nuclei. These states have been interpreted as the neutron-proton oscillations predicted by the IBM-2. Similarly, the O(6) limit can be associated, via the Hamiltonian, with a potential that has a (deformed) minimum at $\beta = 1$ but which is independent of γ. Therefore, the O(6) limit is associated with the γ-unstable deformed rotor and has a similar spectrum to that obtained in the γ-unstable model of Wilets and Jean [Wil 56]. Examples of nuclei which can be associated with these three limits of the IBM are given in [Ari 81, Ari 76, Ari 78, Ari 79, Ciz 78, Cas 85a, Cas 85b]. Finally, the SU*(3) symmetry corresponds [Die 82, Die 83] to different matter distributions for the protons and neutrons; one being prolate ($\beta_\pi = \frac{2}{\sqrt{3}}, \gamma_\pi = 0^\circ$) and the other being oblate ($\beta_\nu = \frac{2}{\sqrt{3}}, \gamma_\nu = 60^\circ$), with the axes of symmetry perpendicular to one another to maximize their overlap. The overall matter distribution is that of a $\gamma = 30^\circ$ triaxial rotor and the spectrum of excited states is similar to that produced in the collective model for this geometry [Dav 76].

CHAPTER 3

EXPERIMENTAL STUDY OF ^{80}Sr

3.1 Introduction

The first experimental study of ^{80}Sr was undertaken in 1974 by Nolte *et al.* [Nol 74] who used the ^{66}Zn(^{16}O, $2n$)^{80}Sr reaction and identified the first three excited yrast states by the observed 386, 595 and 783 keV γ-ray decays. The assignment of these γ-rays to ^{80}Sr was based on experimental γ-ray yield curves, which were consistent with two particle evaporation; these γ-rays were not identifiable with known transitions associated with the pn or $2p$ reaction channels forming ^{80}Rb and ^{80}Kr, respectively. (The placement of these transitions within the ^{80}Sr level scheme is illustrated by the level scheme derived by Higo *et al.* [Hig 83] (fig. 3.1). For some of the levels and transitions mentioned in this Chapter, it may also be useful to refer to the level scheme derived from the present study (fig. 4.1, this figure is also reproduced inside the back cover).) To confirm this assignment, the γ-rays associated with the ^{66}Zn(^{16}O, $2n$)^{80}Sr reaction channel were identified by detecting the ^{80}Sr γ-rays in coincidence with pairs of emitted neutrons. Nolte *et al.* also measured the mean life of the first excited state in ^{80}Sr to be $\tau = 63 \pm 9$ ps using the recoil distance method. This corresponds to a transition strength of 74 ± 11 Weisskopf single particle units (see Appendix B) and indicates a collective excitation. The assignment of these γ-rays to ^{80}Sr was confirmed independently by Lister *et al.* in two separate studies. The first was a study of the β-decay of ^{80}Y to ^{80}Sr [Lis 81] (the ^{80}Y was produced in three different reactions, in separate experiments, through the pn, $p2n$ and αpn channels). The second

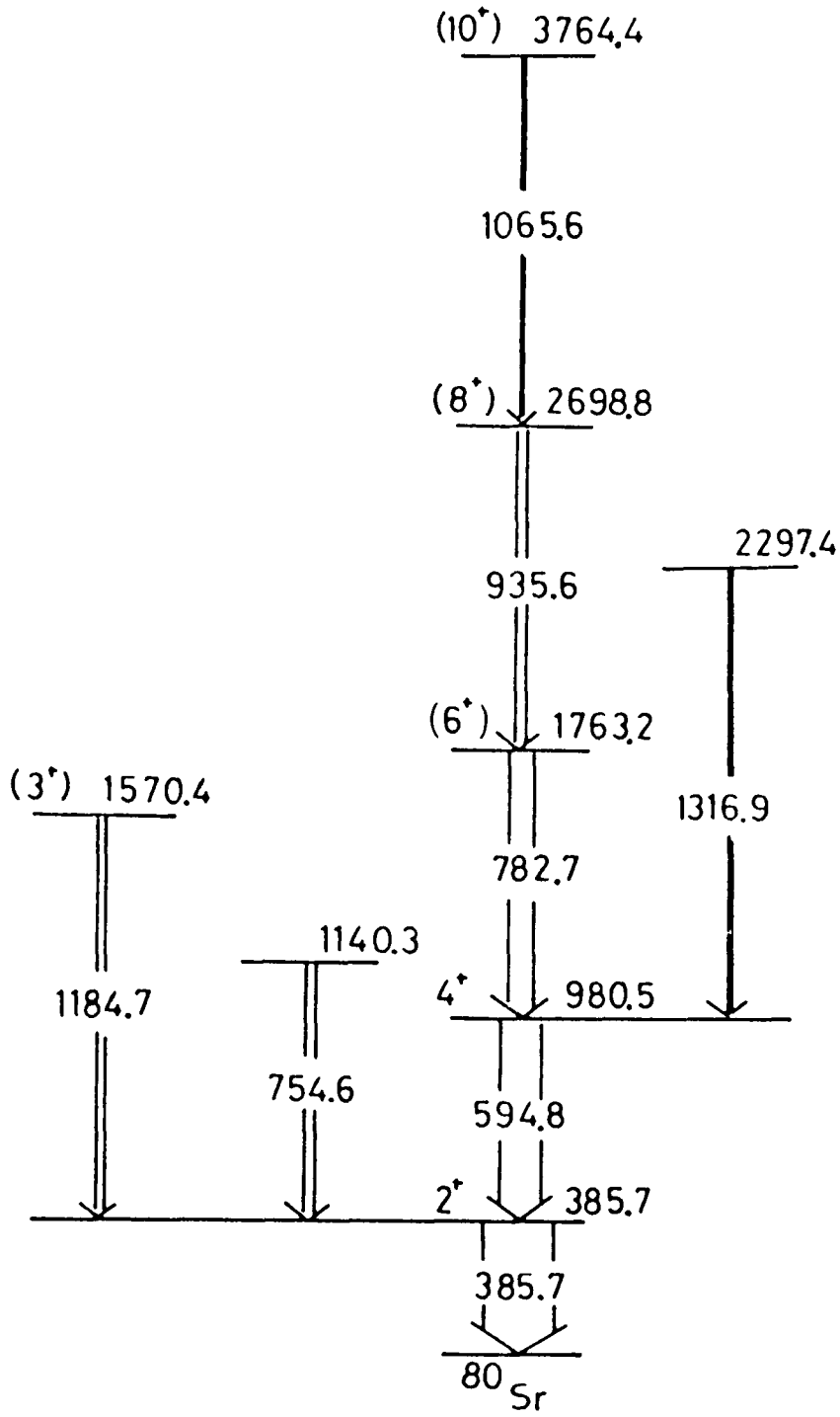


Figure 3.1 The level scheme of ^{80}Sr as proposed following the earlier work of Higo *et al.* [Hig 83]. The arrow widths are approximately proportional to the in-beam γ-ray intensities, and the energies are given in units of keV.

was a study of the ^{58}Ni(^{24}Mg, $2p$)^{80}Sr reaction using particle-γ coincidence techniques [Lis 82]. These two studies also identified several other states in ^{80}Sr below 4 MeV. Further confirmation of the assignment of these γ-rays to ^{80}Sr came from the study by Belmont Moreno [Bel 83] who used p-γ and α-γ coincidences to identify the $\alpha 2p$ channel forming ^{80}Sr in the reaction of 115 MeV ^{28}Si on ^{58}Ni. In addition, the studies of Fields *et al.* [Fie 81], Lister *et al.* [Lis 82] and Higo *et al.* [Hig 83] extended our knowledge of the ^{80}Sr ground state band to 4 MeV. Furthermore, an excited 0^+ state has been observed at 1.00 MeV in the ^{78}Kr(^{3}He, n)^{80}Sr reaction [Alf 79].

The aim of the present experimental investigation was to extend our knowledge of the ^{80}Sr level structure to higher spins and to identify sidebands. It was hoped that considerable improvement over the results of previous studies could be achieved by both choosing a reaction which imparts a large amount of angular momentum to the compound nucleus and by using the array of six Compton-suppressed γ-ray detectors which was developed at the SERC Daresbury Laboratory by Twin *et al.* [Twi 83]. To this end, four major experiments were carried out: firstly, the ^{80}Sr level structure was measured using the technique of γ-γ coincidences; secondly, lifetimes of the higher levels were investigated using the Doppler shift attenuation method (DSAM), lifetimes of the first few excited yrast states having already been determined in previous studies using the recoil distance method; and finally both neutron gated and singles γ-ray angular distribution measurements were performed to provide information about the γ-ray multipolarities. All these experiments used the ^{54}Fe(^{29}Si, $2pn$)^{80}Sr reaction at beam energies between 85 and 110 MeV. ^{29}Si beams for the study were produced by the NSF tandem accelerator at the SERC Daresbury

TABLE 3.1

Summary of Experimental Measurements

Reaction	Beam Energy (MeV)	Accelerator[a])	Target	Type of Experiment	Detectors
^{54}Fe(^{29}Si, $2pn$)^{80}Sr	110	NSF	two self supporting ~ 250 μg/cm^2 ^{54}Fe targets separated by ~ 2 mm	γ-γ coincidence DCO ratios	TESSA II
	110	NSF	4.5 mg/cm^2 ^{54}Fe on a thick gold backing	γ-γ coincidence DSAM	TESSA II
	80 – 105	OEG	1 mg/cm^2 ^{54}Fe on a thick gold backing	excitation function	Ge(Li)
	105	OEG	2 mg/cm^2 ^{54}Fe on a thick gold backing	n-gated angular distribution	Ge(Li), NE213
	100	OEG	2 mg/cm^2 ^{54}Fe on a thick gold backing	singles angular distribution	Compton suppressed Ge(Li)

[a]) NSF = Nuclear Structure Facility tandem accelerator at the SERC Daresbury Laboratory

OEG = Folded tandem accelerator at the Nuclear Physics Laboratory, Oxford

Laboratory and by the folded tandem accelerator at Oxford. The experiments undertaken are summarized in table 3.1 and details are given below.

3.2 Choice of Reaction

3.2.1 INTRODUCTION TO HEAVY-ION REACTIONS

Over the last two decades heavy-ion fusion-evaporation reactions have been utilized extensively to study high spin states of nuclei on the neutron deficient side of the valley of stability. The use of these reactions has been favoured for two main reasons. Firstly, they have large cross-sections at reaction energies a few MeV above the Coulomb barrier. Secondly, a large amount of both energy and angular momentum is brought into the compound system, enabling the study of nuclear properties to high excitation energy and spin.

The reaction mechanism favours population of a particular set of states in the product nucleus – the yrast and yrare states – which decay predominantly by γ-ray emission. The yrast states are, by definition, the states with lowest energy for a given spin (or, equivalently, the states with highest spin for a given energy) and yrare states are almost yrast. (These states are preferentially populated because high energy, low multipolarity transitions are favoured in the decay of the compound nucleus.) The population of these states is, to a large degree, independent of nuclear structure effects. Thus, it is possible to study states which may be difficult to produce using other reaction mechanisms. In addition, because of the constraint of producing states with minimum energy for a given angular momentum, yrast states frequently have particularly pure configurations resulting

from simple collective or particle excitations. Therefore, yrast states can often be compared with the predictions of nuclear models with relative ease, providing valuable nuclear structure information. The preferential population of the yrast and yrare states in heavy-ion fusion-evaporation reactions allows detailed spectroscopic studies of the γ-ray decays of these excited states to be carried out.

Traditionally, heavy-ion fusion-evaporation reactions have been used in the heavy mass region ($A \sim 200$) to study neutron deficient nuclei. The application of these reactions to the study of heavy neutron deficient nuclei is particularly straightforward, since a compound nucleus formed from two stable nuclei is necessarily neutron deficient (except when either the target or the projectile is very light). Moreover, charged particle evaporation from the highly excited compound nucleus is retarded by the Coulomb barrier; thus, the compound nucleus de-excites by evaporating neutrons before γ-ray emission, further increasing the neutron deficiency. By a suitable choice of reaction energy, it is possible to choose the dominant number of evaporated neutrons and, hence, the final nucleus.

In contrast, for lighter compound systems the Coulomb barrier is unable to retard charged particle evaporation (particularly for p and α-particles) from an already neutron deficient compound nucleus. This evaporation of charged particles decreases the neutron deficiency, moving the nucleus closer to stability. Thus, in these lighter systems, the cross-section for producing neutron deficient nuclei is reduced and typically several reaction channels, corresponding to different combinations of evaporated particles, are populated at a given beam energy. This splitting of the reaction cross-section between several different product nuclei, apart from reducing the cross-section for forming the nucleus of interest,

complicates the γ-ray spectra with lines emitted from several different nuclei, making experimental studies of these light nuclei more difficult.

Review articles on the study of nuclei formed in heavy-ion fusion-evaporation reactions are given by Newton [New 74] and Diamond and Stephens [Dia 80]. In addition, the theory of these reactions is discussed by Pühlhofer [Püh 77].

3.2.2 THE ^{54}Fe(^{29}Si, $2pn$)^{80}Sr REACTION

High-spin states in ^{80}Sr were populated using the ^{54}Fe(^{29}Si, $2pn$)^{80}Sr fusion-evaporation reaction with a ^{29}Si beam energies of 85 – 110 MeV. As discussed above heavy-ion fusion-evaporation reactions are well suited to studies of high-spin states in neutron deficient nuclei. This particular reaction was chosen for three main reasons. Firstly, the similar ^{58}Ni(^{29}Si, $2pn$)^{84}Zr reaction had been successfully used to study high-spin states in ^{84}Zr [Pri 83]. Secondly, investigation of the reaction with ^{29}Si beam energies of up to 100 MeV by Belmont Moreno had shown ^{80}Sr to be strongly produced in the reaction with relatively little competition from other channels [Bel 84]. Finally, comparison of theoretical predictions of many different possible reactions with stable beams and targets to produce ^{80}Sr, using the statistical model computer program CASCADE [Püh 77], suggested this to be a good reaction for maximizing the ^{80}Sr cross-section and angular momentum, while minimizing competition from other channels.

The range of beam energies used in the experiments (85 – 110 MeV) are about the maximum of the reaction cross-section at $\sim$ 90 MeV. The actual value of the beam energy chosen for a particular experiment depended upon what was being investigated and is discussed below for the individual experiment.

Figure 3.2 shows a schematic representation of the ^{54}Fe(^{29}Si, $2pn$)^{80}Sr reaction at 110 MeV beam energy, as predicted by CASCADE [Püh 77]. Compound nucleus formation populates the nucleus at an excitation energy of 60 MeV and into a range of angular momentum states below a maximum of $\sim 45\hbar$. (In practice, a finite range of excitation energies is populated, corresponding to the energy loss of the beam through the target.) The compound nucleus (^{83}Zr) decays rapidly by evaporating particles (two protons and one neutron, if the product nucleus is ^{80}Sr). These evaporated particles each remove $\sim$ 15 MeV from the nucleus, but carry away only a few units of angular momentum. Once the nucleus is close to the yrast line (the locus of yrast states), further particle decay is inhibited by the absence of final states below the yrast line and the nucleus decays by γ-ray emission. As can be seen from the statistical model prediction (fig. 3.2), the angular momentum distribution in the ^{80}Sr product nucleus reaches its maximum value at about $\sim 25\hbar$. Therefore, it is reasonable to expect that discrete γ-ray transitions will be observed up to $\sim 25\hbar$. This spin is considerably greater than the maximum spin of 10^+ observed in earlier studies [Hig 83]. In these studies much lighter projectiles were used, resulting in less angular momentum being brought into the compound system. For example projectiles of ^{16}O, α, ^{24}Mg and α were used by Nolte *et al.* [Nol 74], Fields *et al.* [Fie 81], Lister *et al.* [Lis 82] and Higo *et al.* [Hig 83], respectively.

An additional feature of the chosen reaction is that the evaporated particles ($2pn$) are all light. This is important if spectroscopic studies of γ-rays emitted from a compound nucleus recoiling into vacuum are to be carried out, since the recoil imparted to the nucleus following evaporation of a heavy particle (for example an α-particle) can cause considerable

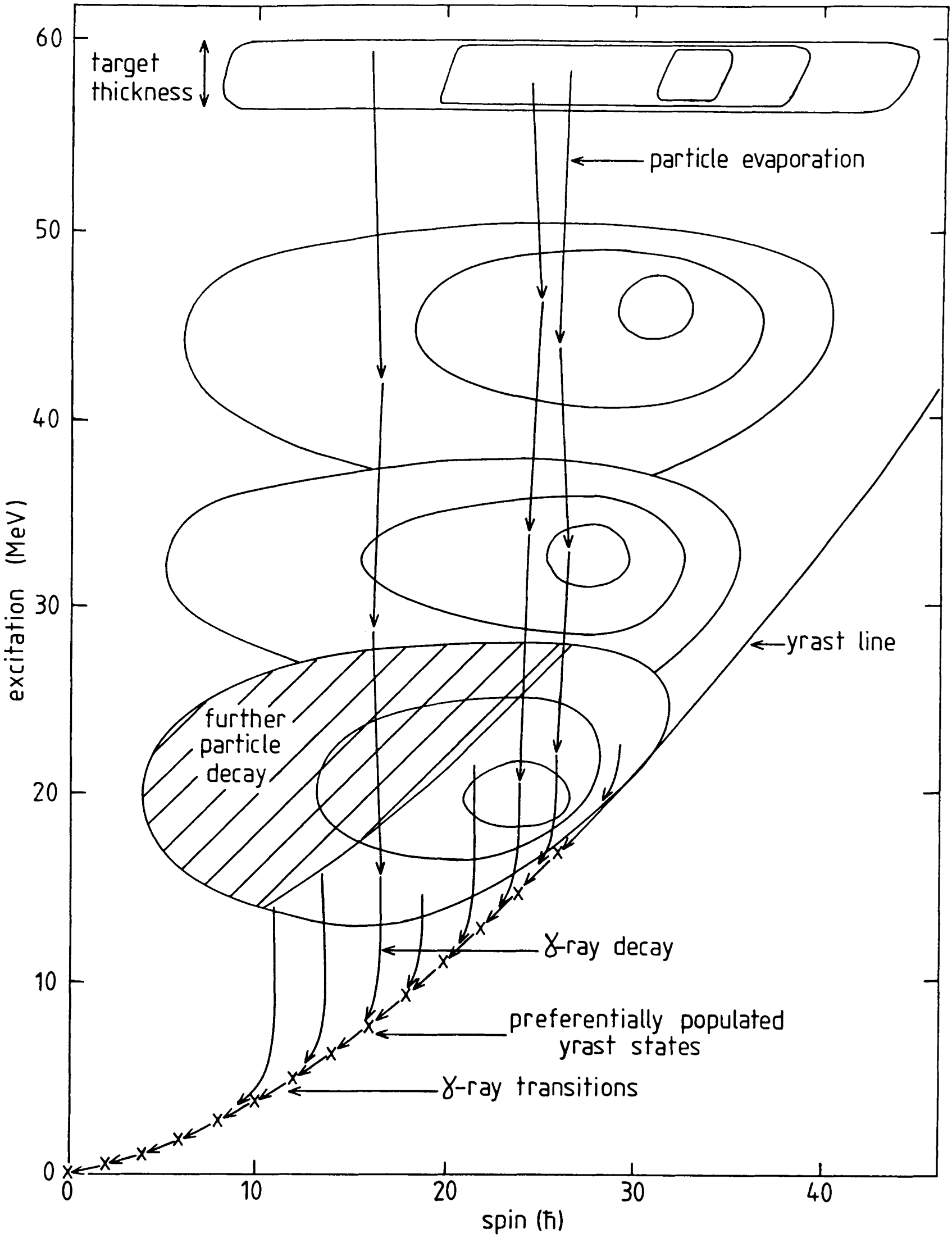


Figure 3.2 Schematic diagram of the ^{54}Fe(^{29}Si, $2pn$)^{80}Sr reaction at a beam energy of 110 MeV, as used in the present study, illustrating the decay of the compound nucleus and its daughters. See sect. 3.2.2 for details.

Doppler broadening of the γ-ray lines.

In addition to the $2pn$ channel, populating ^{80}Sr, several other reaction channels (in particular, the $3pn$ and $\alpha 2p$ channels producing ^{79}Rb and ^{77}Kr, respectively) are populated at the higher beam energies. The relative importance of these competing channels can be seen in the summed γ-γ spectrum shown in fig. 3.3.

3.3 The γ-γ Coincidence Measurement

3.3.1 INTRODUCTION

The ^{80}Sr level structure was investigated using the technique of γ-γ coincidences. A ^{29}Si beam energy of 110 MeV was chosen, some 20 MeV above the peak of the reaction cross-section, to maximize the angular momentum brought into the compound nucleus by the beam, while still maintaining a reasonably large cross-section for the production of ^{80}Sr relative to other reaction channels. The large number of γ-rays from the competing channels (fig. 3.3) often lead to contamination of coincidence spectra by γ-rays coincident with those which were only partially resolved from the γ-ray of interest. This made the interpretation of the data difficult, particularly for weak γ-rays, although usually the difficulties could be resolved by comparison with other coincidence spectra. Examples of such contamination are seen in several of the γ-γ coincidence spectra given in Chapter 4.

The target used was a sandwich of two 250 μg/cm^2 self supporting ^{54}Fe foils, the foils being separated by $\sim$ 2 mm. With such a target arrangement the ^{80}Sr nuclei recoil into vacuum and decay in flight. Thus, all the γ-rays are fully Doppler-shifted and Doppler broadening is avoided, except for that due to the finite spread of the cone of recoiling nuclei,

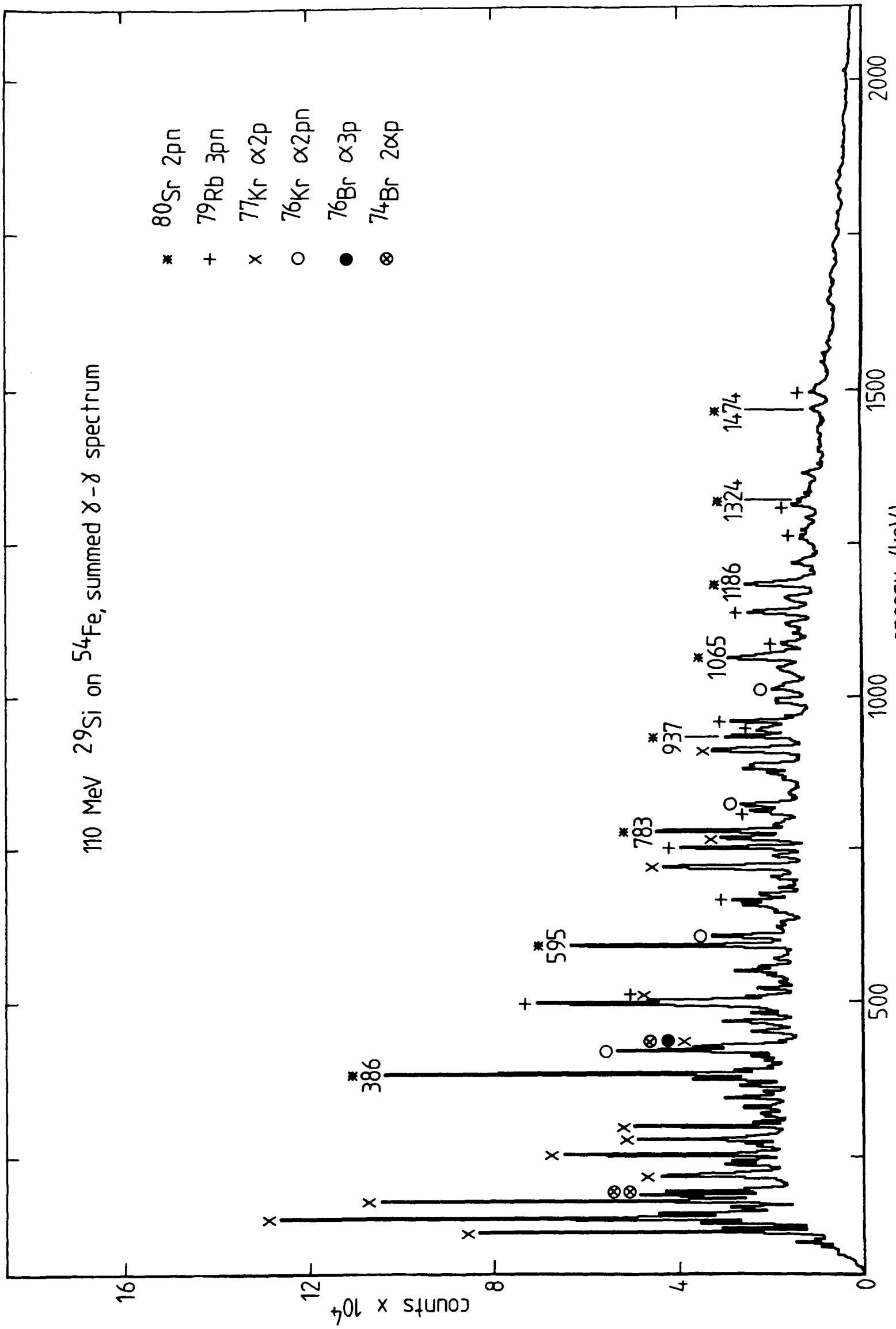


Figure 3.3 Summed γ-γ coincidence spectrum for the reaction of 110 MeV ^{29}Si on ^{54}Fe. This spectrum shows the γ-rays observed in the 150° detector, in coincidence with any γ-ray observed in any of the five other detectors. (In interpreting this spectrum it should be noted that the coincidence efficiencies for the different reaction channels are weighted by the average γ-ray multiplicity for that channel and, therefore, this spectrum is not equivalent to a singles spectrum.) Members of the ^{80}Sr ground state band are labelled by energy in units of keV.

and the range of velocities for the product nuclei due to energy loss straggling in the target. ^{29}Si ion beams for the study, as well as the γ-ray detection facilities, were provided by the Nuclear Structure Facility (NSF) at the SERC Daresbury Laboratory. The γ-rays were detected in the TESSA II array [Twi 83] which consisted of six Compton-suppressed germanium detectors, while the γ-ray multiplicity and the summed γ-ray energy were simultaneously recorded in an array of 62 bismuth germanate scintillation crystals. The hardware time resolution for the γ-γ coincidences was set at 50 ns. However, in this thin target experiment, the velocity (v/c ~0.03) of the fast recoiling nuclei was such that after a time of flight of more than ~ 5 ns γ-rays were emitted into a region shielded from the detectors and were not observed. The data were written event-by-event onto tape for later off-line analysis. A total of 15.8×10^6 coincidence events were recorded.

3.3.2 THE TESSA II DETECTOR ARRAY

TESSA (Total Energy Suppression Shield Array) II was the name given to an array of six Compton-suppressed germanium detectors and 62 bismuth germanate (BGO) crystals which was developed at the Daresbury Laboratory by P.J. Twin *et al.* [Twi 83] for the study of γ-rays following heavy-ion reactions. The properties of TESSA II are well documented [Twi 83] and details of the electronics are given, for example, in the Ph.D. Thesis of D.J.G. Love [Lov 84]. A schematic diagram of TESSA II is given in fig. 3.4.

3.3.2.1 The germanium detectors

Detailed spectroscopic information was obtained from six germanium semiconductor γ-ray detectors mounted, in the vertical plane which includes the beam axis, at $\pm 30°, \pm 90°$

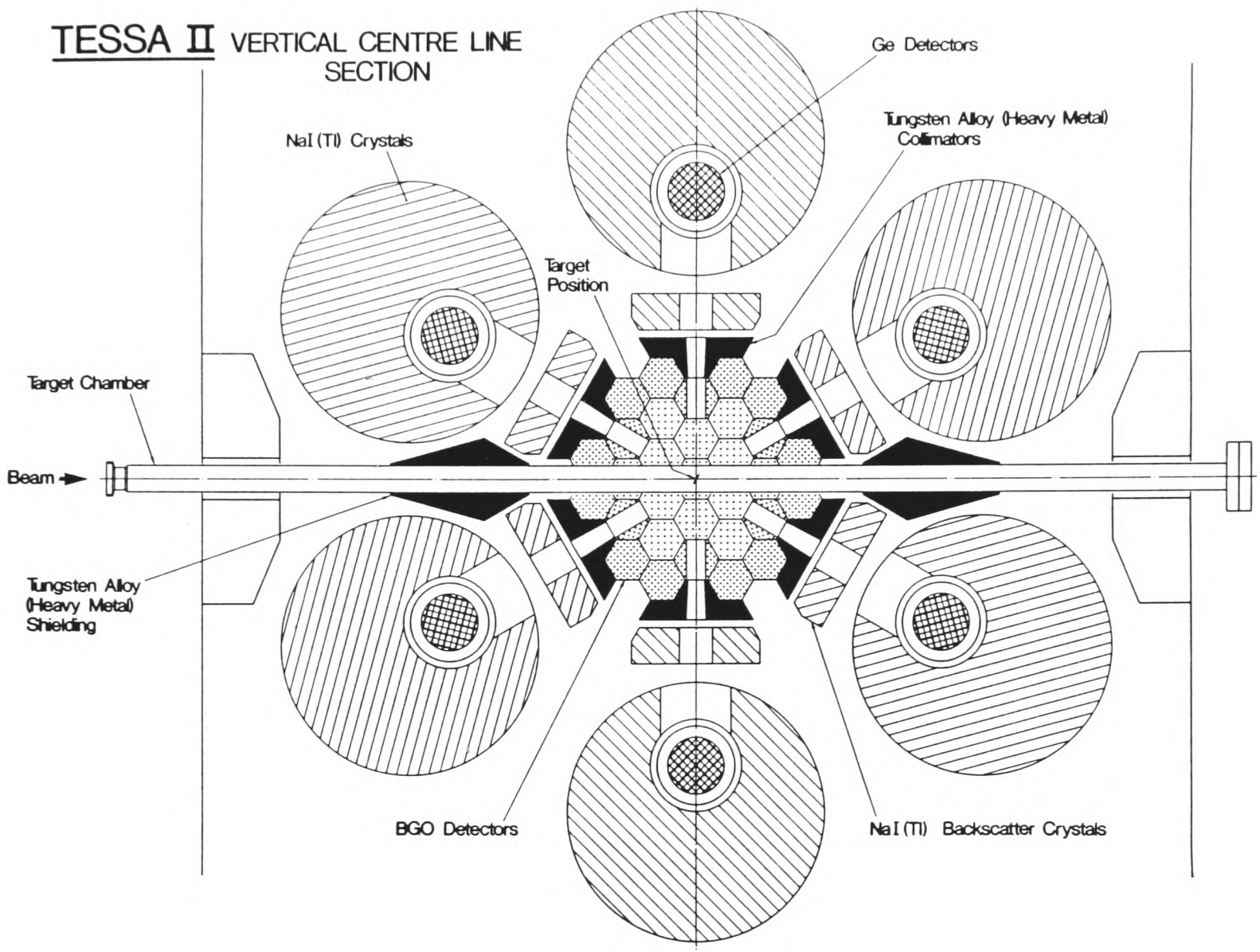


Figure 3.4 Schematic diagram of TESSA II, reproduced from the paper of Twin *et al.* [Twi 83]. See section 3.3.2 for details.

and $\pm 150°$ relative to the direction of the incoming beam. The detectors were mounted so that the γ-rays entered them through what is usually considered the side of the crystal (the curved surface of the germanium). This orientation was convenient for both efficient Compton-suppression of the detectors (see below) and for mounting the detectors. The centres of the germanium detectors were 27 cm from the target and the collimation was such that the γ-rays from the target were restricted to pass through a 4 cm diameter circle at the centre of the germanium detectors. The collimated solid angles of the germanium detectors were 0.16% each. Coincidence events were accepted between any pair of the six germanium detectors, giving a total of 15 pairs.

3.3.2.2 The Compton-suppression shields

Compton-suppression is particularly important for coincidence studies since events in which one or more signal is due to a Compton event contain no useful information. In order to reduce the number of such events, each germanium detector was surrounded by a NaI(Tl) anti-coincidence Compton-suppression shield (except for the collimation hole allowing the germanium detector to view the target, and the entrance hole through which the germanium detector was inserted into the crystal, which was at 90° to the axis between the detector and the target). Each shield consisted of two parts (fig. 3.4): the main shield was a 25 cm long by 20 cm diameter crystal and was mounted perpendicular to the beam axis with the germanium detector inserted parallel to, but offset from, the crystal axis; there was an additional annular shaped crystal positioned around the collimation hole between the germanium detector and the target. The larger of the two shields detected mainly the γ-rays scattered through small angles, while the smaller shield detected the

γ-rays which were scattered through angles close to 180°. These NaI(Tl) detectors were shielded from the target by a tungsten alloy collimator. Each of the large NaI(Tl) shields were optically coupled to five photomultiplier tubes while the smaller backscatter shields were coupled to two tubes.

Events in which a γ-ray was detected in both the germanium detector and the associated NaI(Tl) shield, corresponding to the Compton scattering of a γ-ray from the germanium detector into the NaI(Tl) crystal, were vetoed in hardware. For a 1.2 MeV γ-ray the fraction of events in a typical germanium detector which correspond to photo-absorption is only $\sim$ 17%, but the Compton suppression used in Tessa II increased this to $\sim$ 58%. Thus, the fraction of coincidence events which corresponded to photo-absorption in both detectors was increased from $\sim$3% to $\sim$29%, and the background due to Compton events was greatly reduced in the γ-ray spectra [Twi 83].

3.3.2.3 The BGO ball

In addition to the six Compton-suppressed germanium detectors, there was also a ball of 62 BGO (bismuth germanate) scintillation crystals surrounding the target chamber. These detectors were used to measure summed energy and total number (multiplicity) of the γ-rays in the γ-ray cascade associated with an individual coincidence event. It was important for the ball to be compact, to allow the germanium detectors to be positioned close to the target. Therefore BGO scintillators, which are much more efficient for detecting γ-rays than are NaI scintillators, were chosen. The BGO detectors, which were 38 mm across and 50 mm or 75 mm in length, had a hexagonal cross-section and were arranged in a honeycomb fashion around the target (with gaps for the entrance and exit of the beam

and for the germanium detectors to view the target). The electronics for the BGO ball were designed so that the ball could operate at high rates in excess of 300 k s^{-1}.

The energy signals from the elements of the ball were added in a custom built integrator to provide the total energy information. The timing signals for each element were fed into a specially constructed fold module which provided: an analogue representation of the fold; a digital representation of the fold; and a bit pattern recording which individual detectors had fired.

The multiplicity of γ-rays emitted in the cascade associated with an individual coincidence event is related to the angular momentum carried by the γ-rays in the cascade and hence to the angular momentum of the initial state. The sum energy of the event is directly related to the initial excitation of the γ-decaying nucleus. In some cases this information is useful for selecting the reaction channel, since different reactions may populate different regions of the excitation energy-spin plane, depending upon the angular momentum and energy carried away by the evaporated particles. In addition, if the sum energy and/or multiplicity of the background in a part of the γ-ray spectrum is different to that of the γ-ray peaks of interest in that region, then the sum energy and fold of an event can be used to reduce the background under these peaks. The properties of the sum energy and fold outputs of the BGO ball are discussed in greater detail by Twin *et al* [Twi 83].

3.3.2.4 Writing events onto tape

Valid coincidence events from TESSA II, consisting of two or more coincidence events in the germanium detectors with no signals from the corresponding NaI(Tl) Compton suppression shields and a sum energy and fold signal from the BGO ball, were written

event-by-event directly onto magnetic tape. The number of words per event was variable, depending upon the number of coincident γ-rays in the germanium detectors (two or more). Each word consisted of two eight bit bytes. The first word contained the trigger identifier in the first byte (always "trigger 24" in our experiments) and the total number of words in the event in the second byte. The second word identified which ADCs were to be read in the event. The third and following words contained the digitized signals read from the ADCs. (In our experiment, four ADCs were usually read, corresponding to the BGO sum energy and fold and two γ-ray energies from the germanium detectors.)

3.3.3 ANALYSIS OF THE γ-γ COINCIDENCE DATA

Prior to analysis, the tapes were rewritten onto high density tape. While the tapes were being rewritten, slight gain adjustments were made to remove the variation in in-beam γ-ray energies from the six germanium detectors, allowing signals from the various detectors to be added together. (Coarse adjustments were made to the gains of the spectroscopic amplifiers at the beginning of the experiment to match the energies of the ^{80}Sr γ-rays in the six germanium detectors, removing most of the effects due to Doppler-shifting and differing detector and amplifier responses.)

Before sorting the γ-γ coincidence data, the properties of the sum energy and fold BGO data were investigated. It was found that, for the reaction used in the present study, the sum energy and fold for the dominant competing reaction channels ($2pn$, $\alpha 2p$ and $3pn$) were very similar, so that no significant degree of channel selection could be obtained through a gate on the sum energy and fold. Perhaps more significantly, gates set on the 1474 keV $16^+ \rightarrow 14^+$ ^{80}Sr ground state band transition (with correction for the under-

lying background) and also on a neighbouring background region showed almost identical sum energy and fold spectra (fig. 3.5). This showed that no significant reduction of the background in the high energy part of the spectrum, where the low intensity transitions between the highest spin states are expected to lie, could be obtained by setting a gate on the sum energy and fold.

The data were compressed by a factor of two and sorted, with a gate set on BGO multiplicities greater than 4 to remove the low multiplicity events due to radioactive decay and $e^+ - e^-$ annihilation, into a 2K x 2K coincidence matrix which was stored on disc for easy access. The matrix was then symmetrized by adding it to its transpose, so that all the available coincidence data on a channel could be obtained by examining a single row or column. (In general, a γ-ray spanned several channels. Therefore, to obtain all of the information on a particular γ-ray it was necessary to add together several neighbouring rows (or, equivalently, columns).) The coincidence spectrum of a γ-ray could then be projected in a few seconds by executing a single computer command. It was necessary to subtract from this spectrum coincidences with the statistical γ-rays and the Compton background under the γ-ray peak of interest. This was achieved by projecting out the coincidence spectrum of a suitable nearby background region and subtracting it from the spectrum of interest, following suitable scaling to match the widths (and sometimes heights) of the two gating regions. In the analysis of the data, the coincidence spectrum of every γ-ray observed in singles was projected, background subtracted, plotted and analysed, the total number of spectra involved amounting to over 200 and the detailed analysis of those spectra relevant to ^{80}Sr taking many months.

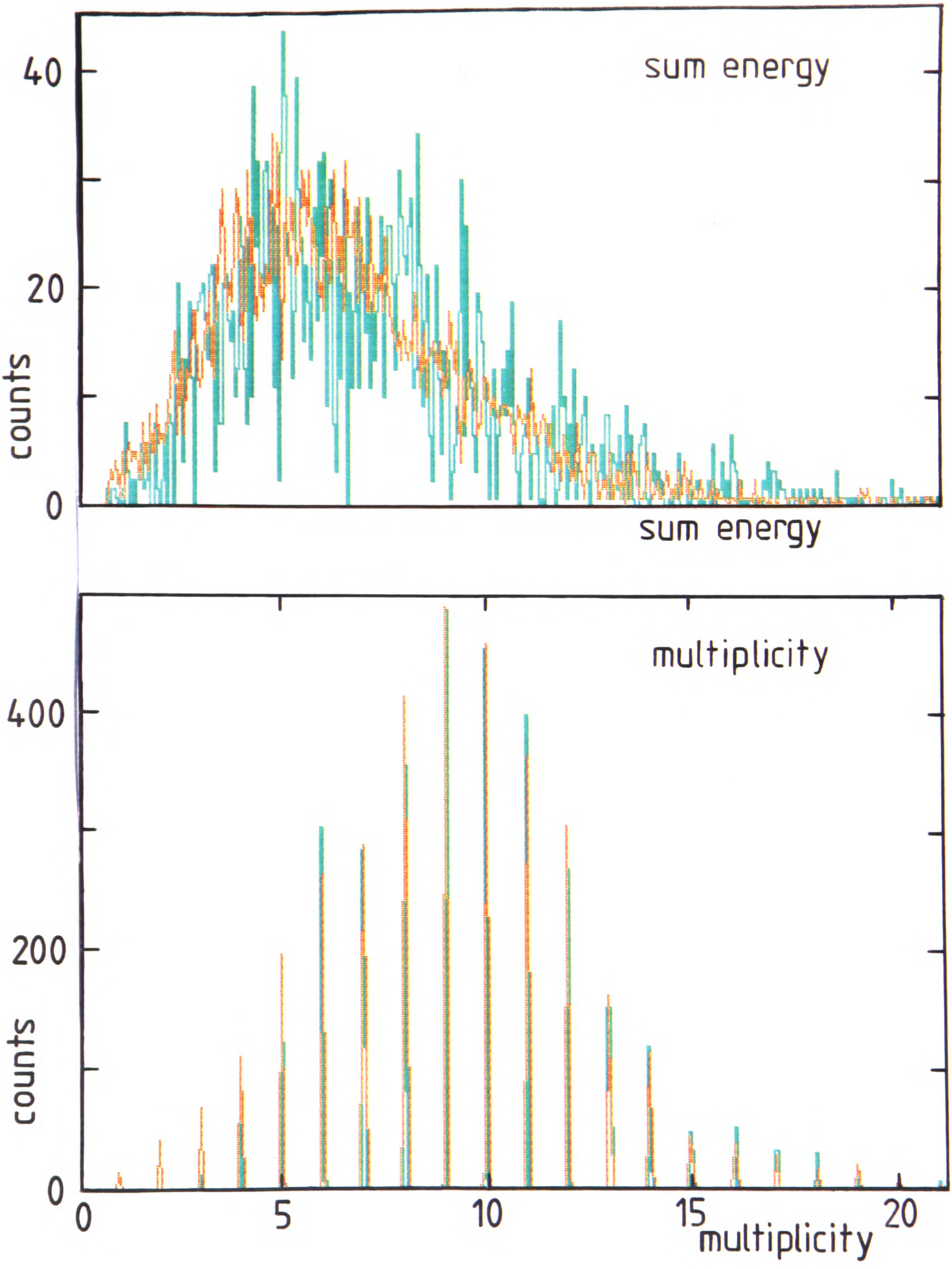


Figure 3.5 Comparison of the γ-ray sum energy and multiplicity, measured in the BGO ball of TESSA II during the γ-γ coincidence measurement of the present study, for the 1474 keV $16^+ \rightarrow 14^+$ ^{80}Sr ground state band transition (green) and a neighbouring background region (orange). (The spectra gated by the 1474 keV transition have been corrected for the background beneath the peak corresponding to the 1474 keV transition.) The orange background spectrum has been scaled down so that the spectra may be more easily compared. The energy scale in the sum energy spectrum is uncalibrated. These spectra are discussed in sect. 3.3.3.

3.3.3.1 Efficiency calibration

The relative efficiencies of the germanium detectors were determined by simultaneously recording the spectrum of an ^{152}Eu calibration source, placed at the target position, in all six detectors. The detector efficiencies are summarized in fig. 3.6 which shows the average detector efficiency as a function of γ-ray energy.

3.3.3.2 Energy calibration

The in-beam Doppler shifted γ-ray energies were calibrated using intense in-beam ^{77}Kr, ^{79}Rb and ^{80}Sr γ-rays [Nol 75, Pan 82, Hig 83]. A least squares fitting program was then used to obtain a linear calibration of energy as a function of channel number (fig. 3.7), the calibration being very close to 2 keV per channel.

Systematic errors in the calibration were kept to a minimum by using γ-ray energies from several different sources. The possible systematic errors in the calibration were estimated, from the errors in the energies of the calibration lines and the goodness of fit of the linear calibration, to be better than 0.1 keV for energies less than 1 MeV rising to an uncertainty of 0.3 keV at 2 MeV.

3.3.3.3 Lineshape calibration

The full width at half maximum (FWHM) of the γ-ray peaks in the coincidence spectra where calibrated by fitting Gaussian lineshapes with variable widths to several strong peaks from ^{77}Kr, ^{79}Rb and ^{80}Sr (corresponding to the $\alpha 2p$, $3pn$ and $2pn$ channels, respectively). It was found that the γ-rays from channels in which α-particles were emitted were considerably broader than those from the other channels (fig. 3.8). The extra width was due to Doppler broadening caused by the recoil of the nucleus during α-particle emission.

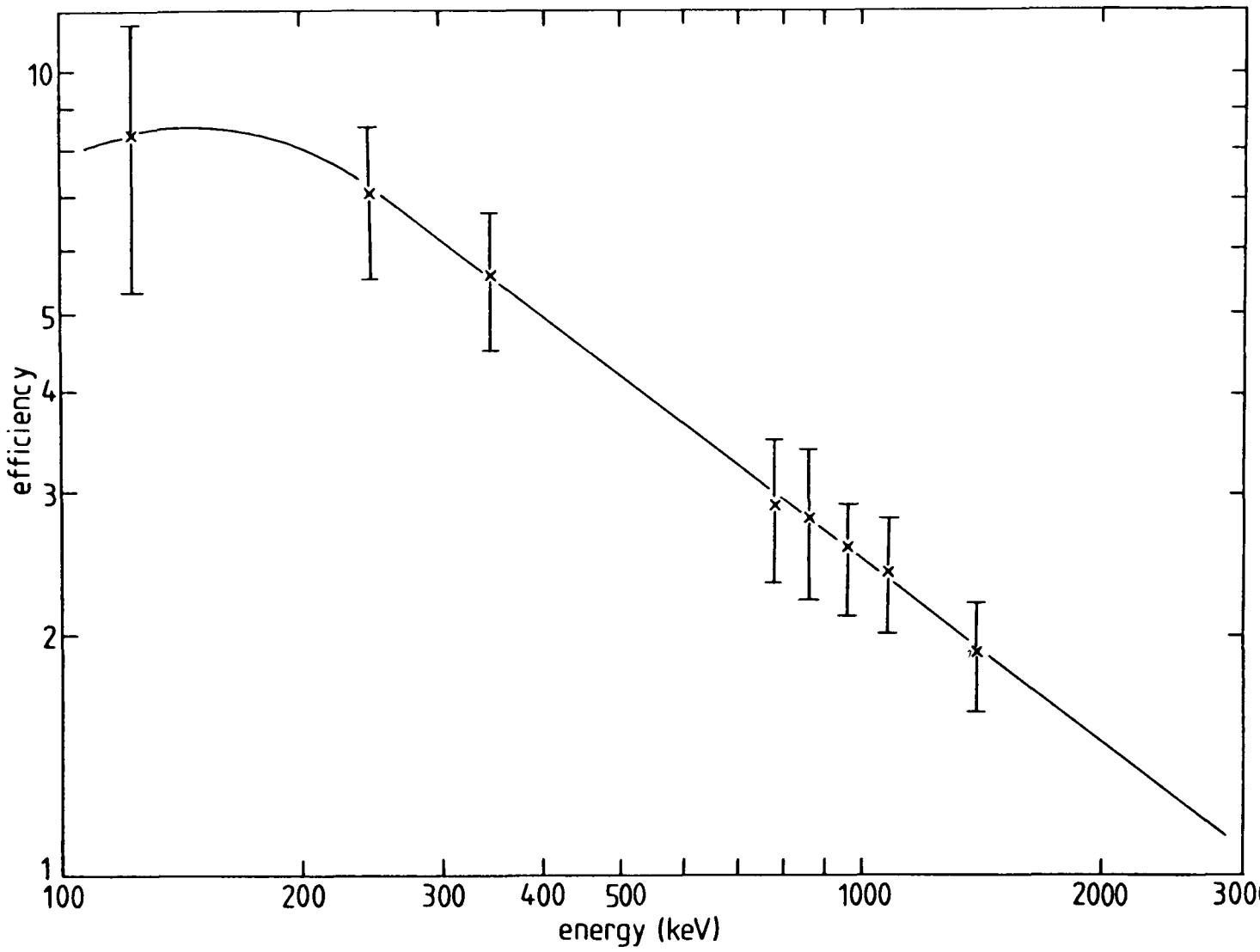


Figure 3.6 Average detection efficiencies measured for the six TESSA II germanium detectors. The "error bars" represent the standard deviation of the efficiencies about the mean value for the six detectors.

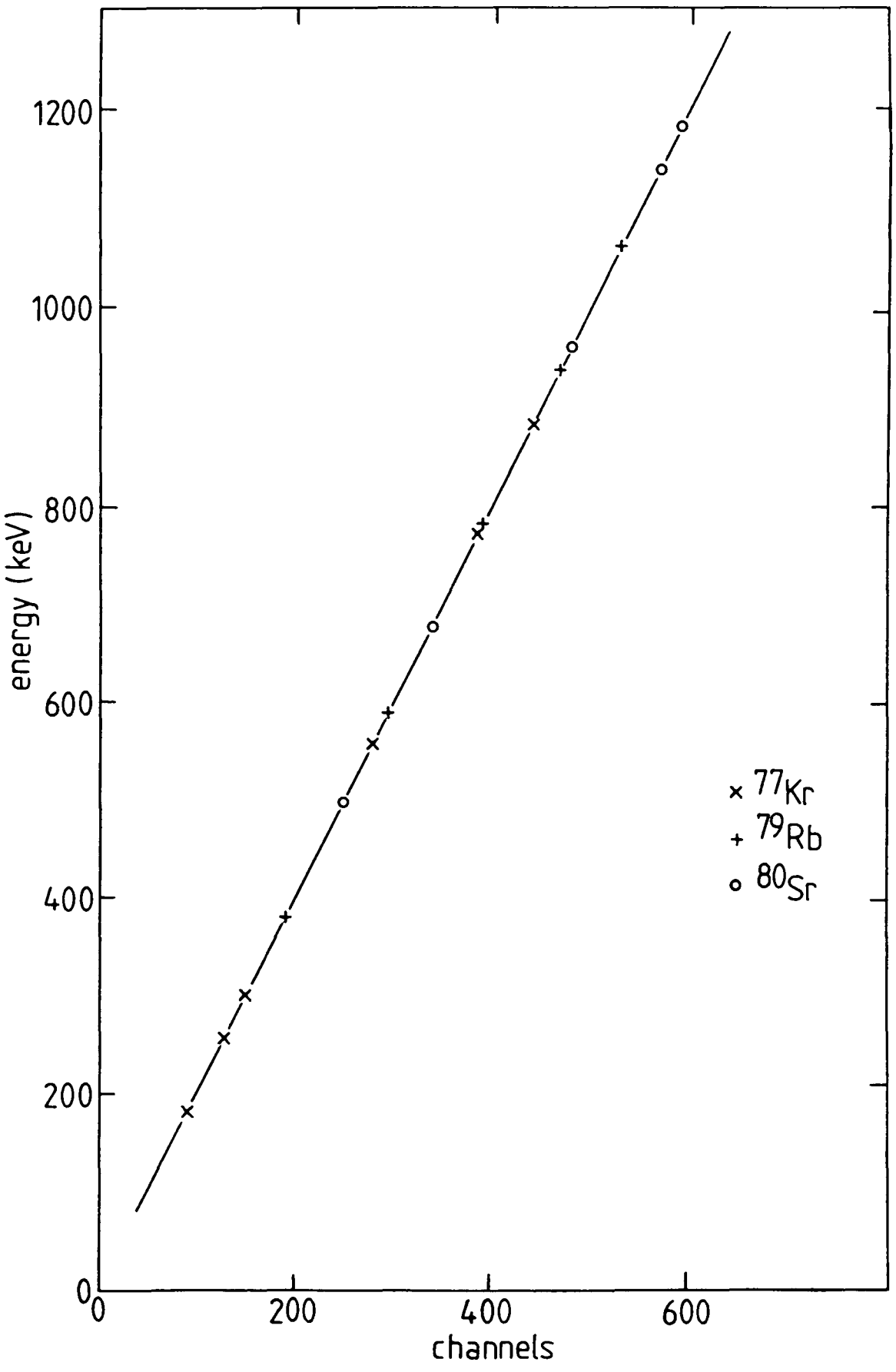


Figure 3.7 Linear energy calibration for the γ-γ coincidence data.

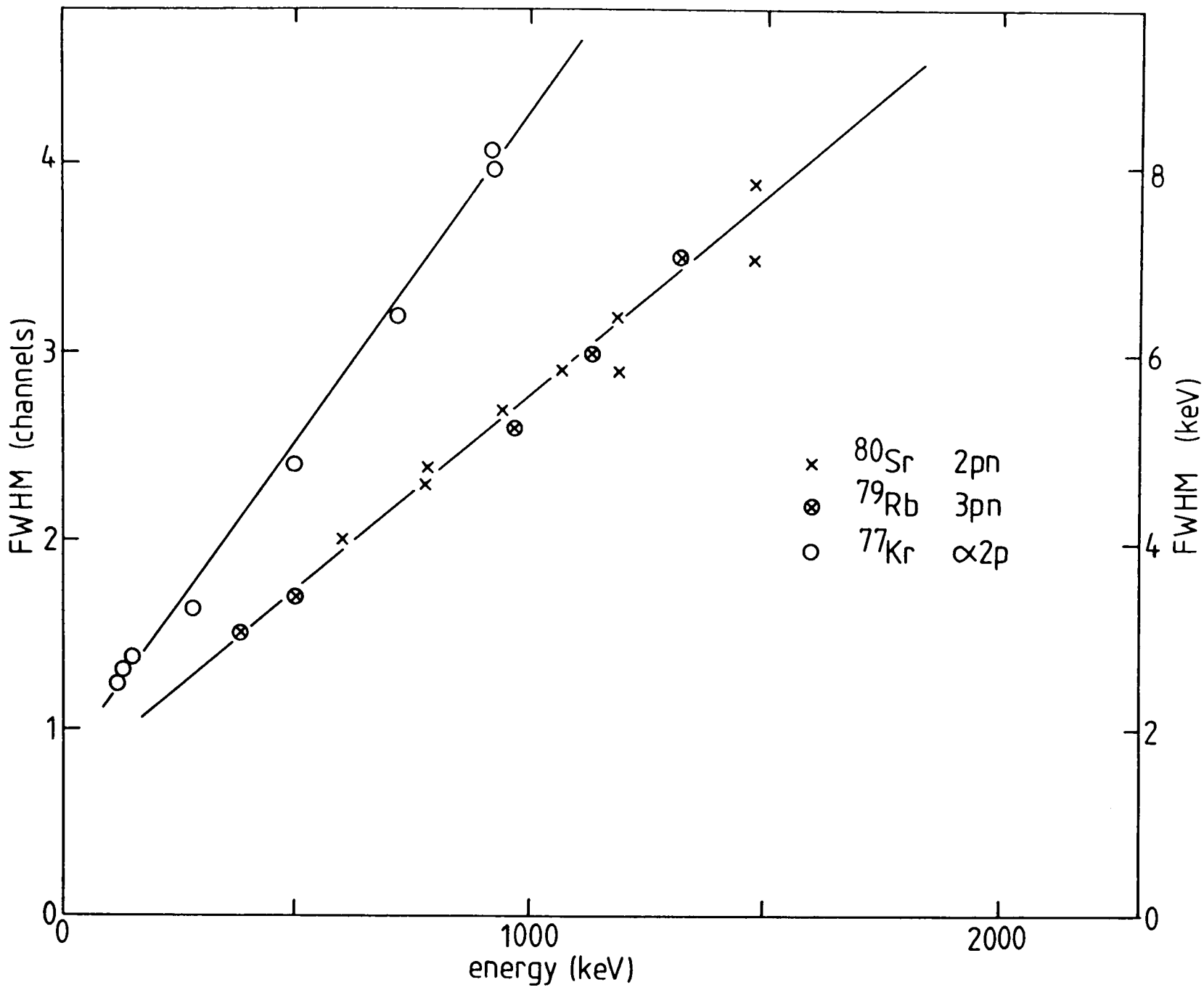


Figure 3.8 Full width at half maximum (FWHM) of the γ-rays in the γ-γ coincidence data. The FWHM is shown both in units of channels (left hand y-axis scale) and in keV (right hand y-axis scale).

This dependence of the γ-ray width upon reaction channel proved to be useful during the following analysis in helping to identify the nucleus from which a γ-ray was emitted. In fitting Gaussian lineshapes to the experimental γ-ray peaks to extract energies and intensities the γ-ray FWHM were fixed to this calibration.

3.3.3.4 Determination of γ-ray energies and intensities

The γ-ray energies were determined from the mean of several measurements extracted from the coincidence data. The error was the standard error in the mean value. If a suitable number of measurements was not available, then the error was estimated from the errors given by the Gaussian lineshape fitting program. The estimated systematic errors due to uncertainties in the calibration (sect. 3.3.3.2) were small compared with the uncertainties in the γ-ray lineshape centroids and their effect on the total error was negligible. The intensities of most of the γ-rays were obtained from the coincidence intensities in the 386 keV gate (fig. 4.3) and, where appropriate, the 595 keV gate. However, the intensities of the 1120, 1260, 1368, 1441, 1533, 1648 and 1746 keV γ-rays were obtained from the summed coincidence spectrum of the 1817, 777, 798 and 970 keV γ-rays (fig. 4.11). In addition, the intensity of the 386 keV γ-ray was obtained from the "pseudo singles" summed spectrum of the γ-γ coincidence data (fig. 3.3).

3.3.3.5 γ-ray directional correlations

In addition to providing information on the structure of the level scheme, the γ-γ coincidence data also yielded some information on γ-ray multipolarities. The nuclei formed in heavy-ion fusion-evaporation reactions are strongly aligned about the M=0 substate, relative to the direction of the incoming beam (see, for example, [Kra 73, Dia 66]). This

alignment causes the γ-rays to have an angular distribution which depends upon the angular momentum carried by the γ-ray and the multipole mixing ratio. (The theory of γ-ray angular distributions is given in detail in the paper by Rose and Brink [Ros 67]; a short discussion is also given in Appendix 2.) Detection of a γ-ray or particle in a detector which does not have cylindrical symmetry with respect to the beam axis perturbs the angular distribution of subsequent γ-rays, by altering the distribution of the magnetic substates. As a result, the probability for detecting pairs of γ-rays in a given pair of TESSA II detectors depends upon the multipolarities of the γ-rays. (The theory of directional correlations of γ-rays emitted from aligned nuclear states is complex with the correlations depending both upon the γ-ray multipolarities and upon the details of the experimental geometry. This theory is discussed in detail by Steffen and Alder [Ste 72] while a more experimentally orientated discussion is given by Krane, Steffen and Wheeler [Kra 73]. Computer programs, for example TRIFAC written by P.J. Twin, exist for predicting the correlations for particular experimental geometries.)

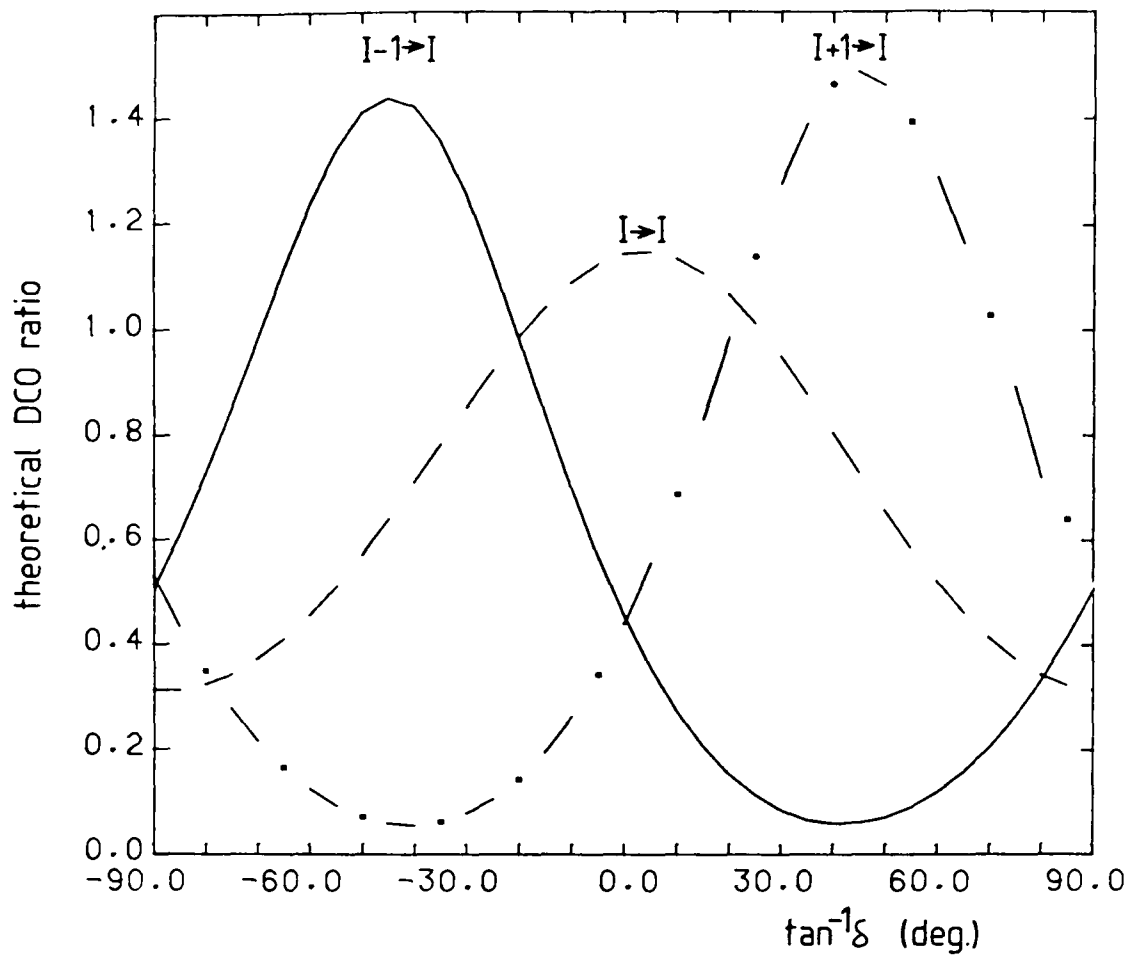
In practice, it is usual to measure the ratio of two angular correlations (called a directional correlation ratio, or DCO ratio) thereby removing normalization factors which contain no useful information. The directional correlation (DCO) ratio which was extracted from the data in the present experiment was

$$\text{DCO ratio} = \frac{\text{intensity for observing } \gamma_1 \text{ at } 30^\circ \text{ gated by } \gamma_2 \text{ at } 90^\circ}{\text{intensity for observing } \gamma_1 \text{ at } 90^\circ \text{ gated by } \gamma_2 \text{ at } 30^\circ} \qquad (3.1)$$

where γ_1 is the γ-ray of interest, and γ_2 is a γ-ray of known $E2$ multipolarity. (This ratio was calculated, from the measured efficiency curves of the TESSA II germanium detectors, to be independent of the γ-ray energies to better than 5%.) The DCO ratio is unity when

γ_1 is also of $E2$ multipolarity, while if γ_1 is dipole the ratio varies continuously between ~ 0 and ~ 2 depending upon the multipole mixing ratio δ of γ_1. (Note, the multipole mixing ratio convention used in angular correlation theory by Krane, Steffen and Wheeler [Kra 73] is opposite in sign to that used for angular distributions by Rose and Brink [Ros 67].) As the nuclear alignment produced in the reaction is such that the populations of substates with projections $\pm$M with respect to the beam axis are equal, the detectors at $\pm 30°$ are equivalent to those at $\pm 150°$, allowing the spectra corresponding to these four detectors to be added.

Examples of this DCO ratio, extracted from the experimental data for γ-rays of known multipolarity in ^{77}Kr and ^{80}Sr, are plotted in fig. 3.9 together with theoretical predictions of the ratio. The theoretical DCO ratios are for complete alignment (all the initial states in the M=0 substate); the DCO ratio tends to unity as the width of the substate distribution about the M=0 substate increases. It can be seen from the theoretical predictions that a DCO ratio significantly different from unity indicates a dipole transition, although a dipole transition may have a DCO ratio equal to unity for particular choices of the multipole mixing ratio δ. Therefore, the DCO ratios were useful as a consistency check on multipolarity assignments, although a DCO ratio alone was usually not sufficient to determine a multipolarity. Thus, the information on γ-ray multipolarities obtained from the DCO ratios complimented that obtained from the γ-ray angular distribution measurements (see below).



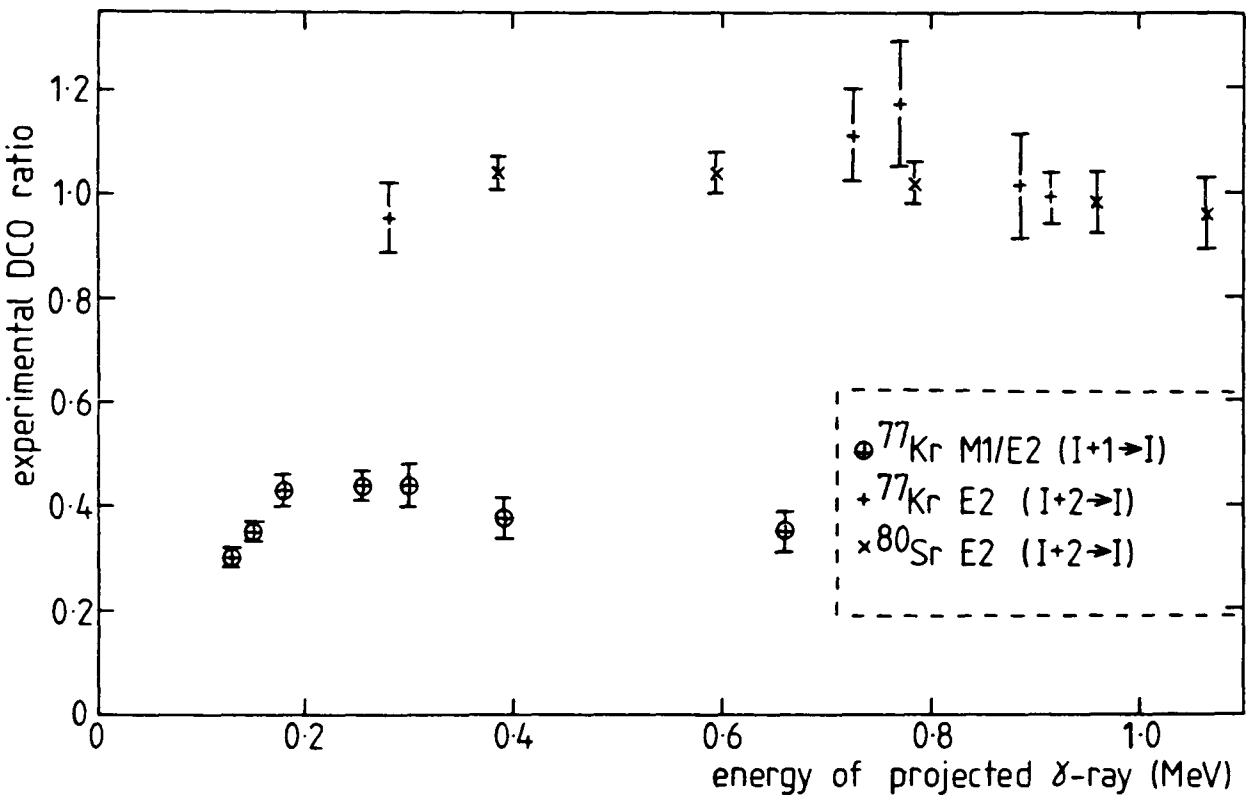


Figure 3.9 Theoretical and experimental DCO ratios, as defined and discussed in sect. 3.3.3.5. The theoretical DCO ratios are given as a function of multipole mixing ratio for $I+1 \rightarrow I$, $I \rightarrow I$ and $I-1 \rightarrow I$ transitions gated by a subsequent stretched quadrupole transition. (The DCO ratios were calculated for $I = 30$ and maximal alignment.) The theoretical DCO ratios for $I+2 \rightarrow I$ or $I-2 \rightarrow I$ quadrupole transitions are unity. DCO ratios measured for stretched transitions in the present experimental study are given as a function of γ-ray energy to separate the measurements. Spin assignments for the transitions in ^{77}Kr and ^{80}Sr come from [Nol 75] and [Lis 82], respectively. The mixing ratio sign convention in this diagram (and throughout the text) is that of Rose and Brink [Ros 67]; this convention is opposite in sign to that of Krane, Steffen and Wheeler [Kra 73] which is often used for angular correlations.

3.4 γ-Ray Angular Distribution Measurements

3.4.1 INTRODUCTION

Heavy-ion fusion-evaporation reactions produce nuclei with angular momenta which are strongly aligned about the M=0 magnetic substate relative to the direction of the incoming beam. Little angular momentum is removed in the decay to the yrast line and, as a result, this alignment is largely retained. Therefore, in most cases, the observed γ-rays emitted in decays of the yrast and yrare states exhibit strong angular distributions depending upon the spins of the initial and final states, the multipolarities and multipole mixing ratios of the emitted γ-rays, and the degree of nuclear alignment. This phenomenon was first investigated experimentally by Diamond *et al.* [Dia 66] and has been treated theoretically by Rose and Brink [Ros 67] (a short discussion of angular distribution theory is given in Appendix 2). The alignment is retained in the stretched transitions which dominate the yrast cascades [Ros 67]. Therefore, the angular distribution effects are still evident in the states at the bottom of the level scheme. The angular distribution $W(\theta)$ is conveniently written as a sum of Legendre polynomials:

$$W(\theta) = \sum_{k} A_k \alpha_k P_k(\cos\theta) \tag{3.2}$$

where: k takes even values only; P_k is the k^{th} Legendre polynomial; A_k depends upon the spins of the initial and final states and the γ-ray multipolarity and multipole mixing ratio; and α_k is a coefficient representing the attenuation of the angular distribution due to the finite width of the magnetic substate distribution. The angular distribution is such that $W(\theta) = W(-\theta) = W(\pi - \theta)$.

For a γ-ray for which the highest contributing multipole is of order λ, the coefficients are non-zero only for $k \leq 2\lambda$. Thus, as for most γ-ray transitions the highest multipole is of order $\lambda = 2$, it is usual to fit the angular distribution to the polynomial:

$$W(\theta) = I_\gamma(1 + a_2^{max}\alpha_2 P_2(\cos\theta) + a_4^{max}\alpha_4 P_4(\cos\theta)) \tag{3.3}$$

where I_γ is the γ-ray intensity and is equal to the coefficient A_0 of eq. 3.2. The angular distribution coefficients $a_k^{max} = A_k/A_0$ are tabulated for various initial and final state spins and the attenuation coefficients α_k are tabulated for substate distributions of various widths [Yam 67, Mat 74a, Mat 74b]. γ-ray angular distributions are routinely used to aid in the assignments of multipolarities and multipole mixing ratios to γ-rays, and of spins to the nuclear levels. (However, the angular distributions contain no explicit information about the nuclear parity, or the electric or magnetic character of the γ-rays.)

Measurements of γ-ray angular distributions were carried out during two separate six day experiments at Oxford. In both cases the targets chosen were thick (2 mg/cm^2) to maximize the amount of ^{80}Sr produced. Prior to the angular distribution measurements an excitation function was performed for ^{29}Si beam energies from $85 - 105$ MeV (fig. 3.10) on a 1 mg/cm^2 ^{54}Fe target with a 48 mg/cm^2 gold backing, to facilitate the choice of beam energies for the angular distribution measurements. (Unfortunately, the 1408 keV ^{54}Fe Coulomb excitation line was considerably Doppler broadened, because of its short lifetime ($\tau_{1/2} = 1.0$ ps), making it unsuitable for normalization purposes. Therefore, the excitation function was normalized to the 279 keV ($\tau_{1/2} = 16$ ps) Coulomb excitation line of the ^{179}Au backing.) Beam energies slightly lower than those used in the γ-γ coincidence experiments were chosen for the angular distribution measurement to minimize the cross-section for

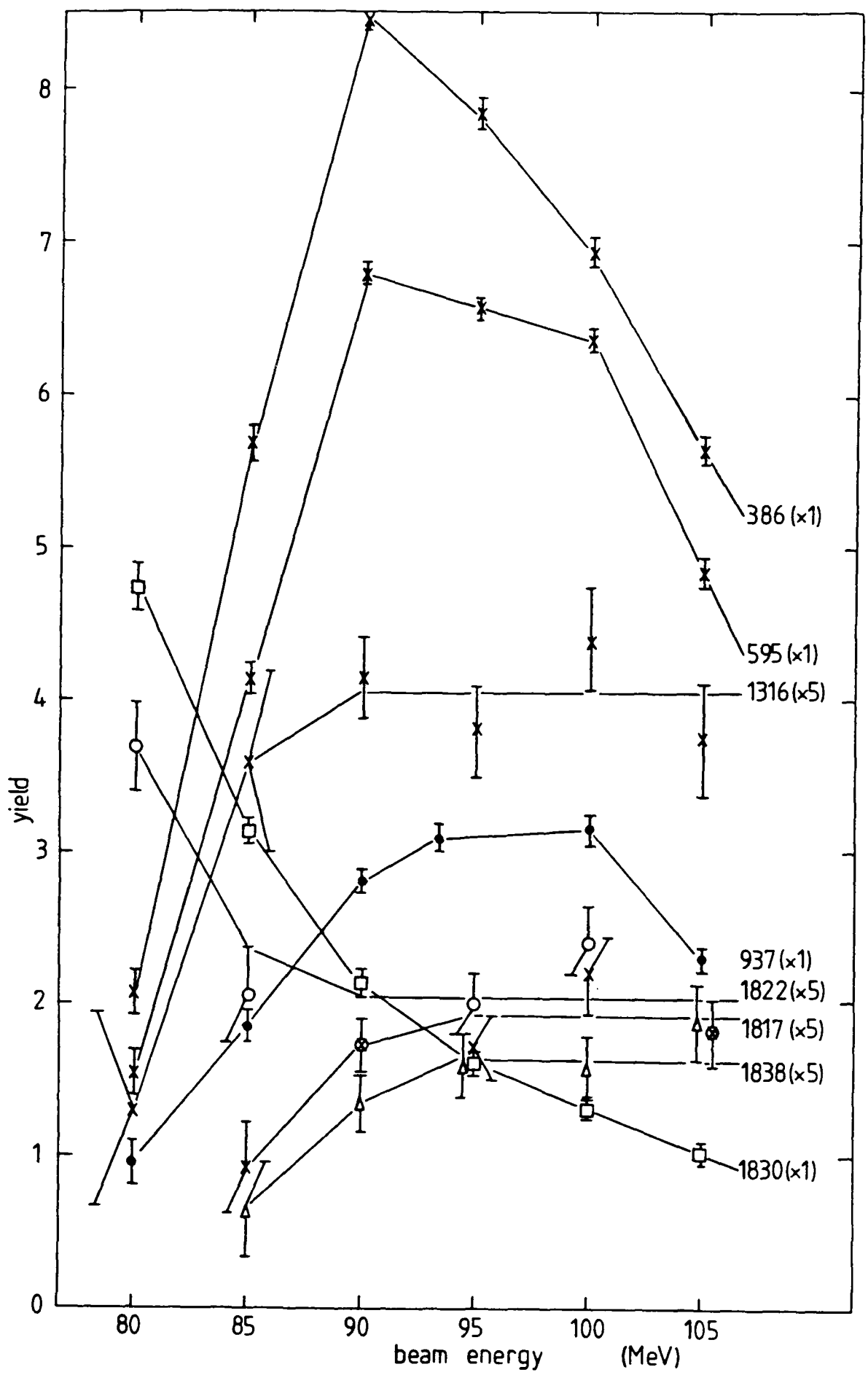


Figure 3.10 Yield curves, as a function of beam energy for the reaction of ^{29}Si on ^{54}Fe, for the 386, 595 and 937 keV ^{80}Sr ground state band transitions; the 1316, 1817 and 1838 keV ^{80}Sr interband transitions; and the 1830 and 1822 keV transitions which are not from ^{80}Sr but which lie close to the 1817 and 1838 keV ^{80}Sr transitions. The yields have been corrected for the efficiency of the γ-ray detector as a function of energy. The yield scale is arbitrary. The yield curves of the 1838, 1822, 1817 and 1316 keV transitions have been scaled up by a factor of five, relative to those of the other γ-rays. The raw beam energy, which does not take account of the energy lost in the target, is shown. The beam energy in the target was on average $\sim$ 6 MeV less than this. In some cases the experimental points have been displaced slightly in the horizontal direction to separate the data for clarity. The lines are drawn to guide the eye and do not represent fits to the data.

competing reaction channels, while maintaining a large cross-section for producing ^{80}Sr. In particular, the beam energies chosen minimize the contamination of the 1817 and 1838 keV ^{80}Sr interband transitions by the close lying 1822 and 1830 keV γ-rays (fig. 3.10). Where possible, γ-ray angular distributions were measured in singles mode. However, it was necessary, in some cases, to perform a neutron-gated angular distribution to reduce the intensities of γ-rays from other reaction channels. (The angular distribution is unaltered by the detection of the neutrons, provided the neutron detector is situated at 0° or 180° with respect to the beam axis and the detector is axially symmetric with respect to this axis.) In both sets of measurements the angular distributions were corrected for attenuation due to the finite solid angle subtended by the detector, calculated using the computer program written by D. Rogers and D.W. Bennett [Rog 72, Ben 80]. Corrections due to absorption of γ-rays by the target were calculated from the tables of γ-ray absorption coefficients of Davisson *et al.* [Dav 52] and were found to be negligible ($< 0.4\%$ at 0.35 MeV and $< 0.1\%$ at 1.0 MeV).

3.4.2 SINGLES ANGULAR DISTRIBUTION

The singles angular distributions were measured by moving a Compton-suppressed Ge(Li) on a rotatable table. The target was a 2 mg/cm^2 ^{54}Fe layer evaporated onto a 20 mg/cm^2 natural Au backing. A total of 11 measurements were made at angles between 0° and 90° (inclusive) to the direction of the incoming beam. The measurements were normalized to intense reaction lines observed in a stationary monitor detector positioned at $-125°$. Dead-time corrections for both detectors were made by applying a pulser, triggered by the output of the target current integrator, to the Ge(Li) "test" inputs; the

number of trigger pulses was recorded in a scaler. Variations in the efficiency of the rotated detector as a function of angle, due principally to non-uniformities in the target chamber walls, were measured by placing a ^{152}Eu source at the target position and measuring the γ-ray detection efficiencies as a function of angle.

The NaI(Tl) Compton-suppression shield used in this experiment was similar to those used in TESSA II (sect. 3.3.2.2) although it did not include a backscatter detector. The beam of γ-rays entering the suppressed germanium detector was defined by a lead collimator. The collimation hole was tapered, being narrowest close to the target (2.5 cm diameter) and widest close to the germanium detector (3.5 cm diameter). The collimation restricted the γ-rays detected from the target to an area of 3 cm radius at the centre of the germanium crystal. Care was taken to position the germanium detector so that the detector crystal was centred about the collimation axis. The face of the movable Compton-suppressed detector was 18 cm from the target. A block diagram of the electronics used in this experiment is given in fig. 3.11.

The resulting angular distributions were fitted to the polynomial

$$W(\theta) = I_\gamma(1 + a_2 Q_2 P_2(\cos\theta) + a_4 Q_4 P_4(\cos\theta)) \qquad (3.4)$$

In this equation experimental quantities a_2 and a_4, defined by $a_i = a_i^{max}\alpha_i$, have been introduced (c.f. eq. 3.3). The coefficients Q_2 and Q_4 represent attenuation of the measured angular distribution due to the finite solid angle subtended by the detector. (Values of $Q_2 = 0.98(1)$ and $Q_4 = 0.95(2)$ were calculated for these attenuation coefficients [Rog 72, Ben 80].)

Information concerning the γ-ray multipolarities and mixing ratios and the level spins

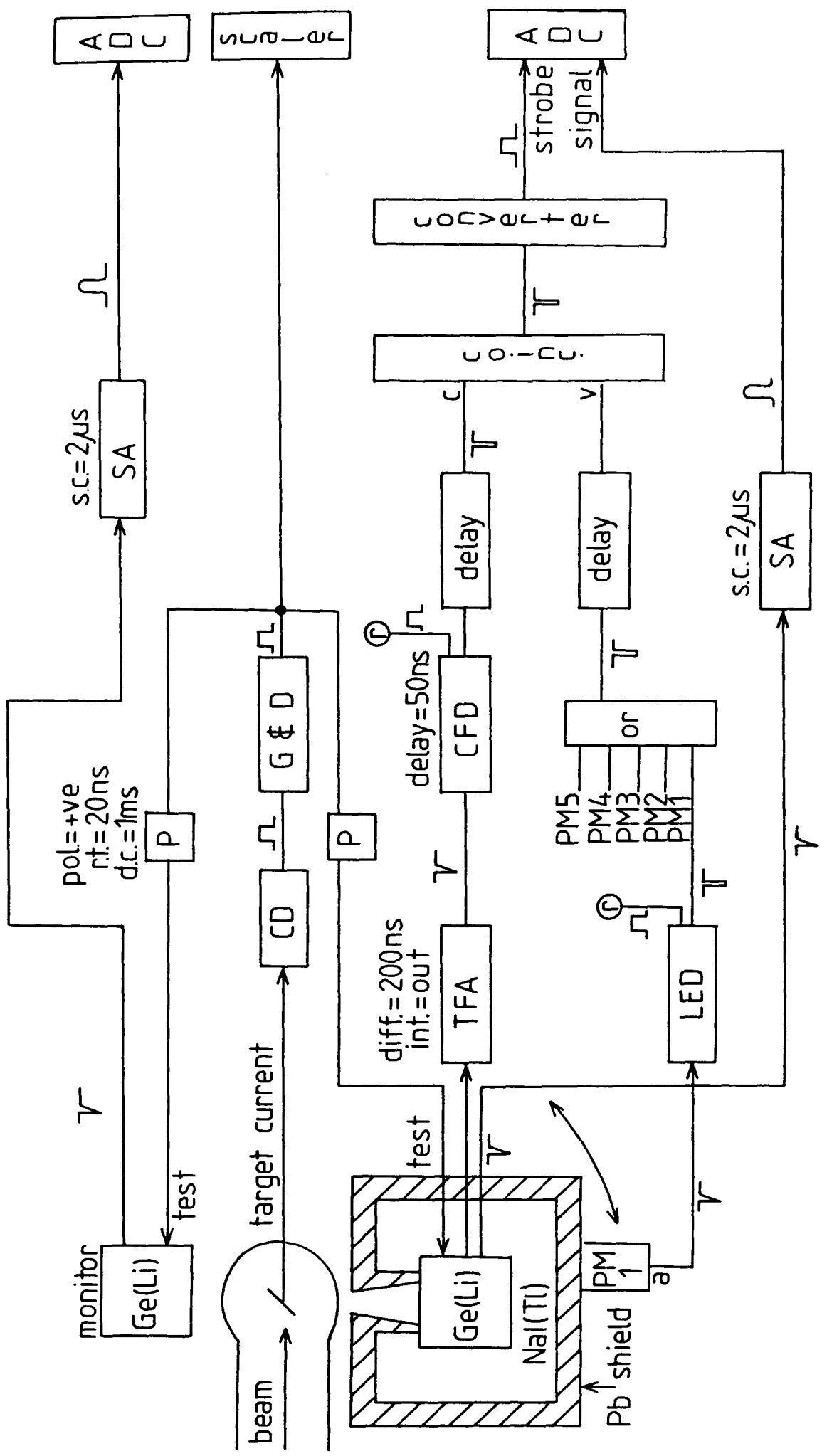


Figure 3.11 Block diagram of the experimental electronics used in the singles angular distribution measurement. Details of the electronics are shown for only one of the five photomultiplier tubes which viewed the NaI(Tl) Compton-suppression shield; the electronics were the same for the other four tubes and the signals were combined at the logical 'or' unit, as indicated. Ge(Li) signals in coincidence with a signal in the suppression shield were vetoed at the coincidence unit. The 'converter' was a custom built unit which converted fast negative logic pulses into positive logic pulses. Dead time corrections were made by applying a pulser to the 'test' inputs of both Ge(Li) detectors; the test pulses were triggered by the output of the target current digitizer, the number of trigger pulses being recorded in a scaler. Typical values of adjustable parameters are shown for the Constant Fraction Discriminator, Timing Filter Amplifier, Spectroscopic Amplifiers and the Pulsers. The abbreviations used in the diagram are explained in the following page.

Key to Figure 3.11

ADC	analogue to digital converter
coinc.	coincidence unit: c = coincidence input; v = veto
CD	current digitizer
CFD	constant fraction discriminator: delay = externally set delay
G&D	gate and delay
LED	leading edge discriminator
P	pulser: pol. = polarity of the output pulse; r.t. = pulse rise time; d.c. = pulse decay constant
PM	photomultiplier tube: a = anode output
r	rate meter
SA	spectroscopic amplifier: s.c. = shaping constant
TFA	timing filter amplifier: diff. = differentiation time constant; int. = integration time constant

were extracted from the angular distributions by comparison with tabulated angular distribution coefficients [Mat 74a, Mat 74b]. It was assumed that the alignment of the nuclear spin about the M=0 substate, relative to the beam direction, had a Gaussian distribution. The widths of the Gaussians (σ/I) were extracted from the angular distributions of known $E2$ transitions in the ^{80}Sr ground state band, and from preliminary fits to the interband transitions in which the substate distribution width was treated as a free parameter. Unfortunately, Doppler broadening of the ground state band transitions from states above $\sim 6\hbar$ made substate distributions extracted for these levels unreliable. For low lying states the widths were of the order of $\sigma/I \sim 0.4$, where I is the level spin, the widths decreasing slightly with increasing spin. Where appropriate, χ^2 analysis was used to extract the γ-ray multipole mixing ratios and investigate possible level spin assignments. Examples of such χ^2 analyses are given in Chapter 4.

3.4.3 NEUTRON DETECTION

Neutrons were detected using a large volume liquid scintillator (NE213). The neutrons interact with the scintillation material to produce knock-on protons which are then detected by the ionization of the scintillator. Unfortunately, γ-rays also interact with the scintillator by either producing photo-electrons or by Compton scattering. The neutron detector can be shielded to some extent from γ-rays by positioning a lead absorber between the target and the neutron detector. However, this shielding is only partially effective and γ-rays invariably cause scintillation in the detector. Therefore, it is necessary to differentiate those signals due to neutrons from those due to γ-rays. There are two general methods of doing this: time-of-flight and pulse shape discrimination.

Time-of-flight utilizes the fact that both neutrons and γ-rays are produced within $\sim$ 1 ns of the formation of the product nucleus (although some isomeric states which decay by γ-ray emission have lifetimes much longer than 1 ns); however, the γ-rays travel at the speed of light, while the neutrons produced in these reactions are much slower. For example, a typical evaporated neutron with energy of 4.5 MeV in the laboratory frame travels at a speed of only $0.10c \sim 3$ cm/ns. Therefore, it is possible to separate neutrons from γ-rays by time-of-flight over a distances of the order of 1 m; the detection of a γ-ray in another detector is used to signal the "start" time, corresponding to the formation of the product nucleus.

Alternatively, neutrons can be separated from γ-rays by the different pulse shapes which they produced in the liquid scintillator. The different mechanisms by which the neutrons and γ-rays interact with the scintillator result in different scintillation light curves and, hence, different pulse shapes. In particular, pulses due to neutrons have a significant delayed component, relative to those from γ-rays. This pulse shape difference can be used to separate those pulses due to neutrons from those due to γ-rays. In the present study, a combination of the three methods discussed above was used to identify the neutron events. Neutron detection and pulse shape discrimination are discussed more fully by Ooi [Ooi 86].

3.4.4 NEUTRON GATED ANGULAR DISTRIBUTION

For the neutron-gated angular distribution, γ-rays were detected in four Ge(Li) detectors positioned at $0°, 45°, 90°$ and $117°$ to the direction of the incoming beam. The γ-ray detectors were placed so that their solid angle attenuation coefficients for the second order Legendre polynomial were equal, all having a value of $Q_2 = 0.97(1)$ as the detector faces

were $\sim$ 12 cm from the target. The target was a 2 mg/cm^2 ^{54}Fe layer evaporated onto a 20 mg/cm^2 natural Au backing. Neutrons were detected in a large circular NE213 liquid scintillator [Ooi 86], positioned at 0°. This neutron detection system was developed by S.S.L. Ooi and is well documented [Ooi 86]; therefore only a brief description will be given here. The neutron detector (fig. 3.12) consisted of an outer annular detector, which was divided into four quadrants each of which was optically coupled to two photomultiplier tubes, and a small circular central detector, which was viewed by a single photomultiplier tube. This neutron detector was positioned 0.7 m from the target. Signal noise was reduced for each quadrant of the annular detector by requiring a coincidence between the pair of photomultiplier tubes viewing that quadrant. γ-rays were discriminated against by 5 cm of lead shielding, n-γ time of flight and pulse shape discrimination. Corrections for differing n-γ coincidence efficiencies were made by normalizing the neutron-gated angular distribution for the 596 keV γ-ray ($4^+ \rightarrow 2^+$ ground state band transition in ^{80}Sr) to that observed in singles. Since there were only four data points, the angular distributions were fitted to a second order Legendre polynomial.

The experimental electronics arrangement for this experiment is given in fig. 3.13. For time-of-flight, the neutrons were timed with respect to the detection of a γ-ray in the germanium detector. The shape of an individual pulse from the neutron detector was characterized by comparing the time difference between the outputs of leading edge and constant fraction timing circuits for that pulse. This time difference is not the same for neutrons and γ-rays. Thus, the circuit acted as a pulse shape discriminator. The time-of-flight and pulse shape discriminator signals, as well as the γ-ray energies from the Ge(Li)

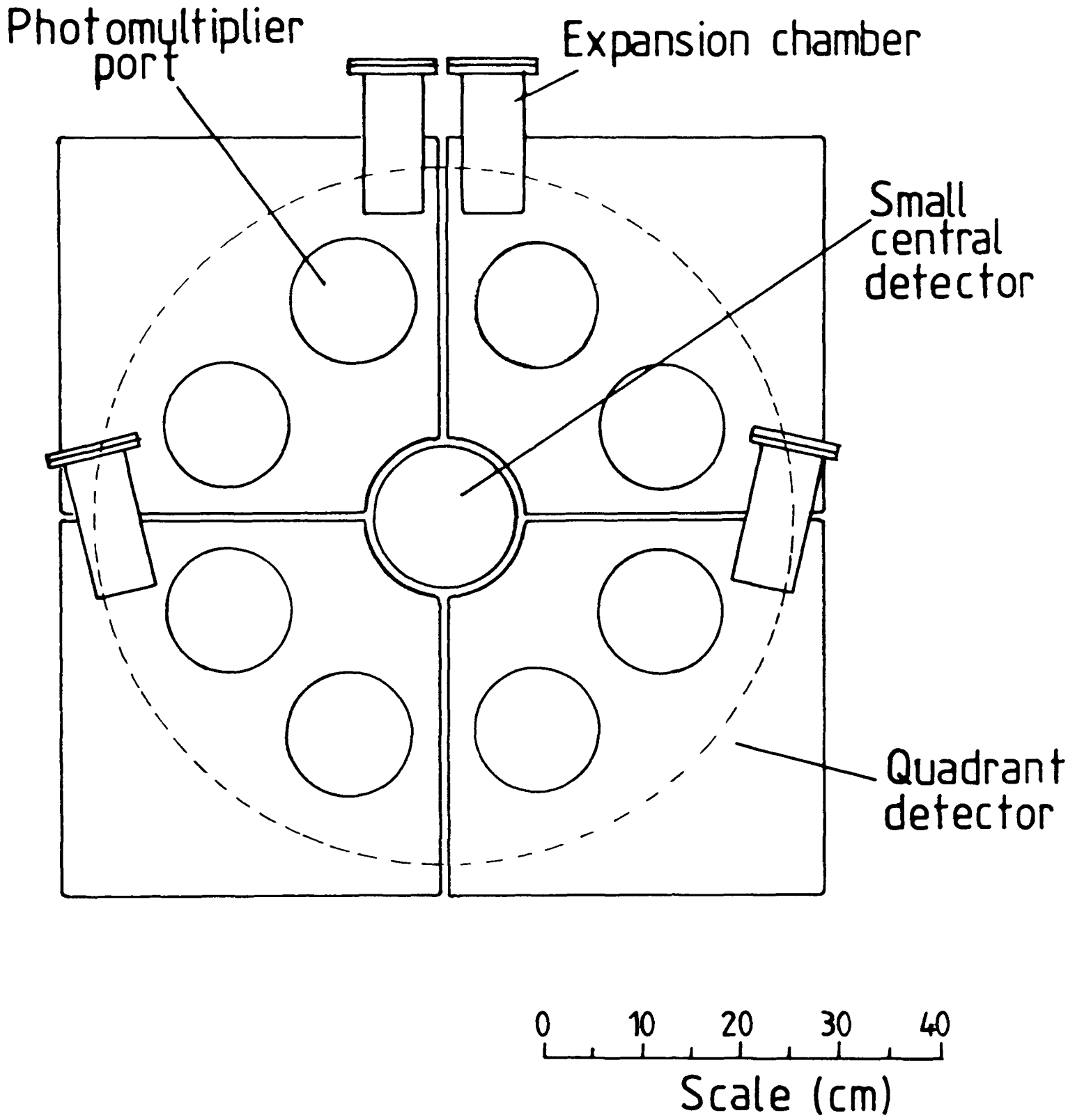


Figure 3.12 End view of the neutron detector, showing the four detectors which comprised the outer annular detector and the small central detector. The NE213 tanks were 15 cm deep. The extent of each tank in the four outer detectors is shown by the dotted line. (Reproduced from [Ooi 86].)

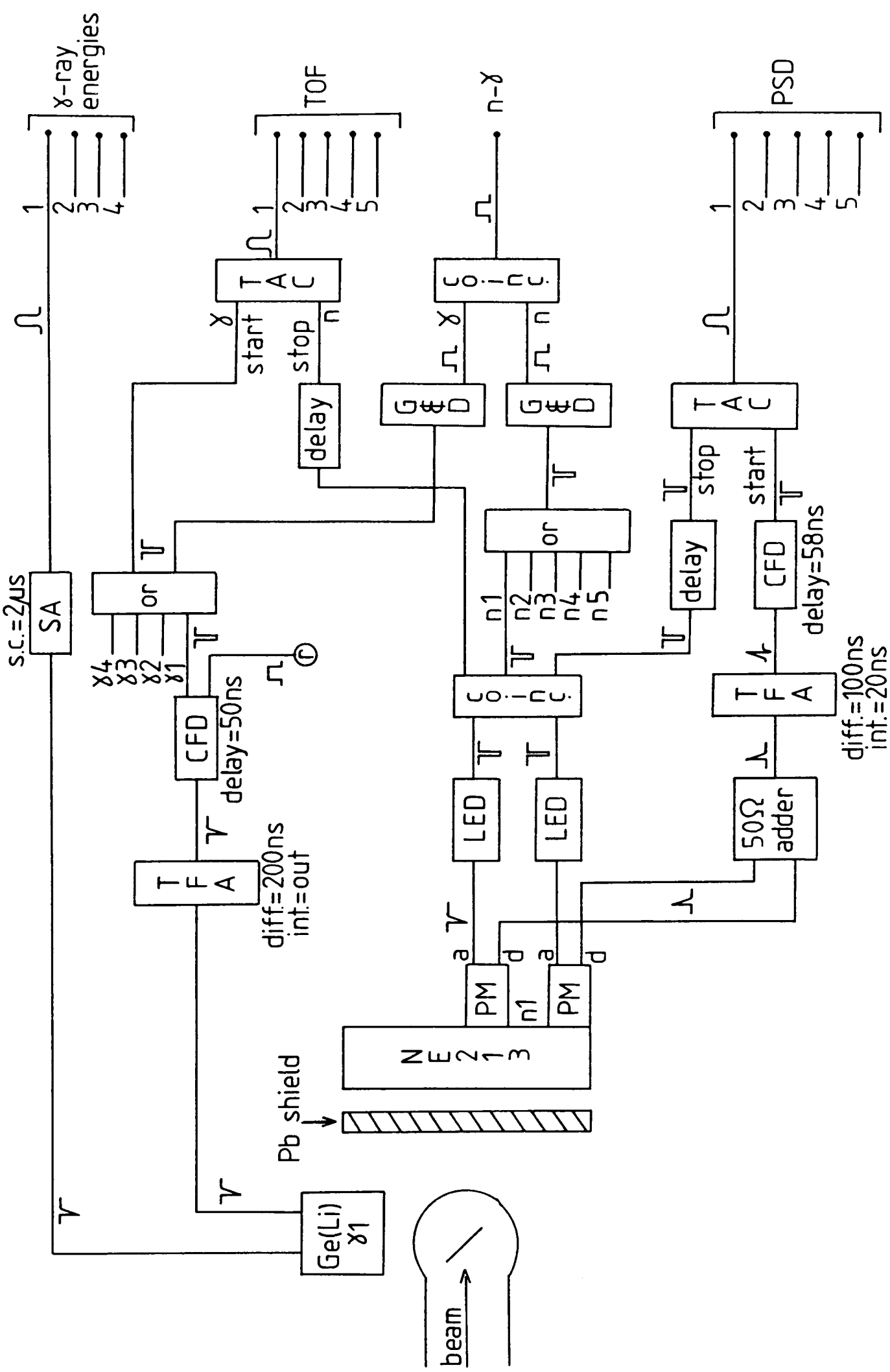


Figure 3.13 Block diagram of the experimental electronics in the neutron-gated angular distribution measurement. Details of the electronics are shown for only one of the five neutron detectors and only one of the four γ-ray detectors. In both cases, the electronics were the same for the other detectors; the signals from the detectors were combined at the two logical 'or' units and the derived signals for each detector were fed into the computer, as indicated. Typical values of adjustable parameters are shown for the Constant Fraction Discriminators, Timing Filter Amplifiers, and the Spectroscopic Amplifiers. The abbreviations used in the diagram are explained in the following page.

Key to Figure 3.13

coinc. coincidence unit

CFD constant fraction discriminator:
delay = externally set delay

G&D gate and delay

LED leading edge discriminator

PM photomultiplier tube:
a = anode output;
d = dynode output

SA spectroscopic amplifier:
s.c. = shaping constant

TAC time to amplitude converter

TFA timing filter amplifier:
diff. = differentiation time constant;
int. = integration time constant

detectors, were written event-by-event onto tape and the $n - \gamma$ discrimination was done off-line. A valid event, corresponding to an event in both the NE213 liquid scintillator and a germanium detector, was signalled by the output of the n-γ coincidence unit.

3.5 The DSAM Lifetime Measurement

3.5.1 INTRODUCTION

Measurements of the lifetimes of excited nuclear states provide valuable information about the structure of the states and the relationships between them, which can be compared to the predictions of nuclear models.

Lifetimes longer than $\sim$ 100 ps can be measured using direct electronic timing of the γ-rays emitted in the decay. For lifetimes between $\sim$ 100 ps and $\sim$ 1 ps the recoil-distance, or "plunger", method can be used (see, for example, the review article by K.W. Allen [All 75]), while for lifetimes in the range from $\sim$ 10 ps to $\sim$ 0.01 ps the Doppler shift attenuation method (DSAM) is used. For deformed nuclei in the mass 80 region, where many of the states decay by strong $E2$ transitions, the lifetimes of the first two or three excited states are typically within the range of the recoil-distance method. Measurement of the lifetimes of the higher levels in these nuclei, and particularly those close to the yrast line, usually requires application of the DSAM.

The DSAM lifetime measurement was carried out at the Daresbury Laboratory over a three day period. The target was a 4.5 mg/cm^2 layer of ^{54}Fe evaporated onto a 11.5 mg/cm^2 natural Au backing, set at 50° to the incident beam. A ^{29}Si beam energy of 110 MeV was chosen so that the lifetimes of levels investigated in the earlier γ-γ coinci-

dence measurement, performed at the same beam energy, could be studied. (Because of the thickness of the ^{54}Fe layer, the average beam energy for the reaction was only 95 MeV, compared with 105 MeV in the thin target γ-γ coincidence experiment. Therefore, the relative population of states at low excitation energy was greater than in the earlier experiment.) The resulting ^{80}Sr nuclei had an initial recoil velocity of $\sim 0.03c$, and thus had a maximum Doppler shift of $\sim$3%. γ-γ coincidence spectra were recorded, rather than ungated singles spectra, to reduce contamination of the spectra by γ-rays from other reaction channels. As with the earlier γ-γ coincidence experiment, γ-rays were detected in the TESSA II array (see sect. 3.3.2), the events being written event-by-event onto magnetic tape and analysed later.

3.5.2 ANALYSIS OF THE DSAM LIFETIME DATA

The energy centroid of a γ-ray line emitted by an ensemble of nuclei recoiling through a target backing is given by

$$E = E_0(1 + (v_0/c)F\cos\theta) \tag{3.5}$$

where: E is the Doppler shifted centroid energy; E_0 is the γ-ray energy measured in the rest frame of the recoiling nuclei; v_0 is the initial velocity of the recoiling nuclei; θ is the angle between the detector and the beam direction; c is the velocity of light; and the coefficient F represents the average attenuation of the Doppler shift due to slowing down and scattering of members of the ensemble as they recoil through the target and backing. The magnitude of the coefficient F depends upon both the interactions between the target and the recoiling nuclei, and on the lifetime of the decaying state.

To extract the attenuation coefficients the Doppler shifted centroid energy E was fitted as a linear function of $\cos\theta$, yielding E_0 and $E_0 F v_0/c$. The Doppler shifted γ-ray centroid energies were obtained from background subtracted γ-γ coincidence spectra or sums of several such spectra. In setting the γ-ray gates care was taken to include all of the Doppler shifted γ-ray, so that the velocity distribution of recoiling nuclei was not artificially altered. The level lifetimes were extracted from the attenuation coefficients with corrections for feeding times, as detailed below. Typical γ-ray lineshapes, from the present study, are shown in figs. 3.14 and 3.15, while fits of the γ-ray centroid energies are given in Chapter 4 (figs. 4.6, 4.12 and 4.18).

3.5.2.1 Energy calibration of the γ-ray detectors

As γ-ray energies from six different detectors were compared to extract the lifetimes, the energy calibrations of the detectors needed to be consistent to a high degree of accuracy. Throughout the experiment, singles spectra were periodically recorded and checked for gain shifts, and these showed the detector gains to be stable to 0.1 keV. At the end of the experiment an ^{152}Eu source spectrum was recorded for each of the detectors. These source spectra were used to determine linear energy calibrations for each detector. Corrections for the small changes in the zeros of the spectra due to the higher in-beam count rate were made by comparing the centroids of the five most intense β-decay activity lines both in and out of beam. (These activity γ-rays spanned the energy range from 589 keV to 1854 keV.) These corrections were less than 0.75 keV and the resulting calibrations were consistent to an accuracy of better than 0.1 keV below 1 MeV and 0.2 keV between 1 and 2 MeV, which is better than the accuracy to which most of the Doppler broadened centroid

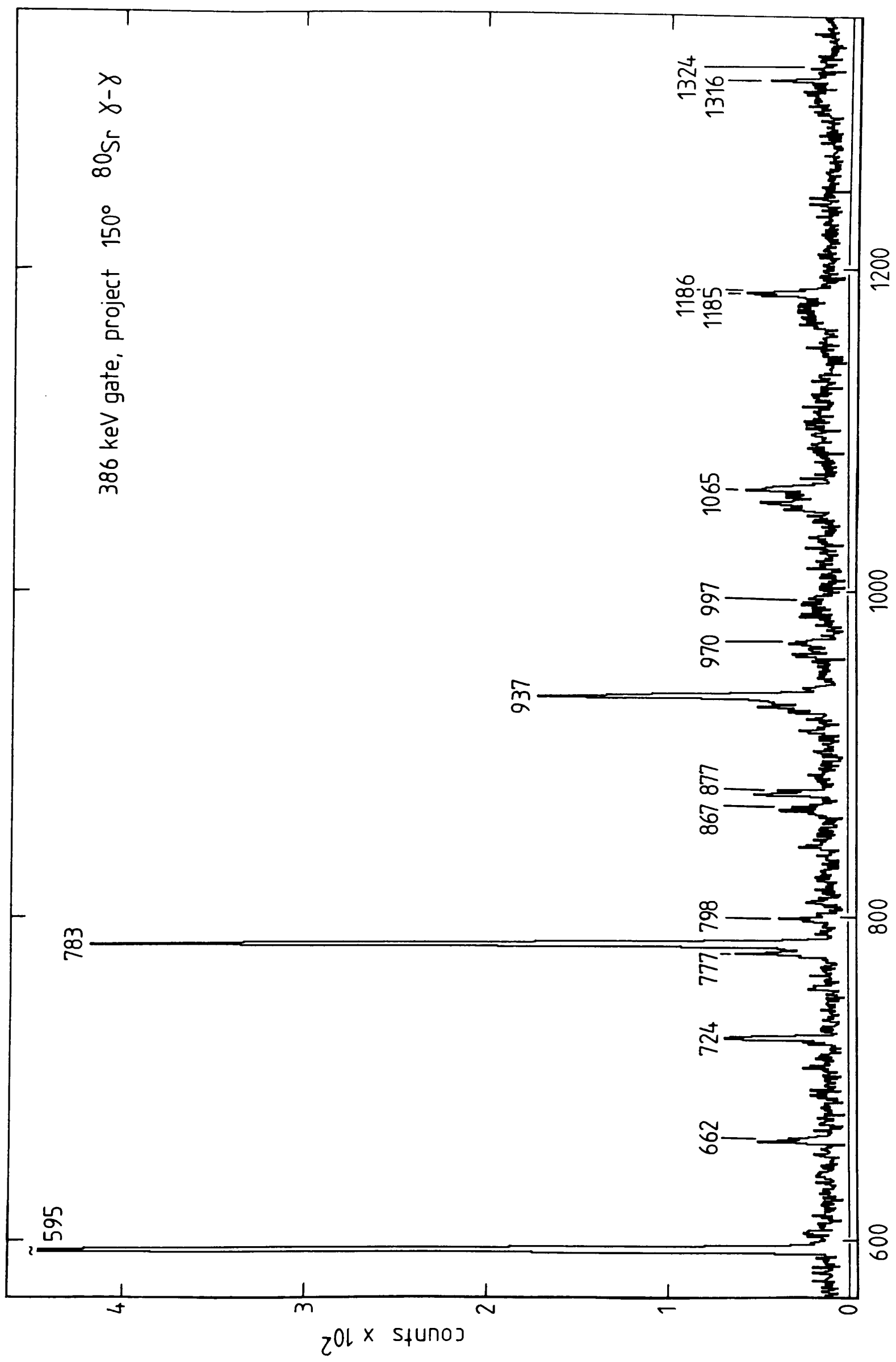


Figure 3.14 Thick target γ-γ coincidence spectrum showing the Doppler shifted γ-ray lineshapes at the backward angle of 150° for transitions in ^{80}Sr in coincidence with the 386 keV $2_1^+ \rightarrow 0_1^+$ ground state band transition.

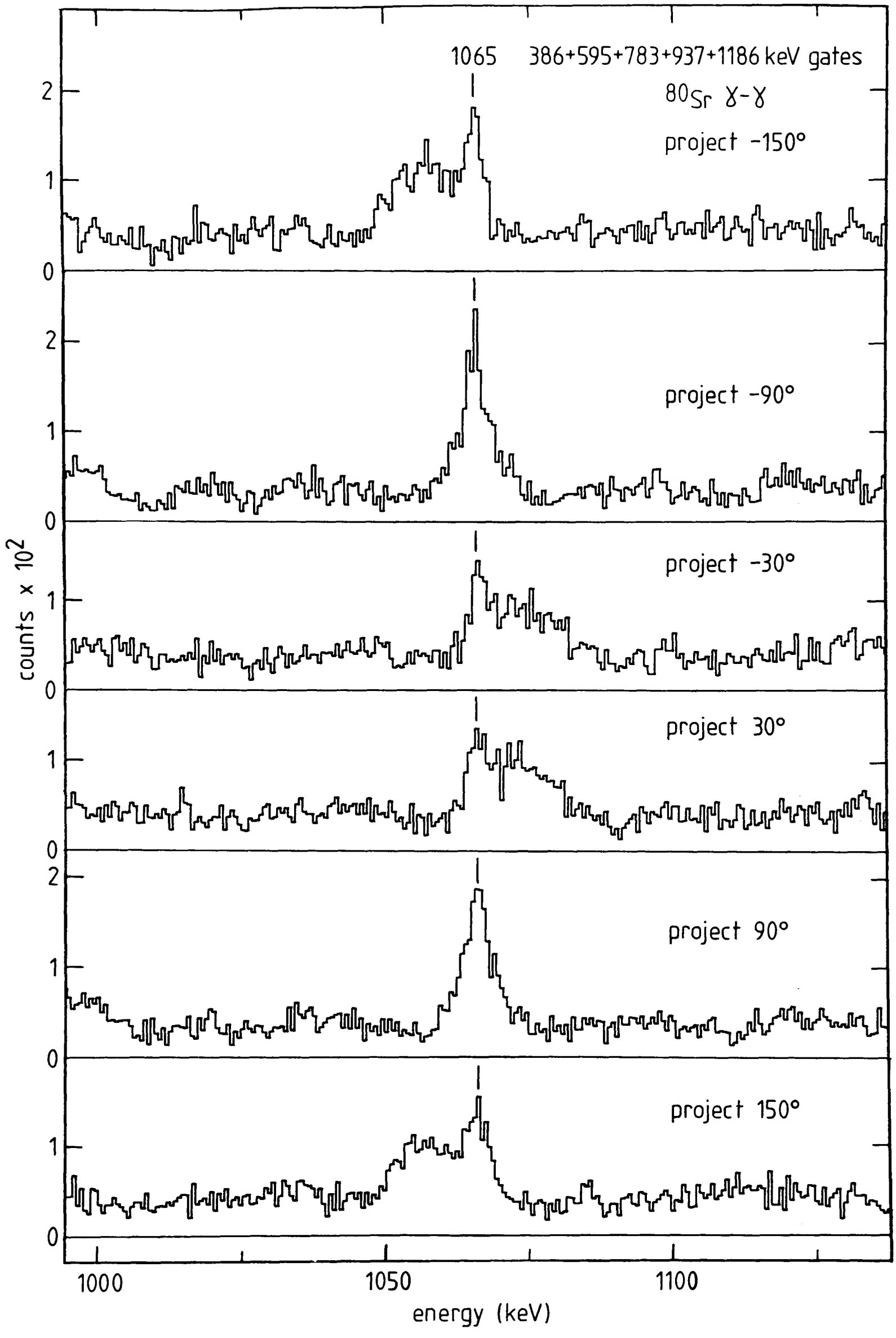


Figure 3.15 Thick target γ-γ coincidence spectra showing the Doppler shifted lineshape of the 1065 keV $10^+ \rightarrow 8^+$ ground state band γ-ray in the 6 TESSA II detectors. The detector angles are indicated (relative to the direction of the incoming beam).

energies could be determined.

3.5.3 CALIBRATION OF THE ATTENUATION COEFFICIENT F

The attenuation coefficient was calculated, as a function of the transition meanlife, using a computer program written by J. Naser (NASER) available on the TSO computer at Daresbury, which could be accessed through the network. This program uses the Lindhard stopping theory [Lin 63, Lin 64], which was scaled in the present work as discussed below to give a better description of known experimental stopping powers. The program included corrections for large angle angle scattering, caused by nuclear collisions, by using the method of Blaugrund [Bla 66].

The electronic stopping power for ^{80}Sr stopping in ^{54}Fe was estimated by scaling the Northcliffe and Schilling stopping powers [Nor 70] to the experimental stopping powers for He [Zie 74] and F, Mg, Al, S and Cl [For 76] in Fe, as suggested by Ward *et al.* [War 76]. (The stopping powers of Forster *et al.* [For 76], which are quoted in units of MeV per mg/cm^2, were increased by a factor of 56/54, since ^{54}Fe has more scattering centres per unit mass than ^{56}Fe.) The scaling formula used was [War 76]

$$(\mathrm{d}E/\mathrm{dx})^{HI} = (\mathrm{d}E/\mathrm{dx})^{HI}_{NS} \times (\mathrm{d}E/\mathrm{dx})^{OI}_{Expt}/(\mathrm{d}E/\mathrm{dx})^{OI}_{NS} \qquad (3.6)$$

where: the superscripts HI and OI denote the heavy-ion of interest and some other ion for which the stopping power is more accurately known by experiment, respectively; and the subscripts NS and $Expt$ indicate stopping powers taken from the tables of Northcliffe and Schilling [Nor 70] and experimental stopping powers [Zie 74, For 76], respectively. The average of these estimates was then taken to be the best measure of the stopping power. (Standard deviations of the estimates were typically 5%.) The Lindhard stopping powers

used in the program were then scaled to these average values, the corrections being of the order of 20%, depending upon the velocity of the incident ^{54}Fe.

The ^{54}Fe target had an effective depth of 5.9 mg/cm^2 (the target angle was 50°) which spanned some 35 MeV in beam energy and, hence, a wide range of initial ^{80}Sr recoil velocities. Therefore, in the analysis of the experimental data, the target was divided into eleven imaginary layers. The attenuation coefficient F, as a function of mean life, was calculated for nuclei produced in each layer, starting from the middle of the layer and recoiling through the remainder of the target. Although most of the nuclei stopped before reaching the Au backing, the stopping in the Au was also taken into account. The beam velocity, as a function of target depth, was calculated from the stopping power curves of Ziegler [Zie 80]. The ^{80}Sr recoil velocity for each layer was calculated from the average beam energy in that layer using simple kinematics, assuming the evaporation of particles was isotropic in the centre of mass. The F values, for each layer, were then multiplied by the initial recoil velocity v_0/c for that layer and weighted by the cross-section in that layer. Finally, the weighted values of Fv_0/c for each layer were added together, to produce a table of average Fv_0/c values for mean lives between 0.01 and 10 ps. (The cross-section used as the weighting function was measured in a separate experiment for beam energies between 85 and 105 MeV, the cross-section outside this range being predicted by the computer program CASCADE [Püh 77] normalized to the experimental measurements.) The densities used for the iron and gold stoppers were 8.483×10^{22} and 5.905×10^{22} atoms per cm^3, respectively [Zie 80].

The size of the initial recoil cone of ^{80}Sr nuclei, following particle evaporation, was

estimated, from the FWHM of the γ-ray energy peaks in the corresponding thin target experiment (sect. 3.3.3.3), to have a mean half angle of less than 5°. (This was in good agreement with limits on the recoil cone for the evaporated two protons and one neutron all emitted in the same direction. The energy spectra of the emitted protons and neutrons were estimated, for this limit, from statistical model calculations of the reaction using the computer program CASCADE [Püh 77].) Therefore, corrections due to the finite size of the initial recoil cone were unnecessary.

3.5.4 SIDE FEEDING TIMES AND CORRECTIONS FOR FEEDING

It was necessary to correct the observed Fv_0/c for the influence of the lifetimes of levels which feed the state of interest. The effective lifetimes τ_{eff} of known feeding transitions were measured and used, together with the effective Fv_0/c of the state of interest and a suitable estimate of the side feeding time τ_f, to calculate the mean life of the state of interest using the iterative method of Bell *et al.* [Bel 69]. (The effective lifetime of a level is the lifetime associated with the decay of that level following formation of the compound nucleus. τ_{eff} includes contributions from the lifetimes of any intermediate states which feed the level. Therefore, τ_{eff} can be considerably longer than the actual lifetime τ of the level. The side feeding time into a level is the effective lifetime associated with feeding of the level by unidentified transitions.)

Side feeding times for the yrast 6^+, 8^+ and 10^+ states in ^{80}Sr were measured experimentally. The method used to extract these experimental feeding times is detailed in fig. 3.16. The resulting values of τ_f are listed in column 3 of table 3.2. τ_{eff} of the respective preceding yrast transition is given in column 4 for comparison. Unfortunately, it was not

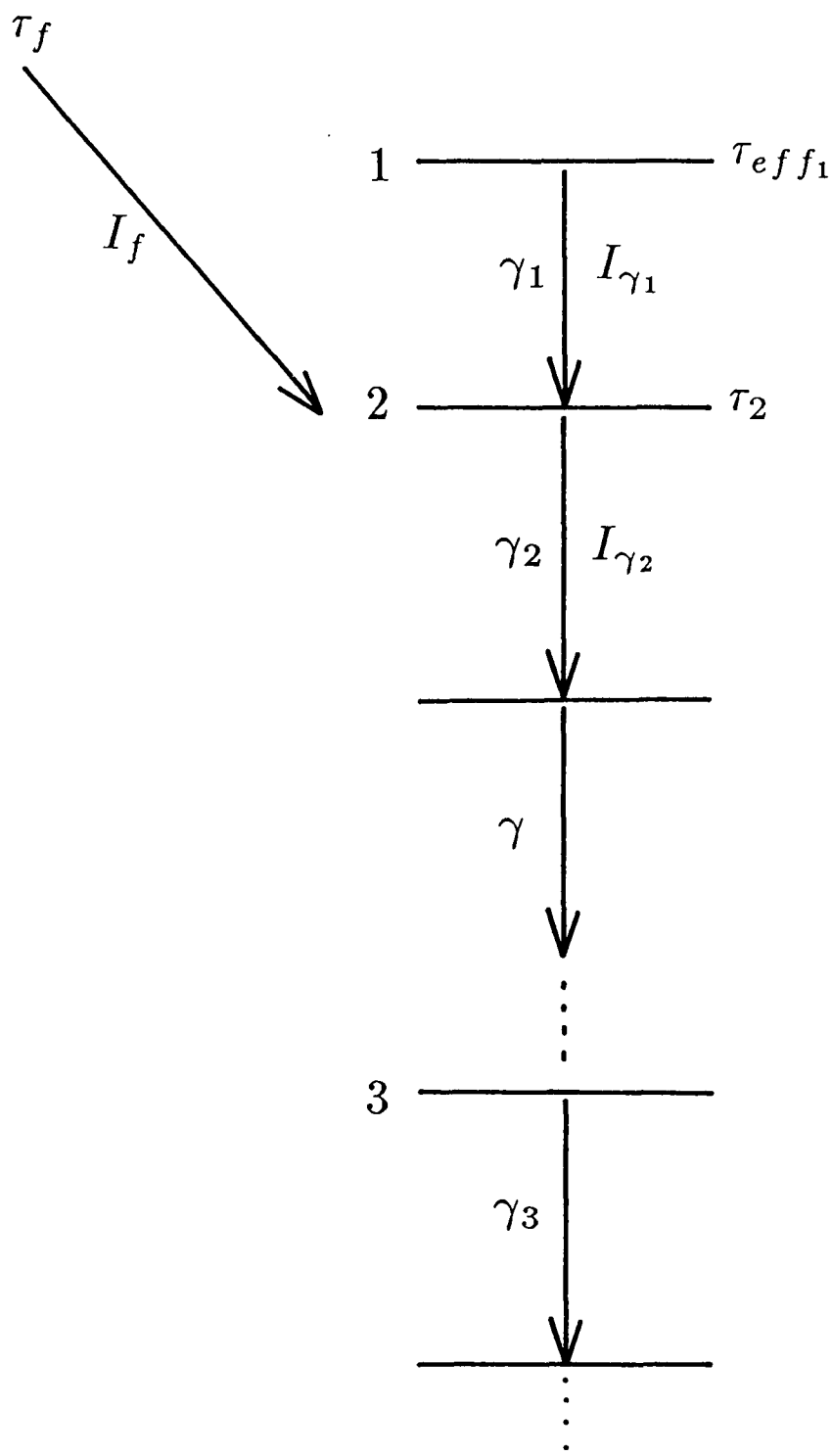


Figure 3.16 The side feeding time τ_f into level 2 can be determined from γ-γ coincidence data, as detailed below. The effective lifetime τ_{eff_1} of level 1 can be obtained from the lineshape of γ_1 gated by any subsequent γ-ray (γ_3). The lifetime of level 2 τ_2 can then be determined from the lineshape of γ_2 gated by γ_1. Since, this coincidence requirement restricts the decaying nuclei to those fed through level 1, and thus the feeding time is τ_{eff_1}. (Meanlives determined in this manner, with full feeding correction, are labelled "^{e})" in table 4.2.) The lineshape of γ_2 gated by any subsequent γ-ray (γ_3) depends upon τ_f, τ_{eff_1}, τ_2 and the relative intensities of the two feeding paths (I_{γ_1} and I_f). Hence, as τ_{eff_1} and τ_2 are known, and I_{γ_1} and $I_f = I_{\gamma_2} - I_{\gamma_1}$ can be obtained from the coincidence spectra, τ_f can be determined.

TABLE 3.2

Yrast Side Feeding Times and Cascade Feeding Times in ^{80}Sr

Spin ($\hbar$)	Excitation Energy (keV)	τ_f [a] (ps)	τ_{eff} [b] (ps)
6	1763	> 2.2 (18)	2.94 (10) (18)
8	2700	1.3 $(^{27}_{6})$	1.42 (6) (9)
10	3765	1.4 $(^{40}_{9})$	0.54 (4) (3)
12	4951	–	0.348 (17) (16)
14	6276	–	0.267 (15) (13)
16	7750	–	0.240 (21) (11)
18	9328	–	0.165 (30) (7)

[a]) Errors quoted are due to the uncertainties in the measurements, the uncertainties in the stopping powers being comparatively negligible.

[b]) Errors quoted are due to the uncertainties in the measurements, followed by the uncertainties in the stopping powers.

possible to use this method to measure the side feeding times into levels at higher excitation energy than the 3765 keV (10^+) level, or to measure the lifetimes of these higher lying levels directly. This was because the method used requires the γ-γ coincidence lineshape of a transition depopulating the level of interested gated by the preceding cascade transition. The lineshapes of the transitions feeding levels with spins $I \geq 12$ in the ground state band were very broad and their intensities low, resulting in coincidence spectra with poor peak to background ratios and poor statistical quality. Therefore, coincidence spectra gated by these high lying transitions were not of sufficient quality to enable side feeding times to be extracted. Extraction of side feeding times from the sideband data was even more difficult, since the sideband transitions were less intense and the fraction of sidefeeding was less on average than in the ground state band.

The measured τ_f for the yrast 6^+, 8^+ and 10^+ levels in ^{80}Sr were equal, within experimental error, to τ_{eff} of the preceding cascade transition (table 3.2). This similarity suggested that the continuum and yrast γ-ray transition rates were similar and that τ_{eff} of the preceding yrast transition may be a good approximation to τ_f for the yrast states. Comparison with other experimental measurements and theoretical calculations of side feeding times in this mass region [Lüh 85, Hel 78] showed that the observed side feeding times into the 6^+, 8^+ and 10^+ states were somewhat longer than would have been expected from a simple extrapolation of the (sparse) data available on other A$\sim$80 nuclei. (Although the errors in the experimental data were relatively large.) In contrast, although direct comparison with other reactions is difficult, the measured τ_{eff} of the higher states in the ^{80}Sr yrast cascade were comparable with both the τ_f calculated for $^{72}_{34}Se_{38}$ in statistical model

calculations by Hellmeister *et al.* [Hel 78] and also with the τ_f measured by Lühmann *et al.* [Lüh 85] in $^{75}_{35}Br_{40}$. In particular, Lühmann *et al.* [Lüh 85] found that for the ^{62}Ni(^{16}O, $p2n$)^{75}Br reaction at 60 MeV (for which the entry region predicted by CASCADE [Püh 77] was similar to that predicted for the ^{54}Fe(^{29}Si, $2pn$)^{80}Sr reaction at 110 MeV used in the present study, in that it was very close to the yrast line) the feeding times of the highest yrast states decreased at a rate of 56 fs per MeV of excitation energy compared with a 39 (8) fs per MeV decrease in yrast effective lifetimes for the $12^+ - 18^+$ yrast transitions in ^{80}Sr (table 3.2). In addition, the statistical model calculations of Hellmeister *et al.* [Hel 78] predicted a 0.2 ps side feeding time for the 7.04 MeV 14^+ yrast state in ^{72}Se, while the effective lifetime of the 1474 keV yrast transition into the 6.276 MeV 14^+ yrast state in ^{80}Sr was 0.27 (2) ps. Statistical model calculations made using the computer program CASCADE showed that the ^{72}Se was populated at a similar spin, although a few MeV higher in excitation energy, to the ^{80}Sr produced in the present study.

Because of these similarities between the cascade feeding times (τ_{eff}) into the yrast states in ^{80}Sr and both the measured τ_f in ^{80}Sr at low spin and the measured and calculated τ_f in other nuclei of similar mass (and similar N/Z ratios) at higher spin, the approximation was made that τ_f into a given state was equal to the cascade feeding time (τ_{eff} of the preceding transition) into that state. As discussed above, this is thought to be a good approximation to the yrast feeding times, for which the side feeding is about 30% of the total feeding. In addition, such an approximation has only a small effect on the calculated lifetimes of the sideband transitions, since there is very little side feeding into these bands. Mean lives calculated with this side feeding approximation are labelled "^{f})" in table 4.2.

No estimate of the error in this approximation is included in the quoted errors (except for the uncertainty in τ_{eff}), however in the extreme case of the side feeding times being reduced to zero the effect would typically be to double the quoted yrast lifetimes. For states for which no estimate of the feeding times was available, the effective lifetime of the state is quoted as an upper limit, being the composite of the real lifetime and the feeding times.

CHAPTER 4

EXPERIMENTAL RESULTS

4.1 Introduction

The present study has identified 33 new γ-rays in ^{80}Sr, extending the ground state band (GSB) to ~17 MeV excitation energy and to a tentative spin assignment of 26^+, and defining three previously unobserved sidebands (hereafter referred to as SB1, SB2 and SB3, as defined in fig. 4.1). These results confirm many of the low lying states assigned to ^{80}Sr in earlier in-beam work on this nucleus [Nol 74, Fie 81, Lis 82, Hig 83, Bel 83]. However, a few of the yrare levels observed in these studies were not observed, but this is not unexpected, because of the very different entry regions in the spin-excitation energy plane of the various reactions used. The extent to which the present study has extended our knowledge of the ^{80}Sr level structure is illustrated by the level scheme derived by Higo *et al.* [Hig 83] (fig. 4.2). This earlier investigation identified levels in the GSB only up to the 10^+ state at 4 MeV, some 13 MeV below the 26^+ GSB level identified in the present work. In addition, Higo *et al.* identified two interband transitions, although none of the sideband transitions were observed.

Multipolarities were assigned to the new levels reported here on the basis of the γ-ray angular distributions and γ-γ DCO ratios (see Chapter 3). In cases where evidence for multipolarity assignments was absent or inconclusive, in-band transitions were tentatively assigned $E2$ multipolarities. The order of γ-ray transitions within a cascade was determined from both the γ-ray intensities and the effective level lifetimes τ_{eff} or, equivalently,

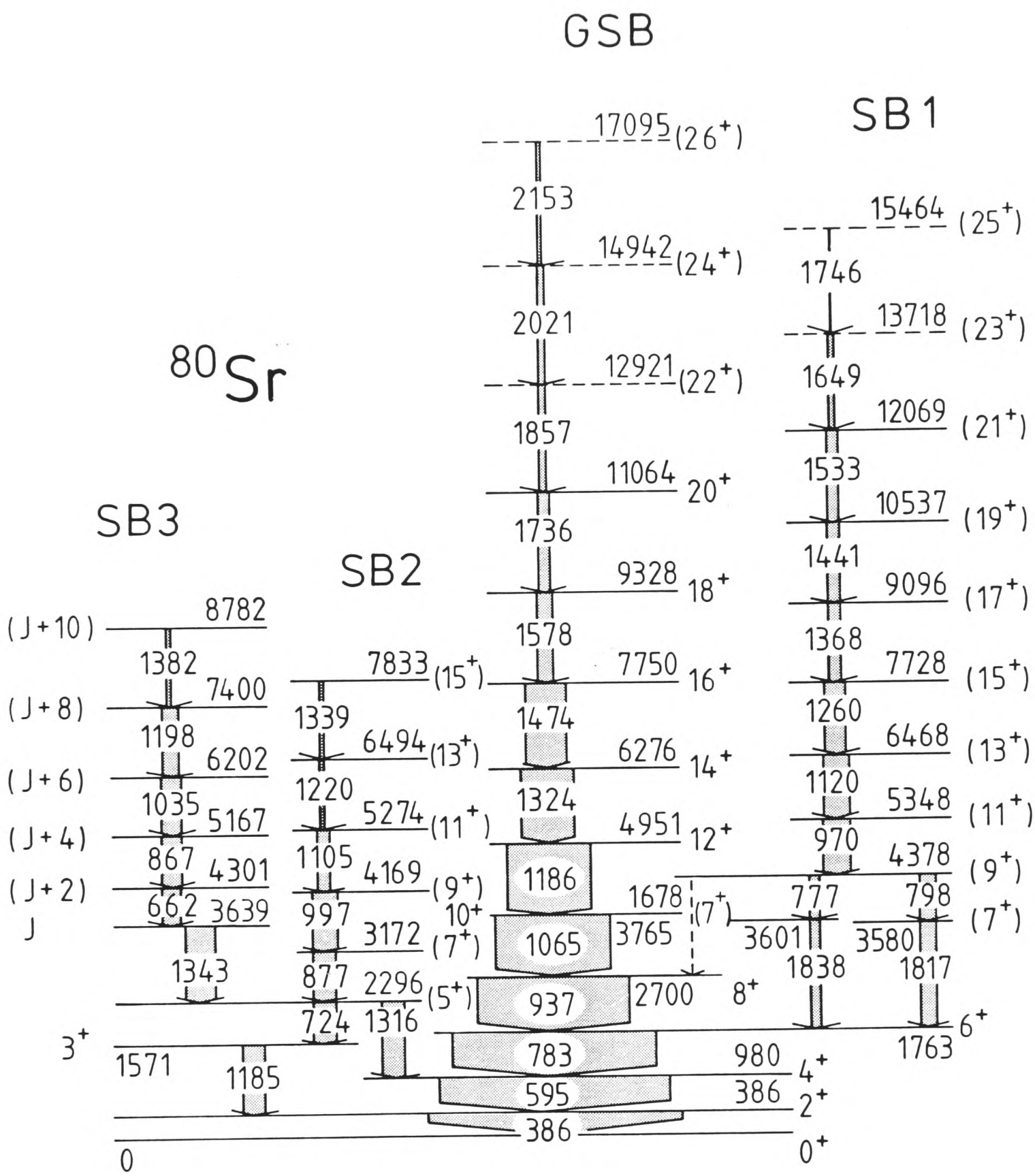


Figure 4.1 Proposed energy level scheme of ^{80}Sr. The arrow widths are approximately proportional to the in-beam γ-ray intensities, and energies are given in units of keV rounded to the nearest integer.

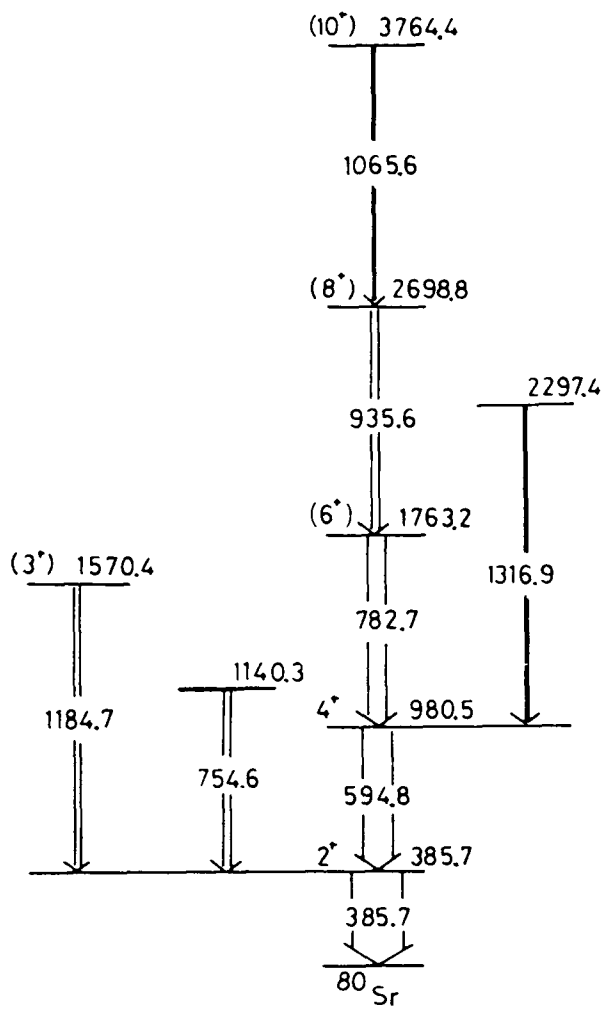


Figure 4.2 The level scheme of ^{80}Sr as proposed following the earlier work of Higo *et al.* [Hig 83]. The arrow widths are approximately proportional to the in-beam γ-ray intensities, and the energies are given in units of keV.

TABLE 4.1

Energies, Intensities, Placement, Angular Distributions, DCO Ratios and Mixing Ratios of γ-rays in ^{80}Sr

Energy (keV)	Intensity[a]	Initial State (keV)	Final State (keV)	a_2 [b]	a_4 [b]	DCO Ratio	Assignment	Mixing Ratio for $M1/E2$ Transitions
385.9(1)	1100(50)	386	0	+0.23 (2)	−0.065 (7)	0.92 (5)	GSB $2^+ \rightarrow 0^+$	
594.5(1)	1000(10)	980	386	+0.25 (2)	−0.098 (6)	1.02 (6)	GSB $4^+ \rightarrow 2^+$	
662.1(1)	75 (6)	4301	3639	+0.10 (9)	−0.055(24)	1.36(24)	SB3 (J+2) → J	
724.4(2)	102 (8)	2296	1571	+0.13 (7)		1.17(19)	SB2 $(5^+) \rightarrow 3^+$	
776.7(2)	58(10)	4378	3601			1.03(14)	SB1 $(9^+) \rightarrow (7^+)$	
782.6(1)	872(10)	1763	980	+0.21 (3)	−0.042(11)	1.01 (5)	GSB $6^+ \rightarrow 4^+$	
798.3(2)	61 (6)	4378	3580	+0.33(17)		1.19(19)	SB1 $(9^+) \rightarrow (7^+)$	
866.6(1)	89 (8)	5167	4301	+0.18(16)	−0.06 (4)	1.19(23)	SB3 (J+4) → (J+2)	
876.6(3)	86(11)	3172	2296			1.08(19)	SB2 $(7^+) \rightarrow (5^+)$	
885.4(8)	56(20)						unplaced	
936.8(2)	657(11)	2700	1763	+0.25 (5)		0.98 (6)	GSB $8^+ \rightarrow 6^+$	
970.0(2)	124 (7)	5348	4378			0.91(12)	SB1 $(11^+) \rightarrow (9^+)$	

TABLE 4.1 continued

Energy (keV)	Intensity[a])	Initial State (keV)	Final State (keV)	a_2 [b])	a_4 [b])	DCO Ratio	Assignment	Mixing Ratio for $M1/E2$ Transitions
996.7(2)	133(75)	4169	3172			1.12(19)	SB2 $(9^+) \rightarrow (7^+)$	
1034.9(2)	110(11)	6202	5167			0.99(17)	SB3 (J+6) $\rightarrow$ (J+4)	
1065.3(2)	511(11)	3765	2700	+0.16 (9)		1.03 (6)	GSB $10^+ \rightarrow 8^+$	
1104.7(3)	47(24)	5274	4169				SB2 $(11^+) \rightarrow (9^+)$	
1119.8(3)	103(10)	6468	5348			0.81(12)	SB1 $(13^+) \rightarrow (11^+)$	
1184.8(3)	80(30)	1571	386	+0.27(14)[c])	+0.06(4)[c])	0.98(10)	SB1 $3^+ \rightarrow$ GSB 2^+	+0.45(8)
1186.2(2)	370(25)	4951	3765			0.96 (6)	GSB $12^+ \rightarrow 10^+$	
1198.2(2)	83(18)	7400	6202			0.85(26)	SB3 (J+8) $\rightarrow$ (J+6)	
1220.2(3)	30(30)	6494	5274			0.92(23)	SB2 $(13^+) \rightarrow (11^+)$	
1260.4(4)	83(10)	7728	6468			0.95(18)	SB1 $(15^+) \rightarrow (13^+)$	
1315.7(3)	99(12)	2296	980	+0.26 (9)	+0.07 (3)	0.95(18)	SB2 $(5^+) \rightarrow$ GSB 4^+	+0.38(6)
1324.3(3)	235(25)	6276	4951			1.01(10)	GSB $14^+ \rightarrow 12^+$	
1339.4(9)	25(25)	7833	6494				SB2 $(15^+) \rightarrow (13^+)$	
1343.0(2)	135(12)	3639	2296			1.07(18)	SB3 J $\rightarrow$ SB2 (5^+)	
1367.7(5)	61(10)	9096	7728			1.06(20)	SB1 $(17^+) \rightarrow (15^+)$	

TABLE 4.1 continued

Energy (keV)	Intensity[a])	Initial State (keV)	Final State (keV)	a_2 [b])	a_4 [b])	DCO Ratio	Assignment	Mixing Ratio for $M1/E2$ Transitions
1381.7 (3)	14 (6)	8782	7400				SB3 (J+10) → (J+8)	
1440.8 (4)	55(12)	10537	9096			0.83(21)	SB1 $(19^+) \rightarrow (17^+)$	
1474.1 (3)	191(10)	7750	6276			0.90(13)	GSB $16^+ \rightarrow 14^+$	
1532.5 (6)	37(10)	12069	10537				SB1 $(21^+) \rightarrow (19^+)$	
1547 (1)	40(20)						unplaced	
1578.4 (4)	72 (7)	9328	7750			0.88(25)	GSB $18^+ \rightarrow 16^+$	
1648.7 (6)	26(10)	13718	12069				SB1 $(23^+) \rightarrow (21^+)$	
1678.1 (6)	27 (7)	4378	2700				SB1 $(9^+) \rightarrow$ GSB 8^+	
1736.3 (6)	54 (8)	11064	9328			0.97(50)	GSB $20^+ \rightarrow 18^+$	
1746 (2)	13 (6)	15464	13718				SB1 $(25^+) \rightarrow (23^+)$	
1816.8 (6)	68 (7)	3580	1763	−0.40(26)	+0.27(7)	0.53(20)	SB1 $(7^+) \rightarrow$ GSB 6^+	−4.7(15)
1838.1 (6)	49 (6)	3601	1763	−0.48(13)	+0.14(4)	0.75(30)	SB1 $(7^+) \rightarrow$ GSB 6^+	−2.8 (4)
1857.0(11)	35 (7)	12921	11064			0.85(25)	GSB $(22^+) \rightarrow 20^+$	
2020.8 (6)	33 (6)	14942	12921				GSB $(24^+) \rightarrow (22^+)$	
2152.5(11)	19 (6)	17095	14942				GSB $(26^+) \rightarrow (24^+)$	

TABLE 4.1 continued

[a]) Intensities were obtained from the γ-γ coincidence data.

[b]) Where only an a_2 coeffecient is given the angular distribution was gated by neutrons, otherwise the angular distribution was performed in singles mode (see sect. 3.4 for details). For those γ-rays for which both measurements were available, the a_2 angular distribution coefficients measured in the neutron gated angular distribution were equal, within the experimental error, to those measured in the singles mode angular distribution.

[c]) At angles away from 90°, the 1186 keV γ-ray is Doppler shifted away from the 1185 keV γ-ray, allowing the angular distribution of the 1185 keV γ-ray to be determined.

TABLE 4.2

Mean Lifetimes and Rates of γ-Ray Transitions in ^{80}Sr

Level Energy (keV)	γ-Ray Energy (keV)	$100Fv_0/c$	Mean Life[a] (ps)			$E2$ Transition Rate[b] (wu)	
386	386		63	(9)	[c]	74	(11)
			53	(4)	[d]	88	(7)
960	595		<12		[c]	>45	
			4.8	(7)	[d]	112	(16)
1763	783	0.043 (9)	1.8	(9)	$\binom{30}{18}$[e]	>30	
			1.7	(4)	(5)[f]	80	$\binom{40}{20}$
2296	724	0.026(29)			[h]	–	
	1316	−0.008(13)					
2700	937	0.327(10)	0.32	(11)	(2)[e]	180	$\binom{80}{50}$
			0.31	(3)	(2)[f]	179	(21)
3172	877	0.060(27)	1.1	(9)	(1)[f]	70	$\binom{140}{40}$
3580	1817	−0.028(19)	>30	(27)	(2)[f]	–	
3601	1838	−0.017(19)	>30	(27)	(2)[f]	–	
3765	1065	0.622(21)	0.25	(9)	(2)[e]	120	$\binom{70}{30}$
			0.35	(4)	(2)[f]	84	(10)
4169	997	0.28 (9)	<3.5	(11)	(2)[g]	>8	
4301	662	0.03 (4)	0.7	$\binom{21}{7}$	(1)[f]	>110	
4378	798	0.07 (4)	1.3	$\binom{17}{5}$	(7)[f]	50	$\binom{100}{30}$
	777					50	$\binom{110}{30}$
4951	1186	1.25 (5)	0.114	(24)	(5)[f]	150	$\binom{40}{26}$
5167	867	0.09 (5)	1.7	$\binom{21}{6}$	(5)[f]	50	$\binom{40}{26}$

TABLE 4.2 continued

Level Energy (keV)	γ-Ray Energy (keV)	$100Fv_0/c$	Mean Life[a] (ps)	$E2$ Transition Rate[b] (wu)
5348	970	0.39 (4)	0.51 (8) (4)[f]	92 (17)
6202	1035	0.63 (7)	<1.40 (13) (9)[g]	>21
6276	1324	1.60 (4)	0.054 (15) (2)[f]	180 $\binom{70}{40}$
6468	1120	0.99 (5)	0.230 $\binom{40}{80}$ (3)[f]	99 $\binom{50}{14}$
7728	1260	1.62 (10)	<0.34 (4) (2)[g]	>32
7750	1474	1.80 (4)	0.019 (19) (1)[f]	>150
9096	1368	1.50 (11)	<0.39 (5) (2)[g]	>18
9328	1578	1.88 (7)	0.058 (30) (3)[f]	71 $\binom{80}{24}$
10537	1441	1.61 (10)	<0.34 (4) (2)[g]	>16
11064	1736	2.13 (11)	<0.17 (3) (1)[g]	>12

[a]) Errors on lifetimes derived in the present work are quoted as the uncertainty in the measurements, followed by the uncertainty in the stopping power.

[b]) Weisskopf $E2$ transition rates are given, except for transitions assigned as $M1/E2$. Errors represent the full error (combined statistical and stopping power errors).

[c]) E. Nolte *et al.* [25]), recoil distance method.

[d]) C.J. Lister *et al.* [1]), recoil distance method.

[e]) Present work, meanlife calculated with full feeding correction (see sect. 3.5.4 and fig. 3.16 for details).

[f]) Present work, the side feeding time is approximated by the effective lifetime of the preceding cascade transition (see section 3.5.4 for details).

TABLE 4.2 continued

[g]) Upper limits, corresponding to T_{eff}, are quoted for level lifetimes where it was not possible to correct for feeding through the preceding cascade transition.

[h]) It was not possible to assign either a lifetime or a lifetime limit to the 2296 keV level. This was due to the combination of the very small centroid shifts for the 724 and 1316 keV transitions (equal to zero within error) and the unknown feeding time through the 1343 keV transition.

TABLE 4.3

γ-γ Coincidences for the Ground State Band

coinc.→ gate↓	386	595	783	937	1065	1186	1324	1474	1578	1736	1857	2021	2153
386		x	x	x	x	x	x	x	x	x	x	x	x
595	x		x	x	x	x	x	x	x	x	x	x	x
783	x	x		x	x	x	x	x	x	x	x	x	x
937	x	x	x		x	x	x	x	x	x	(x)	x	·
1065	x	x	x	x		x	x	x	x	x	x	x	·
1186	x	x	x	x	x		x	x	x	x	x	(x)	(x)
1324	x	x	x	x	x	x		x	x	x	x	(x)	(x)
1474	x	x	x	x	x	x	x		x	x	(x)	·	·
1578	x	x	x	x	x	x	x	x		x	(x)	·	·
1736	x	x	x	x	x	x	x	x	x		x	(x)	·
1857	x	x	x	x	x	x	x	(x)	(x)	(x)		·	·
2021	x	x	x	x	x	x	x	·	·	·	·		·

Observed coincidences are marked with a cross, uncertain coincidences are bracketed, and coincidences which are implied by the level scheme but not observed are indicated by a dot, see text for details. (γ-ray energies are given in units of keV.)

TABLE 4.4

γ-γ Coincidences for Sideband 1

coinc.→ gate↓	386	595	783	1817	1838	777	798	970	1120	1260	1368	1441	1533	1649	1746	937	1678
386		x	x	x	x	x	x	x	x	x	x	x	x	x	x	x	x
595	x		x	x	x	x	x	x	x	x	x	x	x	x	x	x	x
783	x	x		x	x	x	x	x	x	x	x	x	x	x	x	x	(x)
1817	x	x	x				x	x	x	x	x	(x)	(x)	·	·		
1838	x	x	x			x		x	x	x	(x)	x	(x)	·	·		
777	x	x	x		x			x	x	x	x	x	(x)	(x)	·		
798	x	x	x	x				x	x	x	x	x	x	(x)	·		
970	x	x	x	x	x	x	x		x	x	x	x	x	·	(x)	x	(x)
1120	x	x	x	x	x	x	x	x		x	x	x	x	·	·	(x)	·
1260	x	x	x	x	(x)	x	x	x	x		x	x	(x)	(x)	·	·	(x)
1368	x	x	x	x	(x)	x	x	x	x	x		x	(x)	(x)	(x)	·	(x)
1441	x	x	x	·	·	x	x	x	x	x	x		(x)	·	·	·	·
1533	x	x	x	·	·	x	x	x	x	x	x	x		(x)	·	(x)	·
1649	x	x	x	·	·	x	x	(x)	(x)	(x)	(x)	(x)	(x)		·	·	·
937	x	x	x					x	(x)	(x)	(x)	(x)	·	·	·		(x)
1678	x	x	x					(x)	·	·	·	·	·	·	·	x	

Observed coincidences are marked with a cross, uncertain coincidences are bracketed, and coincidences which are implied by the level scheme but not observed are indicated by a dot, see text for details. (γ-ray energies are given in units of keV.)

TABLE 4.5

γ-γ Coincidences for Sideband 2

coinc.→ gate↓	386	595	1185†	724*	1316	877	997	1105	1220	1339‡
386		x	x	x	x	x	x	x	x	(x)
595	x		( )		x	x	x	x	x	(x)
1185†	(x)	( )		x		x	x	(x)	(x)	(x)
724*	x		x			x	(x)	x	(x)	(x)
1316	x	x				x	x	x	·	(x)
877	x	x	x	x	x		x	x	x	x
997	x	x	x	(x)	x	x		x	x	x
1105	x	x	(x)	·	(x)	x	x		x	x
1220	x	x	x	(x)	(x)	x	x	x		(x)
1339‡	(x)	(x)	(x)	(x)	(x)	x	x	x	x	

Observed coincidences are marked with a cross, uncertain coincidences are bracketed, and coincidences which are implied by the level scheme but not observed are indicated by a dot, see text for details. (γ-ray energies are given in units of keV.)

† Unresolved from the more intense 1186 keV GSB γ-ray, see text for details.

* Several of the gates were contaminated by ^{77}Kr, which has an intense 724 keV γ-ray, see text for details.

‡ Unresolved from the more intense 1343 keV γ-ray in SB3, see text for details.

TABLE 4.6

γ-γ Coincidences for Sideband 3

coinc.→ gate↓	386	595	1185†	724*	1316	1343	662	867	1035	1198	1382
386		x	(x)	x	x	x	x	x	x	x	(x)
595	x		( )		x	x	x	x	x	x	(x)
1185†	(x)	( )		x		x	(x)	x	(x)	(x)	·
724*	x		x			x	(x)	x	(x)	·	·
1316	x	x				x	x	x	(x)	·	·
1343	x	x	(x)	x	x		x	x	x	x	(x)
662	x	x	x	(x)	(x)	x		x	x	x	(x)
867	x	x	x	x	(x)	x	x		x	x	x
1035	x	x	x	x	x	x	x	x		x	x
1198	x	x	x	x	(x)	x	x	x	x		x
1382	x	x	·	x	·	x	x	x	x	(x)	

Observed coincidences are marked with a cross, uncertain coincidences are bracketed, and coincidences which are implied by the level scheme but not observed are indicated by a dot, see text for details. (γ-ray energies are given in units of keV.)

† Unresolved from the more intense 1186 keV GSB γ-ray, see text for details.

* Several of the gates were contaminated by ^{77}Kr, which has an intense 724 keV γ-ray, see text for details.

the magnitude of the centroid Doppler shifts of the γ-ray transitions.

The experimental results are summarized in the level scheme (fig. 4.1; a copy of the level scheme is also given inside the back cover for easy reference). The γ-ray energies, intensities, placement, angular distributions, DCO ratios and mixing ratios are listed in table 4.1. The results of the DSAM lifetime measurements are given in table 4.2, together with the results of earlier lifetime measurements for states in ^{80}Sr, and the γ-γ coincidence measurements are summarized in tables 4.3, 4.4, 4.5 and 4.6. The ^{80}Sr γ-rays are illustrated by the 386 keV γ-ray coincidence spectrum (fig. 4.3), while the higher energy γ-rays are more clearly illustrated by the summed coincidence spectrum for the 386, 595, 783 and 937 keV γ-rays (fig. 4.4). Where appropriate, details of the results for the various bands and interband transitions and the associated multipolarity assignments are discussed below.

4.2 The Ground State Band

The cascade nature of the GSB transitions, up to the 20^+ state at 11 MeV, is well established by the coincidence relationships (table 4.3) and the order of the transitions within that cascade is defined by both the intensities and the centroid Doppler shifts of the transition γ-rays (tables 4.1 and 4.2). The placement of the 1857, 2021 and 2153 keV transitions is less certain. This is because, the 1857 and 2021 keV transitions show mutual coincidences with individual GSB transitions only up to the 1324 keV $14^+ \rightarrow 12^+$ transition, while the coincidence data on the 2153 keV transition are even more sparse (table 4.3). However, the absence of coincidences with the higher members of the GSB is expected, because of the weak population of states at the top of the GSB and the poor

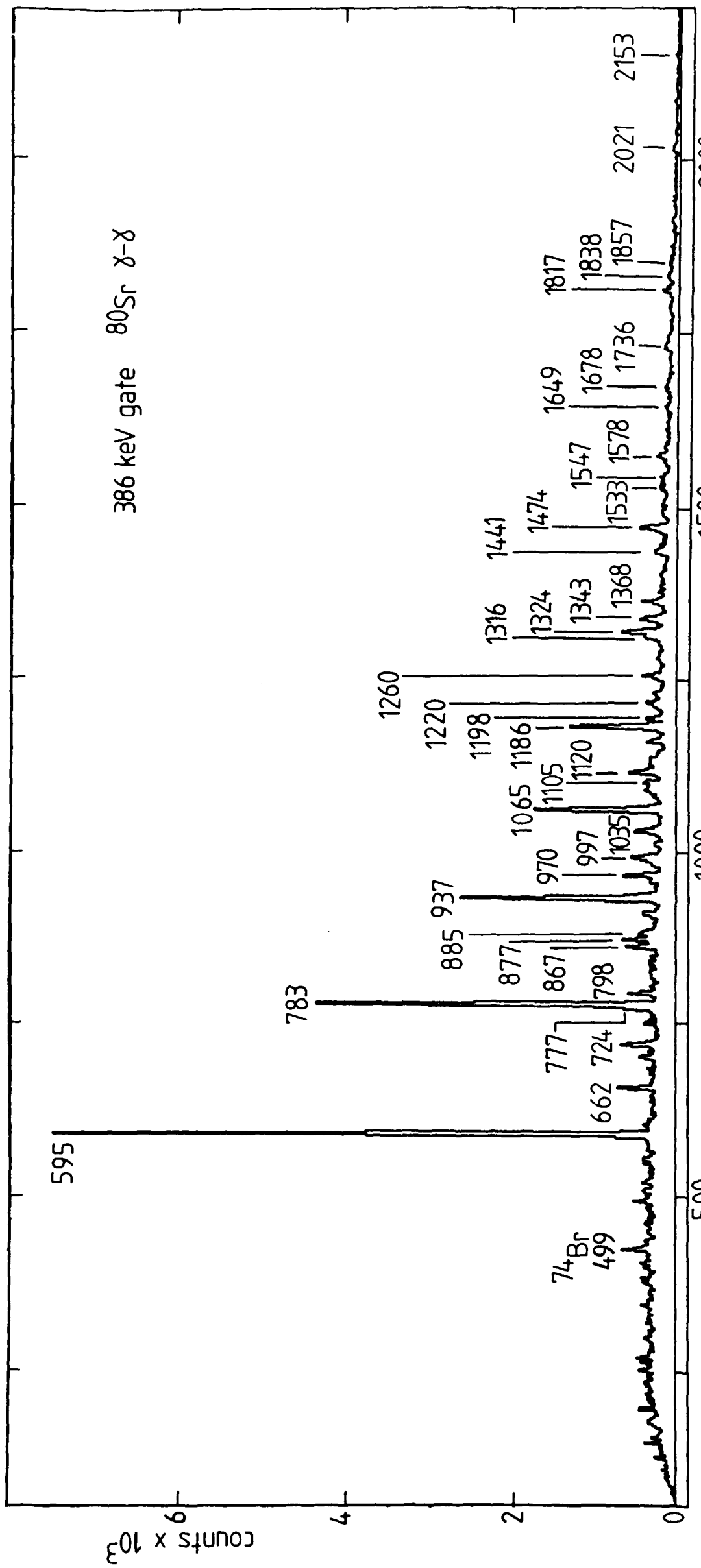


Figure 4.3 Thin target γ-γ coincidence spectrum gated by the 386 keV ^{80}Sr $2^+ \rightarrow 0^+$ ground state band transition, illustrating the ^{80}Sr γ-ray transitions.

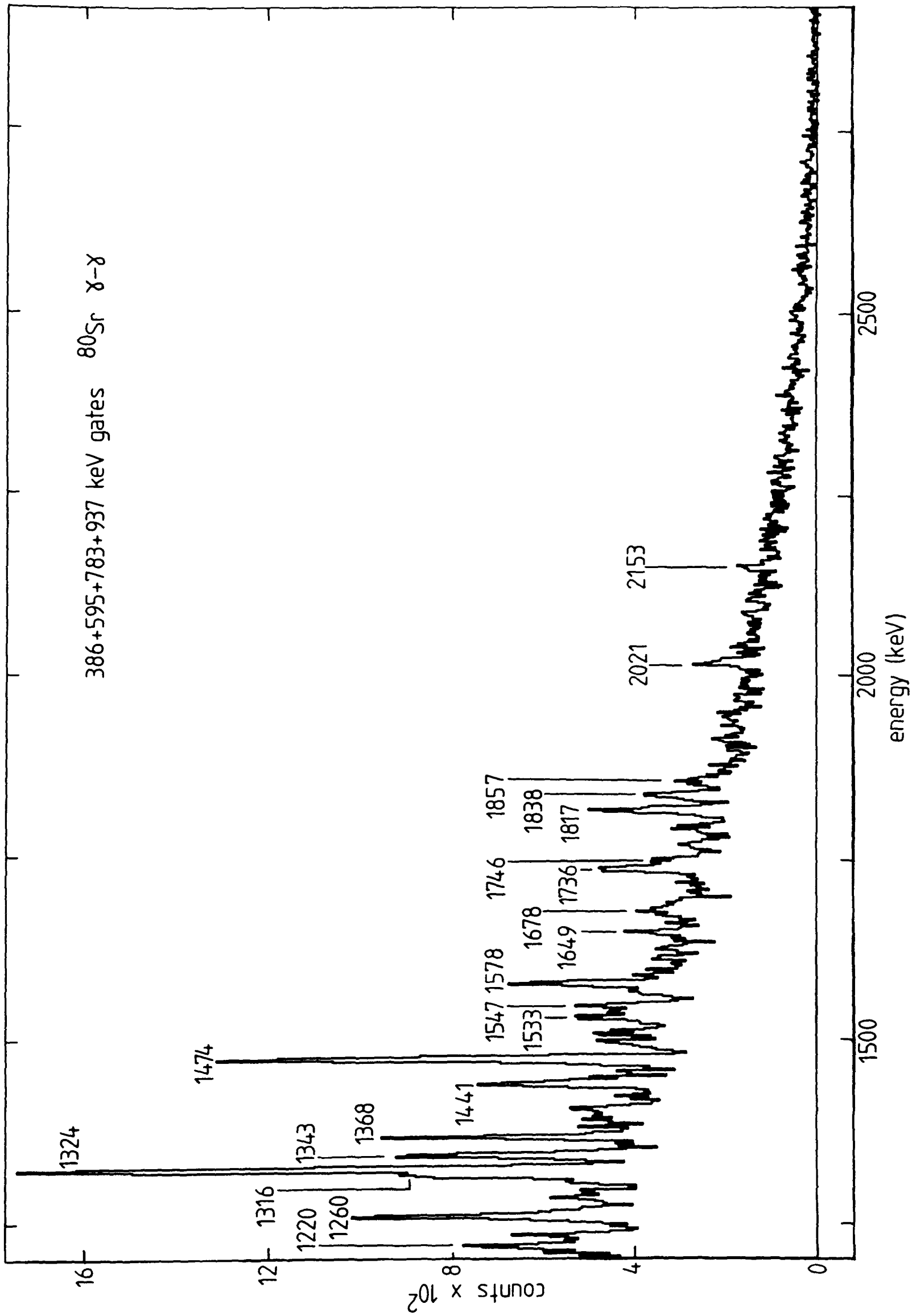


Figure 4.4 Thin target summed γ-γ coincidence spectrum for the ^{80}Sr 386, 595, 783 and 937 keV ground state band transitions, illustrating the higher energy γ-ray transitions in ^{80}Sr.

detection efficiency for high energy γ-rays (see below). Furthermore, the Doppler shifted lineshapes of the GSB transitions do not show a slow component that could be associated with an interband transition feeding into the GSB at the 14^+ level or above (see sect. 4.3). Moreover, feeding of the 1857, 2021 or 2153 keV transitions into the 18^+ GSB level would be incompatible with the observed γ-ray intensities. Therefore, the 1857, 2021 and 2153 keV transitions are tentatively placed in cascade within the GSB and are ordered by their γ-ray intensities. These three high energy γ-rays are clearly seen in the summed γ-γ coincidence spectrum of the 386, 595, 783 and 937 keV GSB transitions (fig. 4.4).

The γ-γ coincidence data for the GSB are illustrated by the coincidence spectra of the 937 and 2021 keV γ-rays (fig 4.5). These spectra show how the (statistical) quality of the coincidence data deteriorates with increasing excitation energy, due to both the decreasing population of the higher energy levels and the relatively low efficiency for detecting the high energy γ-rays which are characteristic of the decay of these highly excited states. The higher energy transitions in the GSB, as well as those in the sidebands, are more clearly illustrated by the summed coincidence spectrum for the 386, 595, 783 and 937 keV γ-rays (fig. 4.4).

In determining the level lifetimes using the DSAM, the data on the GSB benefitted from the summing of the coincidence spectra for several of the GSB transitions (typically the coincidence spectra gated on the 386, 595, 783, 937, 1065 and 1186 keV γ-rays were summed for each detector). As a consequence, the Doppler shift of even the very weak 1736 keV γ-ray could be measured, although poor statistics, relatively large backgrounds and very broad lineshapes prevented measurement of the Doppler shifts of the 1857, 2021

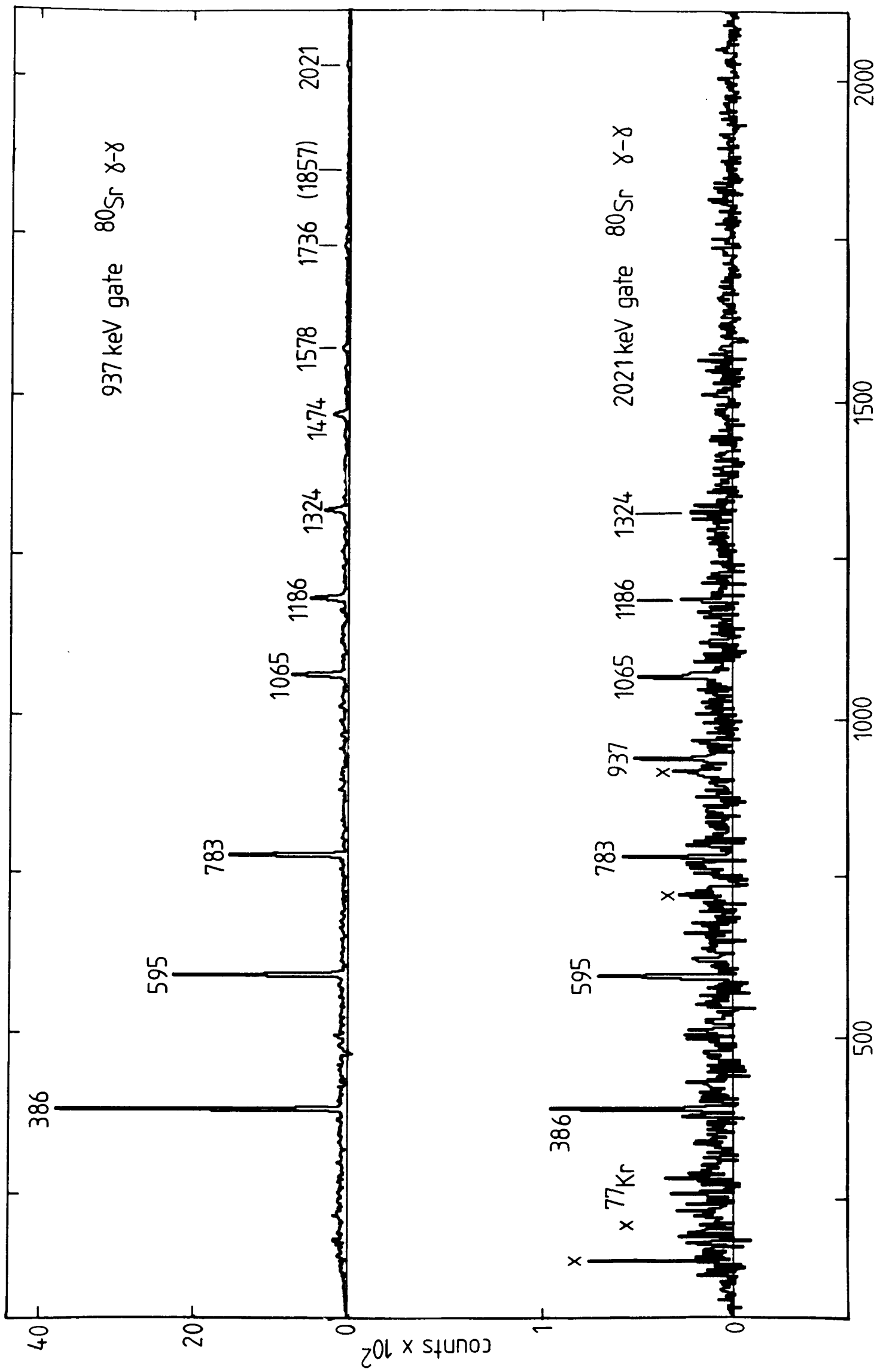


Figure 4.5 Thin target γ-γ coincidence spectra for the 937 keV $8^+ \rightarrow 6^+$ and 2021 keV $(24^+) \rightarrow (22^+)$ ground state band transitions, illustrating the present data on the ^{80}Sr ground state band. (See sect. 4.2 for details.)

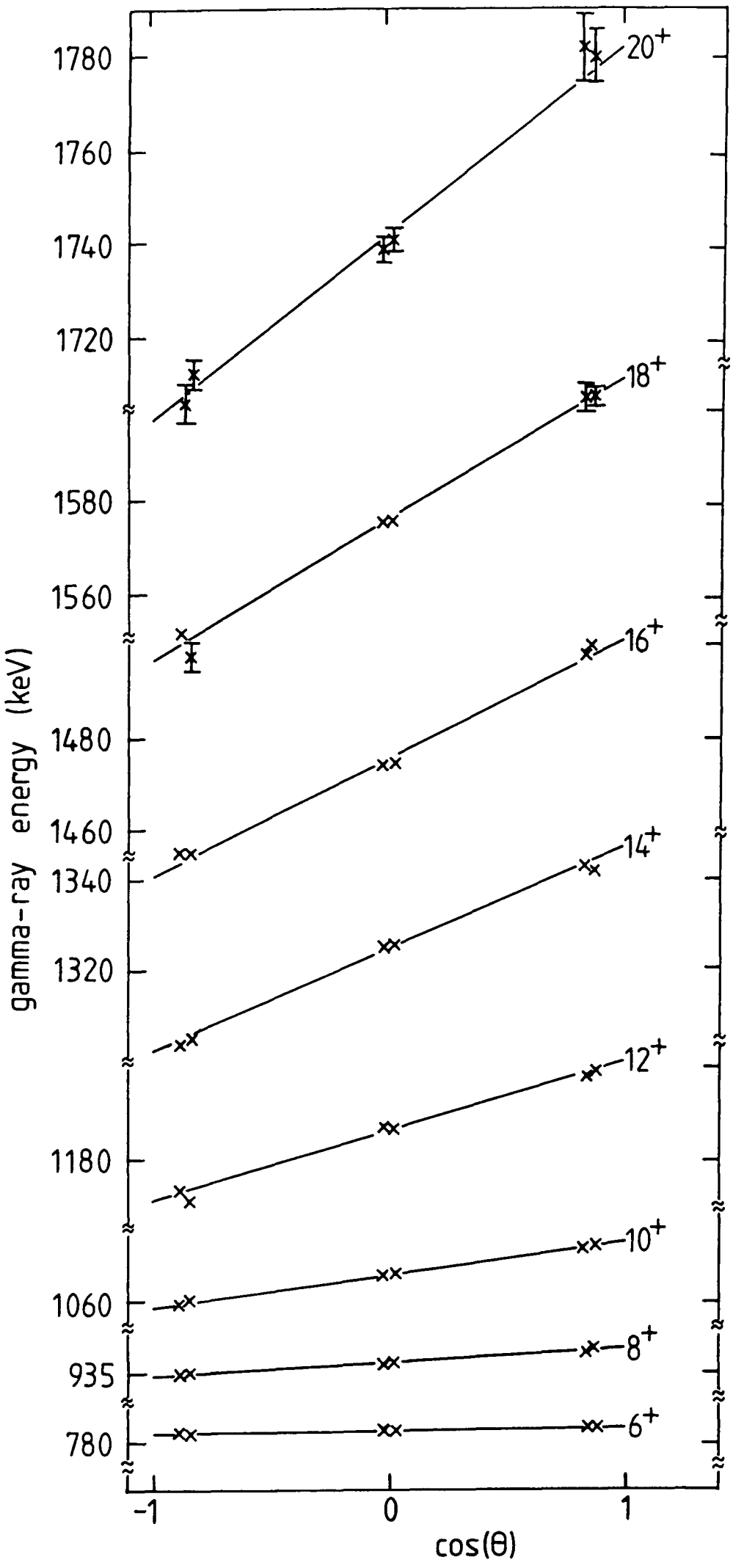


Figure 4.6 Doppler shifted γ-ray centroid energies as a function of $\cos\theta$ for the ^{80}Sr ground state band transitions (where θ is the detector angle, relative to the direction of the incoming beam). As there are two measurements for each value of $\cos\theta$, the pairs of points have been drawn slightly separated for clarity. Error bars are shown only when they are larger than the "$\times$" marking the point. The lines drawn through the the points represent linear fits to the data, as discussed in the text.

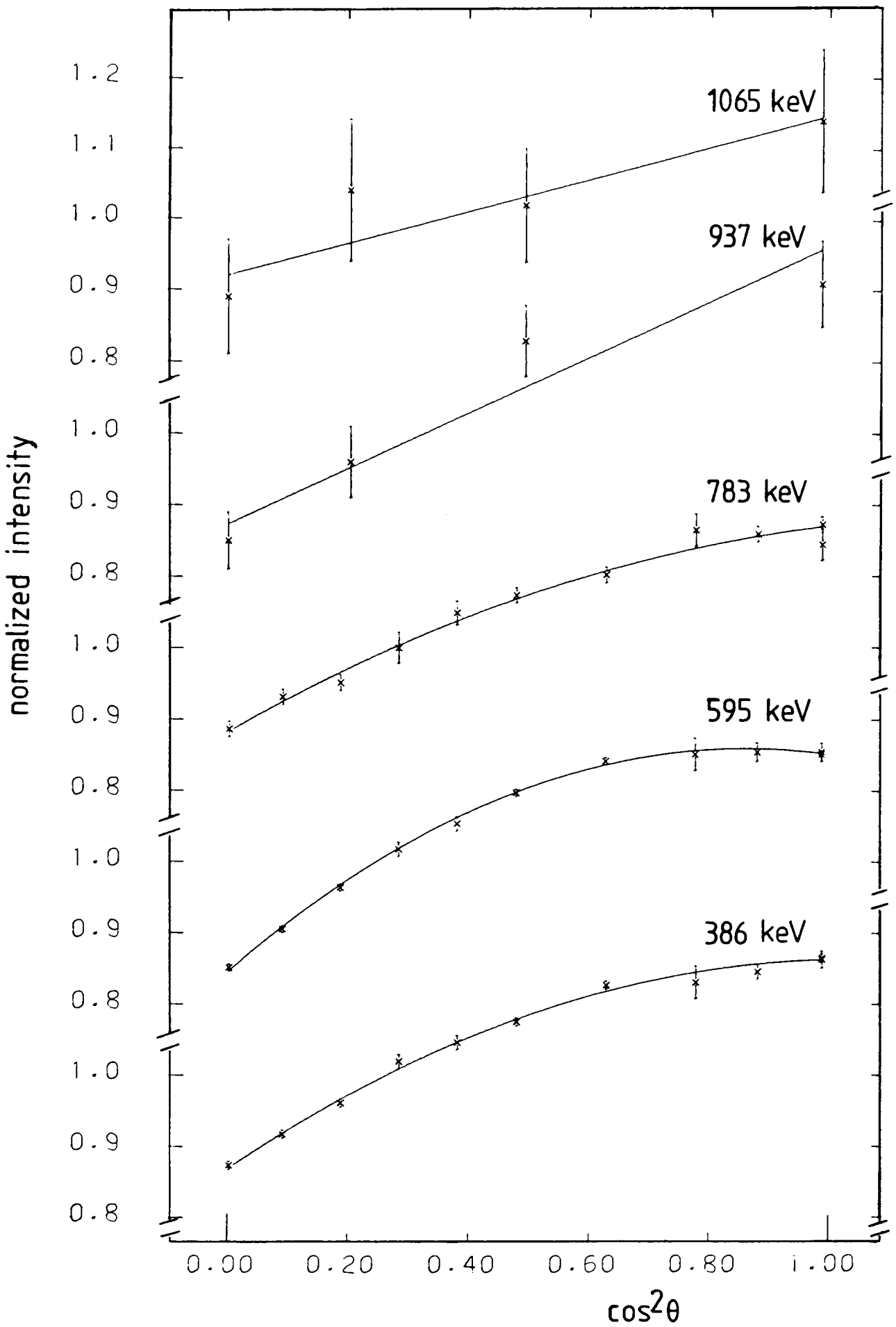


Figure 4.7 γ-ray angular distribution data for the 386, 595, 783, 937 and 1065 keV ^{80}Sr ground state band transitions, as functions of $\cos^2\theta$, where θ is the detector angle relative to the direction of the incoming beam. (An angular distribution with only zeroth and second order Legendre polynomials is linear in $\cos^2\theta$, while an angular distribution with higher order terms is curved.) The angular distributions have been normalized such that the γ-ray intensities are unity. The lines drawn through the points represent Legendre polynomial fits to the data, as discussed in the text.

and 2153 keV γ-rays. The Doppler shifted GSB γ-ray centroid energies, from which the lifetime data were extracted, are illustrated by fig. 4.6. In addition, representative spectra showing DSAM γ-ray lineshapes are given in Chapter 3 (figs. 3.14 and 3.15).

The measured angular distributions and DCO ratios of the GSB transitions (fig. 4.7 and table 4.1) are all consistent with $E2$ multipolarity assignments (however such measurements were not possible for the 2021 and 2153 keV transitions). The results of the GSB lifetime measurements are also consistent with $E2$ transitions. Therefore, all the GSB transitions were assigned $E2$ multipolarities.

4.3 The Slow Feeding Times Identified by Belmont Moreno

Slow feeding times were identified in the earlier DSAM lifetime study of ^{80}Sr carried out by Belmont Moreno [Bel 83]. In this investigation, the DSAM lineshapes which were identified with the yrast $14^+ \rightarrow 12^+$ and $12^+ \rightarrow 10^+$ transitions were found to have stopped components at 1316 and 1185 keV, respectively. These stopped components were interpreted as possibly resulting from slow feeding through transitions high in the GSB.

The new data produced in the present investigation necessitate a reinterpretation of these stopped components. The thick target γ-γ coincidence spectra given in fig. 4.8, taken from the present DSAM lifetime study, show in detail the energy region in question. The upper spectrum is the sum of spectra gated by the low lying 386 keV $2^+ \rightarrow 0^+$ and 595 keV $4^+ \rightarrow 2^+$ GSB transitions, while the lower spectrum is the sum of the coincidence spectra gated by the higher lying 783, 937 and 1065 keV GSB transitions. It is seen that the stopped peaks at 1185 and 1316 keV, which are prominent in the spectrum gated by the transitions at the bottom of the GSB (upper spectrum), are absent from the spectrum gated by the

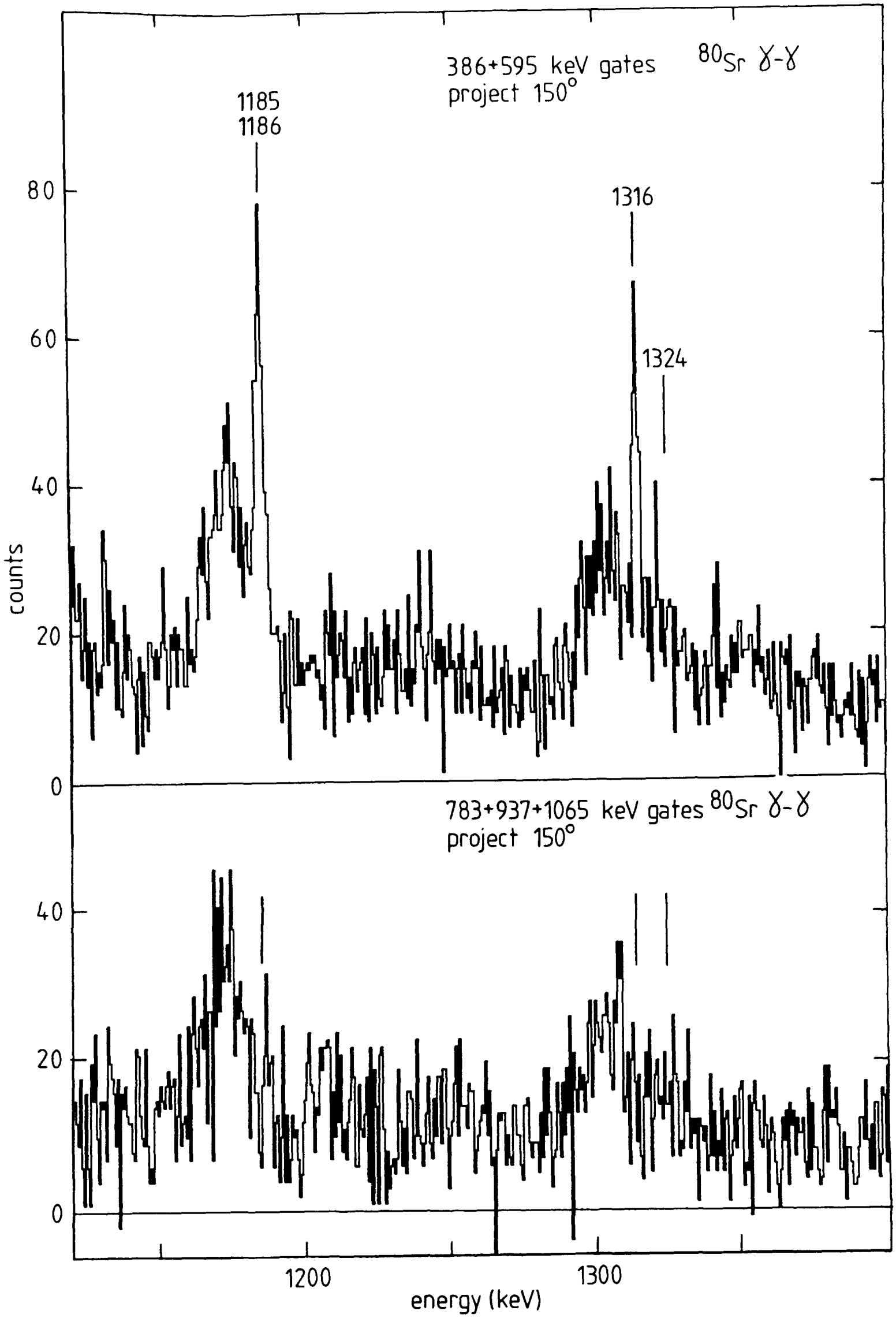


Figure 4.8 Thick target summed γ-γ coincidence spectra gated by both the 386 keV $2^+ \rightarrow 0^+$ and the 595 keV $4^+ \rightarrow 2^+$ ground state band transitions and the 783 keV $6^+ \rightarrow 4^+$, 937 keV $8^+ \rightarrow 6^+$ and the 1065 keV $10^+ \rightarrow 8^+$ ground state band transitions, observed at the backward angle of 150°. These spectra show that the stopped peaks at 1185 and 1316 keV, previously associated with slow feeding through transitions high in the ground state band [Bel 83], are due to 1185 and 1316 keV interband transitions which feed into the base of the ground state band. (See sect. 4.3 for details.)

transitions higher up in the GSB (lower spectrum). Therefore, the stopped components are not associated with the 1324 keV $14^+ \rightarrow 12^+$ and 1186 keV $12^+ \rightarrow 10^+$ GSB transitions. (The Doppler broadened lineshapes associated with these GSB transitions can be seen, in both the upper and lower halves of fig. 4.8, as the broad humps on the low energy sides of 1324 and 1186 keV, respectively.) In addition, it is known from the results of the present study that the energy of the 1316 keV stopped peak is different to that of the $14^+ \rightarrow 12^+$ GSB transition (1324 keV) and, thus, is not associated with this transition. Both the energies of these stopped peaks and their coincidence relationships indicate that these peaks are due to the 1185 and 1316 keV interband transitions which connect SB2 to the GSB (see fig. 4.1). These interband transitions are expected to have large stopped components, independent of their intrinsic strengths, since the low energy transitions which feed them are largely stopped. (These transitions were not identified by Belmont Moreno and he did not carry out a γ-ray gated DSAM measurement.) Therefore, it is concluded that the slow feeding components identified in the earlier study are associated with the 1316 and 1185 keV interband transitions and are not due to effects in the GSB as previously suggested.

The lineshapes of transitions high in the GSB can be used to further restrict the intensity of possible slow feeding through the GSB. In particular, the absence of a stopped component, characteristic of feeding times $\tau_f \gtrsim 1$ ps, in the DSAM γ-ray lineshape of the 1324 keV $14^+ \rightarrow 12^+$ transition (fig. 4.8) limits the intensity of slow feeding through the 14^+ GSB state to less than 10% of the intensity of this transition. Similarly, the observed centroid shift of the higher lying 1736 keV $20^+ \rightarrow 18^+$ GSB transition (table 4.2) limits

the intensity of slow feeding through the 20^+ GSB state to less than 30% of the intensity of the 1736 keV transition.

4.4 Sideband 1

4.4.1 INTRODUCTION

The transitions in cascade in SB1 show mutual coincidences, except that a few of the coincidences implied by the suggested level scheme for the weak 1649, 1678 and 1746 keV γ-rays were not observed (table 4.4). The placement of these latter γ-rays must therefore be considered tentative, although (as for the GSB) the coincidence relationships are consistent with the γ-ray intensities. The 1678 keV transition is discussed in more detail below. The ordering of the γ-rays is well determined by the combined Doppler shift and intensity data (tables 4.1 and 4.2). The γ-γ coincidence data for SB1 are illustrated by the coincidence spectra of the 1817, 798, 777 and the 970 keV γ-rays (figs. 4.9 and 4.10), while the higher energy γ-rays are more clearly seen in the sum of these coincidence gates (fig 4.11). In addition, the SB1 transitions can be seen in the spectra gated by the low lying GSB transitions (figs. 4.3 and 4.4).

As with the GSB, levels in SB1 benefitted from the summing of several coincidence gates, in determining lifetimes using the DSAM. This allowed lineshapes to be measured for all the levels in this sideband below 11 MeV. Unfortunately, the measured DSAM centroid shift attenuation coefficients for the levels at 7728, 9096 and 10537 keV were equal, within error. Therefore, only upper limits could be assigned to the lifetimes of these levels, since the lineshapes were dominated by the cascade feeding times. Fig. 4.12 illustrates the

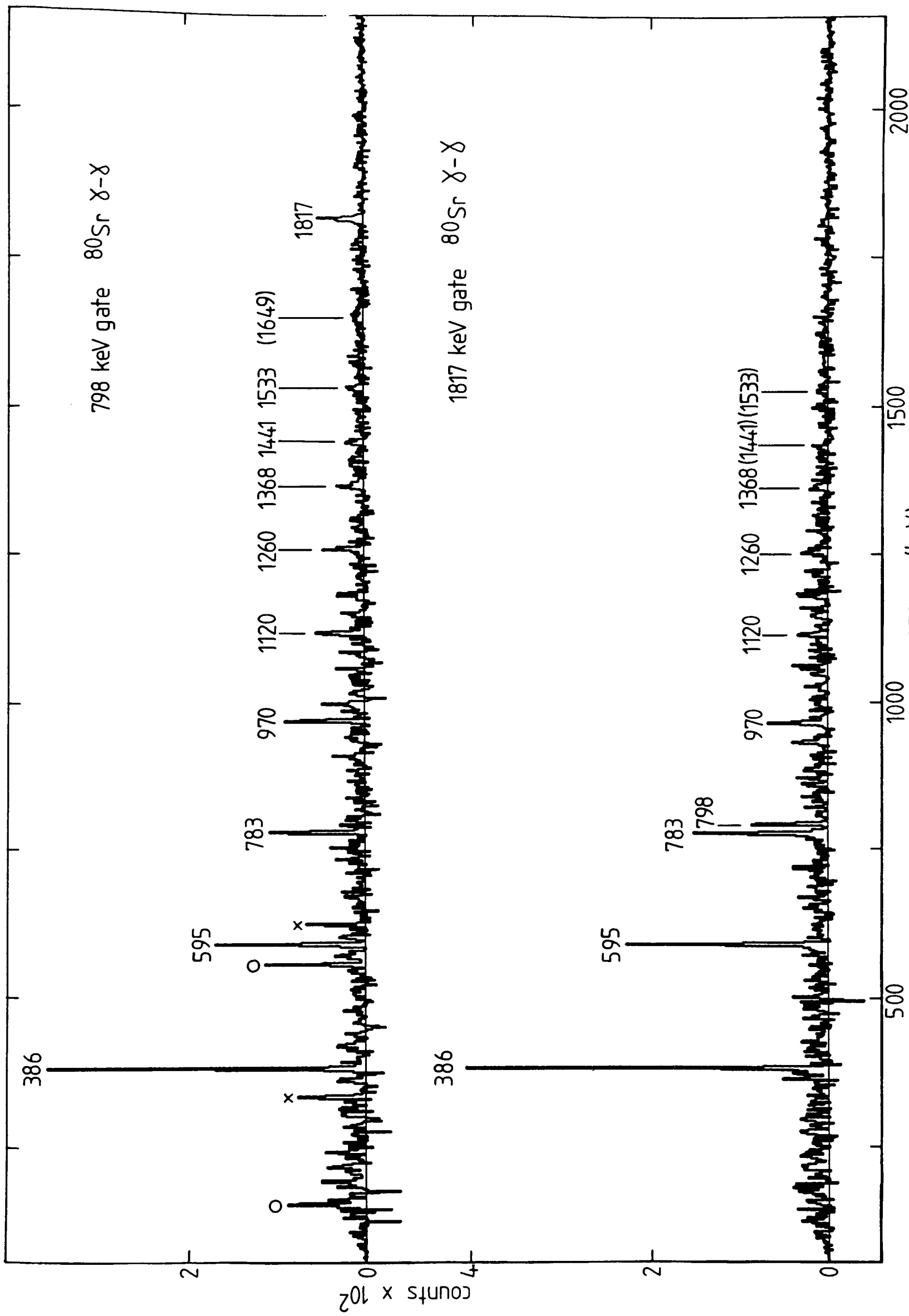


Figure 4.9 Thin target γ-γ coincidence spectra for the 798 and 1817 keV γ-rays associated with SB1, illustrating SB1 and the decay of the 4378 keV SB1 level to the GSB through the 798 and 1817 keV transitions. (See sect. 4.4 for discussion.)

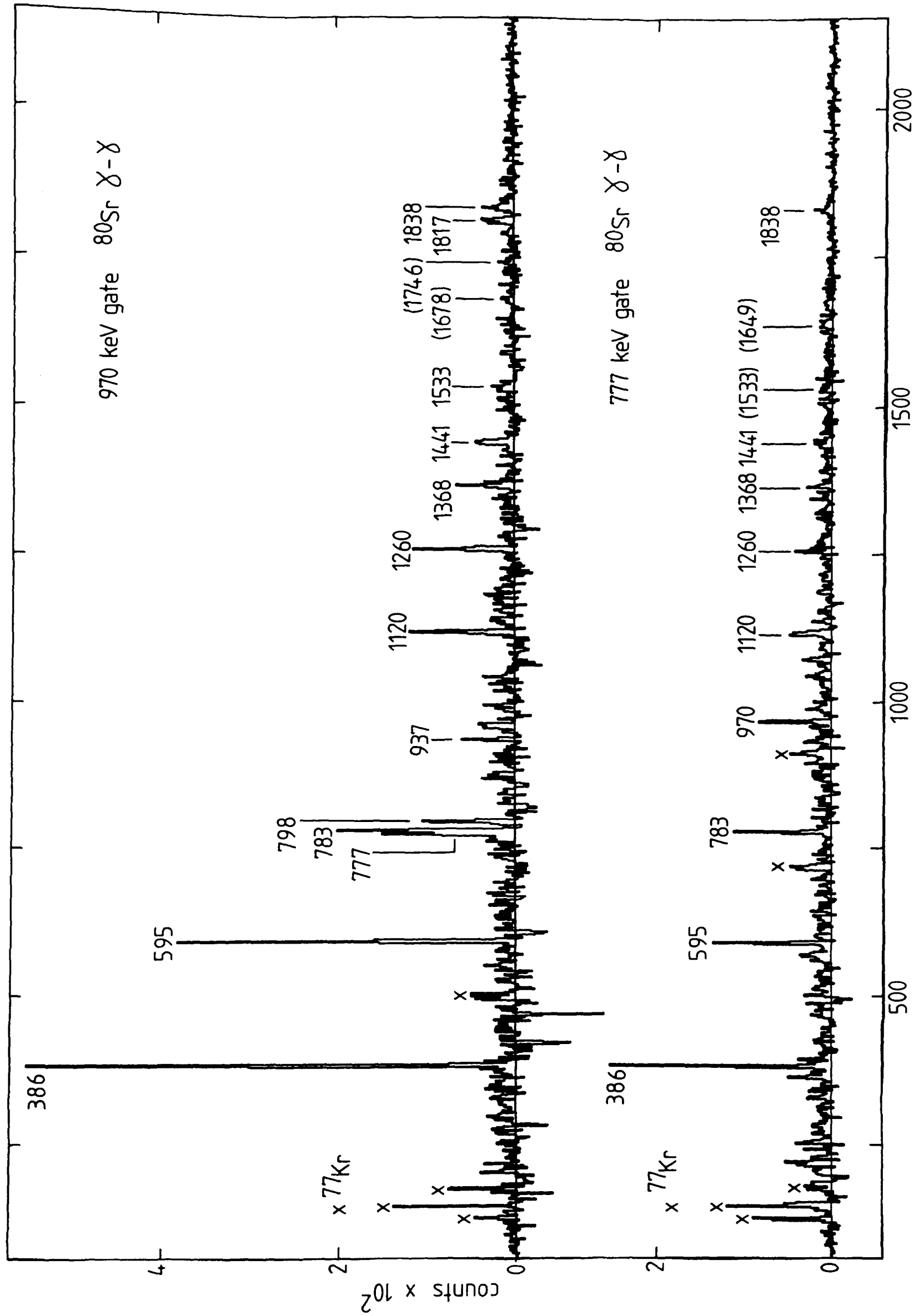


Figure 4.10 Thin target γ-γ coincidence spectra for the 970 and 777 keV SB1 γ-rays, illustrating SB1 and the decay of the 4378 keV SB1 level to the GSB through both the 777 and 1838 keV transitions and the 798 and 1817 keV transitions, and possibly the 1678 keV transition. (See sect. 4.4 for discussion.)

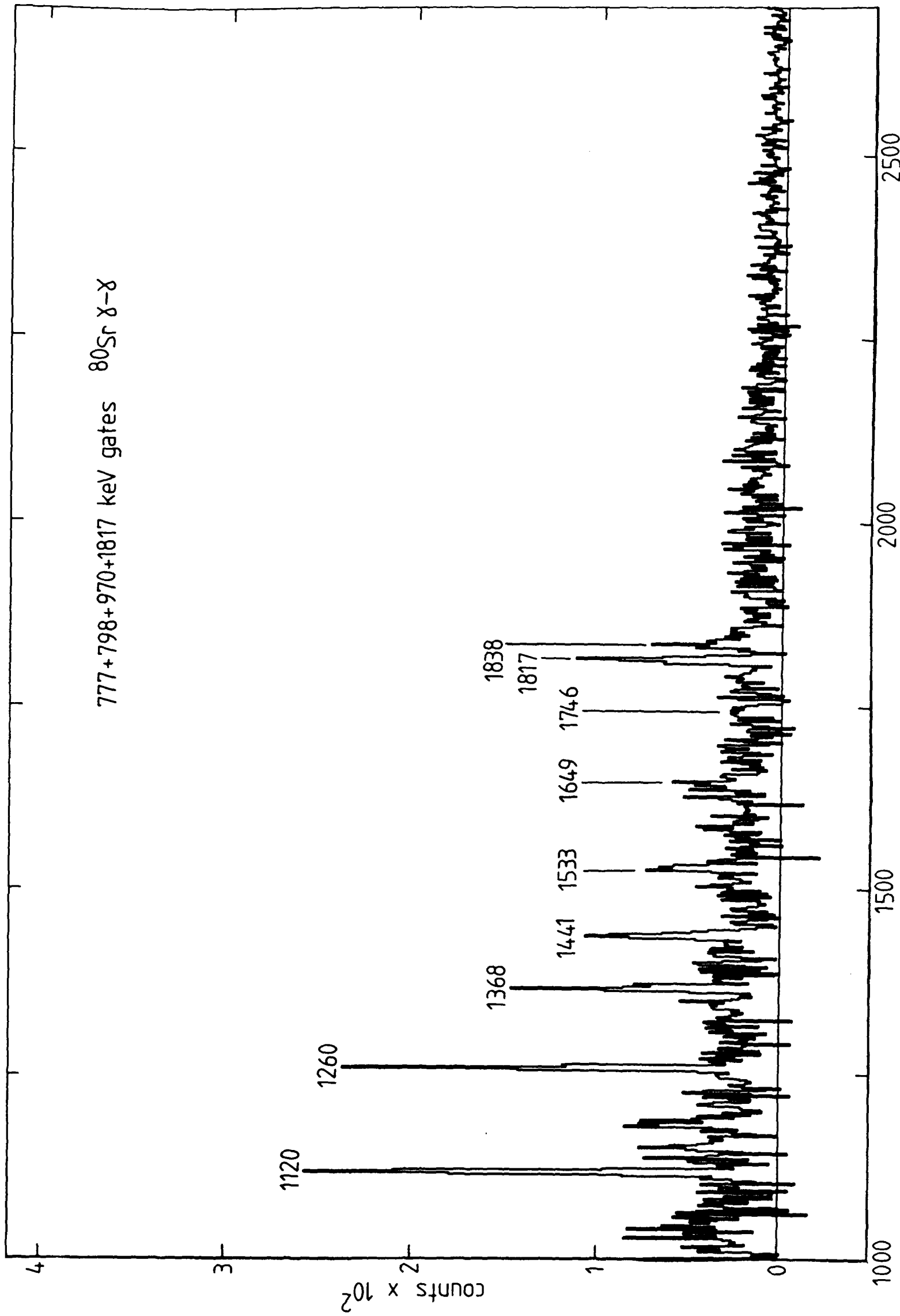


Figure 4.11 Summed thin target γ-γ coincidence spectra for the 777, 798, 970 and 1817 keV SB1 γ-rays, illustrating the high energy transitions in SB1. (See sect. 4.4 for discussion.)

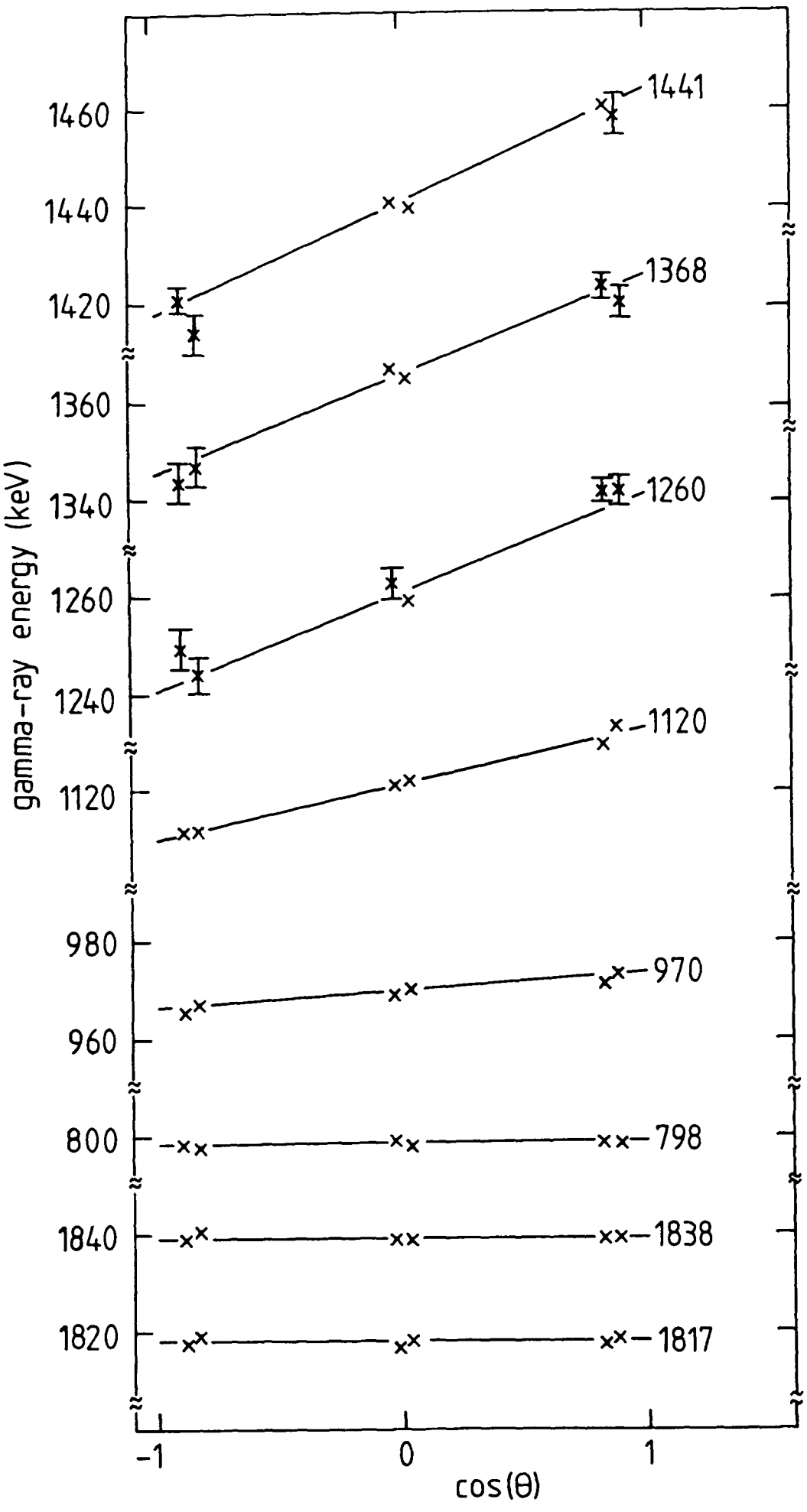


Figure 4.12 Doppler shifted γ-ray centroid energies as a function of $\cos\theta$ for the SB1 transitions, where θ is the detector angle relative to the direction of the incoming beam. As there are two measurements for each value of $\cos\theta$, the pairs of points have been drawn slightly separated for clarity. Error bars are shown only when they are larger than the "$\times$" marking the point. The lines drawn through the the points represent linear fits to the data, as discussed in the text.

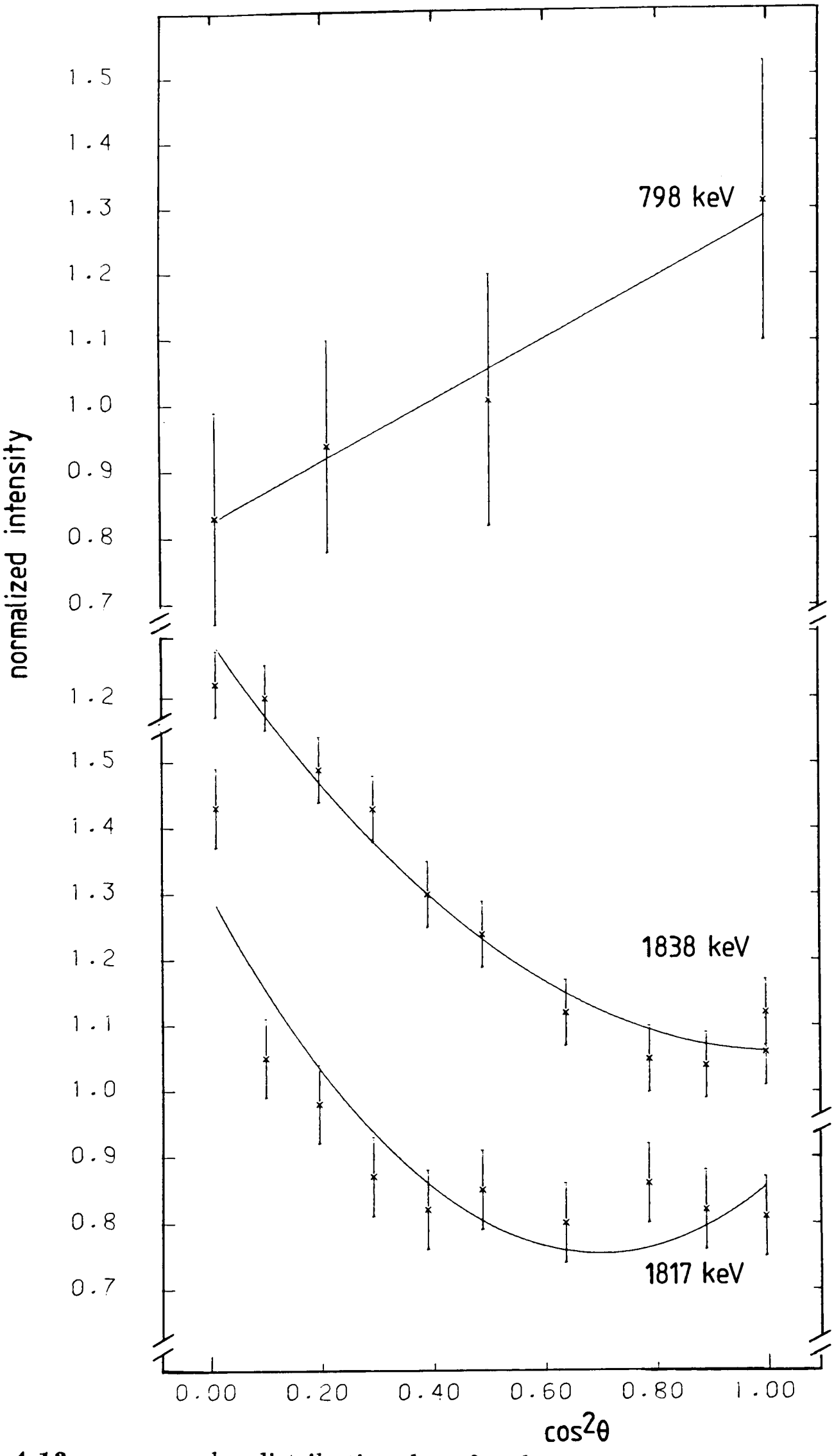


Figure 4.13 γ-ray angular distribution data for the 1817, 1838 and 798 keV ^{80}Sr SB1 transitions, as functions of $\cos^2\theta$, where θ is the detector angle relative to the direction of the incoming beam. (An angular distribution with only zeroth and second order Legendre polynomials is linear in $\cos^2\theta$, while an angular distribution with higher order terms is curved.) The angular distributions have been normalized such that the γ-ray intensities are unity. The lines drawn through the points represent Legendre polynomial fits to the data, as discussed in the text.

Doppler shifted γ-ray centroid energies, from which the SB1 lifetime data were extracted.

The angular distribution of the 798 keV γ-ray (fig. 4.13) and the DCO ratios of the 777, 798, 970, 1120, 1260, 1368 and 1441 keV γ-rays are consistent with those expected for stretched $E2$ transitions (table 4.1). The rates of the 777, 798, 970, 1120, 1260, 1368 and 1441 keV transitions are also consistent with $E2$ multipolarity assignments (table 4.2). Therefore, these transitions were all tentatively assigned $E2$ multipolarities.

4.4.2 THE 777, 798, 1817 AND 1838 keV TRANSITIONS

The two dominant decay paths of the 4378 keV level, via the 777 and 1838 keV transitions and the 798 and 1817 keV transitions, are illustrated by the coincidence spectra of the 970, 777, 798 and 1817 keV γ-rays (figs. 4.9 and 4.10). For example, the 970 keV γ-ray is in coincidence with the γ-rays emitted in both decay paths (fig. 4.10). In addition, the 798 and 1817 keV γ-rays (fig. 4.9) are in mutual coincidence, but do not show coincidences with the 777 and 1838 keV γ-rays, as expected from their placement in the decay scheme. The energy sums of these two dominant decay paths of the 4378 keV level agree very well, the difference being 0.3 ± 0.9 keV.

The angular distributions and DCO ratios of the 1817 and 1838 keV γ-rays (fig. 4.13 and table 4.1) suggest that these are dipole transitions with large mixing ratios involving spin changes of $1\hbar$ yielding spins of either 5 or 7 for the levels at 3580 and 3601 keV. (The signs of the a_4 coefficients were found to be wrong for $\Delta I = 0$ transitions.) In order to quantify the relationships between the possible spin assignments and the angular distribution data, and to extract multipole mixing ratios, a χ^2 analysis of the angular distribution data was carried out. A Gaussian substate distribution about the M=0 substate relative

to the beam axis was assumed, as suggested by previous workers [Yam 67, Mat 74a]. The width of this Gaussian distribution was estimated from the experimental angular distribution data of the low lying GSB $E2$ transitions and from preliminary fits to the dipole interband transitions, in which the substate distribution width σ was treated as a free parameter. The effect of the substate distribution on the γ-ray angular distribution was included using a parameterization of the tables of der Mateosian and Sunyar [Mat 74a]. Unfortunately, it was not possible to use the angular distributions of γ-rays de-exciting GSB levels with spins $I \geq 6$, since Doppler broadening makes the substate Gaussian widths extracted from the angular distributions of these γ-rays unreliable. (In particular, Doppler shifted tails at forward angles can be obscured by other peaks, reducing the apparent γ-ray intensity at these angles and thus reducing the a_2 coefficient. Such reduced a_2 coefficients increase the apparent width of the Gaussian substate distribution.) The resulting Gaussian widths are given, as a function of level spin, in fig. 4.14. On the basis of this calibration, Gaussian widths of $\sigma/I = 0.35(5)$ were chosen for the levels at 3601 and 3580 keV (where I is the level spin).

The χ^2 plots for the 1817 and 1838 keV transitions are given in figs. 4.15 and 4.16, respectively, for possible spin assignments of $I = 4$, 5, 6, 7 or 8 for the 3580 and 3601 keV levels. (Thus, although unlikely, the possibility of mixed quadrupole/octupole transitions was investigated.) The χ^2 plots for both the 1817 and the 1838 keV γ-rays eliminate $I = 4$, 6 and 8 as possible spin assignments for the 3580 and 3601 keV levels. However, both $I = 5$ and $I = 7$ give good fits to the data, although in both cases the $I = 7$ solution has the lowest χ^2. The absence of transitions to the 4^+ state in the GSB and the strong intensity

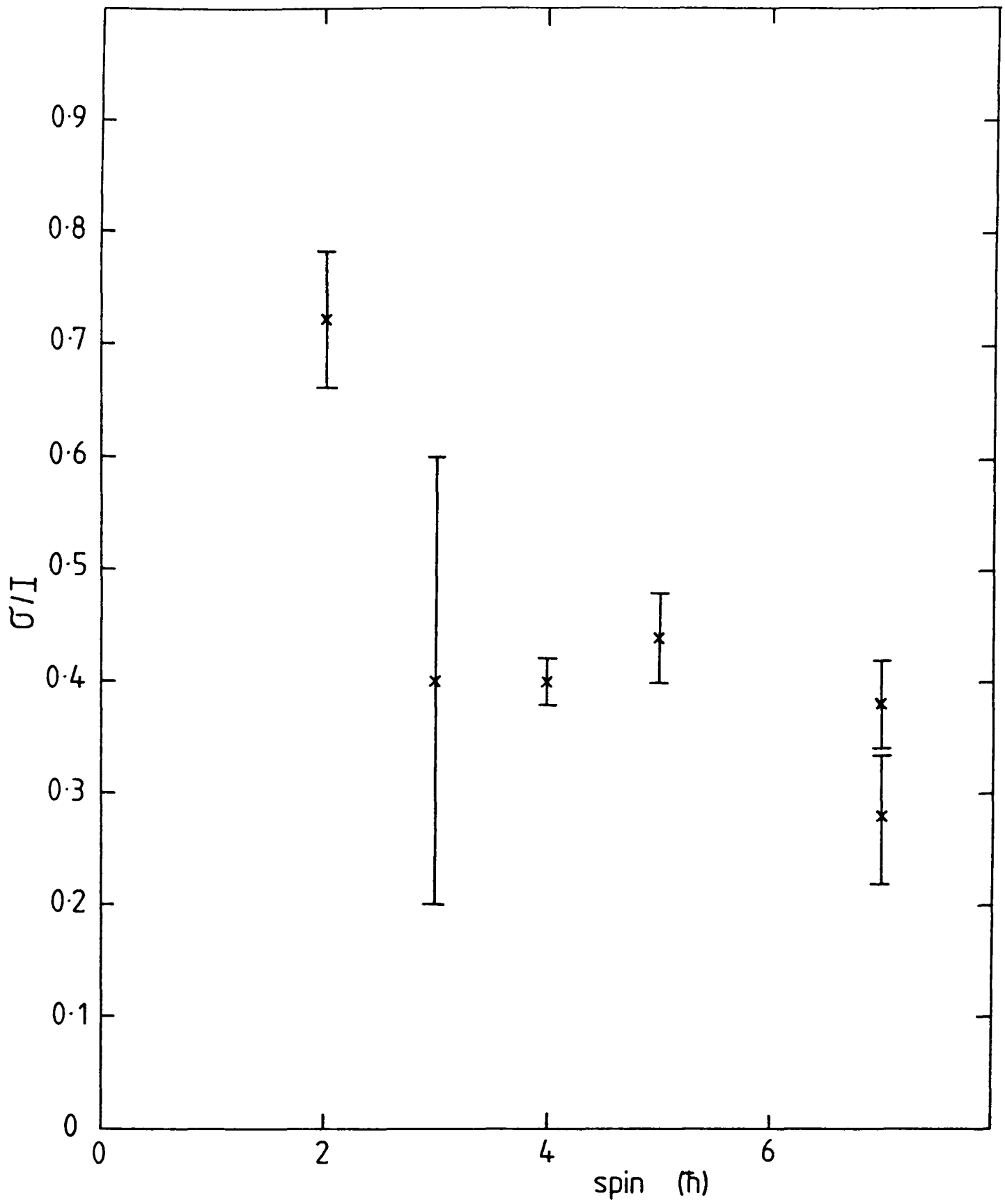


Figure 4.14 Values of the width of the Gaussian spin substate distribution σ/I (where I is the level spin) extracted from the angular distribution data (see sect. 4.4.2 for details). These values determined the substate distribution widths used in the χ^2 analysis of the angular distributions of the 1185, 1316, 1817 and 1838 keV γ-rays (sects. 4.4.2 and 4.5.3).

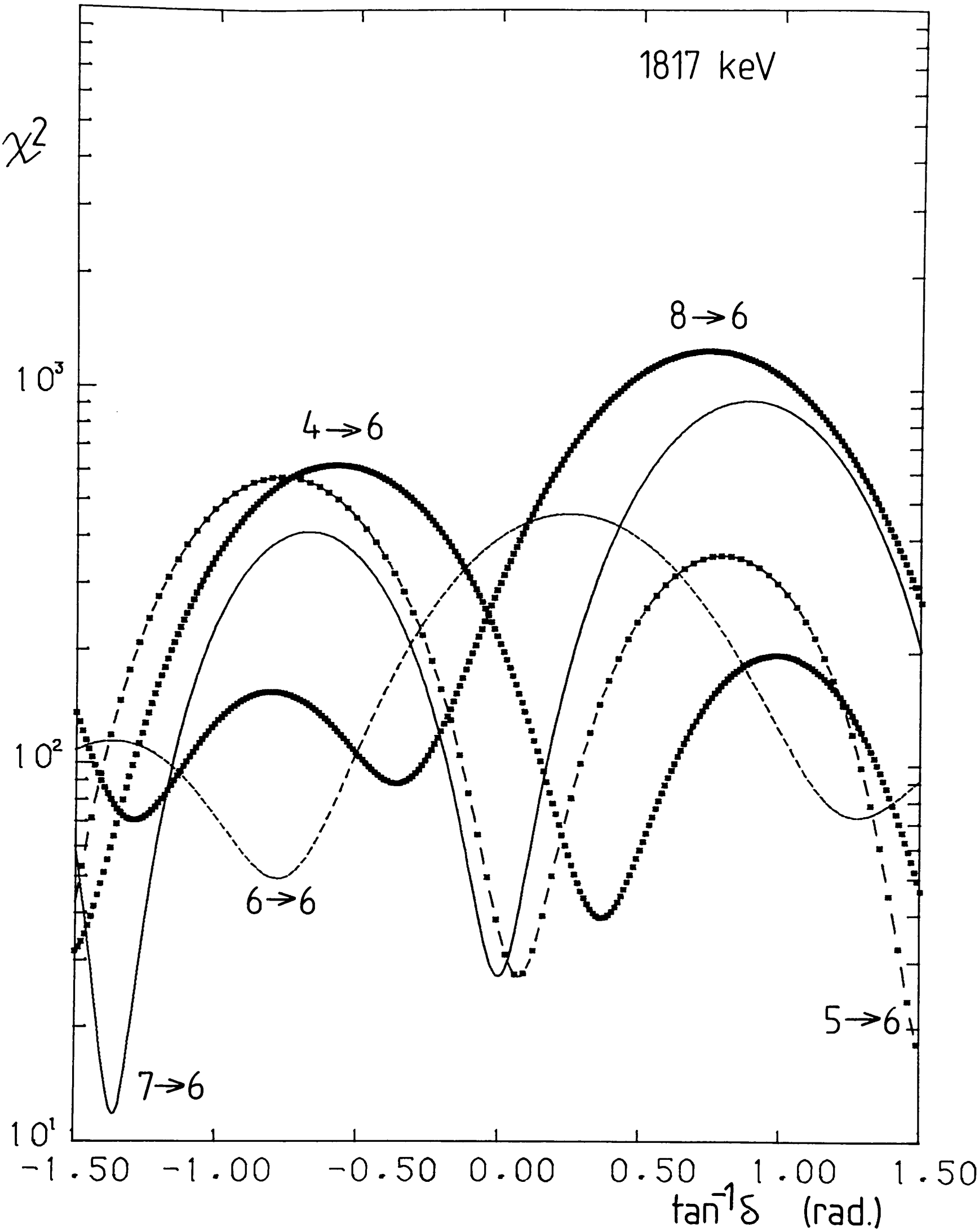


Figure 4.15 χ^2 analyses of the angular distribution of the 1817 keV SB1 γ-ray as a function of multipole mixing ratio δ for various spin assignments to the 3580 keV level. (See sect. 4.4 for discussion.) This particular plot is for a substate Gaussian width of $\sigma/I = 0.35$ and a γ-ray intensity determined from a Legendre Polynomial fit to the 1817 keV γ-ray's angular distribution (fig. 4.13). In determining the errors associated with the multipole mixing ratio, the uncertainties in both σ/I and the γ-ray intensity were taken into account. There were 8 degrees of freedom in the fit.

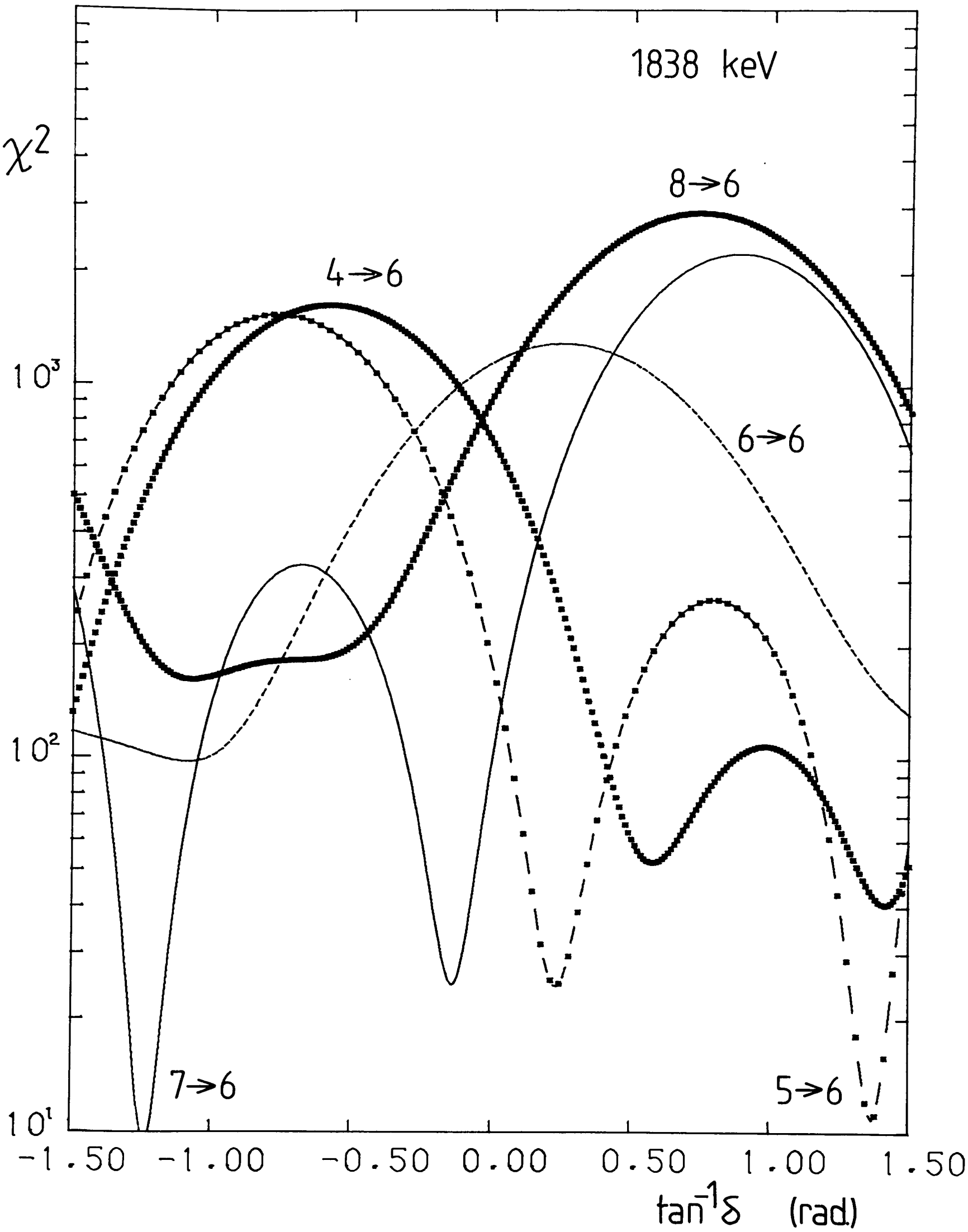


Figure 4.16 χ^2 analyses of the angular distribution of the 1838 keV SB1 γ-ray as a function of multipole mixing ratio δ for various spin hypotheses for the 3601 keV level. (See sect. 4.4.2 for discussion.) This particular plot is for a substate Gaussian width of $\sigma/I = 0.35$ and a γ-ray intensity determined from a Legendre Polynomial fit to the 1838 keV γ-ray's angular distribution (fig. 4.13). In determining the errors associated with the multipole mixing ratio, the uncertainties in both σ/I and the γ-ray intensity were taken into account. There were 9 degrees of freedom in the fit.

with which SB1 is populated at high spins, relative to the GSB, suggesting that SB1 is close to yrast, make $I = 5$ assignments unlikely for both the 3580 and the 3601 keV levels. Finally, the large mixing ratios for the 1817 and 1838 keV transitions ($\delta = -4.7(15)$ and $\delta = -2.8(4)$, respectively) suggest that these transitions are unlikely to change the nuclear parity [End 79]. (By way of contrast, similar analysis of the angular distribution data of Hellmeister *et al.* [Hel 79] for the $7^- \rightarrow 6^+$ 1310 keV and $5^- \rightarrow 4^+$ 1630 keV transitions, in the neighbouring deformed even-even nucleus ^{78}Kr, yields mixing ratios of $\delta = -0.09(3)$ and $\delta = -0.01(2)$, respectively.) Therefore, the spins and parities of the levels at 3580 and 3601 keV are tentatively assigned as 7^+. These spin assignments and mixing ratios are also consistent with the observed DCO ratios, within the rather large experimental errors. The experimental DCO ratios are 0.53(20) and 0.75(30) compared with the theoretical ratios of 0.51 and 0.40 for the 1817 and 1838 keV transitions, respectively.

The 777 and 798 keV transitions are assigned $E2$ multipolarities on the basis of their DCO ratios and of angular distribution the of the 798 keV γ-ray; these data are given in fig. 4.13 and table 4.1. (Unfortunately, it was not possible to measure the angular distribution of the 777 keV γ-ray, because it was not resolved from the intense 782 keV γ-ray. However, the 777 keV γ-ray's DCO ratio was measured by gating on the 782 keV transition.) Therefore, the 4378 keV level is tentatively assigned spin and parity of 9^+. As noted above, these assignments are consistent with the lifetime of the 4378 keV level (corresponding to rates of $\sim$ 50 Weisskopf single particle units for the two decay transitions).

4.4.3 THE 1678 keV TRANSITION

The evidence for the placement of the weak 1678 keV transition is unfortunately not complete. Firstly, the presence of a fairly convincing coincidence between the 970 keV transition and the 937 keV GSB transition (fig. 4.10) suggests a decay from the 4378 keV level to the 2700 keV GSB level. Such a transition would imply coincidences between the 937 keV γ-ray and the γ-rays emitted from levels above 5348 keV level in SB1. Unfortunately, such coincidences are statistically at noise level in the appropriate spectra, although there is some evidence for them (table 4.4). However, a γ-ray of the correct energy and intensity for a transition from the 4378 keV SB1 level to the 2700 keV GSB level is in coincidence with the 386, 595, 783 and 937 keV γ-rays (fig. 4.4 and table 4.4). Therefore, a 1678 keV transition is tentatively placed in the level scheme. This transition connects the 4378 and 2700 keV levels and the placement is consistent with all the available data.

4.5 Sideband 2

4.5.1 INTRODUCTION

In contrast to the GSB and SB1, nearly all of the coincidences implied by the suggested level scheme for the SB2 transitions have been observed (table 4.5). However, there were some complications with the coincidence relationships of the 1185 and 724 keV transitions (see below) and some of the coincidences of the 1339 keV transition were obscured by the more intense and unresolved 1343 keV interband transition. The γ-γ coincidence data on SB2 are illustrated by the coincidence spectra of the 1105 and 877 keV γ-rays (fig. 4.17).

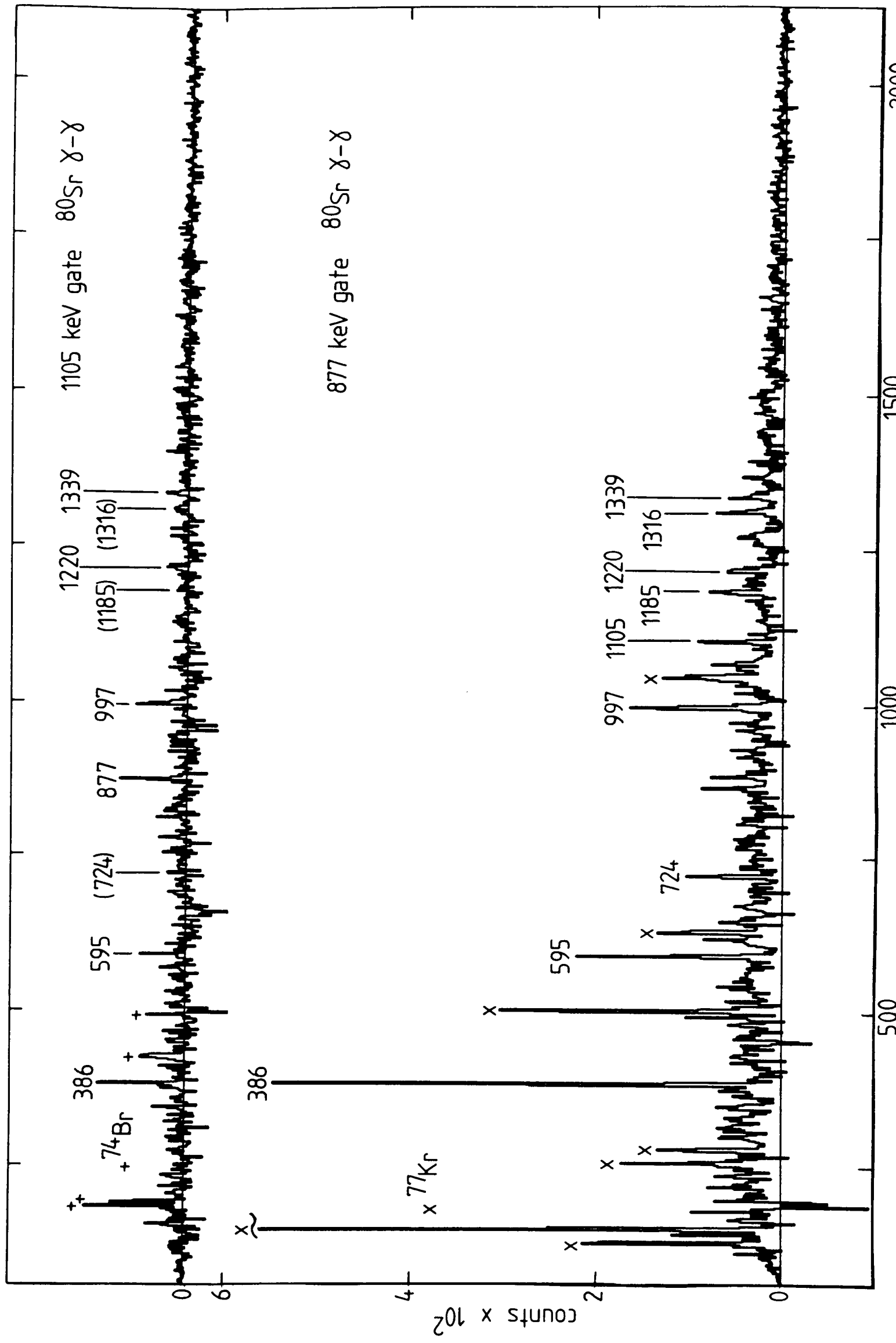


Figure 4.17 Thin target γ-γ coincidence spectra for the 1105 and 877 keV SB2 γ-rays, illustrating SB2. (See sect. 4.5 for details.)

In addition, the SB2 γ-rays can be seen in the γ-γ coincidence spectrum of the 386 keV $2^+ \rightarrow 0^+$ GSB transition (fig. 4.3).

The ordering of the SB2 transitions was determined from the observed intensities and the centroid Doppler shifts (tables 4.1 and 4.2, respectively.) In particular, the ordering of the 997, 877 and 724 keV transitions was determined by the γ-ray centroid Doppler shifts, which strongly support the ordering given in the level scheme (fig 4.1). Although the observed intensities are consistent with the suggested ordering (within the experimental uncertainties), there is some suggestion of a lack of intensity at the bottom of SB2. This may possibly be due to unobserved feeding out of SB2 and into the GSB; however, the experimental data were not of sufficient quality to either confirm or refute this. The ordering of the 724 and 1185 keV transitions is well determined, as the 1571 keV level has been populated, and its 1185 keV decay to the 386 keV level studied, in the β-decay of ^{80}Y to ^{80}Sr [Lis 81].

The Doppler shifted lineshapes of γ-rays depopulating the 2296, 3172 and 4169 keV levels in SB2 were measured (fig. 4.18 and table 4.2). However, it was, unfortunately, not possible to assign a lifetime to the 2296 keV level, because of uncertainties in the feeding time into this level through the 1343 keV interband transition (see sect. 4.6). In such circumstances it is often possible to assign an upper limit to the level lifetime (τ_{eff}). However, in this case the centroid Doppler shifts of both the transitions which depopulate the 2296 keV level are consistent with zero (table 4.2: $100Fv_0/c(724) = 0.026(29)$, $100Fv_0/c(1316) = -0.008(13)$) corresponding to an infinite τ_{eff}. Therefore, neither a lifetime nor a lifetime limit could be assigned to the level at 2296 keV. The DSAM lifetime data for SB2 (and

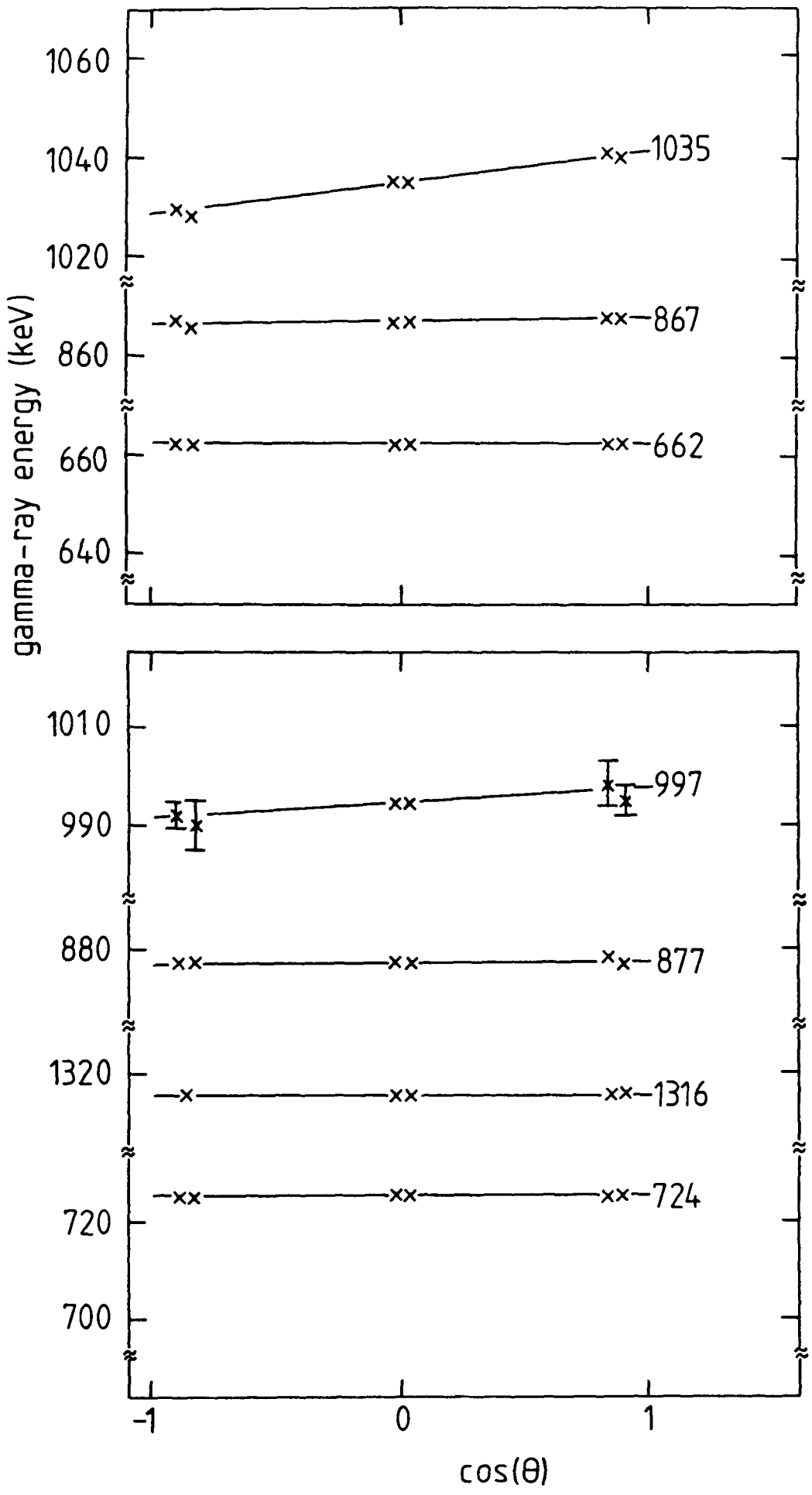


Figure 4.18 Doppler shifted γ-ray centroid energies as a function of cosθ for the SB2 and SB3 transitions, where θ is the detector angle relative to the direction of the incoming beam. As there are two measurements for each value of cos θ, the pairs of points have been drawn slightly separated for clarity. Error bars are shown only when they are larger than the "×" marking the point. The lines drawn through the the points represent linear fits to the data, as discussed in the text.

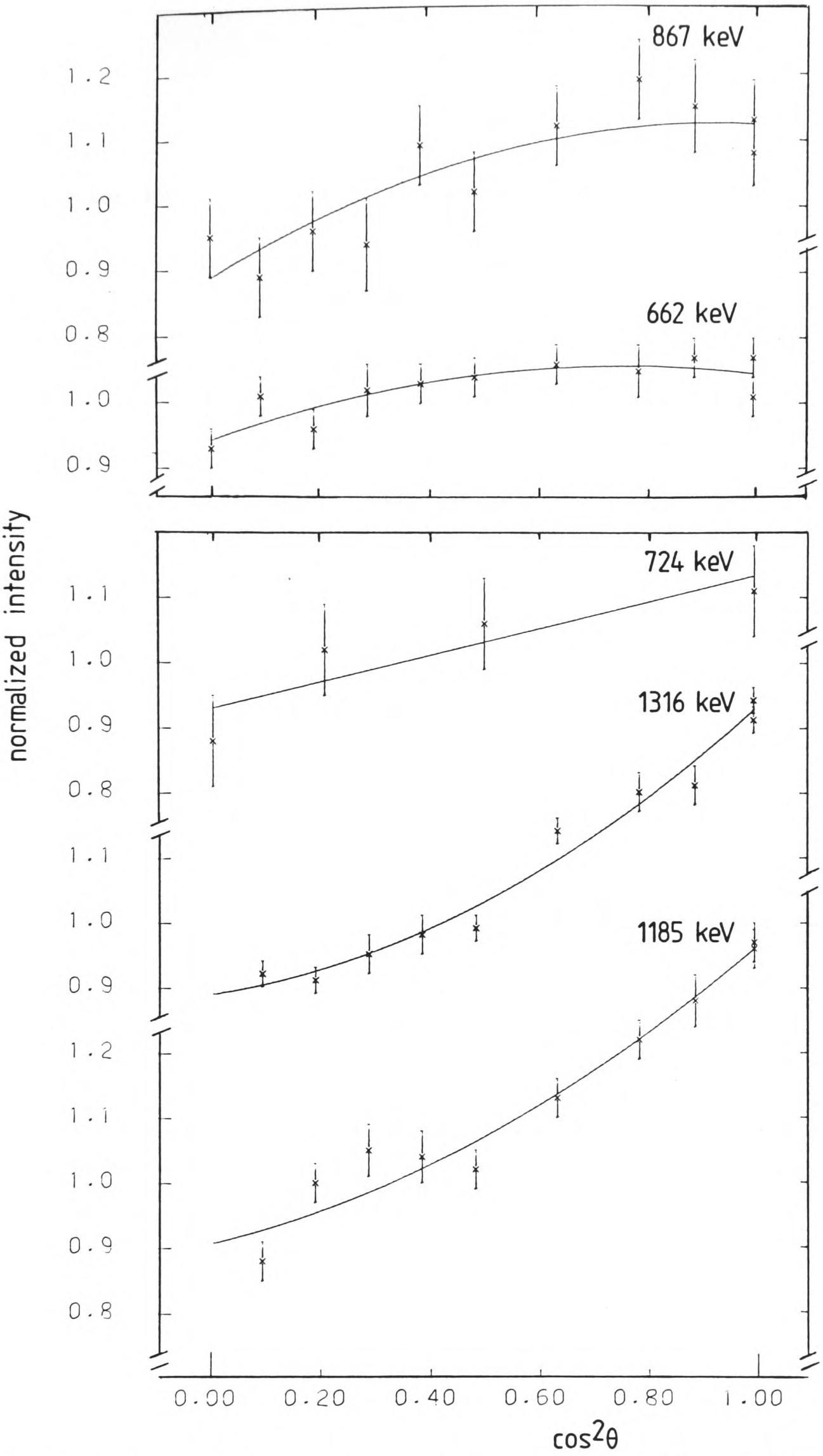


Figure 4.19 γ-ray angular distribution data for transitions in SB2 and SB3, as functions of $\cos^2\theta$, where θ is the detector angle relative to the direction of the incoming beam. (An angular distribution with only zeroth and second order Legendre polynomials is linear in $\cos^2\theta$, while an angular distribution with higher order terms is curved.) There is no 90° datum point for either the 1185 or the 1316 keV γ-ray, as at this angle these γ-rays are poorly separated from the 1186 and 1324 keV γ-rays, respectively. The angular distributions have been normalized such that the γ-ray intensities are unity. The lines drawn through the points represent Legendre polynomial fits to the data, as discussed in the text.

SB3) are illustrated by fig. 4.18.

The angular distribution of the 724 keV γ-ray and the DCO ratios of the 724, 877, 997 and 1220 keV γ-rays suggest that these are stretched $E2$ transitions (fig. 4.19 and table 4.1). Such an assignment is consistent with the observed rates of the 877 and 997 keV transitions (table 4.2). Therefore, these transitions were tentatively assigned $E2$ multipolarities.

4.5.2 THE 724 keV TRANSITION

The 724.4 keV transition in ^{80}Sr was unresolved from the 724.5 keV transition in ^{77}Kr [Wör 84]. This transition is strongly populated in γ-ray de-excitation of ^{77}Kr, which was produced with a large cross-section in the reaction of ^{29}Si on ^{54}Fe via the competing $\alpha 2p$ channel (see fig. 3.3 and sect. 3.2.2). As discussed in sect. 3.3.3.3, the γ-rays emitted in the $\alpha 2p$ reaction channel are very broad and, since the decay of the odd A nucleus ^{77}Kr is complex and involves the emission of many γ-rays [Nol 75, Wör 84], ^{77}Kr γ-rays contaminated many of the coincidence gates set on ^{80}Sr transitions. In some cases, this lead to uncertainty as to whether a particular ^{80}Sr γ-ray exhibited a coincidence with the 724 keV γ-ray in ^{80}Sr. Furthermore, the presence of intense ^{77}Kr transitions in the 724 keV coincidence gate made identification of ^{80}Sr transitions difficult in that coincidence spectrum. Nevertheless, the evidence for a 724 keV transition in ^{80}Sr is strong. For example, the 724 keV γ-ray can be clearly seen in the 386 keV γ-ray's coincidence spectrum (fig. 4.3) which is not contaminated by ^{77}Kr.

4.5.3 THE 1185 AND 1316 keV INTERBAND TRANSITIONS

The 1186 keV GSB γ-ray, which was not resolved from the 1185 keV interband transition, masked the coincidence relationships between the 1185 keV γ-ray and the 386 and 595 keV GSB γ-rays. However, the thick target DSAM γ-γ coincidence data, in which the 1186 keV GSB γ-ray was considerably Doppler broadened while the 1185 keV interband transition was stopped, helped to clarify the coincidence relationships with the 386 and 595 keV GSB γ-rays (see fig. 4.8 and sect. 4.3). Furthermore, the 1185 keV interband transition has been observed in the study of the β-decay of ^{80}Y to ^{80}Sr [Lis 81]. Thus, the existence of separate 1185 (SB2) and 1186 (GSB) keV transitions and their placement within the level scheme are well established. Unfortunately, the intense GSB transitions in the 1185/6 keV coincidence gate, and their associated background, made identification of sideband transitions in coincidence with the 1185 keV transition difficult in this spectrum. The two competing decay paths from the 2296 keV level are well supported by the observed coincidence relationships (table 4.5) and can be seen in the coincidence spectrum of the 877 keV SB2 γ-ray (fig. 4.17; although not in the coincidence spectrum of the 1105 keV SB2 γ-ray, which is not of adequate statistical quality to show clearly the two decay branches of the 2296 keV level) and also in the coincidence spectra of SB3 γ-rays which also decay through the 2296 keV level (fig. 4.22). The energy sums for the two different decay paths of the 2296 keV level differ by 1.0 ± 0.6 keV.

The angular distributions of the 1185 and 1316 keV γ-rays (fig. 4.19 and table 4.1) suggest that these transitions are stretched dipoles. (The sign of the a_4 coefficients makes $I \rightarrow I$ and $I \rightarrow I \pm 2$ transitions unlikely. For the 1185 keV transition the non-zero

$a_4 = +0.06(4)$ coefficient makes a spin assignment of $I = 1$ for the 1571 keV level also unlikely.) To investigate possible spin assignments for the levels at 1571 and 2296 keV, χ^2 analyses, similar to those performed for the 1817 and 1838 keV transitions (see sect. 4.4.2), were carried out for the 1185 and 1316 keV transitions; the results of these analyses are discussed below.

The χ^2 plots for the angular distribution of the 1185 keV γ-ray as a function of multipole mixing ratio, for spin assignments of $I = 0$, 1, 2, 3 or 4 for the 1571 keV level, are given in fig. 4.20. (The Gaussian width of the substate distribution used in this analysis, determined from fig. 4.14, was $\sigma/I = 0.45(10)$.) A spin assignment of $I = 3$ for the 1571 keV level is clearly favoured, although the χ^2 is not very much larger for $I = 2$. In addition to the angular distribution data from the present study, studies by Lister *et al.* [Lis 81] of ^{80}Sr following β-decay of ^{80}Y suggest that there is an allowed β-decay from the (4^+) ground state of ^{80}Y to the 1571 keV state in ^{80}Sr. Such an allowed transition restricts the 1571 keV level to $I = 3$, 4 or 5 and even parity. Therefore, it is concluded that the 1571 keV level has $I^\pi = 3^+$. This assignment is consistent with the absence of an observed transition from this level to the 0^+ ground state. In addition, the positive parity assignment is consistent with the relatively large mixing ratio of the 1185 keV transition ($\delta = +0.45(8)$) extracted from the χ^2 plot (fig. 4.20). Furthermore, the $I = 3$ assignment and the extracted multipole mixing ratio are consistent with the DCO data; the experimental DCO ratio is 0.98(10), while the theoretical DCO ratio for the assigned spin and mixing ratio is 1.08. Such a spin and parity assignment for the 1571 keV level had been previously suggested by Higo *et al.* [Hig 83] on the basis of an angular

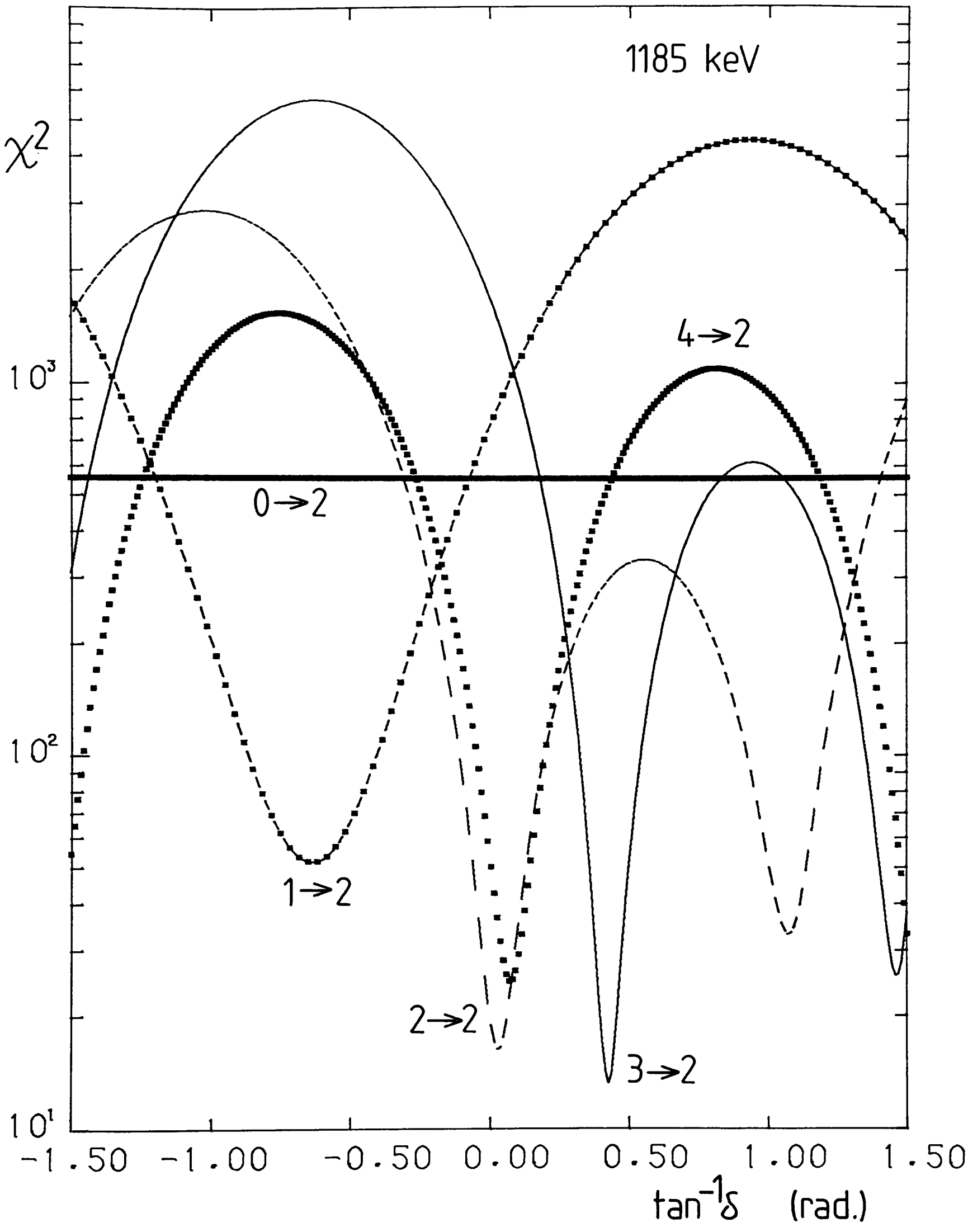


Figure 4.20 χ^2 analyses of the angular distribution of the 1185 keV SB2 γ-ray as a function of multipole mixing ratio δ for various spin hypotheses for the 1571 keV level. (See sect. 4.5.3 for discussion.) This particular plot is for a substate Gaussian width of $\sigma/I = 0.45$ and a γ-ray intensity determined from a Legendre Polynomial fit to the 1185 keV γ-ray's angular distribution (fig. 4.19). In determining the errors associated with the multipole mixing ratio, the uncertainties in both σ/I and the γ-ray intensity were taken into account. There were 8 degrees of freedom in the fit.

distribution measurement for the 1185 keV γ-ray and IBA calculations.

The χ^2 analysis of the 1316 keV γ-ray (fig. 4.21; $\sigma/I = 0.40(5)$) was not as successful as those of the 1185, 1817 and 1838 keV γ-rays (see above) with the separation of the different spin hypotheses for the 2296 keV level being less clear than in the other cases. However, $I = 3$, 5 and possibly $I = 2$ with large mixing ratios give the best fits to the data. Therefore, the 2296 keV level is assumed to have a spin of either 5, 3 or 2. The absence of a transition from the 2296 keV level to the GSB 2^+ or 0^+ states suggests that this level probably does not have $I = 3$ or 2. In addition, a quadrupole/octupole transition with a large mixing ratio would be unlikely [End 79]. Therefore, the spin of the level at 2296 keV is tentatively assigned as $I = 5$. This is consistent with the DCO ratio of the 1316 keV transition (the experimental DCO ratio is 0.95(18) compared with a theoretical DCO ratio of 0.99) and also with the observed angular distribution and DCO ratio of the 724 keV transition (fig. 4.19 and table 4.1) both of which suggest that the 724 keV transition is a stretched quadrupole transition. Finally, the size of the mixing ratio of the 1316 keV transition ($\delta = +0.38(6)$; extracted from the χ^2 analysis) and the roughly equal branching between the 1316 keV (predominantly stretched dipole) and the 724 keV (stretched quadrupole) transitions suggest that the parity of the 2296 keV level is the same as that of the 1571 keV level and the GSB. Therefore, tentative assignments are made of $I^\pi = 5^+$ to the level at 2296 keV and positive parity to the other members of SB2.

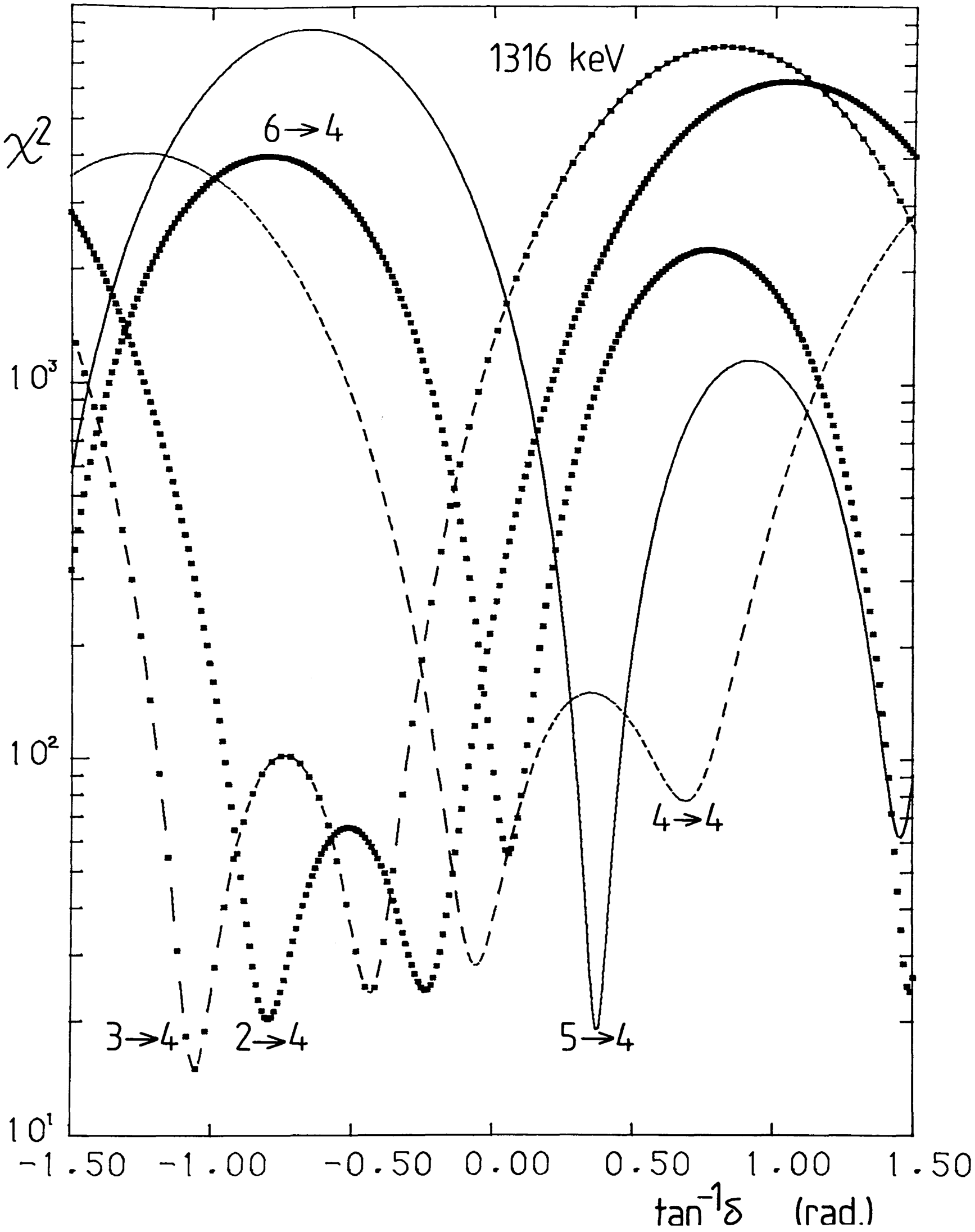


Figure 4.21 χ^2 analyses of the angular distribution of the 1316 keV SB2 γ-ray as a function of multipole mixing ratio δ for various spin hypotheses for the 2296 keV level. (See sect. 4.5.3 for discussion.) There are 8 degrees of freedom. This particular plot is for a substate Gaussian width of $\sigma/I = 0.40$ and a γ-ray intensity determined from a Legendre Polynomial fit to the 1316 keV γ-ray's angular distribution (fig 4.19). However, in determining the errors associated with the multipole mixing ratio, the uncertainties in both σ/I and the γ-ray intensity were taken into account.

4.6 Sideband 3

As with SB2, nearly all of the coincidences implied by the suggested level scheme have been observed (table 4.6). The coincidence data on this sideband are illustrated by the γ-γ coincidence spectra of the 1343 and 1035 keV transitions (fig. 4.22) and also the coincidence spectrum of the 386 keV $2^+ \rightarrow 0^+$ GSB transition (fig. 4.3). In addition, the DSAM lifetime data and the angular distribution data for SB3 are shown alongside those of SB2 in figs. 4.18 and 4.19, respectively.

The ordering of the SB3 transitions, as with the other sidebands, was determined from the γ-ray intensities and centroid Doppler shifts. As with SB2, the order of lower members of SB3 was determined from their γ-ray centroid Doppler shifts. Also, as in SB2, there is some evidence for low intensity unobserved feeding out of SB3, possibly into the GSB or SB2. It is emphasized that this possible feeding out of SB3 is of the order of $\sim 1\%$ of the total decay intensity and is at or below the limit of sensitivity of the present experimental data.

The angular distributions of the 662 and 867 keV γ-rays and the DCO ratios of the 662, 867, 1035 and 1198 keV transitions are all consistent with stretched $E2$ transitions (fig. 4.19 and table 4.1). $E2$ multipolarity assignments are also consistent with the strengths of the 662, 867 and 1035 keV transitions (table 4.2). Unfortunately, a reliable measurement of the angular distribution of the 1343 keV γ-ray could not be obtained, because of Doppler broadening of both the 1343 keV γ-ray and other close lying γ-rays. Therefore, it was not possible to assign a spin or suggest a parity for the 3639 keV level. Similarly, it was not possible to measure the lifetime of the 3639 keV level although the DSAM spectra

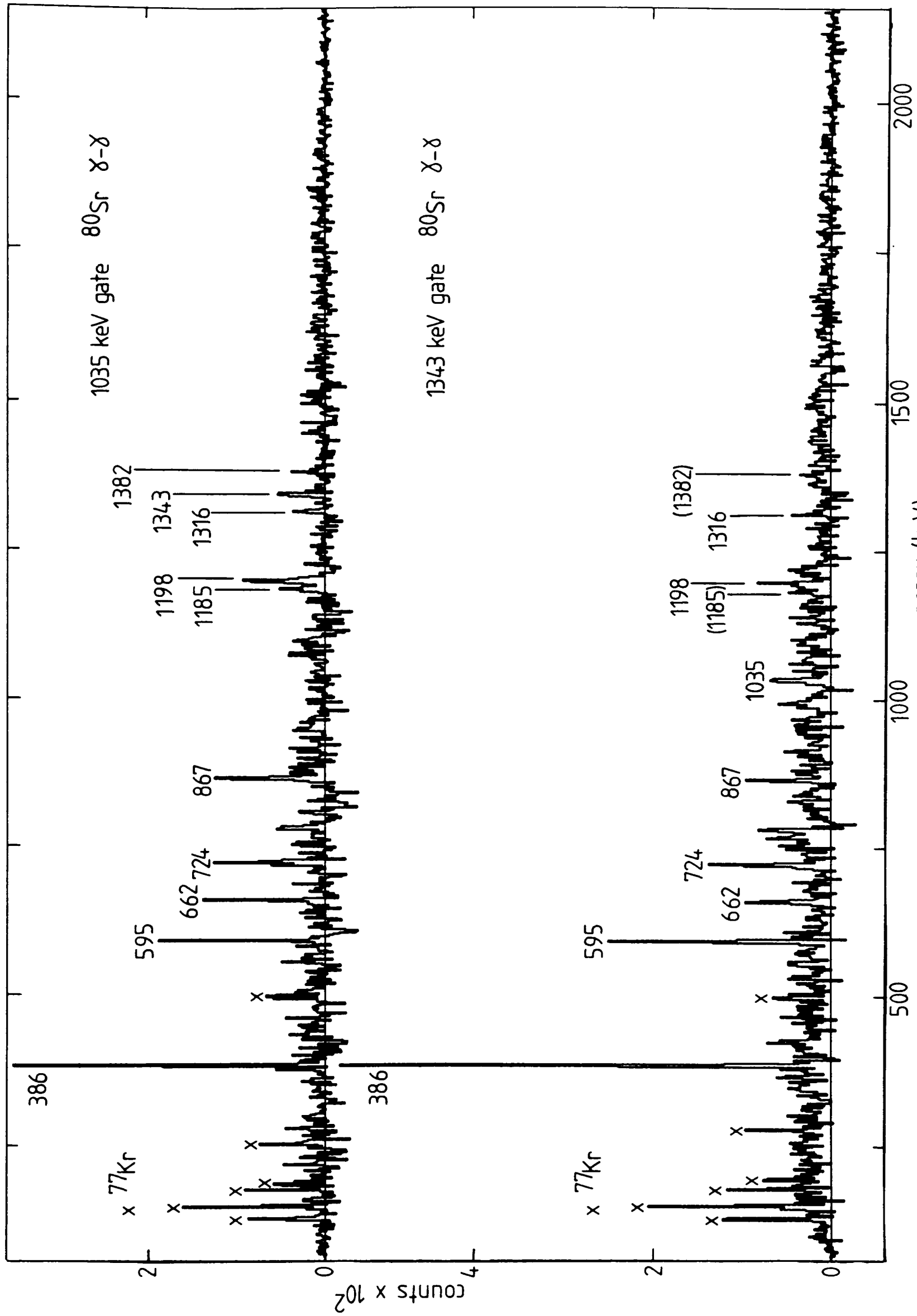


Figure 4.22 Thin target γ-γ coincidence spectra gated by the 1035 and 1343 keV SB3 γ-rays, illustrating SB3. (See sect. 4.6 for details.)

indicated that the lineshape was considerably Doppler broadened which suggests a short lifetime ($\tau \ll 1$ ps).

4.7 Unplaced Transitions

In addition to the transitions placed within the ^{80}Sr level scheme, there are two unplaced transitions with energies of 885 and 1547 keV. Both of these transitions had very low intensities, relative to other transitions placed in ^{80}Sr with similar energies. Therefore, the statistical quality of their coincidence spectra was not good enough to determine their position within the level scheme. Interpretation of their coincidence spectra was further hampered by strong contamination from ^{77}Kr. Both the 885 and the 1547 keV γ-rays showed coincidences only with the first three members of the ^{80}Sr GSB. It is possible that coincidences with other transitions placed within the level scheme were masked by the poor quality of the coincidence spectra. However, there was no clear evidence from the coincidence spectra of the other ^{80}Sr transitions for the existence of such coincidences. There is no evidence to suggest that these two transitions are members of the GSB or any of the three identified sidebands. Therefore, the most likely interpretation of these γ-rays is that they represent transitions feeding into the GSB from levels not identified in the present study.

CHAPTER 5

DISCUSSION

5.1 Introduction

The large $E2$ transition rates ($\sim$ 90 Weisskopf units (wu)) and the energy systematics of the four bands observed in the present study of ^{80}Sr are characteristic of collective rotation of intrinsic states with large quadrupole deformation. However, the moments of inertia of the ground state band (fig. 5.1) vary with rotational frequency, indicating that the nucleus is not behaving as a rigid rotor. The transition electric quadrupole moments, Q_0, of the states in the GSB were calculated, assuming a quadrupole deformation, using the simple rotational formula

$$\mathrm{B}(E2) = \frac{5}{16\pi} Q_0^2 (IK20|I-2K)^2 \tag{5.1}$$

The results are given in fig. 5.2, and are consistent with the interpretation of a constant quadrupole moment of ($\pm$)2.8(1) eb. The study of the multipole mixing ratios of the in-band $M1/E2$ transitions in the neighbouring isotope ^{79}Sr by Lister *et al.* [Lis 82] suggests that these light Sr isotopes have positive ground state band quadrupole moments. (A positive quadrupole moment corresponds to prolate deformation, as opposed to an oblate one.) Therefore, a positive sign for Q_0 will be assumed in the following discussion. A quadrupole moment of this magnitude corresponds to a deformation parameter of $\beta_2 =$ 0.34(1) for the GSB, assuming axial symmetry. Because the K quantum numbers of the other bands are unknown, quadrupole moments were not calculated for the three sidebands. However, the $E2$ transition rates in these bands are similar to those in the GSB, suggesting

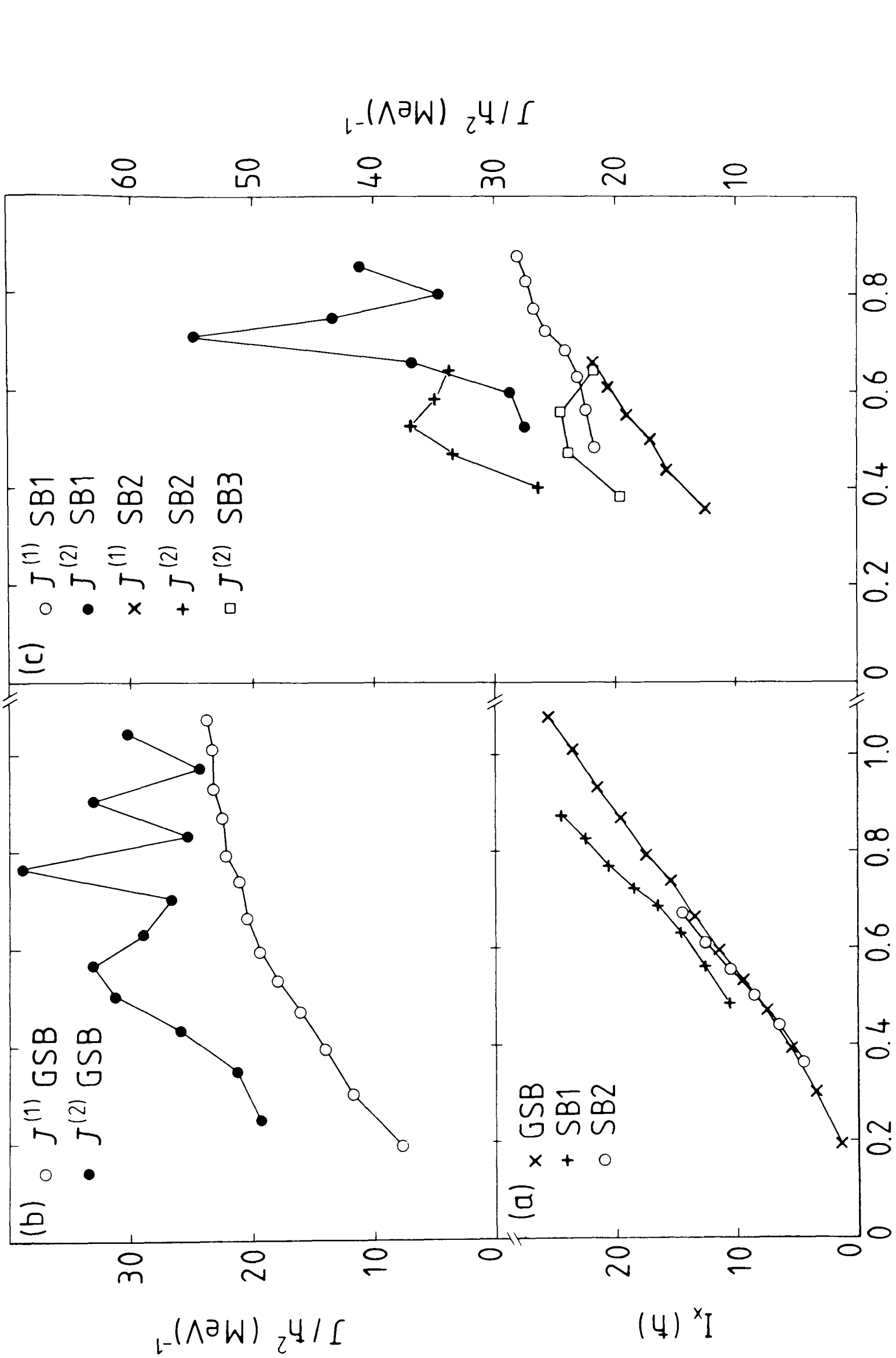


Figure 5.1 The component of angular momentum along the rotational axis (a) and the moments of inertia, $J^{(1)}$ and $J^{(2)}$, as a function of rotational frequency for the ground state band (b) and the sidebands (c) in ^{80}Sr. (As spins have not been assigned to SB3, it was possible to extract $J^{(2)}$ for this sideband but not I_x or $J^{(1)}$. $K = 0$ has been used in calculating the moments of inertia of the sidebands. The principal effect of $K \neq 0$ would be to reduce I_x, thus further lowering $J^{(1)}$ relative to $J^{(2)}$.)

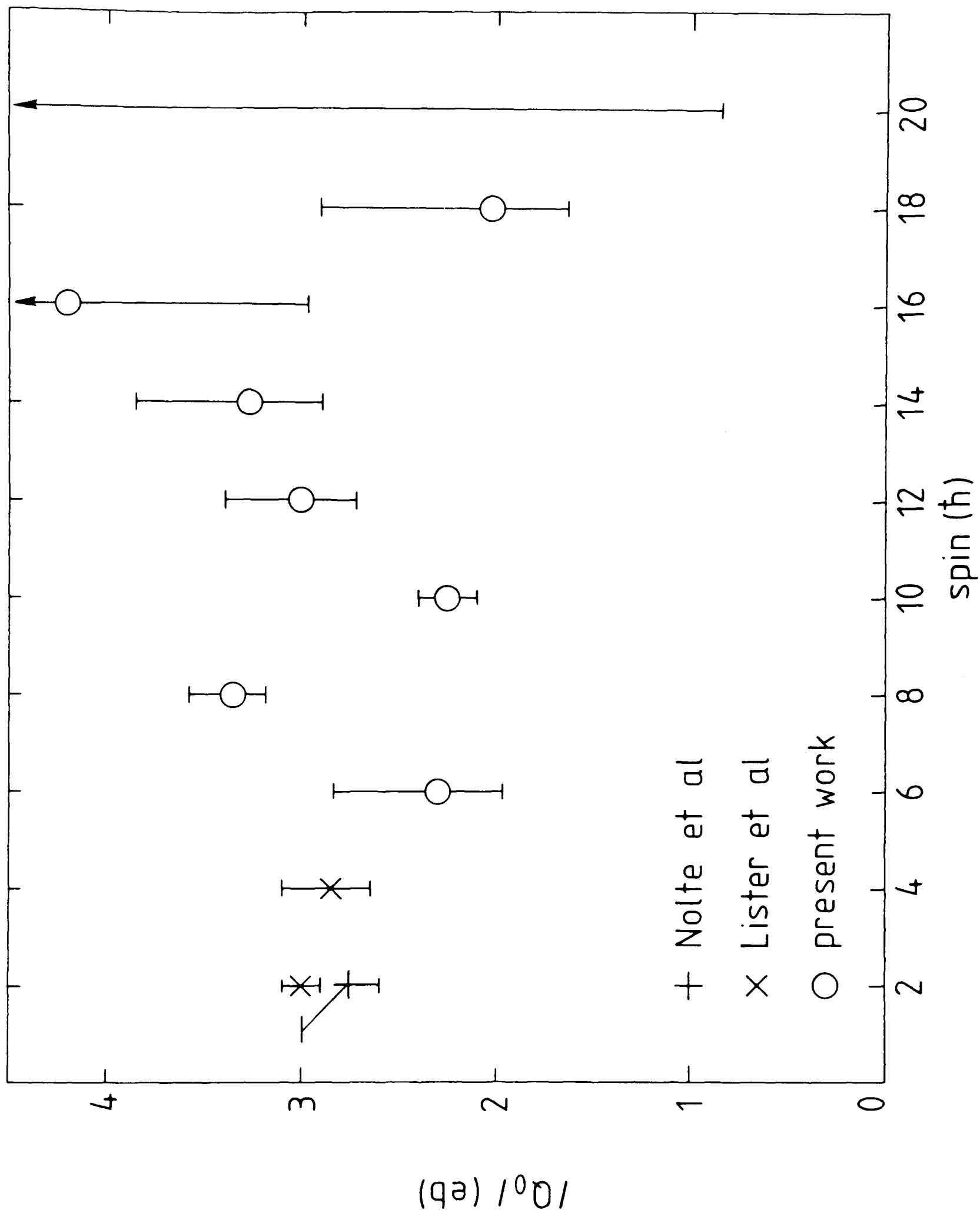


Figure 5.2 Absolute values of the transition quadrupole moment in the ^{80}Sr ground state band as a function of spin, taken from the present work and the lifetime measurements of [Nol 74, Lis 82]. (When comparing the quadrupole moments (lifetimes) quoted for adjacent levels from the present study, it should be recalled that the feeding correction for a level is derived from τ_{eff} of the preceding transition. Therefore, these measurements are not entirely independent.)

that they have similar deformations. This large prolate deformation observed in ^{80}Sr, and in the neighbouring Sr isotopes, was first investigated in detail by Lister *et al.* [Lis 82].

The ^{80}Sr level scheme exhibits several interesting and unusual phenomena. Firstly, the $J^{(2)}$ moment of inertia is larger than the $J^{(1)}$ moment of inertia of the GSB, and two of the sidebands, over the full range of angular frequencies observed (fig. 5.1). This feature, which is also seen in several neighbouring nuclei, is possibly related to the softness of the nuclear shape to deformation in the γ degree of freedom. Secondly, the staggering in the transition energies of the states high in the GSB, which is of the order of $\pm$20 keV and is most easily seen in the $J^{(2)}$ moment of inertia (fig. 5.1), is a very unusual feature. Finally, ~~and~~ the splitting of the decay intensity in SB1 between the two close lying 7^+ states and their subsequent decay to the 6^+ GSB level is also very unusual. In the following sections the ^{80}Sr level scheme is discussed and compared with the predictions of the cranking model, TPE surface calculations and IBM-2 calculations.

5.2 The 3601 and 3580 keV 7^+ States

The splitting of the decay intensity of SB1 between the two close lying 7^+ states and the subsequent decay of these levels to the 6^+ GSB level are very unusual features. The two $9^+ \rightarrow 7^+$ transition energies are very similar to that expected for the $9^+ \rightarrow 7^+$ transition in SB1 from a simple extrapolation of the energy systematics of the band ($\sim$ 810 keV). This similarity of the level energies, in addition to the large transition rates for the two transitions ($50(^{110}_{30})$ wu and $50(^{100}_{30})$ wu for the 777 and 798 keV transitions, respectively) and the roughly equal branching to the two 7^+ states, suggests that the amplitude for the collective state is shared between the two 7^+ states. Such a splitting of the collective

state between the two levels could occur if the collective member of SB1 was mixed with another close lying 7^+ state [Dav 76]. Such mixing would tend to increase the energy difference between the two levels. As the energy separation between the two observed 7^+ levels is only 21 keV, the maximum interaction strength is only 10.5 keV. However, the 7^+ member of SB1 would be shared with roughly equal amplitudes between the two observed 7^+ states provided the separation of the unperturbed levels was $\ll$ 10 keV. Furthermore, the decays of these two 7^+ states to the 6^+ state in the GSB are also very unusual. In particular, these transitions are predominantly $E2$ (the multipole mixing ratios of the 1817 and 1838 keV transitions are $-4.7(15)$ and $-2.8(4)$, respectively) and have long mean lives ($\tau \geq 30(27)$ ps).

5.3 Comparison with Cranked Shell Model Calculations

Extensive microscopic calculations for ^{80}Sr, using a shell correction approach and the cranking model, have been carried out by Nazarewicz *et al.* [Naz 85]. These calculations predict that the TPE surface of the ^{80}Sr ground state will have a soft prolate minimum with deformation $(\beta_2, \gamma) \simeq (0.36, 0°)$, and secondary minima for both spherical and oblate shapes. The excited states lying closest to the yrast line with spins below $I \simeq 18\hbar$ are predicted to be collective rotations of a prolate shape with $(\beta_2, \gamma) \simeq (0.36, 0°)$, while above $I \sim 18\hbar$ both collective and non-collective excitations of an oblate shape are predicted to dominate.

The theoretical predictions of both the deformation parameter, β_2, and the collective nature of the ground state band below $I = 16\hbar$ are in good agreement with experiment. However, the $2^+ \rightarrow 0^+$ transition energy is underestimated by theory. It is suggested by

Nazarewicz *et al.* that this discrepancy is possibly due to a repulsive interaction between the ground state and a low lying 0^+ state(s) corresponding to the secondary oblate or (and) spherical minima in the $\hbar\omega = 0$ TPE surface. One such low lying 0^+ state has been observed at 1.00 MeV in ^{80}Sr in a study of the ^{78}Kr(^{3}He, n) reaction [Alf 79]. (A similar mechanism has been proposed [Hami 85] to explain the large $2^+ \rightarrow 0^+$ transition energies in ^{74,76}Kr.) The broad peak centred about $\hbar\omega \simeq 0.55$ MeV in the $J^{(2)}$ moment of inertia of the ground state band (fig. 5.1) is attributed to the slow alignment of a pair of $g_{9/2}$ protons, predicted to occur at this frequency (fig. 5.3). The slow alignment of a pair of $g_{9/2}$ neutrons is predicted, in these calculations [Naz 85], to occur at the somewhat higher frequency of $\hbar\omega \simeq 0.8$ MeV (fig. 5.3). No clear indication of this slow alignment of the neutron pair is evident in the data. However, the sharp peak in the $J^{(2)}$ moment of inertia (fig. 5.1) that occurs at a frequency just below $\hbar\omega \simeq 0.8$ MeV may possibly be due to this alignment; although, the sharpness of this structure, compared with the broad bump associated with the proton pair alignment, casts considerable doubt on this interpretation.

The theoretical predictions of Nazarewicz *et al.* for spins greater than $I \simeq 18\hbar$ are less successful. Although the experimental level scheme above $I = 20\hbar$ is somewhat tentative, there is no evidence, from either the energy systematics (figs. 4.1 and 5.1) or the feeding times and transition rates (sect. 4.3 and fig. 5.2), for the predicted change in nuclear shape from prolate to oblate. In particular, the absence of a stopped component in the DSAM γ-ray lineshape of the 1324 keV $14^+ \rightarrow 12^+$ GSB transition limits the intensity of slow feeding through the 14^+ GSB state, which could be associated with a major change in the nuclear structure, to less than 10% of the intensity of this transition. Similarly,

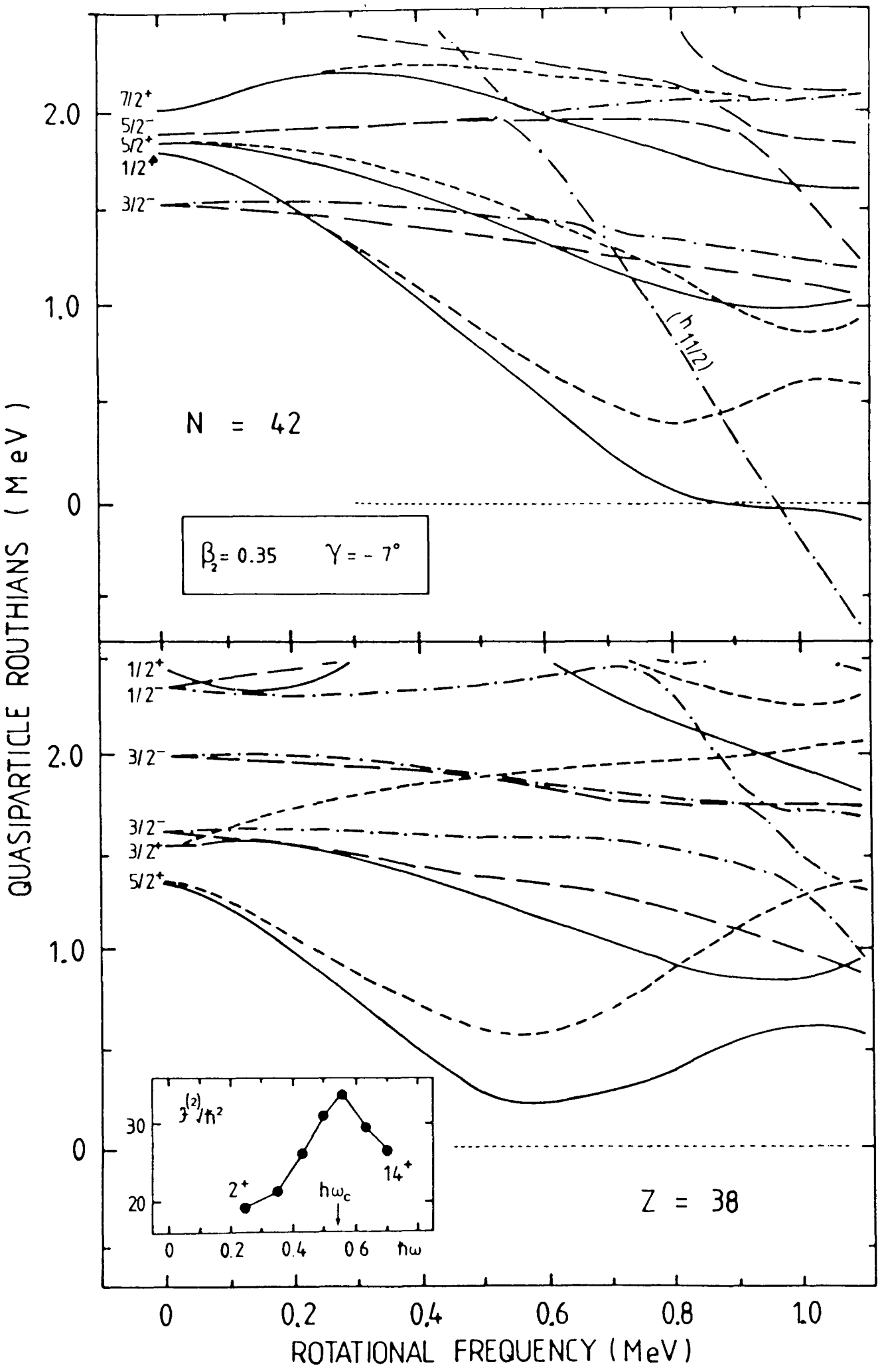


Figure 5.3 Quasiparticle Routhians for the neutrons (top) and protons (bottom) in ^{80}Sr, taken from the cranking model calculations of Nazarewicz *et al.* [Naz 85]. This figure illustrates the predicted alignment of pairs of $g_{9/2}$ protons and neutrons at $\hbar\omega \simeq 0.55$ and 0.8 MeV, respectively. The inset shows the $J^{(2)}$ moment of inertia of the ^{80}Sr GSB as a function of ω to allow easy comparison.

the observed centroid shift of the 1738 keV transition limits the intensity of slow feeding through the 20^+ GSB state to less than 30% of the intensity of the 1738 keV transition. (Limits on slow feeding into the GSB are discussed in sect. 4.3.) It is unlikely that the staggering in the γ-ray energies which starts at $I = 18\hbar$ represents such a dramatic change in the nuclear structure. However, this very unusual energy staggering (which is most clearly seen in the $J^{(2)}$ moment of inertia shown in fig. 5.1) remains unexplained.

Although the $J^{(2)}$ moments of inertia of the sidebands are observed over a relatively small range of angular frequencies (fig. 5.1) making their interpretation difficult, they do exhibit structural features which it is possible to tentatively interpret in terms of particle alignments, as is done above for the GSB. The peak of the SB2 $J^{(2)}$ is at a similar frequency ($\hbar\omega \simeq 0.55$ MeV) to the broad peak observed in the GSB $J^{(2)}$, which has been associated [Naz 85] with the alignment of a pair of $g_{9/2}$ protons (see fig. 5.3). This suggests that SB2 also exhibits proton alignment and, therefore, that SB2 corresponds to an excited neutron configuration. (Neutron excitations do not affect proton alignment. However, a low lying proton excitation would block this proton alignment.) Similarly, the $J^{(2)}$ of SB3 shows a broad hump at $\hbar\omega \simeq 0.55$ MeV, suggesting that this may also correspond to an excited neutron configuration. In contrast, the $J^{(2)}$ moment of inertia of SB1 exhibits a peak at the higher rotational frequency of $\hbar\omega \simeq 0.70$ MeV, which is close to the frequency at which the alignment of a pair of $g_{9/2}$ neutrons is predicted ($\hbar\omega \simeq 0.8$ MeV [Naz 85]), while no structure is observed at lower frequencies. This suggests that SB1 exhibits neutron alignment, but not proton alignment. Therefore, SB1 may be interpreted as having a proton excited intrinsic structure.

It is stressed that this association of neutron and proton excited intrinsic states with the sidebands is both tentative and qualitative. In addition, the assumption that the nuclear shape in the sidebands is the same as that of the GSB is implicit in the above discussion. (The excited particle states near the Fermi surface, which are responsible for the alignments, depend upon the nuclear deformation.) The shape coexistence phenomena that occur in this region make this assumption particularly questionable. In particular, collective excitations of an oblate shape are predicted in cranking model calculations to lie close to the yrast line even at low spin [Naz 85]. Furthermore, the possible association of particle alignments with the various sidebands does not exclude the possibility of collective, rather than excited particle, intrinsic states.

In order to further investigate the possible role of excited neutron and proton configurations in ^{80}Sr, it would be necessary to study the sidebands experimentally over a wider range of angular frequencies, to clarify the behaviour of $J^{(2)}$, and to make a detailed comparison between theoretical predictions for particular excited configurations and the experimental data. Unfortunately, a detailed comparison between the cranking model calculations and the experimental data for ^{80}Sr is difficult (if not impossible). This is because the energy levels in the cranking model (which are called 'quasiparticle routhians'; see, for example fig. 5.3 and sect. 2.3) are calculated in the intrinsic frame of the rotating nucleus as a function of angular frequency and are given relative to a reference energy (which is also a function of angular frequency) that corresponds to pure collective rotation of the even-even core (without particle alignments). As the particle alignments in ^{80}Sr are predicted by the cranking model calculations to take place over most of the observed range

of frequencies, the GSB is not predicted to exhibit pure collective rotation. Therefore, it was not possible to extract an experimental set of reference energies from the ^{80}Sr GSB. In such situations it is often possible to extract reference energies from the ground state band of a neighbouring odd nucleus in which particle alignments are blocked by the odd particle(s), if it is assumed that the collective properties of the core of this neighbouring nucleus are close to that of the nucleus of interest. However, in the N$\sim$Z$\sim$ 40 region the collective properties change rapidly as a function of particle number, so that it was not possible to extract suitable reference energies for the ^{80}Sr core from the neighbouring nuclei (although this possibility was investigated).

5.4 The $J^{(1)}$ and $J^{(2)}$ Moments of Inertia in ^{80}Sr and the Light Sr Isotopes

5.4.1 INTRODUCTION

In the preceding section the structures observed in the $J^{(2)}$ moments of inertia were discussed. In this section the large scale systematic behaviour of $J^{(2)}$, particularly with respect to the $J^{(1)}$ moment of inertia, will be detailed. Theoretical calculations [Hama 84, Hama 85] for triaxial nuclei have shown that $J^{(2)}$ can be systematically larger than $J^{(1)}$ if the rotational motion of the triaxial body is correctly treated. In particular, rotations about all three principal axes were found to be important. More recent calculations [Oni 86] have shown that such effects are also important for axially symmetric nuclei which are soft to γ-deformations, both because of quantum fluctuations in the γ degree of freedom and because of favouring of $\gamma = -30°$ due to its higher moment of inertia. (Strictly, the nucleus must be soft to deformations with $\gamma < 0$ in the Lund cranking model convention.)

These fluctuations in the γ degree of freedom were shown to be important for axially symmetric nuclei even when the energy associated with deforming the nucleus from the axially symmetric $\gamma = 0°$ to $\gamma = -30°$ was as high as five times the energy of the first excited state of the unperturbed (purely $\gamma = 0°$) Hamiltonian. Such behaviour is not usually predicted within the framework of the cranking model, for which $J^{(1)} \simeq J^{(2)}$ at low frequencies and $J^{(1)} \sim J^{(2)} + i_x/\omega > J^{(2)}$ following an alignment of angular momentum i_x with the rotational axis, except in the backbending region (as discussed above).

Total Potential Energy (TPE) surface calculations [Buc 83, Naz 85, Bon 85] (fig. 5.4) predict that ^{80}Sr is soft to γ-deformations (the degree of γ-softness depending upon the details of the particular calculation) and that this softness should persist [Naz 85] (fig. 5.5) to the highest spins observed. One calculation [Bon 85] even predicts that ^{80}Sr may be triaxial in its ground state. These calculations also indicate that the softness to γ-deformations should increase along the ^{78,80,82}Sr isotope chain, as the TPE surface is dominated first by the prolate shell gap at N=38 in the lighter isotopes and then by the spherical shell gap at N=50.

5.4.2 ^{80}Sr

In view of the TPE surface calculations showing that ^{80}Sr should exhibit some softness to γ-deformations and the recent theoretical predictions for the behaviour of such nuclei, it is interesting to study the moments of inertia in ^{80}Sr in order to test these predictions. A plot of the component of the GSB angular momentum along the rotational axis, I_x, as a function of rotational frequency, ω, yields a negative value of I_x if extrapolated to $\omega = 0$ (fig. 5.1). Therefore, $J^{(2)}$ is systematically larger than $J^{(1)}$ in the GSB throughout the

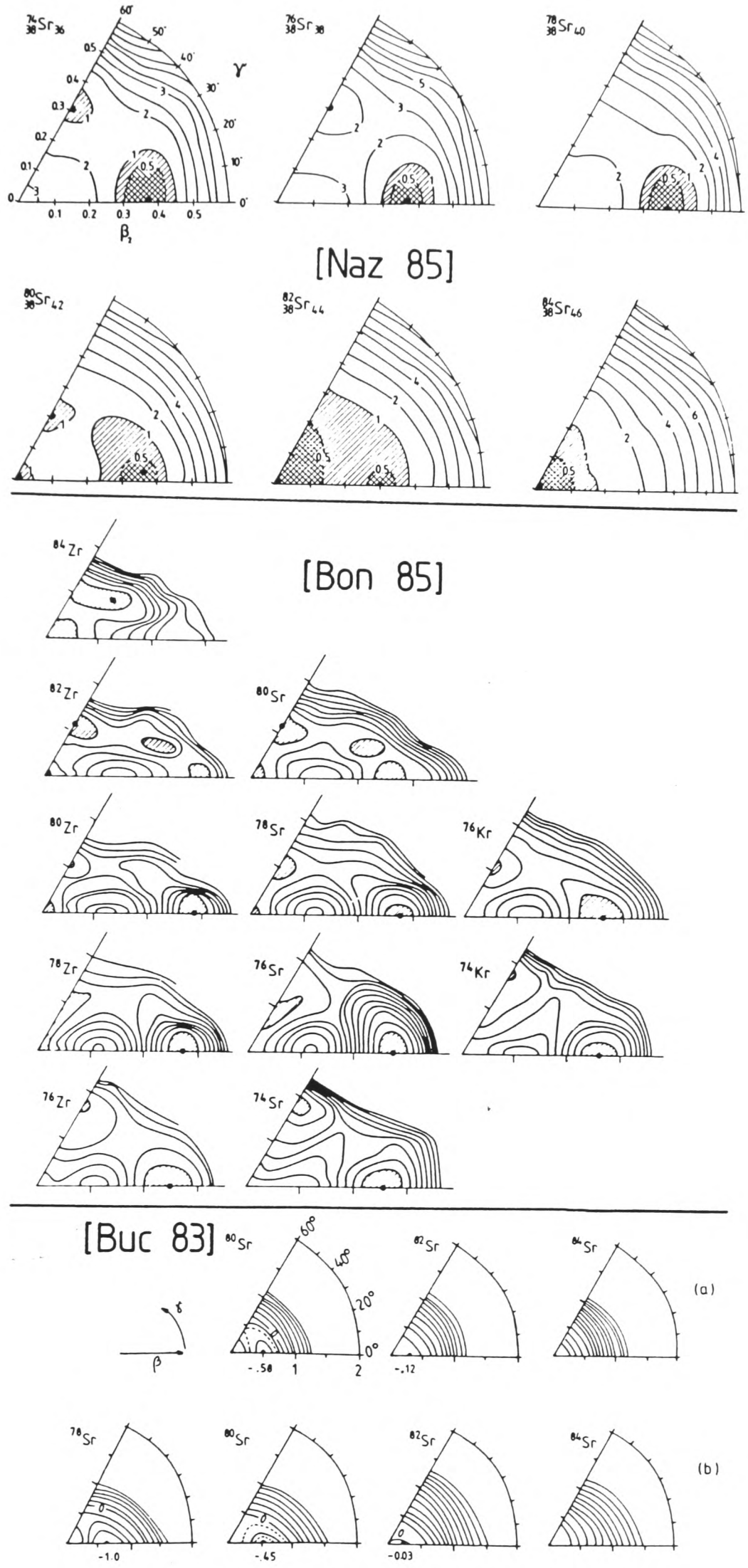


Figure 5.4 TPE surface calculations taken (from top to bottom) from [Naz 85], [Bon 85] and [Buc 83], based on the Strutinsky shell correction method, the Hartree-Fock self-consistent method and the IBM, respectively. (See the original works for details.) The contour lines in the top TPE surface calculations represent changes of 1 MeV, while those in the middle and bottom TPE surfaces represent changes of 0.5 and 0.25 MeV, respectively.

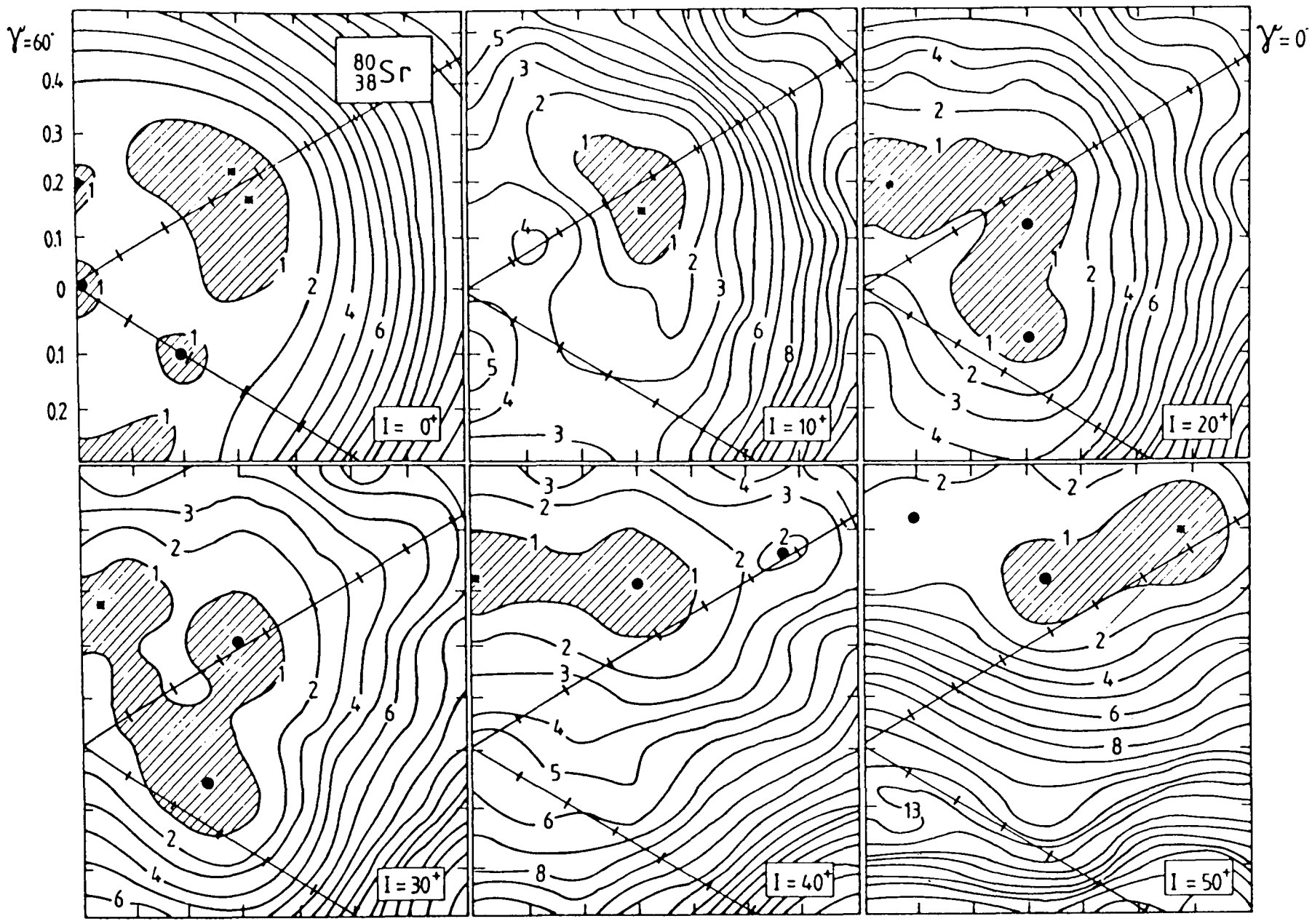


Figure 5.5 TPE surface calculations for ^{80}Sr as a function of spin taken from the work of Nazarewicz *et al.* The contour lines refer to the energy in MeV above the absolute minimum, which is indicated by an asterisk. The positions of secondary minima are indicated by black dots. See [Naz 85] for further details.

observed range of frequencies (fig. 5.1), since $J^{(1)} = I_x/\omega$ whereas $J^{(2)} = dI_x/d\omega$. The systematic behaviour of the moments of inertia is in good agreement with the calculations of Onishi *et al.* [Oni 86] for γ-soft or triaxial nuclei, while the structure in the moments of inertia can be interpreted in terms of particle alignments predicted in cranking model calculations [Naz 85] (see sect. 5.3). Hence, the ^{80}Sr GSB moments of inertia are interpreted as indicating that the nucleus exhibits either static or dynamic γ-deformation throughout the observed range of angular frequencies, possibly becoming triaxial in the higher spin states due to the favouring of $\gamma = -30°$. This is in good agreement with the TPE surface calculations. Such an interpretation is consistent with the observation that ^{80}Sr maintains an approximately constant quadrupole moment throughout the GSB (fig. 5.2), since the γ-soft model [Oni 86] predicts that the strengths of the $\Delta I = 2$ quadrupole transitions should remain close to those predicted for an axially symmetric rotor.

In contrast with the GSB, the ^{80}Sr sidebands are observed over a relatively small range of angular frequencies, making interpretation of their moments of inertia (fig. 5.1) more difficult. (For example, the moment of inertia of a band can be distorted by particle alignment over a range of angular frequencies, as discussed above). However, the moments of inertia of SB1 and SB2 also have $J^{(1)} < J^{(2)}$ suggesting that the deformation properties of these sidebands are qualitatively similar to those of the GSB, although SB1 attains a slightly higher value of $J^{(1)}$ than observed in the GSB. This is in agreement with the similarity between the transition rates in sidebands and the ground state band (table 4.2), which suggests that these bands have quadrupole moments of similar magnitude. The $J^{(2)}$ moment of inertia of SB3 is interesting, as it has a similar shape to that of the $J^{(2)}$ of the

GSB and SB2 (as discussed in sect. 5.3) although it is reduced in magnitude by $\sim$ 30% relative to these other two bands. This reduction in $J^{(2)}$ observed in SB3 may represent a reduction of γ-softness in this band. However, it is difficult to draw a definite conclusion, as in the absence of spin assignments for SB3, the $J^{(1)}$ moment of inertia for this band is unknown.

5.4.3 THE LIGHT Sr ISOTOPES

As indicated in Chapter 1, the changes in the nuclear properties which occur as a function of neutron number in the light Sr isotopes are complex. In particular, there is a transformation [Lis 82, Fie 81, Fie 83] from rotational excitations of a deformed prolate shape near N=38 to vibrational and single particle excitations near N=50. This transformation is reflected in the increasing excitation energies of the first excited 2^+ states and their decreasing decay strengths to the ground state with increasing neutron number (fig. 5.6). However, even though changes occuring in the TPE surface are coupled to changes in the dominant modes of excitation, it is interesting to observe the behaviour of the $J^{(1)}$ and $J^{(2)}$ moments of inertia as a function of neutron number in the transitional region. At low angular frequencies $J^{(1)}$ is found to systematically decrease with respect to $J^{(2)}$ (which remains roughly constant) as successive neutron pairs are added, as can be seen from fig. 5.7 which gives the I_x vs ω plots for ^{78,80,82,84}Sr. Also, the systematics of the ratio of the 2_2^+ to 4_1^+ level energies (fig. 5.7), which is a measure of stiffness to γ-deformation [Oni 86], indicates increasing γ-softness as neutron pairs are added. This can be qualitatively understood as increasing γ-softness as the nuclei move away from the prolate shell gap at N=38 and towards the spherical shell gap at N=50 and is in agreement

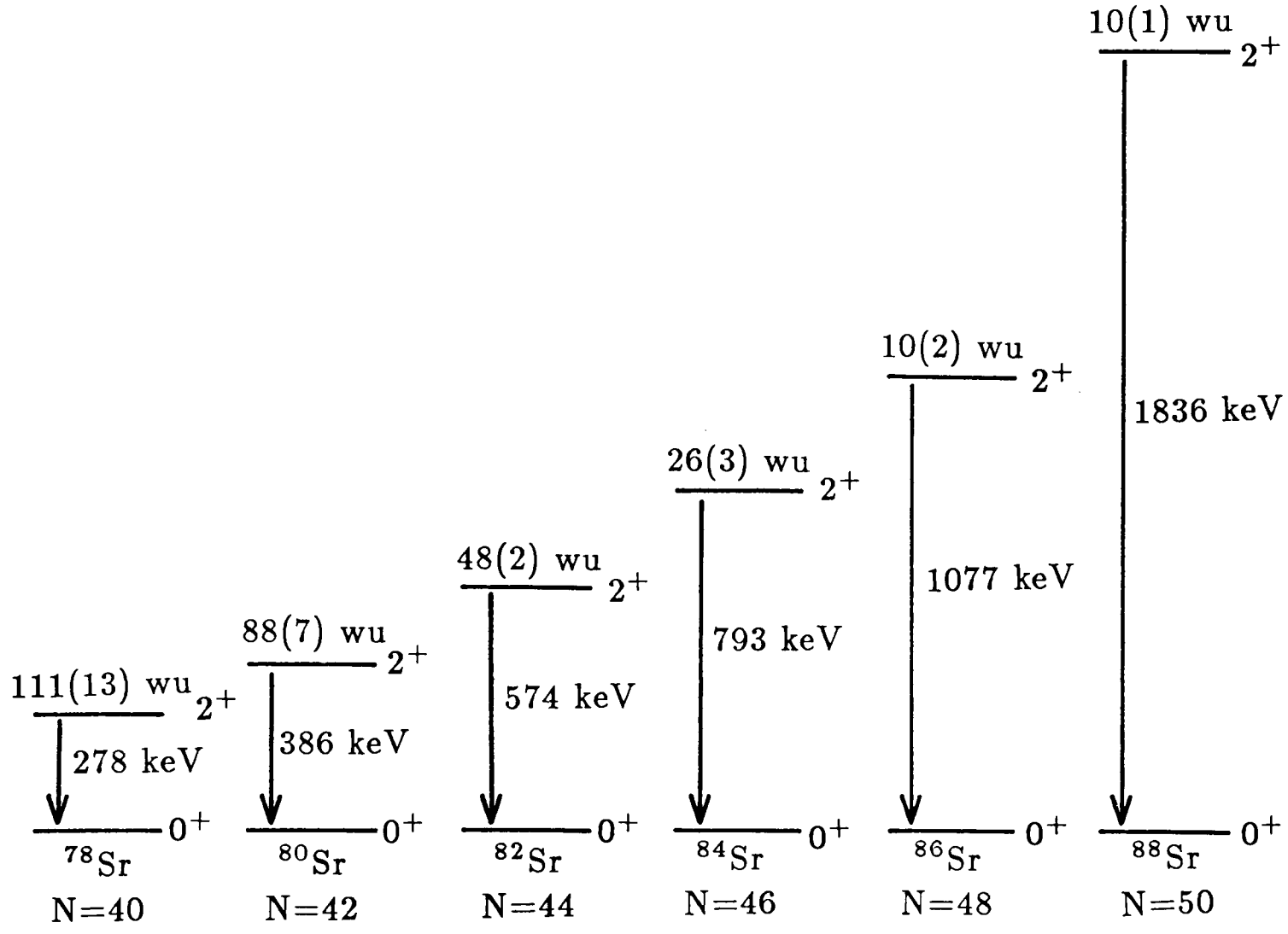


Figure 5.6 Energies and decay strengths of the first excited states of the neutron deficient even Sr isotopes. Experimental data were taken from [Lis 82, Dew 81, Dew 82, Sym 64, Bun 76].

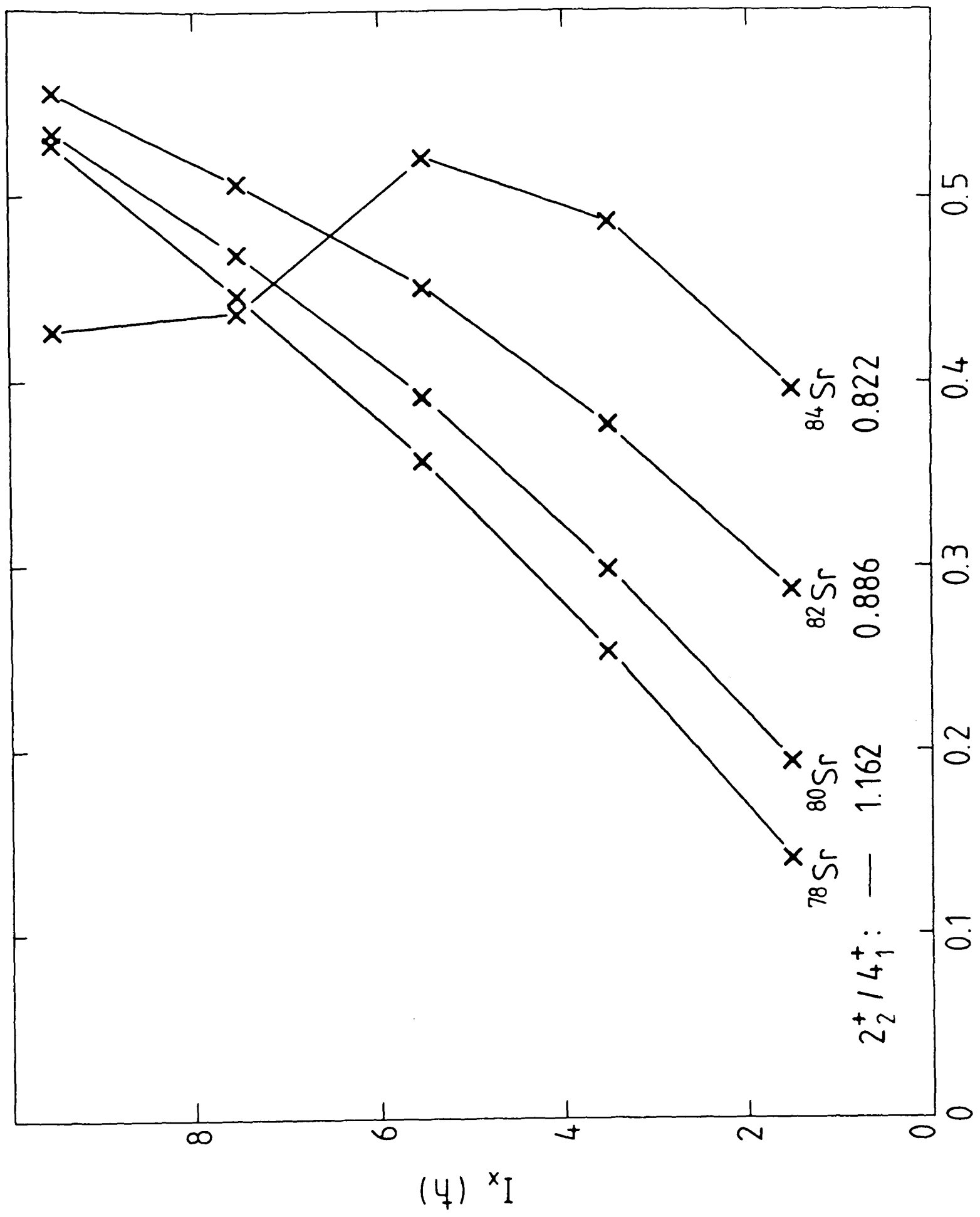


Figure 5.7 I_x vs ω plots for the ground state bands and the $2_2^+/4_1^+$ ratios in ^{78,80,82,84}Sr. (For a nucleus exhibiting rotational motion of a rigid prolate (or oblate) shape the plot would pass through the origin, if extrapolated to $\omega = 0$. ^{84}Sr shows the effect of particle alignment at $\omega \sim 0.5\hbar$.) Experimental data were taken from [Lis 82, Dew 81, Dew 82].

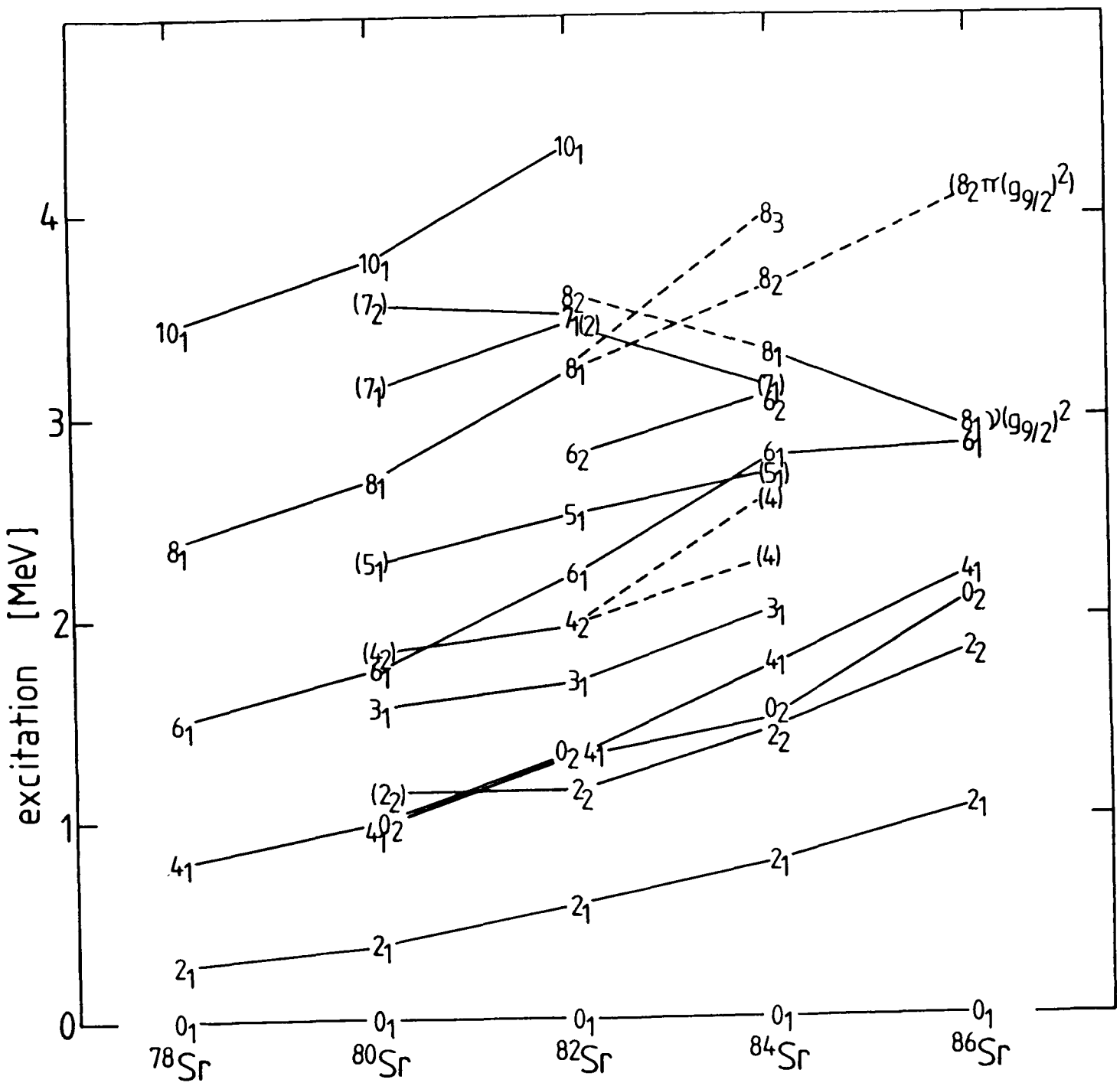


Figure 5.8 Experimental systematics of the positive parity excited states in the neutron deficient even Sr isotopes. The level energies are indicated by small numbers corresponding to the level spin. The experimental data were taken from [Alf 79, Bal 73, Dew 81, Dew 82, Fie 83, Has 85, Lis 81, Lis 82] as well as from the present study.

with the trends predicted by the TPE surface calculations. This systematic behaviour is also illustrated by fig. 5.8, which shows the systematics of the known low lying even parity levels in ^{78,80,82,84,86}Sr. As the neutron number increases from N=42, the $2_2, 3_1, 4_2$ and 5_1 states, which can be associated with either static or dynamic γ-deformation [Boh 52, Boh 53, Boh 75, Dav 58, Oni 86], decrease in excitation energy relative to the $2_1, 4_1, 6_1$ and 8_1 levels, which are the rotational states in an axially deformed nucleus. The 2_2 reaches its absolute minimum excitation energy in ^{82}Sr, which is midway between the deformed and spherical closed shells at N=38 and N=50, respectively. The value of the experimental $2_2^+/4_1^+$ energy ratio, which is within 20% of unity, is a further indication that softness to γ-deformation is a general feature of these isotopes. The situation at the higher spins in the heavier Sr isotopes is unclear, because of the effects of particle alignments on the moments of inertia. However, in ^{78}Sr $J^{(1)}$ remains smaller than $J^{(2)}$ over the limited range of spins known ($I \leq 10\hbar$).

5.5 Comparison with IBM-2 Calculations

5.5.1 INTRODUCTION

Comprehensive IBM-2 calculations have recently been carried out for the neutron deficient even Sr isotopes [Hey 84]. However, in light of the new experimental data resulting from the present study of ^{80}Sr, it was decided to perform a revised IBM-2 calculation for these isotopes. It was hoped that this new IBM-2 study would aid in the identification of bands built on collective excitations of the ^{80}Sr core, and also that discrepancies between the experimental and theoretical transition rates, which were present in the work of Heyde

et al. [Hey 84], could be resolved.

In the earlier IBM-2 study of Heyde *et al.* the number of proton bosons N_π was calculated with respect to the full spherical proton shell (Z= 28 – 50) yielding $N_\pi = 5$. However, the IBM-2 study of the neutron rich Mo nuclei (Z=42) [Sam 82] showed that the spherical subshell gap at Z=40 plays an important role in nuclei in this region. Indeed, although not included explicitly in the calculations of Heyde *et al.*, the presence of this subshell gap is reflected implicitly in them by the behaviour of the χ_π parameter of the IBM-2 quadrupole operator. Explicit inclusion of this subshell gap in the proton shell would reduce the number of proton bosons; thus reducing the transition rates, which were found to be too large in the earlier IBM-2 calculations of the Sr isotopes ([Hey 84], see also below).

The number of proton bosons in the Sr nuclei, with respect to the Z=40 subshell gap, is $N_\pi = 1$. However, 2p-2h excitations across this subshell gap (corresponding to the creation of an extra pair of bosons) were found to be important in the IBM-2 study of the Mo (Z=42) isotopes carried out by Sambataro and Molnár [Sam 82]. In particular, it was found that proton pair excitation across the Z=40 subshell gap became important as the number of neutron bosons was increased. Thus, with five neutron bosons the configuration with three proton bosons was found to be dominant. The importance of two configurations with different numbers of proton bosons in these isotopes corresponds to the coexistence of two different shapes. The configuration with no excitations across the subshell gap exhibits a vibrator-like spectrum, while the configuration corresponding to excitation across the subshell gap exhibits a spectrum which is more like that of a

deformed rotor. The energy of the excited configuration is reduced by the attractive quadrupole interaction between neutron and proton bosons. Thus, the excited proton configuration may become the ground state if there are a large number of neutron bosons, as is observed in the Mo isotopes [Sam 82]. (On a microscopic level, this can be related to the situation where deformation (and, hence, collective rotational behaviour) is produced by exciting nuclei to higher levels by taking advantage of the attractive $n-p$ interaction, as discussed by Federman and Pittel [Fed 77, Fed 79]. This effect is particularly important when the excitation produces neutrons and protons in orbitals with the same shape, so that advantage can be taken of the strong short-range part of the $n-p$ force.)

In view of the above, the excitation of a pair of protons, into the $g_{9/2}$ orbital above the subshell gap, is expected to be particularly important in the light Sr isotopes for two main reasons. Firstly, such excitations are known to have a large influence in the Mo isotopes (Z=42), which also have a single valence proton boson with respect to the subshell closure (although in the case of the Sr isotopes there is, strictly, a valence proton boson-hole). Secondly, the protons are excited into the $g_{9/2}$ orbital which, in the light Sr isotopes, contains the valence neutrons; therefore, the attractive interaction between the excited protons and the valence neutron holes is expected to considerably lower the energy of this excitation. Therefore, it was decided to investigate IBM-2 configurations for the Sr isotopes with 1, 3 and 5 proton bosons.

5.5.2 THE MODEL

The interacting boson Hamiltonian was used in the form

$$H = \epsilon(\mathrm{n}_{d_\pi} + \mathrm{n}_{d_\nu}) + \kappa \mathrm{Q}^{(2)}.\mathrm{Q}^{(2)} + V_{\pi\pi} + V_{\nu\nu} + M_{\pi\nu} \tag{5.2}$$

where: $\mathrm{n}_{d_{\pi(\nu)}}$ is the boson number operator for protons (neutrons); $\mathrm{Q}^{(2)}=\mathrm{Q}_\pi^{(2)}+\mathrm{Q}_\nu^{(2)}$ is the quadrupole operator; $V_{\pi\pi(\nu\nu)}$ is the residual interaction between like bosons; and $M_{\pi\nu}$ is the Majorana operator. The choice of the quadrupole-quadrupole interaction includes, in addition to the proton-neutron interaction, a quadrupole interaction between like bosons, which is thought to be important for nuclei with triaxial equilibrium shapes [Die 82]. As a consequence, the parameter κ is only half of the value normally used for the strength of the $\mathrm{Q}_\pi^{(2)}.\mathrm{Q}_\nu^{(2)}$ interaction. This more complex form of the quadrupole-quadrupole interaction, which was found to be necessary to reproduce the experimental spectra, introduces no additional parameters into the Hamiltonian. All other parameters of the above Hamiltonian have their standard meaning (see sect. 2.5).

In addition to the level spectra, $E2$ and $M1$ transition rates were calculated and compared with the experimental data. The $M1$ and $E2$ transition operators were (see, for example, [Sam 84, Ell 85] and [Ari 81])

$$T(M1,\mu) = \sqrt{3/4\pi}(g_\pi L_{\pi,\mu}^{(1)} + g_\nu L_{\nu,\mu}^{(1)}) \tag{5.3}$$

where

$$L_{\pi(\nu),\mu}^{(1)} = \sqrt{10}(d_{\pi(\nu)}^\dagger \tilde{d}_{\pi(\nu)})_\mu^{(1)} \tag{5.4}$$

and g_π, g_ν are boson g-factors, in units of $\mu_\mathrm{N} = e\hbar/2mc$, for protons and neutrons (taken

as 1 and 0), respectively; and

$$T(E2,\mu) = e_\pi \mathrm{Q}^{(2)}_{\pi,\mu} + e_\nu \mathrm{Q}^{(2)}_{\nu,\mu} \tag{5.5}$$

where e_π, e_ν are boson effective charges, in units of eb, for protons and neutrons, respectively. Thus, the reduced transition rates are given by

$$\mathrm{B}(M1, I_i \rightarrow I_f) = |\langle I_f \| T(M1) \| I_i \rangle|^2 / (2I_i + 1), \tag{5.6}$$

$$\mathrm{B}(E2, I_i \rightarrow I_f) = |\langle I_f \| T(E2) \| I_i \rangle|^2 / (2I_i + 1), \tag{5.7}$$

and the $E2/M1$ multipole mixing ratio is

$$\delta = -0.832 \times E_\gamma[\mathrm{MeV}] \times \langle I_f \| T(E2) \| I_i \rangle[e\mathrm{b}] / \langle I_f \| T(M1) \| I_i \rangle[\mu_\mathrm{N}] \tag{5.8}$$

in the phase convention of Rose and Brink [Ros 67]. The computer program used was NPBOS written by T. Otsuka [Ots 77, Ots 79]. Minor modifications to this program, necessary in order to run it on the Nuclear Physics Laboratory VAX 11/780 computer, were carried out by T. Shaw and J. Rikovska of the Clarendon Laboratory.

5.5.3 RESULTS AND DISCUSSION OF THE IBM-2 CALCULATIONS

5.5.3.1 Introduction

IBM-2 calculations of the light Sr isotopes were carried out for one, three and five proton bosons, in order to investigate the subshell gap at Z=40. The philosophy behind the investigation was to vary the IBM-2 parameters to obtain the best fit to the experimental data, and then interpret the resulting parameters in terms of nuclear structure. The IBM-2 parameters for the Sr isotopes from the work of Heyde *et al.* [Hey 84] were used as a

starting point for the calculations. The parameters were varied manually in small steps in order to obtain the best fit to both the known excited states below $\sim$ 4 MeV and the ground state band B($E2$) values. (The precise experimental and theoretical levels used in the fits are given in figs. 5.9, 5.10 and 5.11, while the B($E2$) values are given in fig. 5.12.) In the calculations for the ^{78,80,82,84,86}Sr isotope chain, both microscopic predictions of the parameters of the quadrupole interaction [Sch 80, Ots 78b, Duv 81a, Duv 81b], and the phenomenological observation that the IBM-2 parameters vary smoothly as a function of nucleon number (see, for example, [Sch 80, Ari 81]) were taken into account.

5.5.3.2 IBM-2 results for the light Sr isotopes

The resulting parameters, which are summarized in table 5.1, vary smoothly with neutron number. Although the neutron subshell closure at N=40, which was found to be less pronounced than the subshell closure at Z=40 in earlier IBM-2 studies of the N$\sim$Z$\sim$40 region [Kau 83, Hey 84], was not taken into account explicitly, this subshell closure is reflected implicitly in the behaviour of the parameter χ_ν. It is interesting to note that the behaviour of the χ_π and χ_ν parameters can be interpreted (as is discussed, for example, by Dieperink and Bijker [Die 82, Die 83]) as corresponding to a prolate shape for ^{78}Sr which, as successive pairs of neutrons are added, evolves into a softer triaxial shape. In this way, the IBM-2 calculations may reflect the increasing importance of the γ degree of freedom with increasing neutron number which was suggested in sect. 5.4 on the basis of the behaviour of the $J^{(1)}$ and $J^{(2)}$ moments of inertia.

The theoretical IBM-2 energy level spectra are given in figs. 5.9, 5.10 and 5.11 for one, three and five proton bosons, respectively, where they are compared with the energy

TABLE 5.1

Parameters of the IBM-2 Hamiltonian

Nucleus	N_ν	N_π	ϵ	κ	χ_ν	c_ν^0	c_ν^2	c_ν^4	ξ_2^*
$^{78}_{40}$Sr	5	5	0.84	−0.066	−0.30	−0.35	−0.15	0.02	0.005
	"	3	0.69	−0.082	"	"	"	"	0.015
	"	1	0.40	−0.090	"	"	"	"	0.015
$^{80}_{42}$Sr	4	5	0.87	−0.060	−0.20	−0.35	−0.15	0.02	0.005
	"	3	0.72	−0.080	"	"	"	"	0.007
	"	1	0.52	−0.082	"	"	"	"	0.120
$^{82}_{44}$Sr	3	5	0.89	−0.042	−0.10	−0.35	−0.15	0.08	0.015
	"	3	0.81	−0.080	"	"	"	"	0.020
	"	1	0.60	−0.084	"	"	"	"	0.150
$^{84}_{46}$Sr	2	5	0.995	−0.032	+0.10	−0.55	−0.15	0.30	0.050
	"	3	0.93	−0.080	"	"	"	"	0.070
	"	1	0.76	−0.084	"	"	"	"	0.200
$^{86}_{48}$Sr	1	5	1.15	−0.015	+0.45	−0.55	−0.15	0.30	0.100
	"	3	1.13	−0.080	"	"	"	"	0.100

The parameter χ_π was held constant at $\chi_\pi = -1.3$ throughout the sequence of fits. Parameters of $V_{\pi\pi}$ were $c_\pi^L = -0.3$, 0.2 and 0.02 (L=0, 2, 4), respectively, for N_π=5, and were set equal to zero otherwise.

* $\xi_1 = \xi_3 = 0$ for all cases except for A = 84 and 86 with $N_\pi = 3$ where $\xi_3 = 0.08$.

" indicates that the parameter is the same as in the preceding row

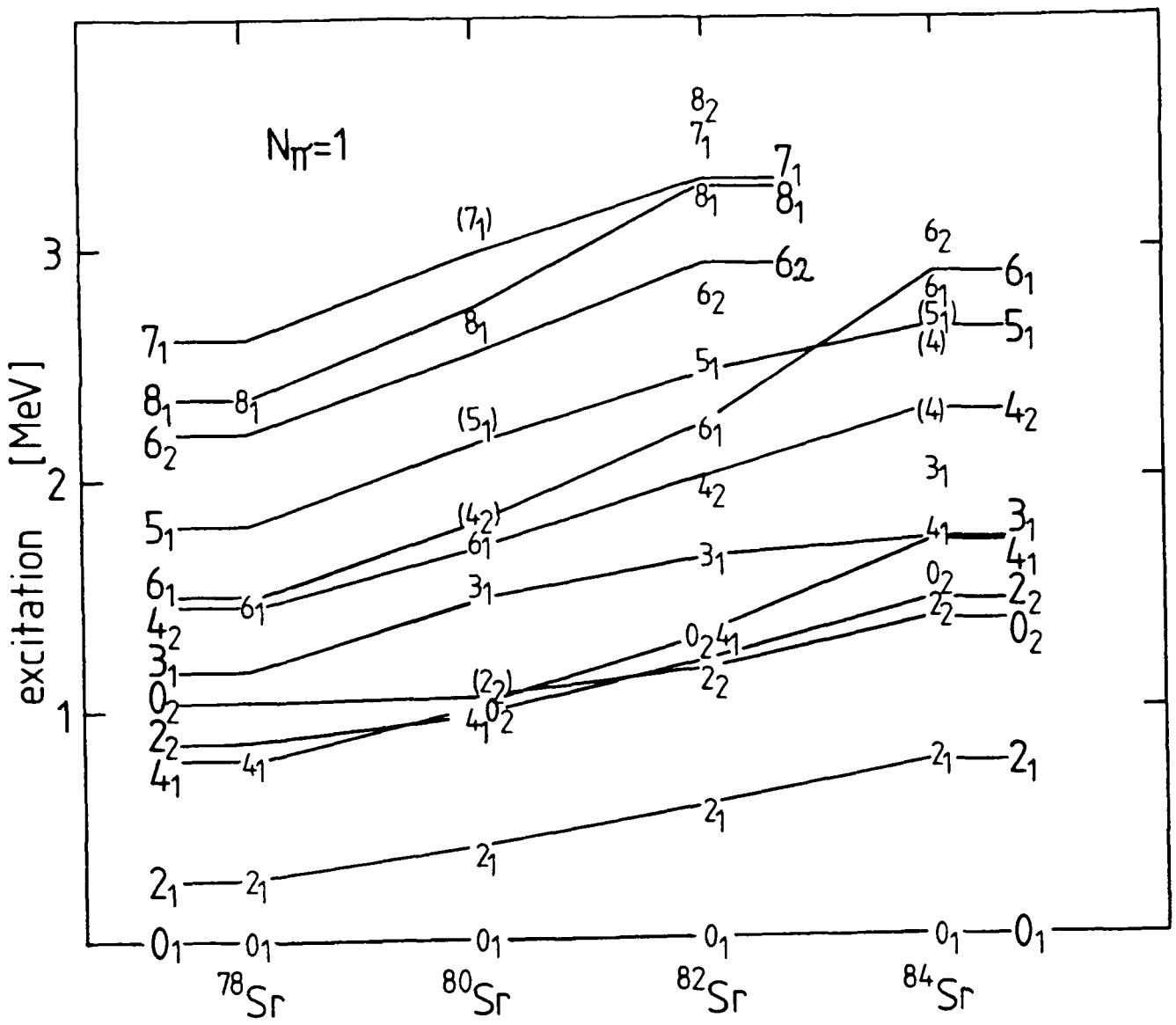


Figure 5.9 Comparison between the IBM-2 calculations of the present study with one proton boson (indicated by lines labelled in large numbers by the level spin) and the experimental energy level systematics (indicated by small numbers; see also fig. 5.8) for ^{78,80,82,84}Sr. See text for details.

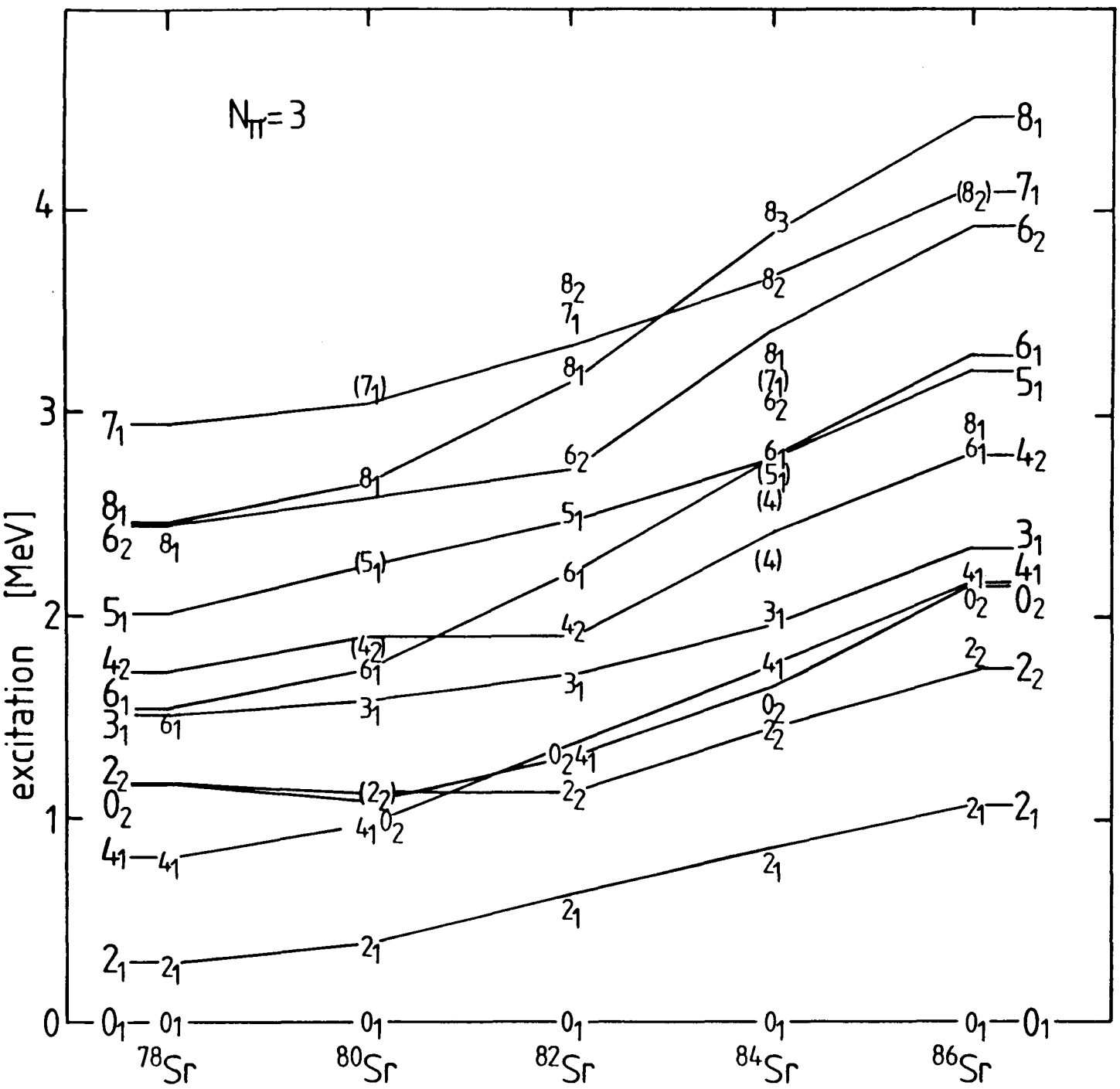


Figure 5.10 Comparison between the IBM-2 calculations of the present study with three proton bosons (indicated by lines labelled in large numbers by the level spin) and the experimental energy level systematics (indicated by small numbers; see also fig. 5.8) for ^{78,80,82,84,86}Sr. See text for details.

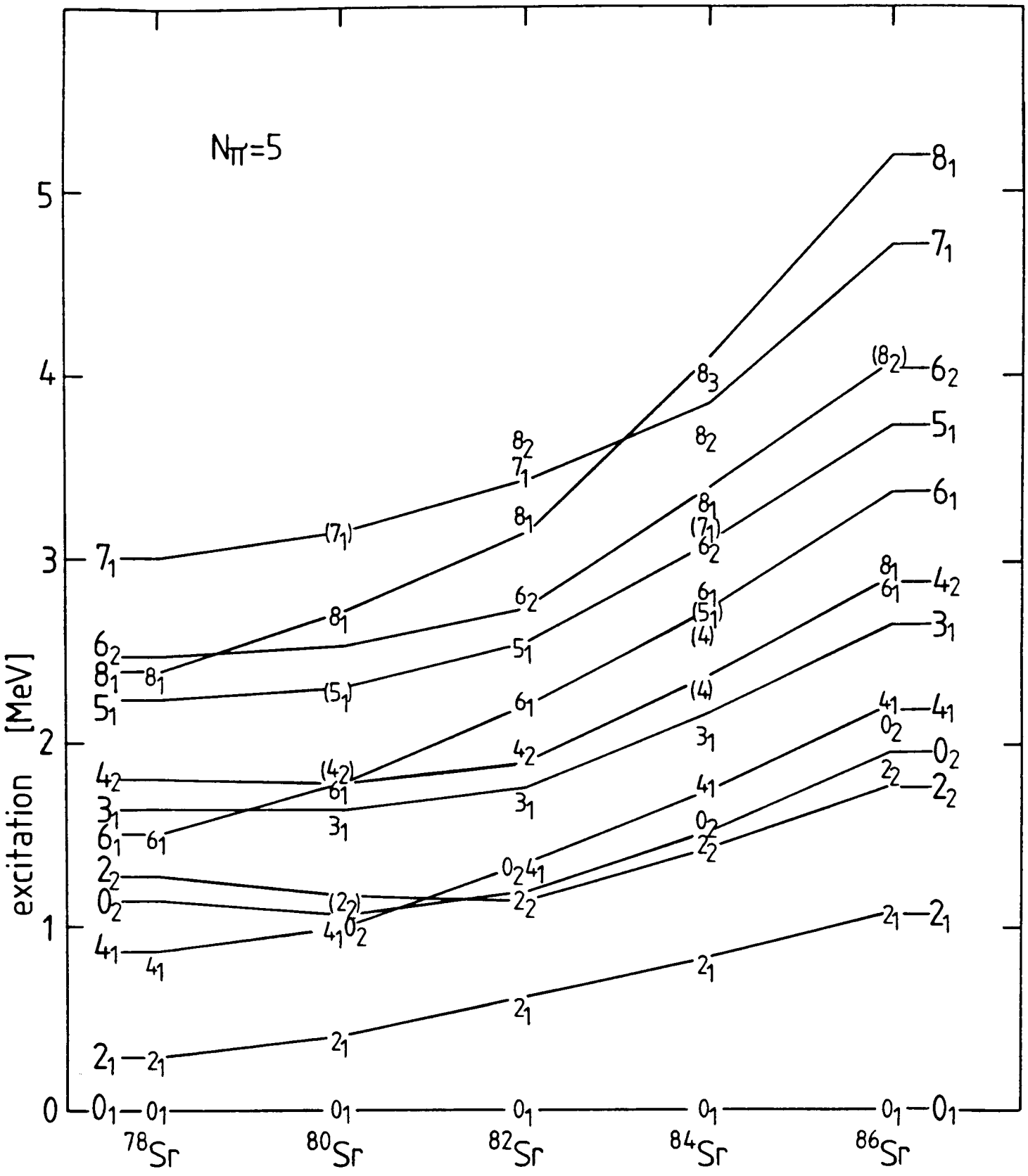


Figure 5.11 Comparison between the IBM-2 calculations of the present study with five proton bosons (indicated by lines labelled in large numbers by the level spin) and the experimental energy level systematics (indicated by small numbers; see also fig. 5.8) for ^{78,80,82,84,86}Sr. See text for details.

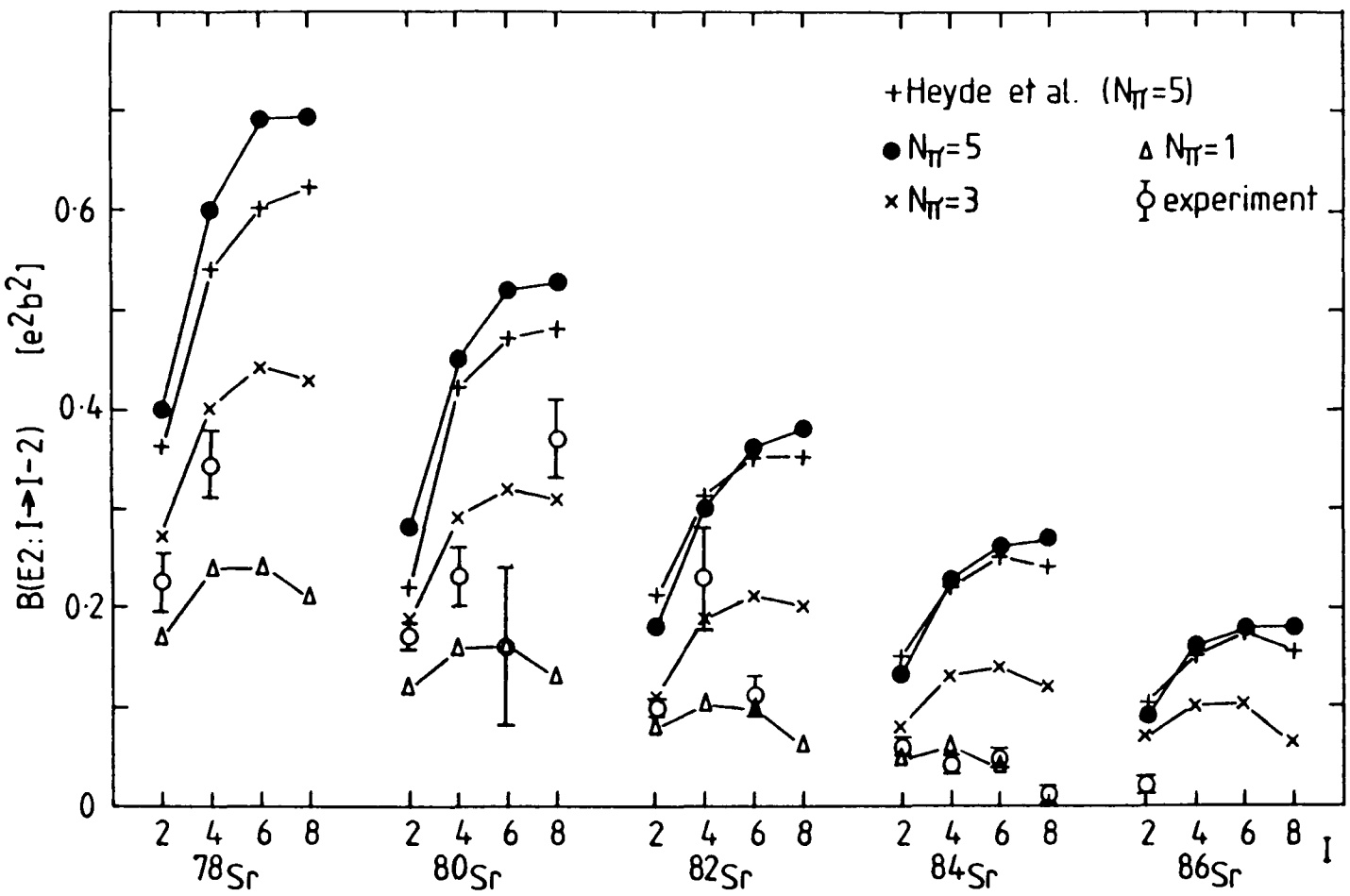


Figure 5.12 Comparison between the experimental ground state band B($E2$) values and those calculated in the present study in IBM-2 calculations for one, three and five proton bosons. B($E2$) values calculated from the IBM-2 parameters of Heyde *et al.* [Hey 84] are also shown for comparison. See text for details. The experimental data were taken from [Dew 81, Dew 82, Lis 82, Sym 64] and the present work.

systematics of the even parity levels in the light Sr isotopes (fig. 5.8). As can be seen from these figures (and the results of Heyde *et al.* [Hey 84]) it is possible to obtain a good fit to the energy spectra independent of the number of proton bosons involved in the calculation. This is not surprising, as the number of parameters in the model calculations, for a given number of proton and neutron bosons, is almost as large as the number of experimentally determined level energies. However, in addition to predicting the positions of experimentally observed levels, the calculations also give the positions of many levels which have not been observed experimentally as well as the $E2$ and $M1$ matrix elements between any pair of levels within a given nucleus. Unfortunately, most of these predicted matrix elements have not yet been determined by experiment. However, the B($E2$) values between states in the ground state band are known for many of these nuclei, allowing a comparison between the theoretical and experimental matrix elements to be made for a few transitions. Such a comparison is shown in fig. 5.12. The boson effective charges were $e_\pi = e_\nu = 0.12$ eb. Different values of e_π and e_ν were considered (for example, similar to the proton and neutron effective charges of 1.5 e and 0.5 e, respectively, used in Hartree-Fock calculations in this region [Aha 85b]). However, it was found that the qualitative results of the study were independent of these alternative choices of effective charges.

It is clear from fig. 5.12 that the ground state band B($E2$) values for both sets of parameters with $N_\pi = 5$ (the results of the present study and those calculated from the parameter set of [Hey 84]) yield the poorest agreement with experiment. In contrast, the configuration with $N_\pi = 3$ gives good results for N=40 and 42, while for N=44 and 46 the data favours the $N_\pi = 1$ configuration. This is in good agreement with the trends observed

in the Mo isotopes [Sam 82] where the $N_\pi = 1$ configuration was found to dominate close to the N=50 spherical closed shell, while the $N_\pi = 3$ configuration became increasingly more important as the number of valence neutron bosons increased (as discussed in sect. 5.5.1, above). It is interesting to note that the $N_\pi = 3$ configuration, which corresponds to the excitation of a pair of protons into the $g_{9/2}$ orbitals above the Z=40 spherical subshell, can be seen as an IBM-2 analogue of the lowering of the $g_{9/2}$ orbitals relative to the those below the Z=40 subshell. This latter factor is responsible for the deformed prolate subshell gap at Z=38 and is the microscopic basis for the strongly collective behaviour in the lightest Sr isotopes (see fig. 1.1 and [Naz 85]).

5.5.3.3 IBM-2 ($N_\pi = 3$) results for ^{80}Sr sideband 1 and sideband 2

In order to investigate possible correspondence between the theoretical and experimental ^{80}Sr sidebands, detailed comparisons were made between the theoretical calculations for $N_\pi = 3$ and the experimental data for SB1 and SB2. As is noted above there is a good correspondence between the energies of the experimental levels and those predicted by the IBM. However, for both SB1 and SB2 associated even spin levels are predicted in addition to the observed odd spin levels. It is not clear from the calculations why these even spin levels were not observed experimentally in the present study.

5.5.3.3.1 Sideband 2

Comparison between the theoretical and experimental decay properties of the levels in SB2 (table 5.2) is reasonably good. The strong branching from the 2_2, 3_1 and 5_1 SB2 states to the GSB is predicted in the IBM-2 calculations and there is excellent agreement between experiment and theory for both the signs and the magnitudes of the multipole

TABLE 5.2

Comparison Between IBM-2 Calculations and Experiment for SB2

Transition	IBM-2 Calculation	Experiment
$2_2 \rightarrow$ GSB 0_1	18%	$< 9\%$
$2_2 \rightarrow$ GSB 2_1	82%	100%
$3_1 \rightarrow$ GSB 2_1	65%	100%
$\delta(3_1 \rightarrow$ GSB $2_1)$	+0.59	+0.45(8)
$3_1 \rightarrow$ GSB 4_1	20%	$< 40\%$
$3_1 \rightarrow$ SB2 2_2	10%	$< 40\%$
$5_1 \rightarrow$ GSB 4_1	62%	49(8)%
$\delta(5_1 \rightarrow$ GSB $4_1)$	+0.37	+ 0.38(6)
$5_1 \rightarrow$ GSB 6_1	22%	$< 14\%$
$5_1 \rightarrow$ SB2 3_1	11%	51(6)%
$5_1 \rightarrow$ SB2 4_2	4%	$< 14\%$
$\tau(7_1 \rightarrow$ SB2 $5_1)$	0.72 ps	1.1(9) ps
$7_1 \rightarrow$ GSB 6_1	63%	$< 35\%$
$7_1 \rightarrow$ SB2 5_1	34%	100%
$7_1 \rightarrow$ SB2 6_2	3%	$< 35\%$
$9_1 \rightarrow$ GSB 8_1	48%	$< 35\%$
$9_1 \rightarrow$ SB2 7_1	50%	100%
$9_1 \rightarrow$ SB2 8_2	2%	$< 35\%$

Branching ratios are given as percentages (%); limits on unobserved transitions are given as percentages of the total observed decay intensity. Where appropriate, multipole mixing ratios (δ) are given. All experimental data were taken from the present work, except for the experimental data on the decay of the 2_2 state which were taken from the work of Lister *et al.* [Li 81].

mixing ratios of the $3_1^+ \rightarrow$ GSB 2_1^+ and $5_1^+ \rightarrow$ GSB 4_1^+ transitions. In addition, strong branching is predicted out of SB2 to the GSB from the 7_1^+ and 9_1^+ levels. Such feeding out of SB2 may be responsible for the lack of decay intensity observed at the bottom of SB2 (as discussed in sect. 4.5.1). The predicted strength of the $7_1^+ \rightarrow 5_1^+$ transition is also in good agreement with the experimental data. Thus, the overall agreement between the IBM-2 calculations and the experimental data on SB2 is good, suggesting that this sideband may be identified with the odd spin members of the IBM-2 quasi-γ band, at least at low spins (although, the alignment of a pair of $g_{9/2}$ protons may also play an important role in SB2 at higher spins, as discussed in sect. 5.3).

5.5.3.3.2 Sideband 1

Comparison between the IBM-2 calculations and SB1 was not as successful as for SB2. This is not altogether unexpected, since the observed states in SB1 have spin $I \geq 7$ and, therefore, it is unlikely that they can be fully described by a model based on spin 0 and spin 2 states. A pair of close lying 7^+ states (7_2^+ and 7_3^+) at excitation energies of 3631 and 3695 keV arose naturally in the calculations from fits to the lower lying levels. In table 5.3 the decay properties of the 7_2^+, 7_3^+, 9_2^+ and 9_3^+ theoretical IBM-2 levels are compared with those of the 7^+ and 9^+ states in SB1. The 7_2^+ is predicted to decay predominantly to the GSB 6_1^+ with an $E2$ matrix element which is in reasonable agreement with the experimental data, although the theoretical $M1$ matrix element is greater than that observed experimentally (this is reflected in the theoretical multipole mixing ratio, which is of the correct sign but is an order of magnitude smaller than the experimental mixing ratio). In contrast the theoretical 7_3^+ decays strongly to SB2, contrary to the

TABLE 5.3

Comparison Between IBM-2 Calculations and Experiment for SB1

Transition	IBM-2 Calculation	Experiment
$7_2 \rightarrow$ GSB 6_1	43%	100%
$\delta(7_2 \rightarrow$ GSB $6_1)$	-0.23	$-4.7(15)$
$\tau(7_2 \rightarrow$ GSB $6_1)$	12 ps*	$> 30(27)$ ps
$7_2 \rightarrow$ GSB 8_1	23%	$< 35\%$
$7_2 \rightarrow$ SB2 5_1	0%	$< 35\%$
$7_2 \rightarrow$ SB2 6_2	8%	$< 35\%$
$7_2 \rightarrow$ SB2 7_1	12%	$< 35\%$
$7_2 \rightarrow$ SB1 5_2	7%	$< 35\%$
$7_2 \rightarrow$ SB1 6_3	2%	$< 35\%$
$7_2 \rightarrow$ [SB1] 5_3	1%	$< 35\%$
$7_2 \rightarrow$ [SB1] 6_4	4%	$< 35\%$
$7_3 \rightarrow$ GSB 6_1	7%	100%
$\delta(7_3 \rightarrow$ GSB $6_1)$	-0.62	$-2.8(4)$
$\tau(7_3 \rightarrow$ GSB $6_1)$	23 ps*	$> 30(27)$ ps
$7_3 \rightarrow$ GSB 8_1	4%	$< 50\%$
$7_3 \rightarrow$ SB2 5_1	9%	$< 50\%$
$7_3 \rightarrow$ SB2 6_2	59%	$< 50\%$
$7_3 \rightarrow$ SB2 7_1	7%	$< 50\%$
$7_3 \rightarrow$ SB1 5_2	2%	$< 50\%$
$7_3 \rightarrow$ SB1 6_3	2%	$< 50\%$
$7_3 \rightarrow$ [SB1] 5_3	6%	$< 50\%$
$7_3 \rightarrow$ [SB1] 6_4	4%	$< 50\%$
$\tau(9_2 \rightarrow$ SB1 $7_2 \& 7_3)$	2.0 ps	$1.3(^{17}_{5})$ ps
$9_2 \rightarrow$ GSB 8_1	32%	(18(5)%)
$9_2 \rightarrow$ SB2 7_1	0%	$< 20\%$
$9_2 \rightarrow$ SB2 8_2	26%	$< 20\%$
$9_2 \rightarrow$ SB1 7_2	40%	42(4)%
$9_2 \rightarrow$ SB1 8_3	0%	$< 20\%$
$9_2 \rightarrow$ [SB1] 7_3	2%	40(7)%

TABLE 5.3 continued

Transition	IBA2 Calculation	Experiment
$\tau(9_3 \rightarrow$ SB1 $7_2\&7_3)$	2.4 ps	[1.3($^{17}_{5}$) ps]
$9_3 \rightarrow$ GSB 8_1	23%	[18(5)%]
$9_3 \rightarrow$ SB2 7_1	2%	[< 20%]
$9_3 \rightarrow$ SB2 8_2	22%	[< 20%]
$9_3 \rightarrow$ SB1 7_2	13%	[42(4)%]
$9_3 \rightarrow$ SB1 8_3	1%	[< 20%]
$9_3 \rightarrow$ [SB1] 7_3	38%	[40(7)%]

Branching ratios are given as percentages (%); limits on unobserved transitions are given as percentages of the total observed decay intensity. Where appropriate, meanlives (τ) and multipole mixing ratios (δ) are given. All experimental data were taken from the present work. [Decays to or from the levels associated with the IBM-2 band containing the 7_3 are indicated in square brackets.]

* Meanlife calculated from the IBM-2 $7_{2(3)} \rightarrow 6_1$ $E2$ matrix element and the experimental transition energy and multipole mixing ratio.

experimental data. However, as with the 7_2^+, the $E2$ matrix element for the decay of the 7_3^+ to the GSB 6_1^+ is in agreement with experiment, although again the multipole mixing ratio is predicted to be smaller than that observed experimentally. The observed splitting of the decay intensity of the SB1 9^+ state between the two SB1 7^+ states is not convincingly reproduced by either the theoretical 9_2^+ or 9_3^+ levels, casting further doubt on the association of the levels predicted in the IBM-2 calculations with those of SB1.

CHAPTER 6

SUMMARY AND CONCLUSIONS

The present study has considerably extended our knowledge of ^{80}Sr, with the ground state band observed up to a spin tentatively assigned as $26\hbar$ and with the identification of three previously unobserved sidebands. The band structure of ^{80}Sr is comparable to that of ^{84}Zr, being better defined than that of the neighbouring Kr isotopes. The ^{80}Sr ground state band remains collective to the highest spins observed, indicating that there has not been a transition to mostly non-collective excitations of an oblate shape. In particular, the slow feeding times, which were previously associated with effects high in the ground state band, have been investigated more fully and found to be due to interband transitions feeding into the ground state band at low spins. Irregularities in the ground state band level energies at high spin, compared with the smooth behaviour expected for a simple rotor, are unexplained and remain an outstanding problem. In addition, the decay of the 4378 keV 9^+ level to the two 7^+ states, with roughly equal intensities, and their subsequent decay to the 6^+ state in the GSB via slow transitions with large quadrupole/dipole mixing ratios, are interesting and unusual features which remain unexplained.

The systematic features of the ^{80}Sr $J^{(1)}$ and $J^{(2)}$ moments of inertia are interpreted as indicating either static or dynamic γ-deformation, in good agreement with TPE surface calculations, while the structures superimposed on this systematic behaviour are interpreted as the particle alignments predicted in cranking model calculations. The close proximity of the 2_2^+ and 4_1^+ levels are presented as evidence that softness to γ-deformation

is a general property of the light Sr isotopes, while the systematics of both the moments of inertia and the $2_2^+/4_1^+$ ratios suggest that the importance of the γ degree of freedom increases as the nuclei move away from the prolate shell gap at N=38. This is in qualitative agreement with TPE surface calculations.

New IBM-2 calculations have been carried out for the neutron deficient Sr isotopes. These calculations have provided a better description of the experimental data than previous calculations. In particular, these calculations have resolved earlier discrepancies between the experimental and theoretical ground state band B($E2$) values by the explicit inclusion of the Z=40 spherical subshell gap. Furthermore, in these calculations the strongly collective nature of the lightest Sr isotopes results from the excitation of protons across the Z=40 subshell into the $g_{9/2}$ orbital, in close correspondence with microscopic theory. In addition, the behaviour of the χ_π and χ_ν parameters of the IBM-2 quadrupole interaction can be interpreted as indicating increasing importance of the γ degree of freedom as successive neutron pairs are added to ^{78}Sr; this is in good agreement with the trends observed in the $J^{(1)}$ and $J^{(2)}$ moments of inertia and their interpretation in terms of either static or dynamic γ-deformation, above. Detailed comparison between the predictions of the IBM-2 calculations and the data suggest that the experimental 2_2^+, 3_1^+, 4_2^+, 5_1^+... band (SB2) can be identified with the collective IBM-2 quasi-γ band (although, behaviour of the moments of inertia suggest that the alignment of a pair of $g_{9/2}$ protons may also play an important role in the higher spin members of the band), reinforcing the interpretation of these states in terms of static or dynamic γ-deformation.

APPENDIX A

UNITS

In carrying out the calculations performed in the present study, the following set of units and values were found to be useful:

$$\hbar c = 197.3 \text{ MeV fm}$$

$$e^2 = 1.44 \text{ MeV fm}$$

$$\frac{e^2}{\hbar c} = \frac{1}{137}$$

$$1 \text{ amu} = 932 \frac{\text{MeV}}{c^2}$$

$$1 \text{ b} = 100 \text{ fm}^2$$

APPENDIX B

NUCLEAR γ-RAY TRANSITIONS

B.1 Introduction

In this section the properties of γ-ray transitions which are important in the experimental studies of γ-ray spectroscopy are presented. This treatment follows closely sections in both the simplified presentation of Morinaga and Yamazaki [Mor 76] and the more detailed treatment of Blatt and Weisskopf [Bla 52] where more complete treatments can be found. In addition, the theory of angular distributions of γ-rays is covered in detail by Rose and Brink [Ros 67].

B.2 Conservation of Energy, Angular Momentum and Parity

In nuclear transitions in which a γ-ray is emitted, the energy (E), total angular momentum (I, with z-projection m) and parity (π) are conserved; the change in nuclear E, I and π being carried away by the γ-ray. Therefore, we have the following conservation laws

$$I_i = I_f + I_\gamma \tag{B.1}$$

$$m_i = m_f + m_\gamma \tag{B.2}$$

$$\pi_i = \pi_f \pi_\gamma \tag{B.3}$$

$$E_i = E_f + E_\gamma \tag{B.4}$$

where the subscripts i, f and γ represent the initial and final nuclear states and the γ-ray,

respectively. The vector conservation law for angular momentum can be rewritten

$$|\mathrm{I}_i - \mathrm{I}_f| \leq \mathrm{I}_\gamma \leq \mathrm{I}_i + \mathrm{I}_f \qquad (B.5)$$

where I is the maximum z-projection of I. (Since the photon has intrinsic spin 1, it follows immediately that γ-ray transitions between states with $I_i = I_f = 0$ are forbidden.)

It is common to use the notation λ, μ for the angular momentum eigenvalue and z-projection of the γ-ray. Therefore, this convention will be used in the following description when convenient. λ is often called the multipole order of the γ-ray. The parity of the γ-ray determines whether an electric $(E\lambda)$ or magnetic $(M\lambda)$ multipole is associated with the γ-ray, according to

$$\mathrm{ElectricMultipole}\lambda \Rightarrow \pi = (-1)^\lambda$$

$$\mathrm{MagneticMultipole}\lambda \Rightarrow \pi = (-1)^{\lambda+1} \qquad (B.6)$$

This terminology is convenient because of the similarities between both the probability distribution and polarization of the γ-ray, and the angular distribution and polarization of the corresponding classical radiation field associated with a given multipolarity.

B.3 γ-rays of Mixed Multipolarity

Usually the γ-ray of lowest allowed multipole order is emitted in a nuclear transition. However, in some cases a higher order multipole (of the same parity) will also compete. (For example, mixed $M1/E2$ transitions are common, because in general electric transitions are stronger than magnetic ones.) In such cases it is useful to define the multipole mixing ratio δ by

$$\delta = \frac{\langle f \| \lambda' \| i \rangle}{\langle f \| \lambda \| i \rangle} \qquad (B.7)$$

where $\lambda' = \lambda + 1$ and $\langle f \| \lambda \| i \rangle$ represents the transition amplitude independent of geometric factors, but including the energy dependence of the transition rate. $\langle f \| \lambda \| i \rangle$ is directly proportional to the reduced matrix element connecting the initial and final states [Ros 67]. For an ensemble of nuclei decaying from the same excited state, the intensities of the λ' and λ multipoles are related by [Bla 52, Ros 67]

$$\delta^2 = \frac{\text{the intensity of } \lambda'}{\text{the intensity of } \lambda} \qquad (B.8)$$

B.4 Angular Distribution of γ-rays

The angular momentum of a photon is the sum of its intrinsic spin (s) and its orbital angular momentum (l); $j = l + s$. The eigenfunctions of L^2 and L_z are the spherical harmonics Y_{lm}

$$L^2 Y_{\mathrm{lm}} = \mathrm{l}(\mathrm{l}+1) Y_{\mathrm{lm}}\ \hbar^2 \qquad (B.9)$$

$$L_z Y_{\mathrm{lm}} = \mathrm{m} Y_{\mathrm{lm}}\ \hbar \qquad (B.10)$$

Thus the eigenfunctions of J^2 and J_z, with eigenvalues $\lambda(\lambda+1)$ and μ, respectively, are

$$X_{\lambda \mathrm{l} \mu} = \sum_{\mathrm{m}} (\mathrm{l}\mu - \mathrm{m}1\mathrm{m} | \lambda\mu) Y_{\mathrm{l}\mu-\mathrm{m}} \xi_{\mathrm{m}} \qquad (B.11)$$

where ξ_{m} is the eigenfunction of the photon spin operator S with z-projection m (maximum z-projection is 1).

$X_{\lambda \mathrm{l} \mu}$ has the parity of Y_{lk}, i.e. $\pi = (-1)^{\mathrm{l}}$. Thus, for given values of λ and μ the parity of the function with $\mathrm{l} = \lambda$ is $(-1)^{\lambda}$, while the parities of the functions with $\mathrm{l} = \lambda \pm 1$ are $(-1)^{\lambda+1}$. Now, the emitted photon obeys Maxwell's equations in free space

$$curlH = \frac{1}{c}\frac{\partial E}{\partial t}$$
$$curlE = \frac{-1}{c}\frac{\partial H}{\partial t}$$
$$divE = 0$$
$$divH = 0 \qquad (B.12)$$

(in Gaussian units; $\epsilon_0 = \mu_0 = 1$). Therefore, the parities of the magnetic H and the electric E components of the electromagnetic field are opposite, since the *curl* transformation has negative parity. (This can be seen as necessary, since the Poynting vector S

$$S = \frac{c}{4\pi} E \times H \qquad (B.13)$$

which describes the flow of electromagnetic energy must be odd under parity, in order that the flow of energy is outwards from the source at both r and $-$r.) It can be shown [Bla 52] that for an electric multipole the parity of H is $(-1)^\lambda$ and that of E is $(-1)^{\lambda+1}$, while for a magnetic multipole the parities are reversed. Thus, since the parity of $X_{\lambda\lambda\mu}$ is $(-1)^\lambda$ we have

$$E_{\lambda\mu}(M\lambda) = -H_{\lambda\mu}(E\lambda) \; \alpha \; X_{\lambda\lambda\mu} \qquad (B.14)$$

The probability distribution $Z(\theta, \phi)$ of the emitted photon is given by the Poynting vector (eq. $B.13$), which has magnitude $\frac{c}{4\pi}|E|^2 = \frac{c}{4\pi}|H|^2$. Thus, the probability distribution for a photon of multipolarity λ and z-projection μ is given by

$$Z_{\lambda\mu}(\theta,\phi) = |X_{\lambda\lambda\mu}|^2 = |\sum_m (\lambda\mu - m1m|\lambda\mu) Y_{\lambda\mu-m}\xi_m|^2$$
$$= \frac{(-1)^{\mu-1}}{4\pi}\sum_k (\lambda 1\lambda - 1|k0)(\lambda\mu\lambda - \mu|k0) P_k(\cos\theta) \qquad (B.15)$$

where: k is an even integer such that $|k| \leq 2\lambda$; and P_k is the k^{th} Legendre polynomial. The angular distribution function $Z_{\lambda\mu}$ is normalized so that $\int Z_{\lambda\mu}(\theta,\phi)d\Omega = 1$ and $Z_{\lambda\mu}$ has the following properties:

(i) $Z_{\lambda\mu}$ is independent of the azimuthal angle ϕ

(ii) $Z_{\lambda\mu}(\theta) = Z_{\lambda-\mu}(\theta) = Z_{\lambda\mu}(\pi - \theta)$

(iii) When μ takes all allowed values with equal weight, the angular distribution is isotropic.

We see that the angular distributions of $E\lambda$ and $M\lambda$ radiations are the same. However, for a given λ and μ the polarizations of the electric and magnetic radiations differ by 90°. This can be seen from the fact that the electric and magnetic components of a given multipole field are perpendicular and that to obtain the electric radiation field from the magnetic radiation field E and H are interchanged (eq. $B.14$). Thus, measurements of γ-ray angular distributions will yield information about the angular momentum carried by the γ-rays, while information concerning the parity change of the nucleus is contained in the γ-ray polarization.

B.4.1 ANGULAR DISTRIBUTIONS OF γ-RAYS EMITTED FROM ALIGNED STATES

Excited states populated in nuclear reactions frequently have their angular momenta aligned with respect to the direction of the projectile. (See, for example, the discussion of heavy-ion reactions in Chapter 3, in which the nuclei are strongly aligned about the $m = 0$ magnetic substate, relative to the direction of the incoming beam.) It is the angular distribution of the γ-rays emitted by an ensemble of nuclei produced in such reactions which are of interest in experimental nuclear physics. Let P(m) represent the probability

of forming the nucleus in a state (j, m) with respect to some quantization axis. The angular distribution of emitted photons of multipolarity λ and component μ is given by $Z_{\lambda\mu}(\theta, \phi)$ (eq. $B.15$). Then, since the transition probability for each sub-process is given by (the Wigner Eckart Theorem)

$$\langle j_f m_f | \lambda\mu | j_i m_i \rangle = (j_i m_i \lambda\mu | j_f m_f) \langle j_f \| \lambda \| j_i \rangle \qquad (B.16)$$

the probability of emitting a photon of angular momentum (λ, μ) is

$$a_{\lambda\mu} = \sum_{m_i} |(j_i m_i \lambda\mu | j_f m_f)|^2 \mathrm{P}(m_i) \qquad (B.17)$$

Thus, the γ-ray angular distribution becomes

$$W(\theta) = \sum_{m_i, \mu} |(j_i m_i \lambda\mu | j_f m_f)|^2 \mathrm{P}(m_i) Z_{\lambda\mu}(\theta) \qquad (B.18)$$

Since for each value of μ independently the relationship $Z_{\lambda\mu}(\theta) = Z_{\lambda\mu}(\pi - \theta)$ holds, we have that $W(\theta) = W(\pi - \theta)$, i.e. the angular distribution is symmetric about 90° under reflection. Finally, by using eq. $B.15$ the angular distribution can be expressed as the sum of even Legendre polynomials

$$\mathrm{W}(\theta) = \sum_k A_k P_k(\cos\theta) \qquad (B.19)$$

where: k takes even values such that $k \leq 2\lambda$; and the coefficients A_k depend upon the magnetic substate distribution $\mathrm{P}(m_i)$.

This treatment can be generalized to γ-rays of mixed multipolarity [Mor 76, Ros 67]. Tables of angular distribution coefficients, suitable for the analysis of the γ-rays emitted from the aligned states produced in heavy-ion reactions exist [Yam 67, Mat 74a, Mat 74b].

B.5 γ-ray Transition Probabilities

The transition probability for a γ-ray emission of multipolarity $\sigma\lambda\mu$ ($\sigma = E$ or M, denoting an electric or magnetic multipole, respectively) is given by [Bla 52, Mor 76]

$$\mathrm{T}(\sigma\lambda,\mu) = \frac{8\pi(\lambda+1)}{\lambda[(2\lambda+1)!!]^2}\frac{1}{\hbar}(\frac{\omega}{c})^{2\lambda+1}|\langle f|M(\sigma\lambda,\mu)|i\rangle|^2 \qquad (B.20)$$

where the frequency of the radiation is related to the energy of the γ-ray by $\omega = E_\gamma/\hbar$. In deriving this equation it is assumed that the source of the radiation (the nucleus) is much smaller than the wavelength of the emitted radiation $\bar{\lambda}$

$$\bar{\lambda} = \frac{\hbar c}{E_\gamma} = \frac{197.3}{E_\gamma[\mathrm{MeV}]}\ \mathrm{fm} \qquad (B.21)$$

This approximation holds well for γ-ray energies up to a few MeV which is the range relevant to nuclear spectroscopy. In this limit the regular† solution $F_l(r)$ of the equation

$$(-\frac{\mathrm{d}}{\mathrm{d}r^2} + \frac{l(l+1)}{r^2} - k^2)F_l(r) = 0 \qquad (B.22)$$

which is used in solving Maxwell's equations for a periodically varying field (see, for example, Appendix B of [Bla 52]) is replaced by its asymptotic form for small values of r ($kr \ll 1$)

$$F_l(r) \sim \frac{(kr)^{l+1}}{(2l+1)!!} \qquad (B.23)$$

where the wave number $k = 1/\bar{\lambda} = \omega/c$. The transition rate $\mathrm{T}(\sigma\lambda,\mu)$ is calculated by dividing the energy flux defined by the Poynting vector (eq. $B.13$) by the energy $\hbar\omega$ of

† A regular solution is defined as a real function which satisfies eq. $B.22$ and which vanishes at $r = 0$.

the emitted photons. The transition operators $M(\sigma\lambda,\mu)$ in eq. $B.20$ are given by

$$M(E\lambda,\mu) = er^{\lambda}Y^{*}_{\lambda\mu}(\theta,\phi)$$

$$M(M\lambda,\mu) = (\frac{2}{(\lambda+1)}g_l l + g_s s)\cdot[\bigtriangledown(r^{\lambda}Y_{\lambda\mu}(\theta,\phi))]^{*}\mu_N \qquad (B.24)$$

where $\mu_N = e\hbar/2mc$ is the nuclear magneton (m is the mass of a nucleon). For a nucleon in free space

g_l is 1 for protons and 0 for neutrons

g_s is 5.586 for protons and -3.826 for neutrons

However, the values of g_l and g_s may be different from those given above within a nucleus, due to meson exchange currents between the nucleons.

The operators $M(E\lambda,\mu)$ and $M(M\lambda,\mu)$ are for a single nucleon with charge e. Therefore, in a nucleus the transition operators are the sum of those for the constituent nucleons. $M(E\lambda,\mu)$ is the electric multipole operator of order λ,μ and is related to the shape of the nuclear charge distribution (see sect. $B.4$). The magnetic operator $M(M\lambda,\mu)$ consists of two parts: the first term is due to the orbital motion of the nucleon and the second is due to its intrinsic magnetic moment.

We see from the formula for $T(\sigma\lambda,\mu)$ that the transition probabilities increase dramatically with the energy of the emitted γ-ray (E^{2l+1}). Thus, high energy transitions are strongly favoured. In addition, the $(\lambda+1)/\lambda[(2\lambda+1)!!]^2$ term strongly favours low multipolarity transitions. This is not unexpected since classically a photon with momentum $p = E/c$ emitted at a radius equal to its wavelength $\bar{\lambda} = \hbar c/E$ carries only one unit of angular momentum, and the nuclear radius is generally much smaller than $\bar{\lambda}$. Finally, although not immediately obvious from eq. $B.20$, electric transitions are favoured over

magnetic transitions. This can be demonstrated qualitatively [Bla 52] by the fact that the nuclear electric moments are of the order of er (where r is the nuclear radius), while the magnetic moments are of the order of the nuclear magneton $e\hbar/2mc$. Thus, the ratio of the electric to magnetic moments is of the order of $\hbar/mcr$ (for A=100 this ratio ~ 0.04). This qualitative relationship can also be deduced from the transition operators (eq. $B.24$) by using order of magnitude estimations of the integrals involved [Bla 52].

B.5.1 TOTAL TRANSITION RATES AND REDUCED TRANSITION PROBABILITIES

$\mathrm{T}(\sigma\lambda,\mu)$ is the rate for emitting radiation with projection μ on the quantization axis. Usually we are not interested in the orientation of either the initial or final nucleus, so we sum $\mathrm{T}(\sigma\lambda,\mu)$ over m_f and average over m_i. Thus, the total transition probability $\mathrm{T}(\sigma\lambda)$ is

$$\begin{aligned}\mathrm{T}(\sigma\lambda) &= (2j_i+1)^{-1}\sum_{m_i,m_f}\mathrm{T}(\sigma\lambda,\mu : j_i m_i \rightarrow j_f m_i-\mu)\\ &= \frac{8\pi(\lambda+1)}{\lambda[(2\lambda+1)!!]^2}\frac{1}{\hbar}\left(\frac{\omega}{c}\right)^{2\lambda+1}\mathrm{B}(\sigma\lambda) \qquad (B.25)\end{aligned}$$

where

$$\begin{aligned}\mathrm{B}(\sigma\lambda) &= (2j_i+1)^{-1}\sum_{m_i,m_f}|\langle j_f m_i-\mu|M(\sigma\lambda,\mu)|j_i m_i\rangle|^2\\ &= (2j_i+1)^{-1}|\langle j_f\|M(\sigma\lambda)\|j_i\rangle|^2 \qquad (B.26)\end{aligned}$$

$\mathrm{B}(\sigma\lambda)$ is called the reduced transition probability. Since $\mathrm{B}(\sigma\lambda)$ does not include the $E^{2\lambda+1}$ dependence on the transition energy, it is very useful for comparing the strengths of the nuclear matrix elements involved in different transitions of the same multipolarity.

It is possible to estimate the nuclear transition rates starting from the above formulae

[Bla 52, Mor 76]. A useful estimate is that derived assuming that only a single nucleon takes part in the transition. If we assume an extreme single particle picture in which

(i) only one proton moves in an average central potential,

(ii) the wave functions of the initial and final states are independent of radius over the nuclear volume,

(iii) the factor $(2\lambda+1)|(j_i\frac{1}{2}\lambda 0|j_f\frac{1}{2})|^2$ which arises in the reduced transition matrix element from the coupling of the orbital and spin angular momenta is taken as unity, and

(iv) the approximation $(\frac{\lambda}{2}g_s - \frac{\lambda}{\lambda+1}g_l)^2 \sim 10$ is made for magnetic transitions

then we get the Weisskopf estimates for the transition rates:

$$\mathrm{T}^W(E\lambda) = \frac{4.38(\lambda+1)}{\lambda[(2\lambda+1)!!]^2}(\frac{3}{\lambda+3})^2(\frac{E[\mathrm{MeV}]}{197})^{2\lambda+1} \times (1.2)^{2\lambda} A^{2\lambda/3} \times 10^{21}\ \mathrm{sec}^{-1} \quad (B.27)$$

$$\mathrm{T}^W(M\lambda) = \frac{1.94(\lambda+1)}{\lambda[(2\lambda+1)!!]^2}(\frac{3}{\lambda+3})^2(\frac{E[\mathrm{MeV}]}{197})^{2\lambda+1} \times (1.2)^{2\lambda-2} A^{(2\lambda-2)/3} \times 10^{21}\ \mathrm{sec}^{-1} \quad (B.28)$$

Since they assume that only a single nucleon takes part in the transition, the Weisskopf estimates are extremely useful as an order of magnitude estimate of the number of nucleons which take part in an experimentally observed transition. For example, $E2$ transitions in which a single nucleon plays a dominant role typically have rates of the order of 10 times the Weisskopf estimates (10 wu), while those with rates of $\sim$ 100 wu are collective transitions in which many nucleons are involved in the transition. The Weisskopf transition rate estimates for some common multipoles are summarized in table B.1.

TABLE B.1

Weisskopf Transition Rate Estimates

Multipolarity	Transition Rate (s^{-1})
$E1$	$1.02 \times 10^{14} A^{2/3} E^3$
$E2$	$7.23 \times 10^{7} A^{4/3} E^5$
$E3$	$3.37 \times 10^{1} A^{2} E^7$
$M1$	$3.12 \times 10^{13} E^3$
$M2$	$2.21 \times 10^{7} A^{2/3} E^5$
$M3$	$1.03 \times 10^{1} A^{4/3} E^7$

E is the transition energy in units of MeV, and A is the atomic number of the nucleus. (These values were taken from the table 2.2 of [Mor 76].)

B.6 Electric Quadrupole Moments

The nuclear intrinsic electric quadrupole moment Q_0 is defined by

$$Q_0 = \langle Q_2(r') \rangle \tag{B.29}$$

$$Q_2(r') = \sqrt{\frac{16\pi}{5}} e \sum_{k=1}^{z} r'^2_k Y_{20}(\theta', \phi') \tag{B.30}$$

where: the primed co-ordinates are in the body-fixed system of the nucleus; and the summation is over the nuclear protons. Q_0 is a measure of the quadrupole deformation of the nucleus and Q_2 is directly proportional to the $E2$ transition operator $M(E2,0)$ (eq. $B.24$). Therefore, strong $E2$ transitions are a feature of nuclei with large quadrupole deformations.

In experimental studies the lifetimes of excited nuclear states are often measured. It can be shown from the geometric model (see, for example, [Boh 75, Pre 75]) that the intrinsic quadrupole moment is related to the reduced transition probability (eq. $B.26$) of the in-band $E2$ transitions in an axially symmetric nucleus† by the expression

$$\mathrm{B}(E2, I \rightarrow I-2) = \frac{5}{16\pi} Q_0^2 (IK20|I-2K)^2 \tag{B.31}$$

Although this equation is model dependent, no systematic differences beyond experimental error limits have been observed between intrinsic quadrupole moments determined from the $E2$ transition rates within a collective band and intrinsic quadrupole moments determined from other experimental data [Löb 75, Löb 70]. (For example, studies of the hyperfine splitting of atomic energy levels caused by the interaction between the electric quadrupole moment of the nucleus and the electric field of the atomic electrons have shown

† This does not necessarily hold for intrinsic states with $K = \frac{1}{2}$ or 1 [Pre 75].

no discrepancies.) The intrinsic quadrupole moment extracted in this manner from the B($E2$) value is sometimes called the transition quadrupole moment.

If we assume that the nuclear charge is distributed uniformly within the nuclear surface defined by eqs. 2.5, 2.7 and 2.8, then the nuclear quadrupole moment can be related to the deformation parameters. For an axially symmetric shape, this yields

$$\begin{aligned} Q_0 &= \frac{3}{\sqrt{5\pi}} ZeR_0^2\beta(1+\frac{1}{8}\sqrt{\frac{5}{\pi}}\beta) \\ &= 0.757ZeR_0^2\beta(1+0.158\beta) \end{aligned} \qquad (B.32)$$

(The coefficient of β^2 depends, within a factor of 2, upon whether R_0 is varied with β to conserve volume and also upon whether a quadrupoloid or rotational ellipsoid shape is assumed. These different conventions for defining the nuclear shape, and their effect on the quadrupole moment, are discussed by Löbner *et al.* [Löb 70].)

The relationship between the nuclear shape and the transition quadrupole moment in triaxial nuclei is more complex and has been discussed by Onishi *et al.* [Oni 86]. It is found that for the in-band $\Delta I = 2$ transitions, in the limit of high spins, the γ-dependence of the matrix element is

$$\langle I \| Q_2 \| I-2 \rangle \quad \alpha \quad \cos(30^\circ + \gamma) \qquad (B.33)$$

where γ is defined as in the Lund convention.

APPENDIX C

Energy Loss of Moving Ions in Matter

Moving ions lose energy through interactions with both the nuclei and the electrons of the stopper medium. Electronic energy loss dominates except at very low energies, where nuclear energy loss becomes important. However, at velocities below $\sim 1\%c$ large angle scattering from nuclei significantly affects DSAM lineshapes and can have more effect than the slowing down of the nuclei [Bla 66].

Typically the energy loss due to interactions with the target nuclei only represents 1% of the total energy loss for ions of energy 0.2 MeV per atomic mass unit (amu) [Zie 80], although nuclear stopping becomes relatively more important at lower energies or for very heavy ion-stopper combinations. The theory of nuclear stopping [Wil 77] is thought to be well understood, reproducing the data to an accuracy of typically better than 1% [Zie 80].

The electronic energy loss dominates for ions of energy greater than about 0.1 MeV per amu. Thus electronic energy loss must be taken into account in DSAM measurements, although as mentioned above nuclear scattering is usually also important. (For example, in the present study the initial recoil energy of the ^{80}Sr product nuclei was $\sim$ 0.4 MeV/amu.) Unfortunately, however, electronic stopping is not as well understood as the nuclear energy loss. The theoretical electronic energy loss formula due to Lindhard *et al.* [Lin 63, Lin 64] reproduces the data to an accuracy of about 20% for ions of energy less than 0.03 MeV/amu [Bla 66, Zie 80] and with somewhat less accuracy for ion energies up to as high as 0.03 $\times$ $Z^{(4/3)}$ MeV/amu, where Z is the atomic number of the ion. (The Lindhard electronic stopping power formula, for a given ion-stopper combination, varies simply as the square

root of the ion energy.) At ion energies above 1 MeV/amu the Bethe stopping formula (see, for example, the review article by U. Fano [Fan 63]) reproduces the experimental data to an accuracy of a few percent.

Several attempts have been made to parameterize the experimental stopping power data and use it to predict the stopping power for energies or for ion and stopper combinations for which no data exists. The extensive tables of Northcliff and Schilling [Nor 70] give stopping powers and ranges for a wide variety ion and stopper combinations, however these tables are typically only accurate to about 20%.

David Ward *et al.* reviewed the problem of predicting stopping powers in 1976 [War 76] in the light of new experimental data. They proposed an effective charge parameterization to predict the electronic energy loss of an ion from the known energy loss of another ion in the same stopping medium at the same velocity (or, equivalently, the same energy per mass). This parameterization was found to reproduce the experimental data to an accuracy of 10% and was used to produce a stopping power table [For 76] for all projectiles in the range $8 \leq Z \leq 20$ in Ti, Fe, Ni, Cu, Ag and Au for energies of 0.2 to 3.5 MeV per nucleon, using measurements of stopping powers for ^{19}F, ^{24}Mg, ^{27}Al, ^{32}S and ^{35}Cl in these six materials. However, Ward *et al.* concluded that, for all the additional data that they had used, their parameterization gave results which were not very different to the earlier results of Northcliffe and Schilling. This means that stopping powers accurate to 10% can be simply obtained by scaling the Northcliffe and Schilling table by the discrepancy between it and the known electronic stopping power for some other ion with the same velocity in the material of interest. That is:

$$(\mathrm{dE/dx})^{HI} = (\mathrm{dE/dx})^{HI}_{NS} \times (\mathrm{dE/dx})^{OI}_{Expt} \;/\; (\mathrm{dE/dx})^{OI}_{NS} \qquad (C.1)$$

where: the superscripts HI and OI denote the heavy ion of interest and some other ion for which the stopping power is known more accurately (by experiment), respectively; and the subscripts NS and $Expt$ indicate stopping powers taken from the tables of Northcliffe and Schilling and experimental stopping powers, respectively. This simple formula is frequently used to estimate stopping powers in materials for which there are some experimental data at velocities close to those of interest. In cases where suitable experimental data are not available for the material of interest, it is common to scale the Northcliffe and Schilling stopping power by Ziegler and Chu 's [Zie 74] table of stopping powers for ^{4}He ions.

The most comprehensive and most recent review of stopping powers is the large many volume work edited by Ziegler. Volume 5 of this work [Zie 80] gives total stopping powers for all ions in all materials for energies between 0.2 and 1000 MeV/amu in the form of plotted curves. All experimental measurements used in determining the curves are plotted on the same graphs, so that they can easily be compared to the parameterized curves (references are given for all the experimental data). The accuracy of these plots is estimated to be 5% double standard error for energies above 2 MeV/amu and 10% (20%) double standard error for energies between 0.2 and 2 MeV/amu for solid (gas) stoppers.

To extract the electronic stopping power from these curves it is necessary to subtract the nuclear stopping power. Alternatively, the electronic stopping power can be approximated, to an accuracy close to that quoted above, by using Ziegler's effective charge for the moving ion (given by equations 13 and 14 of [Zie 80]) to scale (using equation 5 of [Zie 80])

the hydrogen stopping powers of Anderson and Ziegler [And 77] which are given in terms of a table of coefficients (tables 1 and 2 of [And 77]). (However, note that equation 13 of [Zie 80] is incorrectly printed, as it needs to be multiplied by Z1, the ion charge.) This second method of estimating the electronic stopping power is particularly suited to use in computer calculations, since it requires only a few equations and a table of coefficients, and is considerably more accurate than the Lindhard stopping theory which is commonly used.

Several experimenters have observed oscillations in electronic stopping powers at low energies, as a function of the atomic number of the moving ion (see, for example, [All 75] and references therein). These oscillations are clearly not accounted for in the effective charge stopping power parameterizations of Ward *et al.* or Ziegler, or in the scaling formula for the Northcliffe and Schilling tables suggested by Ward *et al.* These oscillations were discussed by Ward *et al.* [War 76] who compared measurements of the oscillation effects at various energies and concluded that the oscillations did not persist above ~0.1 MeV/amu, which is below the energy range considered by either Ziegler or Ward *et al.* for their parameterizations.

APPENDIX D

Side Feeding Times In Heavy-Ion Fusion Evaporation Reactions

The side feeding times τ_f in a heavy-ion fusion-evaporation reaction are defined as the time delays associated with the population of discrete, observed, excited states by unobserved statistical and continuum γ-ray transitions, following formation of the compound nucleus. Although these side feeding times are short, reflecting the nature of the decay to the yrast line, they must be taken into account when measuring short level lifetimes using, in particular, the Doppler shift attenuation method (DSAM) and the recoil distance method (RDM). In the case of very short lifetimes, the side feeding time sets a lower limit on the lifetimes that can be measured following a heavy-ion fusion-evaporation reaction (except in cases where nuclei with fast feeding times can be selected using coincidence techniques, as demonstrated by Rammo *et al.* [Ram 79]).

Side feeding times have been measured for several heavy-ion fusion-evaporation reactions. Bochev et al. [Boc 76] measured τ_f into the collective bands in the four doubly even isotopes $^{160-166}$Yb, following the $^{124-130}$Te(^{40}Ar, $4n$) reactions, and Newton *et al.* [New 73] measured τ_f in ^{166,168,170}Hf and ^{178}Os, populated by the ^{150,152,154}Sm(^{20}Ne, $4n$) and ^{154}Sm(^{28}Si, $4n$) reactions. Both these studies reported side feeding times of between 1 and 12 ps. Newton *et al.* suggested that τ_f in collective nuclei tended to increase as the nuclei became more vibrational and less rotational; while the study of Bochev *et al.*, which included measurements for several states in the collective yrast bands of ^{164,166}Yb, suggested that τ_f decreased with increasing excitation energy (or, equivalently, increasing spin). In both of these studies the RDM was used to investigate the feeding times.

In contrast to the A $\gtrsim$ 160 nuclei discussed above, much faster side feeding times have been reported in the 40 $\lesssim$ A $\lesssim$ 80 mass region. In particular, the statistical model calculations of Hellmeister *et al.* [Hel 78], and the experimental results quoted therein, suggest feeding times which are typically fractions of a picosecond. In addition, Hellmeister's calculations indicate that, for the 7.04 MeV (14^+) state in the collective nucleus ^{72}Se, τ_f increases with the energy of the ^{72}Se entry state; ranging from 0.08 ps for an entry state at 10 MeV to 0.26 ps for an entry state at 18 MeV. More recently, Lühmann *et al.* [Lüh 85] have measured side feeding times in ^{75}Br by analysing DSAM lineshapes, following the ^{62}Ni(^{16}O, $p2n$)^{75}Br reaction. The results of this study yielded sidefeeding times which were fractions of a picosecond or less and which decreased with increasing excitation energy, in good agreement with both the earlier experimental and theoretical studies in this mass region and in qualitative agreement with the trends observed in A$\gtrsim$160 nuclei.

In conclusion then, although there are some experimental measurements and theoretical calculations of side feeding times in heavy-ion fusion-evaporation reactions, as outlined above, there is still no simple method of accurately predicting the side feeding times for a particular reaction. Therefore, the side feeding time can represent a considerable uncertainty in a short lifetime measurement. Futhermore, since the side feeding times are dependent upon the nuclear structure at excitation energies and angular momenta which are currently inaccessible to discrete line spectroscopy, measurements of side feeding times complement studies of unresolved continuum gamma-ray and electron conversion transitions (see, for example, [Lov 85] and [Thi 85], respectively). Thus, side feeding times are interesting in their own right, in addition to being an important parameter in lifetime measurements.

REFERENCES

[Åbe 82] S. Åberg, *High-Spin Potential-Energy Surfaces,* Phys. Scr. **25** (1982) 23

[Aha 85a] D.P. Ahalpara, K.H. Bhatt, R. Sahu, *Collective Bands in* ^{81}Sr, J. Phys. **G11** (1985) 735, and references therein

[Aha 85b] D.P. Ahalpara, A. Abzouzi and K.H. Bhatt, *A Microscopic Description of the Collective Bands in* $^{75-77}Kr$, Nucl. Phys. **A445** (1985) 1

[Alf 79] W.P. Alford, R.E. Anderson, P.A. Batay-Csorba, R.A. Emigh, D.A. Lind, P.A. Smith and C.D. Zafiratos, *A Study of the* $(^3He,n)$ *Reaction on the Isotopes of Krypton*, Nucl. Phys. **A330** (1979) 77

[All 75] K.W. Allen, *Doppler Shift Timing Methods*, in The Electromagnetic Interaction in Nuclear Spectroscopy, ed. W.D. Hamilton (North-Holland Publishing Company, 1975) p.311

[And 77] H.H. Anderson and J.F. Ziegler, *Hydrogen Stopping Powers and Ranges in All Elements*, vol. 3 of The Stopping and Ranges of Ions in Matter, ed. J.F. Ziegler (Pergamon Press, 1970)

[Ari 75] A. Arima and F. Iachello, *Collective Nuclear States as Representations of a SU(6) Group*, Phys. Rev. Lett. **35** (1975) 1069

[Ari 76] A. Arima and F. Iachello, *Interacting Boson Model of Collective States. I. The Vibrational Limit*, Ann. of Phys. **99** (1976) 253

[Ari 77] A. Arima, T. Otsuka, F. Iachello and I. Talmi, *Collective States as Symmetric Couplings of Proton and Neutron Excitations*, Phys. Lett. **66B** (1977) 205

[Ari 78] A. Arima and F. Iachello, *Interacting Boson Model of Collective States. II. The Rotational Limit*, Ann. of Phys. **111** (1978) 201

[Ari 79] A. Arima and F. Iachello, *Interacting Boson Model of Collective States. III. The O(6) Limit*, Ann. of Phys. **123** (1979) 468

[Ari 81] A. Arima and F. Iachello, *The Interacting Boson Model*, Ann. Rev. Nucl. Part. Sci. **31** (1981) 75, and references therein

[Bal 73] J.B. Ball, J.J. Pinajian, J.S. Larsen and A.C. Rester, *Study of ^{82}Sr, ^{84}Sr and ^{86}Sr with the (p,t) Reaction* Phys. Rev. **C8** (1973) 1438

[Bel 69] R.A.I. Bell, J. L'Ecuyer, R.D. Gill, B.C. Robertson, I.S. Towner and H.J. Rose, *Excitation Energies and Lifetimes of Levels in ^{26}Si*, Nucl. Phys **A133** (1969) 337

[Bel 83] E.J.M.S. Belmont Moreno, *Nuclear Spectroscopy in ^{80}Sr*, M.Sc. Thesis, University of Oxford (1983), unpublished

[Bel 84] E.J.M.S. Belmont Moreno, private communication (1984), unpublished

[Ben 80] D.W. Bennett, *Precise Nuclear Magnetic Moment Measurements in Short-Lived States of Carbon and Oxygen*, D.Phil. Thesis, University of Oxford (1980), unpublished

[Ben 84a] R. Bengtsson, P. Möller, J.R. Nix and Jing-ye Zhang, *Nuclear Shapes and Shape Transitions*, Phys. Scr. **29** (1984) 402

[Ben 84b] R. Bengtsson and J.D. Garrett, *The Cranking Model – Theoretical and Experimental Bases* (1984) to be published in International Review of Nuclear Physics, ed. T.T.S. Kuo and E. Osnes, vol. 1 (World Scientific, Singapore)

[Bla 52] J.M. Blatt and V.F. Weisskopf, Theoretical Nuclear Physics, (John Wiley and Sons, New York, 1952)

[Bla 66] A.E. Blaugrund, *Notes on Doppler-Shift Lifetime Measurements*, Nucl. Phys. **88** (1966) 501

[Boc 76] B. Bochev, S.A. Karamian, T. Kutsarova, E. Nadjakov and Yu. Ys. Oganessian, *The Feeding Times and Lifetimes of High-Spin Levels in Ytterbium Doubly Even Isotopes*, Nucl. Phys. **A267** (1976) 344

[Boh 52] A. Bohr, *The Coupling of Nuclear Surface Oscillations to the Motion of Individual Nucleons*, Mat. Fys. Medd. Dan. Vid. Selsk. **26** no. 14 (1952)

[Boh 53] A. Bohr and B.R. Mottelson, *Collective and Individual Particle Aspects of Nuclear Structure*, Mat. Fys. Medd. Dan. Vid. Selsk. **27** no. 16 (1953)

[Boh 75] A. Bohr and B.R. Mottelson, Nuclear Structure, vol. 2 (Benjamin, Reading, Mass., 1975)

[Boh 84] D. Bohle, A. Richter, W. Steffen, A.E.L. Dieperink, N. Lo Iudice, F. Palumbo

and O. Scholten, *New Magnetic Dipole Excitation Mode Studied in the Heavy Deformed Nucleus* ^{156}Gd *by Inelastic Electron Scattering*, Phys. Lett. **B137** (1984) 27

[Bon 85] P. Bonche, H. Flocard, P.H. Heenen, S.J. Krieger and M.S. Weiss, *Self-Consistent Study of Triaxial Deformations: Application to the Isotopes of Kr, Sr, Zr and Mo,* Nucl. Phys. **A443** (1985) 39

[Bra 72] M. Brack, Jens Damgaard, A.S. Jensen, H.C. Pauli, V.M. Strutinsky and C.Y. Wong, *Funny Hills: The Shell-Correction Approach to the Nuclear Shell Effects and its Applications to the Fission Process,* Rev. Mod. Phys. **44** (1972) 320

[Buc 79] D. Bucurescu, G. Constantinescu and M. Ivaşcu, Rev. Roum. Phys. **24** (1979) 971

[Buc 83] D. Bucurescu, G. Căta, D. Cutoiu, G. Constantinescu, M. Ivaşcu and N.V. Zamfir, *Description of the Neutron Deficient Sr and Zr Isotopes in the Interacting Boson Model,* Nucl. Phys. **A401** (1983) 22, and references therein

[Bun 76] R.L. Bunting and J.J. Kraushaar, Nucl. Data Sheets **18** (1976) 87

[Cas 84] R.F. Casten and D.H. Feng, *Nuclear Dynamical Supersymmetry*, Phys. Today **37** no. 11 (November 1984) 26

[Cas 85a] R.F. Casten and P. von Brentano, *An Extensive Region of O(6)-Like Nuclei Near A=130*, Phys. Lett. **152B** (1985) 22

[Cas 85b] R.F. Casten, P. von Brentano, K. Heyde, P. Van Isacker and J. Jolie, *The Interplay of γ-Softness and Triaxiality in O(6)-Like Nuclei*, Nucl. Phys. **A439** (1985) 289

[Ciz 78] J.A. Cizewski, R.F. Casten, G.J. Smith, M.L. Stelts, W.R. Kane, H.G. Börner and W.F. Davidson, *Evidence for a New Symmetry in Nuclei: The Structure of ^{196}Pt and the O(6) Limit*, Phys. Rev. Lett. **40** (1978) 167

[Dav 52] C.M. Davisson and R.D. Evans, *Gamma-Ray Absorption Coefficients*, Rev. Mod. Phys. **24** (1952) 79

[Dav 58] A.S. Davydov and G.F. Filippov, *Rotational States in Even Atomic Nuclei*, Nucl. Phys. **8** (1958) 237

[Dav 76] A.S. Davydov, Quantum Mechanics, translated, edited and with additions by D. ter Haar, second edition (Pergamon Press, 1976) p. 191

[Dew 81] A. Dewald, U. Kaup, W. Gast, A. Gelberg, K.O. Zell and P. von Brentano, *In-Beam Gamma Spectroscopy of ^{82}Sr*, in Proceedings of the 4th International Conference on Nuclei Far From Stability, Helsingør, Denmark, 1981, ed. P.G. Hansen and G.B. Nielsen, CERN report 1981-09 (CERN, Geneva, 1981) p. 418

[Dew 82] A. Dewald, U. Kaup, W. Gast, A. Gelberg, H.-W. Schuh, K.O. Zell and P. von Brentano, *High Spin States of ^{84}Sr*, Phys. Rev. **C25** (1982) 226

[Dia 66] R.M. Diamond, E. Matthias, J.O. Newton and F.S. Stephens, *Nuclear Alignment in Heavy-Ion Reactions*, Phys. Rev. Lett. **16** (1966) 1205

[Dia 80] R.M. Diamond and F.S. Stephens, *Nuclei at High Angular Momentum*, Ann. Rev. Nucl. Part. Sci. **30** (1980) 85

[Die 82] A.E.L. Dieperink and R. Bijker, *On Triaxial Features in the Neutron-Proton IBA*, Phys. Lett. **116B** (1982) 77

[Die 83] A.E.L. Dieperink, *Geometrical Analysis of the Interacting Boson Model*, Prog. Part. Nucl. Phys. **9** (1983) 121

[Duv 81a] P.D. Duval and B.R. Barrett, *Shell Model Description of the Interacting-Boson-Model Parameters for Two Nondegenerate j Shells*, Phys. Rev. Lett. **46** (1981) 1504

[Duv 81b] P.D. Duval and B.R. Barrett, *Shell-Model Determination of the Interacting Boson Model Parameters for Two Nondegenerate j Shells*, Phys. Rev. **C24** (1981) 1272

[Ell 85] J.P. Elliot, *The Interacting Boson Model of Nuclear Structure*, Reports on Prog. in Phys. **48** (1985) 171, and references therein

[End 79] P.M. Endt, *Strengths of Gamma-ray Transitions in* $A = 45 - 90$ *Nuclei*, Atomic Data and Nucl. Data Tables **23** (1979) 547

[Fan 63] U. Fano, *Penetration of Protons, Alpha Particles, and Measons*, Ann. Rev. Nucl. Sci. **13** (1963) 1

[Fed 77] P. Federman and S. Pittel, *Towards a Unified Microscopic Description of Nu-*

clear Deformation, Phys. Lett. **69B** (1977) 385

[Fed 79] P. Federman and S. Pittel, *Unified Shell-Model Description of Nuclear Deformation*, Phys. Rev. **C20** (1979) 820

[Fie 81] C.A. Fields, F.W.N. de Boer, E. Sugarbaker and P.M. Walker, *A Study of* $^{80,82,84}Sr$ *by* $(\alpha, 2n)$ *Reactions*, Nucl. Phys. **A363** (1981) 352

[Fie 83] C.A. Fields, F.W.N. de Boer and J. Sau, *A Study of the* $^{84}Kr(\alpha, 2n\gamma)^{86}Sr$ *Reaction*, Nucl. Phys. **A398** (1983) 512

[For 76] J.S. Forster, D. Ward, H.R. Andrews, G.C. Ball, G.J. Costa, W.G. Davies and I.V. Mitchell, *Stopping-Power Measurements for* ^{19}F, ^{24}Mg, ^{27}Al, ^{32}S *and* ^{35}Cl *at Energies* ~ 0.2 *to* ~ 3.5 *MeV/Nucleon in Ti, Fe, Ni, Cu, Ag and Au*, Nucl. Instr. and Meth. **136** (1976) 349

[Fun 83] L. Funke, F. Dönau, J. Döring, P. Kemnitz, E. Will, G. Winter, L. Hildingsson, A. Johnson and Th. Lindblad, *Shape Change and Fast M1 Transitions in* ^{81}Kr, Phys. Lett. **120B** (1983) 301

[Hama 84] I. Hamamoto, *A Comment on the Analysis of Nuclei with Triaxial Shape*, Phys. Lett. **143B** (1984) 31

[Hama 85] I. Hamamoto, *Nuclear Structure Studies of Rotating Nuclei*, Proceedings of the Winter College on Fundamental Nuclear Physics, Trieste, Italy, 1984, ed. K. Dietrich, M. Di Toro and H.J. Mang, vol. 2 (World Scientific, Singapore, 1985) p. 755

[Hami 85] J.H. Hamilton, P.G. Hansen, E.F. Zganjar, *Advances in Studies of Nuclei far from Stability*, Reports on Progress in Physics **48** (1985) 631, and references therein

[Has 85] P.S. Haskins, F.E. Dunnam, R.L. Coldwell, A.C. Rester, R.B. Piercey, M.L. Muga, H.A. Van Rinsvelt, R.W. Smart, H.J.M. Aarts, J.D. Fox, L.C. Dennis and C.B. Shaw, *In-Beam Gamma-Ray Spectroscopy of* ^{82}Sr, Phys. Rev. **C32** (1985) 1897

[Hel 78] H.P. Hellmeister, K.P. Lieb, W. Müller, *Statistical Model Calculations of Continuum Feeding Times in Heavy-Ion Fusion Reactions*, Nucl. Phys. **A307** (1978) 515

[Hel 79] H.P. Hellmeister, J. Keinonen, K.P. Lieb, U. Kaup, R. Rascher, R. Ballini, J. Delaunay and H. Dumont, *Study of High Spin States in* ^{78}Kr, Nucl. Phys. **A332** (1979) 241

[Hey 84] K. Heyde, J. Moreau and M. Waroquier, *Evidence for Very Large Deformation in the Neutron Deficient Nuclei with* $Z \simeq 40$, Phys Rev. **C29** (1984) 1859

[Hig 83] T. Higo, S. Matsuki and T. Yanabu, *Level Structure of* $^{80,82}Sr$ *via the* $^{78,80}Kr(\alpha, 2n\gamma)$ *Reactions*, Nucl. Phys. **A393** (1983) 224

[Iac 79] F. Iachello, in Interacting Bosons in Nuclear Physics, ed. F. Iachello, [Ettore Majorana International Science Series Vol. 1; Proc. of the First Symp. on Interacting Bosons in Nucl. Phys., Erice, Sicily, June 6-9, 1978] (Plenum Press,

New York, 1979) p. 1

[Iac 83] F. Iachello, *The Interacting Boson Model and Its Symmetries*, Proceedings of the International Conference on Nuclear Physics (Florence 1983), ed. P. Blasi and R.A. Ricci, vol. 2, (Tipografia Compositori, Bologna, 1983) p. 145, and references therein

[Ing 54] D.R. Inglis, *Particle Derivation of Nuclear Rotation Properties Associated with a Surface Wave*, Phys. Rev. **96** (1954) 1059

[Ing 55] D.R. Inglis, *Dynamics of Nuclear Deformation* , Phys. Rev. **97** (1955) 701

[Kau 79] U. Kaup and G. Gelberg, *Description of the Even-Even Krypton Isotopes by the Interacting Boson Approximation,* Z. Phys. **A293** (1979) 311

[Kau 83] U. Kaup, C. Mönkemeyer and P. von Brentano, *Band Structure of the Even-Even Selenium Isotopes in the Proton-Neutron Interacting Boson Model*, Z. Phys. **A310** (1983) 129

[Kem 83] P. Kemnitz, J. Döring, L. Funke, F.R. May, P. Ojeda, E. Will and G. Winter, *Evidence for Non-axial Shapes in* $^{81,82,83}Kr$, Z. Phys. **A313** (1983) 367

[Kra 73] K.S. Krane, R.M. Steffen and R.M. Wheeler, *Directional Correlations of Gamma Radiations Emitted From Nuclear States Oriented by Nuclear Reactions or Cryogenic Methods*, Nucl. Data Tables **11** (1973) 351

[Lin 63] J. Lindhard, M.Scharff and H.E. Schiott, *Range Concepts and Heavy Ion Ranges*

(Notes on Atomic Collisions, II), Mat. Fys. Medd. Dan. Vid. Selsk. **33** no. 14 (1963)

[Lin 64] J. Lindhard, Nucl. Science Series, Report No. 39, Publication 1133 (1964) 1

[Lis 81] C.J. Lister, P.E. Haustein, D.E. Alburger and J.W. Olness, *New Isotope* ^{80}Y, *and the Decays of* ^{79}Sr, ^{81}Y, *and* ^{82}Y, Phys. Rev. **C24** (1981) 260

[Lis 82] C.J. Lister, B.J. Varley, H.G. Price and J.W. Olness, *Extreme Prolate Deformation in Light Strontium Isotopes*, Phys. Rev. Lett. **49** (1982) 308

[Löb 70] K.E.G. Löbner, M. Vetter and V. Hönig, *Nuclear Intrinsic Quadrupole Moments and Deformation Parameters*, Nucl. Data Tables **A7** (1970) 495

[Löb 75] K.E.G. Löbner, *Gamma-ray Transition Probabilities in Deformed Nuclei*, in The Electromagnetic Interaction in Nuclear Spectroscopy, ed. W.D. Hamilton (North Holland, Amsterdam, 1975)

[Lov 84] D.J.G. Love, *Fourth Generation γ-ray Spectroscopy and a Study of* ^{131}Ce, Ph.D. Thesis, University of Liverpool (1984) unpublished

[Lov 85] D.J.G. Love, A.H. Nelson, P.J. Nolan and P.J. Twin, *Measurement of In-Band Transition Probabilities at High Spin*, Phys. Rev. Lett. **54** (1985) 1361

[Lüh 85] L. Lühmann, M. Debray, K.P. Lieb, W. Nazarewicz, B. Wörmann, J. Eberth and T. Heck, *Yrast Transition Strengths and Band Structure of* ^{75}Br, Phys. Rev. **C31** (1985) 828

[Mat 74a] E. der Mateosian and A.W. Sunyar, *Tables of Attenuation Coefficients for Angular Distributions of Gamma-rays from Partially Aligned Nuclei*, Atomic Data and Nucl. Data Tables **13** (1974) 391

[Mat 74b] E. der Mateosian and A.W. Sunyar, *Tables of Angular Distribution Coefficients for Gamma-rays of Mixed Multipolarities Emitted by Aligned Nuclei,* Atomic Data and Nucl. Data Tables **13** (1974) 407

[Moi 69] M. Moinester, J.P. Schiffer and W.P. Alford, *Multipole Analysis of Particle-Particle or Particle-Hole Multiplets*, Phys. Rev. **179** (1969) 984

[Möl 81] P. Möller and J.R. Nix, *Atomic Masses and Nuclear Ground-State Deformations Calculated with a New Macroscopic-Microscopic Model*, Atomic Data and Nucl. Data Tables **26** (1981) 165

[Mor 76] H. Morinaga and T. Yamazaki, In-Beam Gamma-Ray Spectroscopy (North Holland, Amsterdam, 1976)

[Naz 85] W. Nazarewicz, J. Dudek, R. Bengtsson, T. Bengtsson and I. Ragnarsson, *Microscopic Study of the High-Spin Behaviour in Selected* $A \simeq 80$ *Nuclei*, Nucl. Phys. **A435** (1985) 397

[New 73] J.O. Newton, F.S. Stephens and R.M. Diamond, *Feeding Times in (HI,* $xn\gamma$*) Reactions*, Nucl. Phys. **A210** (1973) 19

[New 74] J.O. Newton, *Gamma-Rays from Heavy-Ion Reactions*, in Nuclear Spectroscopy and Reactions Part C, ed. J. Cerney, (Academic Press, New York and London,

1974) p. 185

[Nil 55] S.G. Nilsson, *Binding States of Individual Nucleons in Strongly Deformed Nuclei*, Mat. Fys. Medd. Dan. Vid. Selsk. **29** no. 16 (1955)

[Nol 74] E. Nolte, Y. Shida, W. Kutschera, R. Prestele and H. Morinaga, *Investigation of Neutron Deficient Nuclei in the Region* $28 < N, Z < 50$ *with the Help of Heavy Ion Compound Reactions*, Z. Phys. **268** (1974) 267

[Nol 75] E. Nolte and P. Vogt, *Rotational Bands in* ^{77}Kr, Z. Phys. **A275** (1975) 33

[Nor 70] L.C. Northcliffe and R.F. Schilling, *Range and Stopping-Power Tables for Heavy Ions*, Nucl. Data Tables **A7** (1970) 233

[Oni 86] N. Onishi, I. Hamamoto, S. Åberg and A. Ikeda, *Effects of Quantum Fluctuations on Electromagnetic Properties in Triaxial Nuclei*, Nucl. Phys. **A452** (1986) 71

[Ooi 86] S.S.L. Ooi, R.F. Davie, D. Sinclair, C.J. Lister, B.J. Varley and H.G. Price, *Identification of the First Excited State in the* $N = Z$ *Nucleus* $^{64}_{32}Ge_{32}$, Phys. Rev. **C34** (1986); S.S.L. Ooi, D. Phil. Thesis, University of Oxford (1986) unpublished

[Ots 77] T. Otsuka, computer program *NPBOS*, University of Tokyo, Japan (1977); see also KVI internal report KVI-253 (1979 ?)

[Ots 78a] T. Otsuka, A. Arima, F. Iachello and I. Talmi, *Shell Model Description of*

Interacting Bosons, Phys. Lett. **76B** (1978) 139

[Ots 78b] T. Otsuka, A. Arima and F. Iachello, *Nuclear Shell Model and Interacting Bosons*, Nucl. Phys. **A309** (1978) 1

[Ots 79] T. Otsuka, *Boson Model of Medium-Heavy Nuclei*, Ph.D. Thesis, University of Tokyo, Japan (1979)

[Pan 82] J. Panqueva, H.P. Hellmeister, L. Lühmann, F.J. Bergmeister, K.P. Lieb and T. Otsuka, *Nuclear Structure Studies of High-Spin States in ^{79}Rb and ^{79}Kr*, Nucl. Phys. **A389** (1982) 424

[Pie 81] R.B. Piercey *et al.*, *Evidence for Deformed Ground States in the Light Kr Isotopes,* Phys. Rev. Lett. **47** (1981) 1514, and references therein

[Pre 75] M.A. Preston and R.K. Bhaduri, Structure of the Nucleus (Addison-Wesley, Reading, 1975)

[Pri 83] H.G. Price, C.J. Lister, B.J. Varley, W. Gelletly and J.W. Olness, *Observation of Rigid Nuclear Rotation*, Phys. Rev. Lett. **51** (1983) 1842

[Püh 77] F. Pühlhofer, *On the Interpretation of Evaporation Residue Mass Distributions in Heavy-Ion Induced Fusion Reactions*, Nucl. Phys. **A280** (1977) 267

[Rai 50] J. Rainwater, *Nuclear Energy Level Argument for a Spheroidal Nuclear Model*, Phys. Rev. **79** (1950) 432

[Rag 84] I. Ragnarsson and R.K. Sheline, *Systematics of Nuclear Deformations*, Phys.

Scr. **29** (1984) 385

[Ram 79] N.R.F. Rammo, A.M. Al-Naser, A.H. Behbehani, L.L. Green, A.N. James, J.F. Sharpey-Schafer, H.M. Sheppard and P.J. Nolan, *Lifetime Measurements Using Gamma-Gamma Coincidence Techniques Following a Heavy Ion Induced Fusion Evaporation Reaction;* ^{46}*Ti, an Example*, Nucl. Instr. and Meth. **161** (1979) 291

[Rog 72] D. Rogers and D.W. Bennett, computer program *QC* for calculating, angular distribution attenuation coefficients for Ge(Li) and NaI detectors

[Ros 67] H.J. Rose and D.M. Brink, *Angular Distributions of Gamma Rays in Terms of Phase-Defined Reduced Matrix Elements*, Rev. Mod. Phys. **39** (1967) 306

[Sam 82] M. Sambataro and G. Molnár, *Configuration Mixing in Mo Isotopes*, Nucl. Phys. **A376** (1982) 201

[Sam 84] M. Sambataro, O. Scholten, A.E.L. Dieperink and G. Piccitto, *On Magnetic Dipole Properties in the Neutron-Proton IBA Model*, Nucl. Phys. **A423** (1984) 333

[Sch 76] J.P. Schiffer and W.W. True, *The Effective Interaction Between Nucleons Deduced from Nuclear Spectra*, Rev. Mod. Phys. **48** (1976) 191

[Sch 80] O. Scholten, *The Interacting Boson Approximation Model and Applications*, Ph.D. Thesis, University of Groningen (1980), unpublished, and references therein

[Sha 63] A. de-Shalit and I. Talmi, Nuclear Shell Theory (Academic Press, New York and London, 1963)

[Ste 72] R.M. Steffen and K. Alder, *Angular Distributions and Correlations of Gamma Rays*, in The Electromagnetic Interaction in Nuclear Physics, ed. W.D. Hamilton (North Holland, 1972) p. 505

[Str 67] V.M. Strutinsky, *Shells Effects in Nuclear Masses and Deformation Energies,* Nucl. Phys. **A95** (1967) 420

[Str 68] V.M. Strutinsky, *"Shells" in Deformed Nuclei,* Nucl. Phys. **A122** (1968) 1

[Sym 64] G.D. Symons and J. de Boer, *Coulomb excitation of* ^{86}Sr *and* ^{88}Sr*,* Bull. Am. Phys. Soc. **9** (1964) 554, N9

[Thi 85] J.P. Thibaud, P. Aguer, G. Bastin, L. Nguyen, N. Perrin, H. Sergolle, J. Gizon, P. Hubert and M.M. Villard, *M1 Character of Unresolved Continuum Transitions from X-ray Multiplicity Measurements*, Z. Phys. **A321** (1985) 275

[Twi 83] P.J. Twin, P.J. Nolan, R. Aryaeinejad, D.J.G. Love, A.H. Nelson and A. Kirwan, *TESSA : a Multi-Detector Gamma-Ray Array Designed to Study High Spin States*, Nucl. Phys. **A409** (1983) 343c

[Van 84] P. Van Isacker, K. Heyde, J. Jolie and O. Scholten, *Mixed-Symmetry States in the Neutron-Proton Interacting-Boson Model*, in Workshop on Interacting Boson-Boson and Boson-Fermion Systems, Gull Lake, Michigan, 28-30 May 1984, ed. O. Scholten, (World Scientific, Singapore, 1984) p. 334

[Voi 83] M.J.A. de Voigt, J. Dudek, Z. Szymański, *High Spin Phenomena in Atomic Nuclei*, Rev. Mod. Phys. **55** (1983) 949

[War 76] D. Ward, J.S. Forster, H.R. Andrews, I.V. Mitchell, G.C. Ball, W.G. Davies and G.J. Costa, *Stopping Powers for Heavy Ions*, Atomic Energy of Canada Limited report AECL-5313 (1976)

[Wil 56] L. Wilets and M. Jean, *Surface Oscillations in Even-Even Nuclei*, Phys. Rev. **102** (1956) 788

[Wil 77] W.D. Wilson, L.G. Haggmark and J.P. Biersak, *Calculation of Nuclear Stopping, Ranges, and Straggling in the Low-Energy Region*, Phys. Rev. **B15** (1977) 2458

[Wil 82] D. Wilkinson (ed.), Collective Bands in Nuclei, Prog. Part. Nucl. Phys. **9** (1982); this volume centres on the IBM and its interpretation and relationship with other nuclear models, and contains many interesting and informative articles

[Woo 83] J.L. Wood, *Experimental Aspects of the Interacting Boson Approximation*, Nucl. Phys **A396** (1983) 245, and references therein

[Wör 84] B. Wörmann, K.P. Lieb, R. Diller, L. Lühmann, J. Keinonen, L. Cleemann and J. Eberth, *The Yrast Bands in ^{77}Kr and ^{76}Kr*, Nucl. Phys. **A431** (1984) 170

[Yam 67] T. Yamazaki, *Tables of Coefficients for the Angular Distribution of Gamma-rays from Aligned Nuclei,* Nucl. Data **A3** (1967) 1

[Zie 74] J.F. Ziegler and W.K. Chu, *Stopping Cross Sections and Backscattering Factors for ^4He Ions in Matter, $Z = 1 - 92$, $E(^4He) = 400 - 4000$ keV*, Atomic and Nucl. Data Tables **13** (1974) 463

[Zie 80] J.F. Ziegler, *Handbook of Cross-Sections for Energetic Ions in All Elements*, vol. 5 of The Stopping and Ranges of Ions in Matter, ed. J.F. Ziegler (Pergamon Press, 1980)

^{80}Sr

GSB

SB1

SB2

SB3

17095 (26$^+$)
2153
14942 (24$^+$)
2021
12921 (22$^+$)
1857
11064 20$^+$
1736
9328 18$^+$
1578
7750 16$^+$
1474
6276 14$^+$
1324
4951 12$^+$
1186
1678 10$^+$
1065
3765 (7$^+$)
937
2700 8$^+$
783
980 4$^+$
595
386 2$^+$
386
0 0$^+$

15464 (25$^+$)
1746
13718 (23$^+$)
1649
12069 (21$^+$)
1533
10537 (19$^+$)
1441
9096 (17$^+$)
1368
7728 (15$^+$)
1260
6468 (13$^+$)
1120
5348 (11$^+$)
970
4378 (9$^+$)
777
3601 (7$^+$)
1838
6$^+$
1763

(J+10) 8782
1382
(J+8) 7400
1198
(J+6) 6202
1035
(J+4) 5167
867
(J+2) 4301
662
J 3639
1343
3$^+$
1571
1185

7833 (15$^+$)
1339
6494 (13$^+$)
1220
5274 (11$^+$)
1105
4169 (9$^+$)
997
3172 (7$^+$)
877
2296 (5$^+$)
724
1316

798
(7$^+$)
3580
1817